Carolin Früh

Identification of Space Debris

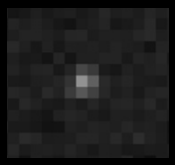

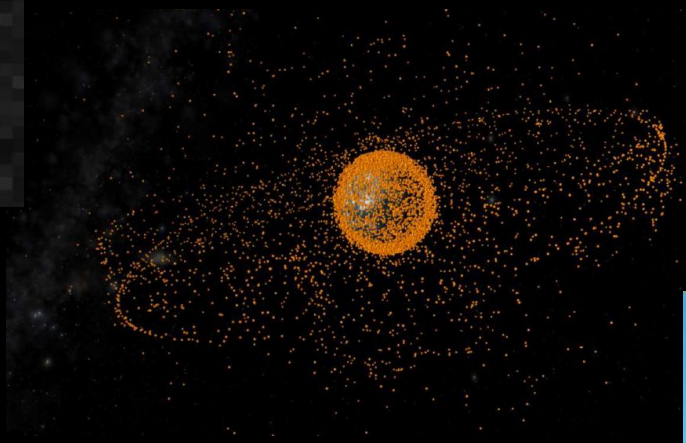

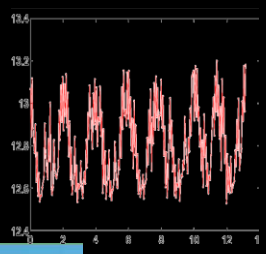

Identification of Space Debris

Inauguraldissertation
der Philosophisch-naturwissenschaftlichen Fakultät
der Universität Bern

vorgelegt von

Carolin Früh

von Deutschland

Leiter der Arbeit:
Prof. Dr. T. Schildknecht
Astronomisches Institut der Universität Bern

Identification of Space Debris

Inauguraldissertation
der Philosophisch-Naturwissenschaftlichen Fakultät
der Universität Bern

vorgelegt von

Carolin Früh

von Deutschland

Leiter der Arbeit:
Prof. Dr. T. Schildknecht
Astronomisches Institut der Universität Bern

Von der Philosophisch-Naturwissenschaftlichen Fakultät angenommen 22.9.2011.

Contents

List of Figures

List of Tables

Frequently Used Acronyms

AMR	Area-to-Mass Ratio
AIUB	Astronomical Institute of the University of Bern, Switzerland
CCD	Charge Coupled Device
CelMech	Celestial Mechanics Program System
DRP	Direct Radiation Pressure
DISCOS	Database and Information System for the Characterization of Objects in Space
ESA	European Space Agency
ESASDT	ESA Space Debris Telescope
FOV	Field Of View
GEO	Geostationary Earth Orbit
GTO	Geostationary Transfer Orbit
HAMR	High Area-to-Mass Ratio
LAMR	Low Area-to-Mass Ratio
HEO	High Eccentricity Earth Orbit
ISON	International Scientific Observation Network
LEO	Low Earth Orbit
NASA	National Aeronautics and Space Administration
rms	Root-Mean-Square (error)
TLE	Two Line Elements
USSTRATCOM	United States Strategic Command
ZIMLAT	Zimmerwald Laser and Astrometry Telescope
ZimSMART	Zimmerwald Small Aperture Robotic Telescope

1. Prologue

> In other words then, if a machine is expected to be infallible, it cannot also be intelligent. There are several theorems which say almost exactly that. But these theorems say nothing about how much intelligence may be displayed if a machine makes no pretence at infallibility.
>
> *Alan Turing, 1947*

An unlimited wide space with nebulae, in which stars are born, space telescopes, which deliver us images of space and wonders unseen, technical progress, which expands the limits of mankind: The sky is not closed and out of reach any more, it has been subdued; there are steps on the Moon, rovers on Mars. Researchers are involved in exploring new parts of space; new missions are planned and launched. Scientists are serving the greater good in protecting our home planet from impacts, understanding the origins of the universe, or being midwives of the exploration of the universe. They follow the insatiable human longing for the total presence of the outer world and nature as the *en-soi*, as J.-P. Sartre puts it. The view from a large enough distance, or at an ideal disconnected setup, apparently allows to fit the world in a mathematical theory.

But it is the human *pour-soi*, which always introduces and spots the imperfect. The dream of unlimited space lasted for not even 50 years. The remnants of space fairing are closely orbiting the Earth, the unlimited sky has been narrowed by densely spaced junk, showing clearly the traces of human efforts.

With space debris and junk, the morticians in space research emerged. They do not bother about new stars, bright new missions, but they dig in the trash. A space debris researcher has many good arguments for his research: the importance of finding the sources and drains of space debris objects, the need to protect space assets, the necessity of enabling space fairing, space missions, and space based research in the future. But for a true space debris researcher, the protection of space assets and assurance of a safe sustainable use of space is only collateral damage.

As for every researcher, the fascination does not lie in the outcome of the research – it may be all useful, necessary, nice, or dangerous – it is the research itself; in this case, the debris and trash itself. Being involved in observational space debris research, it is even the curiosity and enjoyment of *observing the mess*. What comes out of it, in terms of engineering, mitigation strategies, and services, is only secondary to the basic research.

All debris objects are man-made. Although we are their creator, things truly slipped us out of hand. We cannot blame the problem of space debris on an unknowable Creator or evil demiurge. We are overwhelmed by the sheer number of objects, by the complexity of reality and its detail richness. It is a research in the dirt of the laws and theories of physics in a real world, with all uncertainties, unattainability, measurements errors, and statistics. The objects are brought to space and from that very moment we are busy collecting data, to understand what we have done and, what nature does to our own creation. As soon as the objects have been let loose, we are busy getting a hold on them again. It reminds us of the limit of our power, which we were inclined to forget about, when traveling to the Moon.

The human influence is not neglected as in other branches of science – it is the cause of the objects themselves. Space debris research is research about nature and its laws, by means of the objects, which we created and about which we deceived ourselves with the conviction, we would fully understand.

Carolin Früh Bern, 28.3.2011

2. Introduction

> We have found a strange footprint on the shores of the unknown. We have devised profound theories, one after another, to account for its origins. At last, we have succeeded in reconstructing the creature that made the footprint. And lo! It is our own.
>
> *Sir Arthur Eddington, 1920*

2.1 Space Debris

In 1993 (and 2001) the International Academy of Astronautics (IAA) defined the term space debris/orbital debris in its position paper [39] as follows:
Orbital debris is herein defined as any man-made object, which is non-functional with no reasonable expectation of assuming or resuming its intended function, or any other function for which it is or can be expected to be authorized, including fragments and parts thereof.

This definition represents a significant step to rise awareness for the problem of space debris, which evolved slowly over the years. Up to the mid-eighties of the past century the problem of space debris and the protection of space environment was only an issue for a very small group of experts, sometimes viewed as exotics in the space community. Nowadays, the problem of space debris is no longer not only an issue in science but has reached awareness of everybody dealing with space assets and the near earth space environment. Only about 40 years after the launch of the first satellite Sputnik 1 in 1957 the remnants of the space activities could not be ignored any more. Figure 2.1 shows the number of launches per year, from the first launch in 1957. Whereas the total number of launches seems to decrease after 1982, more payload is brought into space by a single launch compared to earlier times. Figure 2.2 shows the increase of the number of resident space objects, just called objects in the following, over the past years, which are listed in the publicly available catalogue of the US Strategic Command (USSTRATCOM). This catalogue is supposed to be complete down to object sizes of ten centimeter in lower orbits with altitudes of several hundred kilometers above Earth's surface, and down to meter objects in higher altitudes around 36 000 kilometers. As of today the catalogue contains 16 000 objects. Figure 2.3 shows a simulation of a snapshot of the catalogued space debris population around the Earth in 2009. The population consists of active space assets, former active satellites, upper stages, and so-called mission-related objects. Among the latter are e.g., adapters used between two satellites in a dual launch, bolts, and instrument covers, to just name a few. But the majority of objects are fragments. There are 203 known historic fragmentations,

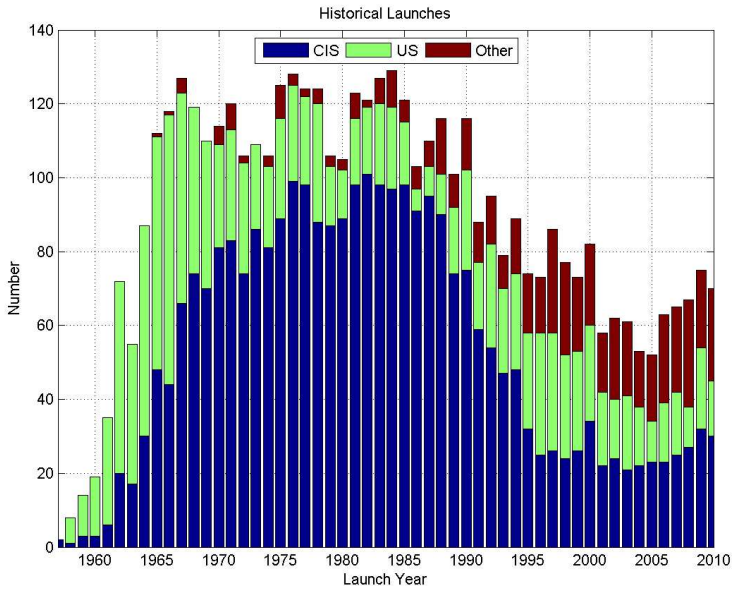

Figure 2.1: Number of successful launches per year (Celestrak).

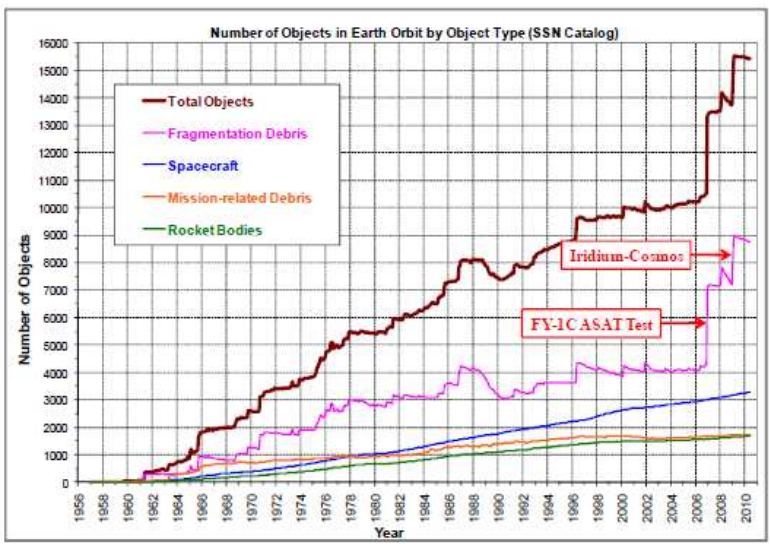

Figure 2.2: Cumulative number of catalogued objects in Earth orbit per year (Liou [55]).

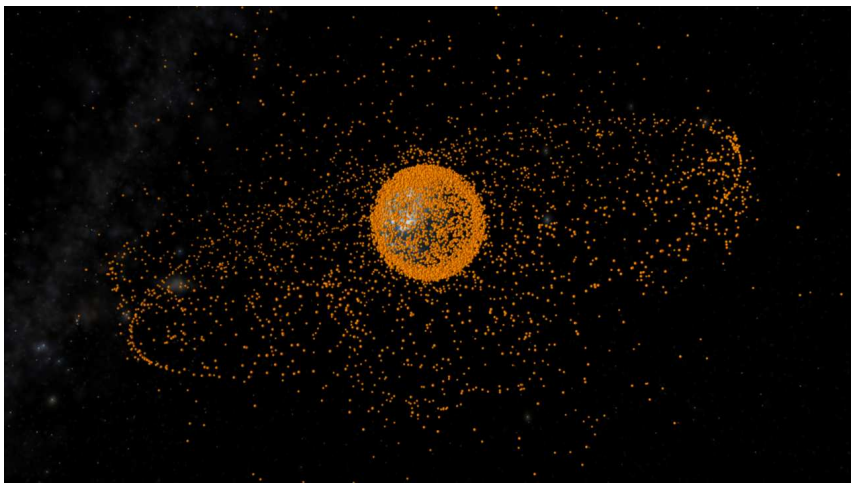

Figure 2.3: Population of all catalogued space objects seen from a distance of 15 Earth radii (ESA, in 2009).

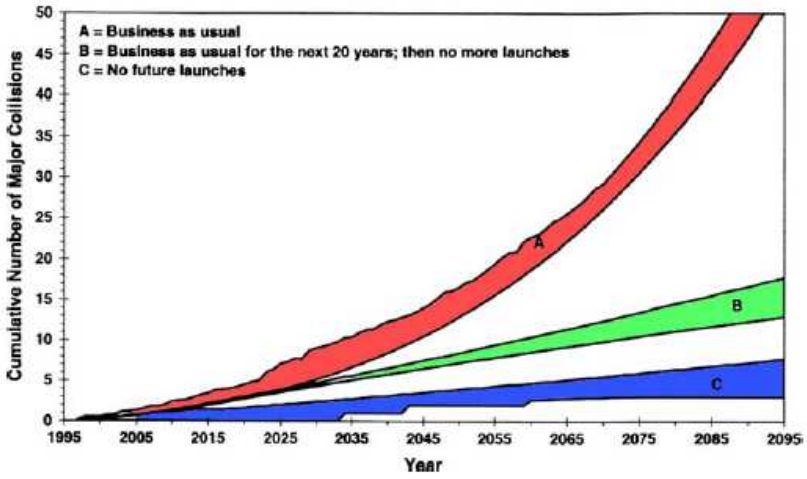

Figure 2.4: Actual and predicted number of major collisions in different scenarios (IAA position paper [40]).

most of them due to explosions. Major recent fragmentations were due to the Chinese anti-satellite test in 2007, as well as due to the collision of an active satellite of the Iridium constellation (Iridium 33) and Cosmos 2251 in 2009. Fragmentations take place due to aging of satellites, and (unobserved) in-orbit collisions between space debris objects. If a critical density of objects is present, a so-called cascading effect may be invoked, also called Kessler syndrome: Near Earth space is populated with more and more fragmentation objects even if new launches are stopped immediately, as illustrated in Fig 2.4. Only about 7% of all catalogued objects are active spacecrafts, 93% are space debris (ESA, 2009).

Due to the large relative velocities of space objects of several kilometers per second, even small fragments may cause tremendous damage. A few examples are shown in Fig 2.5. Figure 2.5a shows the impact of a 0.5 cm aluminum sphere on a solid aluminum cube, with the relative velocity of 6.5 km/s,

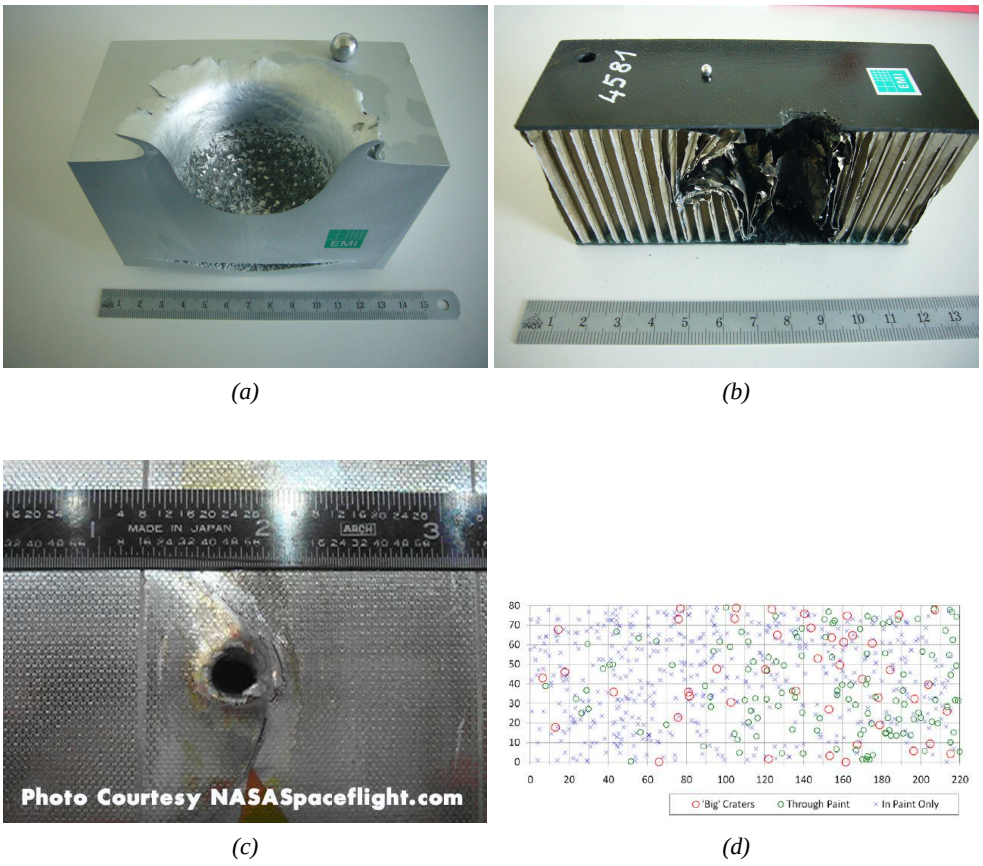

(a) *(b)*

(c) *(d)*

Figure 2.5: Impacts of small sized space debris (a) impact experiment of a 10mm aluminum sphere on a massive aluminum cube at relative velocity of 6.5 km/s (EMI), (b) impact experiment of 3mm aluminum sphere on a standard sandwich panel at relative velocity of 6.0 km/s (EMI), (c) one of many impacts on the Endeavor Space Shuttle after return (NASA), (d) number of impacts on the surface of the Wide Field Camera-2 radiator of the Hubble Space Telescope, the majority stems from space debris (Opiela [68]).

Fig 2.5b the impact of a 2 mm aluminum sphere on a standard sandwich panel with a relative velocity of 6.0 km/s. Both of these realistic models of the impact of space debris on spacecraft materials were produced by the Fraunhofer EMI in Freiburg, Germany. Figure 2.5c shows one of the impacts of the Endeavor Space Shuttle after return, Fig. 2.5d the number of impacts on the surface of the Wide Field Camera-2 radiator of the Hubble Space Telescope. The radiator was 15 years in space and has a size of 2.2 x 0.8 m. A few impacts are also due to micrometeorites, but the far majority is caused by space debris, see [68] for further details.

Near Earth space is subdivided into several regions. The definition from different sources differ in details. The following definition is used in the following: first, there is the so-called low Earth orbit region (LEO) up to 2 000 kilometer altitude, medium earth orbit region (MEO) from 2 000 to 35 586 kilometer, then the geosynchronous Earth orbit region (GEO) 35 586 to 35 986 kilometer. The geostationary transfer orbit region (GTO) is defined by elliptical orbits with an apogee in the GEO or so-called super-GEO (above GEO) region and a perigee in the LEO region. The distribution of the about 16 000 objects cataloged by USSTRATCOM is shown in Fig. 2.6. Only 5% of all objects are in GEO orbits. But despite this small number, the protection of the GEO region is of extreme importance. In contrast to the LEO region, where objects are affected by atmospheric drag, no natural cleaning mechanism exists for the GEO region. The GEO region is used by many operational satellites, due it its unique properties of one revolution per sidereal day. A collision in the geostationary ring, as the one of Iridium and Cosmos in LEO.

Space object orbits in GEO are mainly influenced by the gravitational field of the Earth, but also by those of Sun and Moon, and, depending on their area to mass ratio (AMR), by solar radiation pressure. The term Δ_{22} of the expansion of the Earth gravitational potential, results in a libration motion of the objects around the closest stable point either at 75 degree East or 105 degree West. The Earth's oblateness term, Δ_{20}, in addition with the gravitational field of the Sun and the Moon lead to a precession of the orbital plane with a 53 year period (Allan, Cook [2]) around the the stable, so-called Laplace plane. The Laplace plane, which is orthogonal to the axis of angular momentum, has an inclination of 7.5 degrees with respect to the Earth equatorial plane, its nodal line is in direction of the vernal equinox. This leads to a variation in the inclination of orbits of $\pm$ 15 degrees, T. Schildknecht [78]. The precession of orbital elements is illustrated by Fig 2.7. The controlled objects are mostly at inclination zero in the geostationary ring, periodically performing so-called station keeping maneuvers, to stay in their intended orbits. The uncontrolled objects consequently pass the GEO ring containing active spacecrafts twice a day.

The research related to the space debris environment tells that the sustainable use of space is not warranted. The IADC declared GEO and LEO as so-called protected regions. This declaration was adopted by the United Nations. The protected regions are illustrated in Fig. 2.8. Special rules apply for the population of protected regions as active mitigation strategies: The passivation of upper stages to prevent self-explosion and the post mission disposal rule, asking for a decay within 25 years after the completion of the mission for LEO objects to protect the environment. As Liou [55] points out, the removal of five large objects in key orbits would already have an immense impact on the future fragmentation rate. Technical solutions for active removal are in the planning phase. As of today no concept for the active removal of non-cooperative objects with fast spinning rates are available.

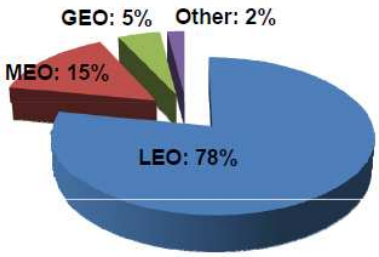

Figure 2.6: Distribution of catalogued objects in the different orbital regimes (Johnson [41]).

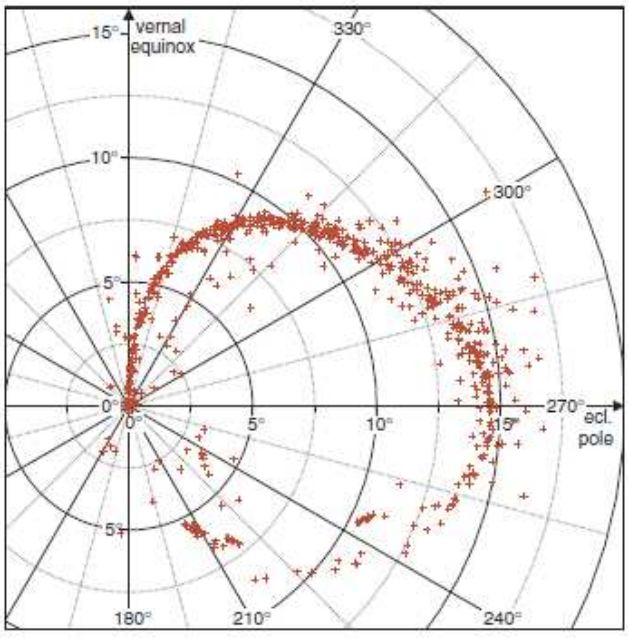

Figure 2.7: Precession of the orbits of geostationary satellites, the coordinates are right ascension and declination (Schildknecht [78]).

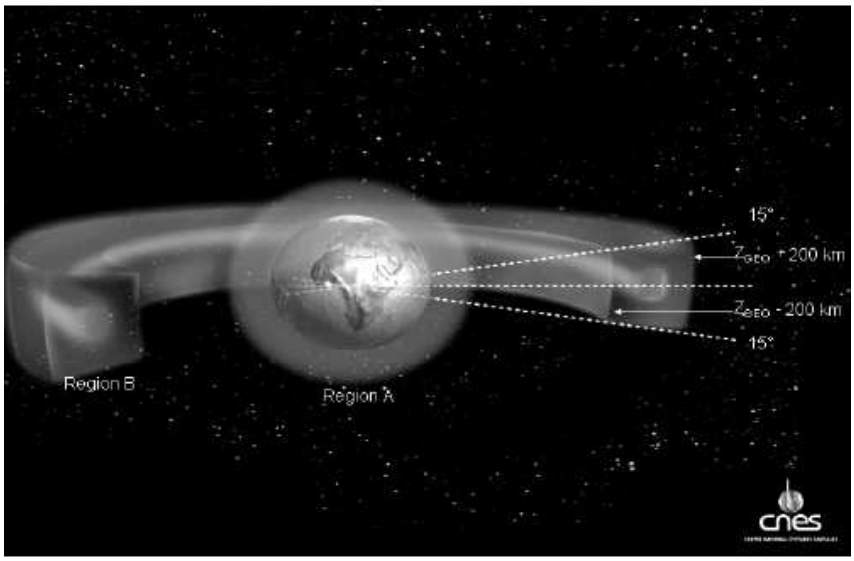

Figure 2.8: Protected orbital regions (CNES).

2.2 Optical Observations of Space Debris

The Astronomical Institute of the University of Bern (AIUB) performs optical observations of space debris in GEO, GTO and other highly elliptical orbits since over ten years. Optical observations measure the apparent brightness of the sunlight reflected by the observed objects. The brightness of objects crucially depends on the distance of the object to the observer, the specific viewing condition, the attitude motion, the size and reflection properties (including color) of the observed objects. In order to convert the apparent brightness (magnitude, calibrated relative to star background) into an object size, an albedo for the overall reflectivity of the object is needed. The albedo is unknown for objects, for which no material properties are known. In optical observations range information is only indirectly available after an orbit determination.

The AIUB performs space debris observations with the ESA Space Debris telescope (ESASDT) on Tenerife, Spain, and, owns and operates the Zimmerwald observatory, Switzerland, with two telescopes, the Zimmerwald Laser and Astrometry Telescope (ZIMLAT) and the Zimmerwald Small Robotic Telescope (ZimSMART). The ESASDT is a one meter telescope on a English mount, with a Ritchey-ChrÃ©tien optic, equipped with a mosaic of four CCD detectors of a total of $4\,096 \times 4\,096$ pixels. The field of view (FOV) is 0.7×0.7 degrees, which corresponds to a pixel scale of 0.6 arcseconds. The ESASDT allows observations of objects as faint as magnitude 20.

The Zimmerwald observatory with two the telescopes is operated on a regular basis. The ZIMLAT telescope is a one meter telescope on a azimuth-elevation fork mount with a Ritchy-Cretien optic, equipped with a $2\,048 \times 2\,048$ pixel camera, with a FOV of 0.43×0.43 degrees, and a pixel scale of 0.7 arcseconds per pixel. The ZimSMART telescope is on a paralactic mount currently operated with two different Newton flat-field optics, and cameras, either with a 18 cm aperture with a FOV of 4.6×4.6 degrees or with a 30 cm aperture with 2.0×2.0 degrees FOV. The pixel scales are 4.8 and 3.8 arcseconds per pixel,

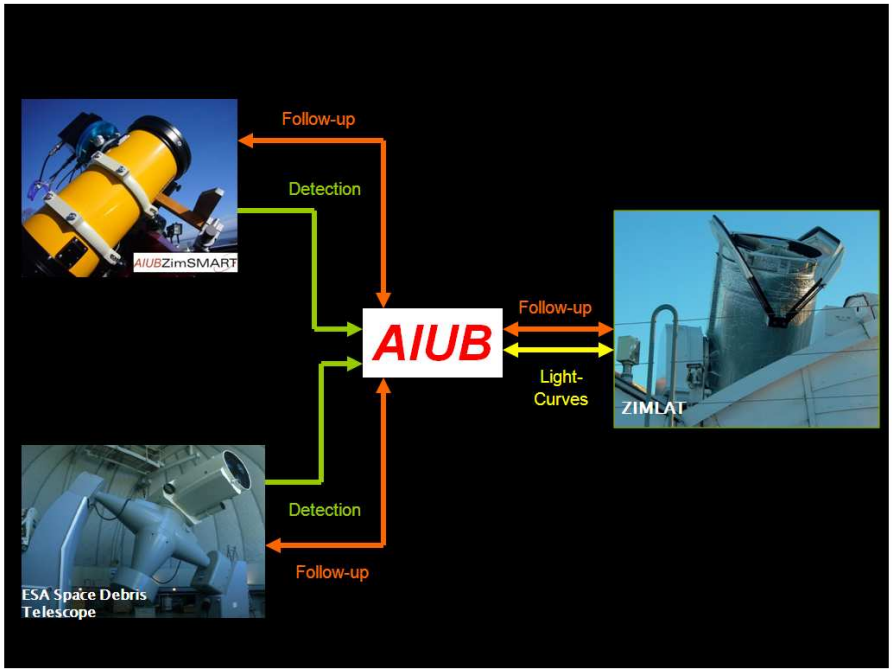

Figure 2.9: Tasking of the telescopes operated by the AIUB.

respectively. Objects of magnitude 18 with ZIMLAT and around magnitude 15 with both ZimSMART optics, respectively, may be observed.

All observations of ZIMLAT and ZimSMART and the space debris observations of the ESASDT, are collected at the AIUB, where all observations are also planned, the different sensors are tasked, and orbits are determined with the CelMech (Beutler [4]) tool. The planning, observation and analysis scenario is shown in Fig. 2.9.

ESASDT and ZimSMART are used in survey and in follow-up mode, ZIMLAT only in the follow-up mode. In survey mode declination stripes of the sky are scanned, in order to detect objects without prior information of their orbital elements. The tracking during a survey can be optimized for different orbital regimes: In so-called blind tracking mode, the telescope is tracking with an apparent velocity typical for objects in a specific orbital region. Blind tracking is chosen in order to reach the highest integration time on the least number of pixels during exposure, to increase signal-to-noise ratio. For detection of new GEO objects, the telescope is kept in staring mode, so the telescope rests in an Earth fixed system. In GTO surveys the telescope is operated with a tracking velocity of 7.5 and 10.5 arcseconds per second. The detection of objects in those orbital regions is mainly limited by their brightness, the size of the FOV of the telescope and the performance of the object image linking algorithms. The FOV together with the temporal spacing between exposures imposes constraints on the maximum and minimum apparent velocity of the objects relative to the blind tracking velocity. For the object image linking, a minimum amount of single object images is needed, to uniquely associate the different images of one object and finally enable a first orbit determination.

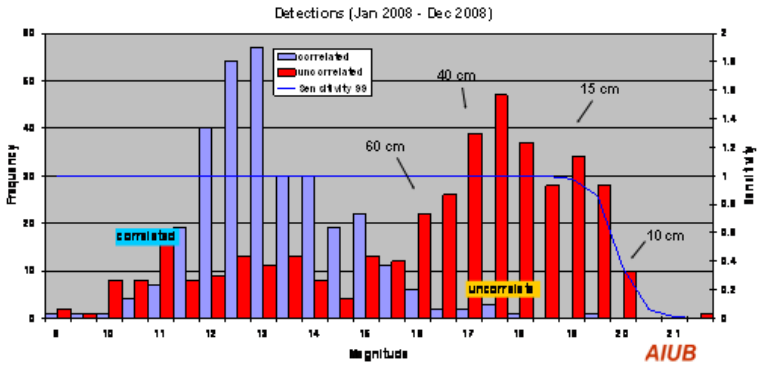

Figure 2.10: Number of correlated (with USSTRATCOM catalogue) and uncorrelated objects in standard surveys of the year 2008 AIUB at the ESASDT as a function of magnitude. The solid line shows the instrument sensitivity determined from independent calibration measurements (AIUB).

After the initial detection, so-called follow-up observations can be scheduled, to improve and secure orbits. In follow-up observations, the first orbit is propagated and observations are scheduled to track this specific object to get more observations for an improved orbit. Additional observations can also be gained with a survey-only strategy. For further details on survey strategy, follow-up and survey only strategies consult Schildknecht [84], Musci et. al. [65][67] and Herzog et. al. [32]. The entire processing and orbit determination software was developed in-house at the AIUB.

This allows the AIUB to maintain a small catalogue of objects, which are not listed in the USSTRATCOM catalogue, which is considered to be complete down to one meter objects in GEO orbits. The AIUB catalogue includes very faint objects, objects in high eccentricity orbits and high area-to-mass ratio (HAMR) objects. To further investigate the physical characteristics of objects, filter measurements may be made at ZIMLAT and ZimSMART and spectral measurements at the ESASDT. Additionally, light curves, that are brightness measurements over time, are routinely made with ZIMLAT. AIUB observations showed that numerous fainter objects, can be found in that orbital region as well. With the assumption of an albedo value of 0.8 the objects are suspected to be as small as 10 centimeter. Figure 2.10 shows the objects detected during the surveys of the year 2008. The optical together with radar and in situ measurements of returned material suggest that instead of the listed 16 000 objects in the USSTRATCOM catalogue (as of 2010) 300 000 objects larger than one centimeter are orbiting the Earth.

The AIUB has a fruitful collaboration with the Keldish Institute of Applied Mathematics (KIAM), Moscow, Russia. The collaboration includes the exchange of observations of very faint objects. The observations of the Keldish Institute are gained by the International Scientific Optical Network (ISON), which consists of 25 optical instruments (as of November 2010). Starting with facilities in the former Soviet Union, ISON reached meanwhile a good distribution of its instruments around the globe.

2.3 Outline

This work addresses the difficulty to identify space objects in GEO and HEO (high eccentricity orbit) regimes by means of ground based optical observations: The identification is understood here in the widest sense, starting with the detection of single object images, over catalogue correlation and orbit determination including an estimation of the area-to-mass ratio up to gaining more insight in the objects' properties through light curve measurements. The aim is to collect information related to an object by investigating all data, which is available via optical observations, including orbit and object properties. The work has been partially published in the papers listed in Chapter 3, but goes beyond the results presented there.

Chapter 4 gives a brief overview of the routine processing pipeline of the ESASDT.

Starting with single observation frames, which contain, apart from the space debris objects, stars, hot pixels and so-called cosmic ray events, new cosmic filters are introduced in Chapter 5. The newly developed filters are compared to the existing filter and their performance is validated. In a next step, a new algorithm is introduced for linking of single images of the same object on series of survey frames. Chapter 6 illustrates the challenges and compares the old and the new algorithm and evaluates their performances.

In Chapter 7 the correlation with external orbital element catalogues is investigated. A new algorithm to perform catalogue correlation without a priori knowledge within the ESASDT processing pipeline is discussed and contrasted to the old algorithm. In Section 7.3 the correlation with data in two line element format (TLE) is studied, especially the data of the USSTRATCOM catalogue. The empirical determination of differences between propagated ephemerides and optical observations is investigated. In a second step, Section 7.4, the correlation with ephemerides of orbit determinations with observations of the internal AIUB catalogue is analyzed, with emphasize on sparse data and HAMR objects.

In Chapter 8 the characterization possibilities of light curve measurements are illustrated for known and unknown space objects. The potential of a catalogue of light curves to assist the orbital element catalogue is discussed.

The results are summarized in Chapter 9.

3. List of Publications

Acting is happy agony.

Jean-Paul Sartre

Papers

C. Früh, R. Musci and T. Schildknecht, Improved Method for Recognizing Unknown Space Debris Objects on Series of CCD Frames. In *Proceedings of the International Astronautical Congress 2008, A6.5.2, Glasgow, Scotland, Great Britain, 29 Sep- 3 Oct, 2008*

C. Früh, T. Schildknecht, R. Musci and M. Ploner, Catalogue Correlation of Space Debris Objects. In *Proceedings of the Fifth European Conference on Space Debris, ESOC, Darmstadt, Germany, 30 March-2 April 2009*

C. Früh, T. Schildknecht and M. Ploner, Comparison of Different Methods of Ephemeris Retrieval for Correlation of Observations of Space Debris Objects. In *Proceedings of the 2009 AMOS Technical Conference, Maui, Hawaii, USA, 1-4 September 2009*

C. Früh and T. Schildknecht, Orbit Propagation and Validation with Angle-Only Observations. In *Proceedings of the 20th AAS/AIAA Astrodynamics Specialist Conference,Toronto, Canada, August 2nd - 5th, 2010*

C. Früh and T. Schildknecht, Investigation of Properties and Characteristics of High-Area-to-Mass Ratio Objects Based on Examples of Optical Observation Data of Space Debris Objects in GEO-like Orbits. In *Proceedings of the 2010 AMOS Technical Conference, Maui, Hawaii, USA,14-17 September 2010*

C. Früh and T. Schildknecht, Analysis of Observed and Simulated Light Curves of Space Debris. In *Proceedings of the International Astronautical Congress 2010, A6.1.9, Prague, Czech Republic, 27 Sep-1 Oct, 2010*

C. Früh, T. Schildknecht, A. Hinze and M. Reber, Optical Observation Campaign in the Framework of the ESA Space Surveillance System Precursor Services. In *Proceedings of the European Space Surveillance Conference, Madrid, Spain, 7 - 9 June, 2011*

C. Früh and T. Schildknecht, Combination of Light Curve Measurements and Orbit Determination for Space Debris Identification. In *Proceedings of the International Astronautical Congress 2011, A6.1.14, Cape Town, South Africa, 3 - 7 Oct, 2011*

Co-authored Papers

T. Flohrer, T. Schildknecht, C. Früh, R. Musci and M. Ploner, Optical Observations at the Zimmerwald Observatory. In *Proceedings of the International Astronautical Congress 2007, Hyderabad, India, 21 - 28 Sep, 2007*

T. Schildknecht, R. Musci, C. Früh and M. Ploner, Color Photometry and Light Curve Observations of Space Debris GEO. In *Proceedings of the International Astronautical Congress 2008, A6.1.4, Glasgow, Scotland, Great Britain, 29 Sep- 3 Oct, 2008*

T. Flohrer, H. Krag, H. Klinkrad, B. Bastida Virgili and C. Früh, Improving ESA's Collision Risk Estimates by an Assessment of he TLE orbit errors of the US SSN Catalogue. In *Proceedings of the Fifth European Conference on Space Debris, ESOC, Darmstadt, Germany, 30 March-2 April 2009*

M. Ploner, T. Schildknecht, C. Früh and A. Vananti, Space Surveillance Observations at the Zimmerwald Observatory. In *Proceedings of the Fifth European Conference on Space Debris, ESOC, Darmstadt, Germany, 30 March-2 April 2009*

J. Herzog, C. Früh and T. Schildknecht, Build-up and Maintenance of a Catalogue of GEO Objects with ZimSMART and ZimSMART2. In *Proceedings of the International Astronautical Congress 2010, A6.5.2, Prague, Czech Republic, 27 Sep- 1 Oct, 2010*

T. Schildknecht, C. Früh, A. Hinze and J. Herzog, Dynamical Properties of High Area to Mass Ratio Objects in GEO-Like Orbits. In *Advances in Space Research*, to be published in 2011

T. Schildknecht, W. Flury, C. Früh, J. Herzog, A. Hinze and A. Vananti, Using Optical Observations to Survey, Track, and Characterize Small-Size Objects at High Altitudes. In *28th International Symposium on Space Technology and Science, June 5-12, Okinawa, Japan, 2011*.

4. Processing Pipeline

To invent you need a good imagination
and a pile of junk.

Thomas A. Edison

4.1 Overview: The Pipeline

All frames taken during surveys and follow-up observations with the ESASDT are processed automatically in real time within the night. The frames pass through a processing pipeline, to extract exact object positions, to determine a first orbit and if listed, to find a correlation with a catalogue object. This chapter describes the processing steps of the ESASDT processing pipeline. Figure 4.1, 4.2 and 4.3 show the graphical user interface, which can be used to manually perform single steps of the processing and illustrates the sequence of algorithms. The processing unit lists can roughly be devided in image processing, precise astrometry and orbit determination. Details presented in the following sections are either taken from the *CCD Off-Line Data Processing Software User Manual* [80], the *Final Report: CCD Algorithms for Space Debris Detection* [81] or extracted directly from the software code.

4.2 Averaged Frame: IPMEDI

In a first step a number of p frames of an observation series are averaged. In the ESASDT processing the default value of $p = 9$ frames are averaged. Five different averaging methods are available: arithmetic average, median, and three so-called clipped averages: so-called clipped median average, clipped minimum or maximum average. For the determination of the clipped median average, the n lower and the m upper values above the median are averaged. As default values $n = 2$ and $m = 2$ are chosen; $n = m = 0$ results in the unclipped median. For the clipped minimum average the n lowest intensities are averaged, for the maximum average the m highest intensities are averaged; the defaults are $n = 2$ and $m = 3$.

In a final step, the averaged frame is normalized to a chosen ADU value, by default this is set to be 10000 ADU.

In surveys, an object class is tracked with so-called blind-tracking, in follow-up observations a specific object is tracked, during the exposure. The telescope is repositioned to the same star field in between

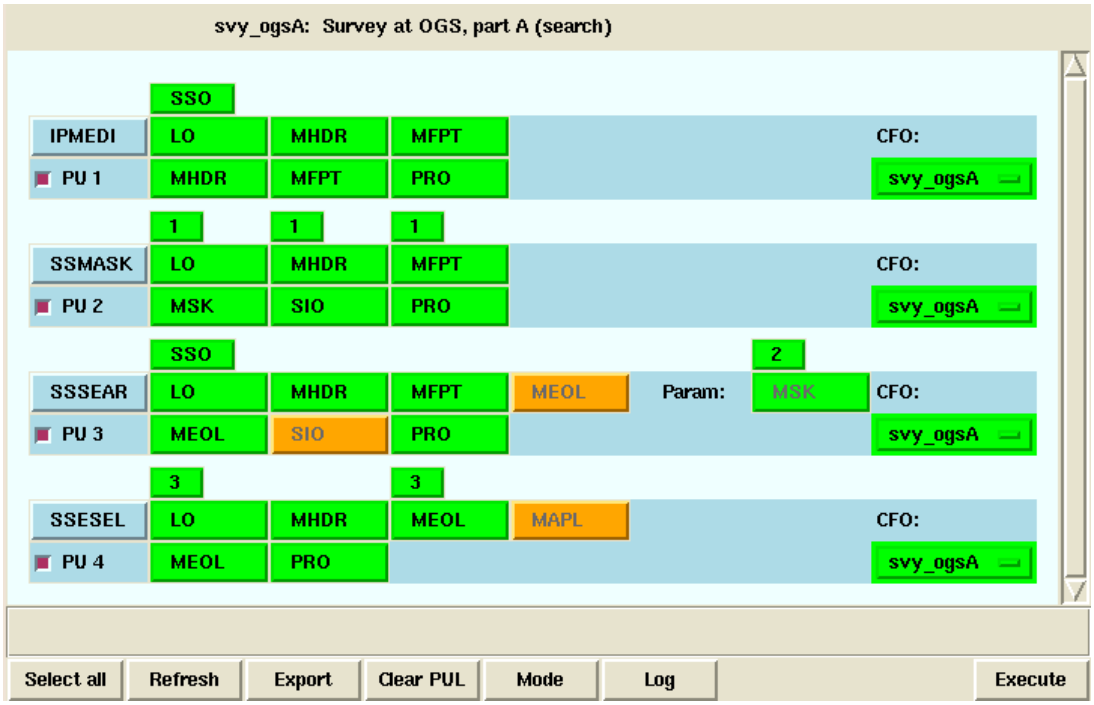

Figure 4.1: First processing unit list (PUL) of the ESASDT automatic processing software: Image processing.

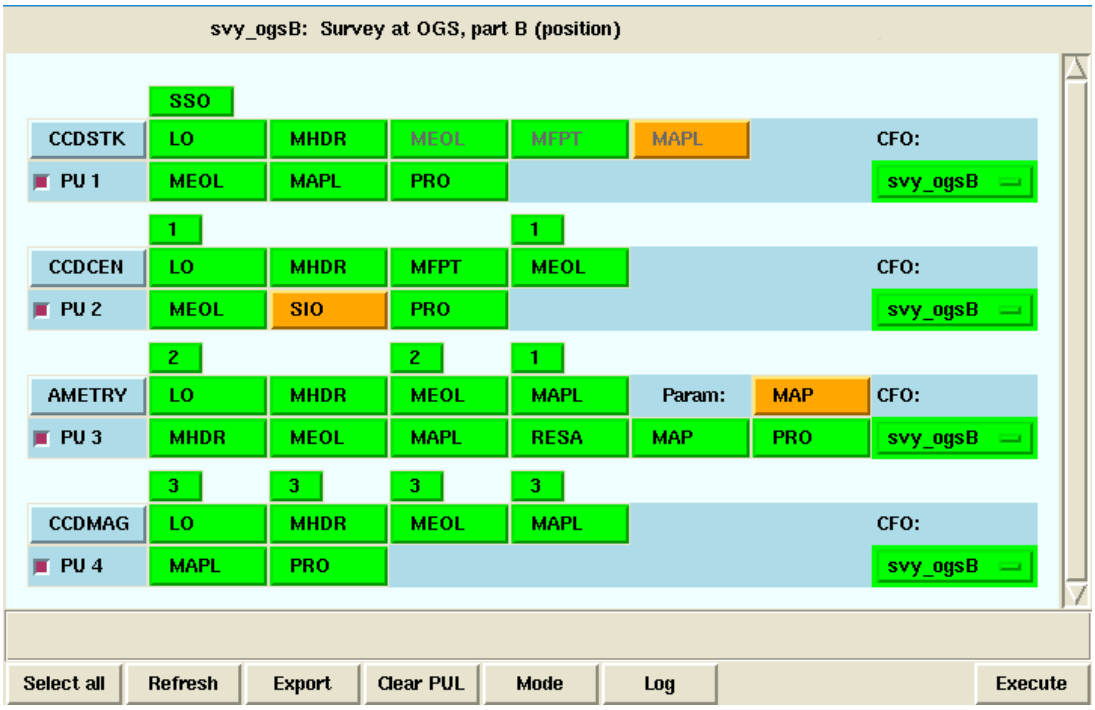

Figure 4.2: Second processing unit list (PUL) of the ESASDT automatic processing software: Precise Astrometry.

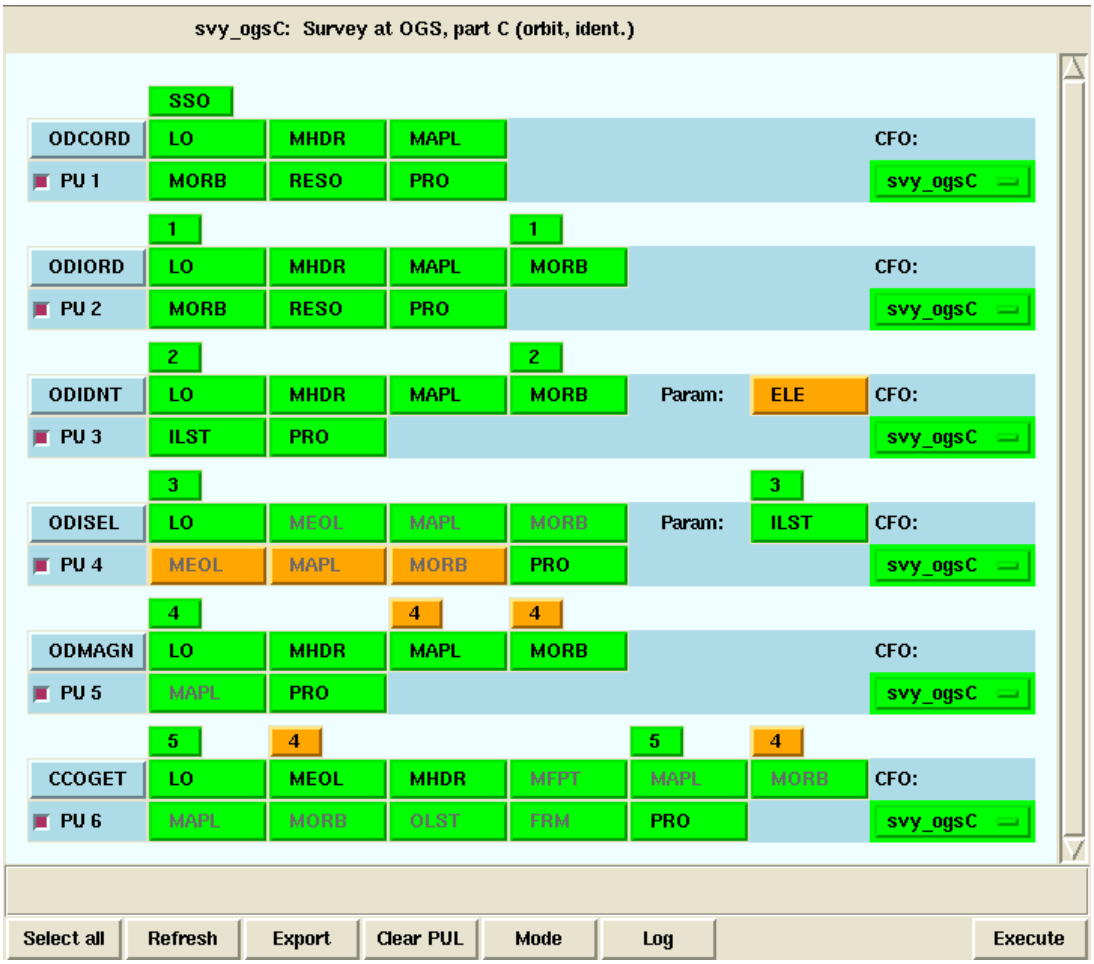

Figure 4.3: Final processing unit list (PUL) of the ESASDT automatic processing software: Orbit Determination.

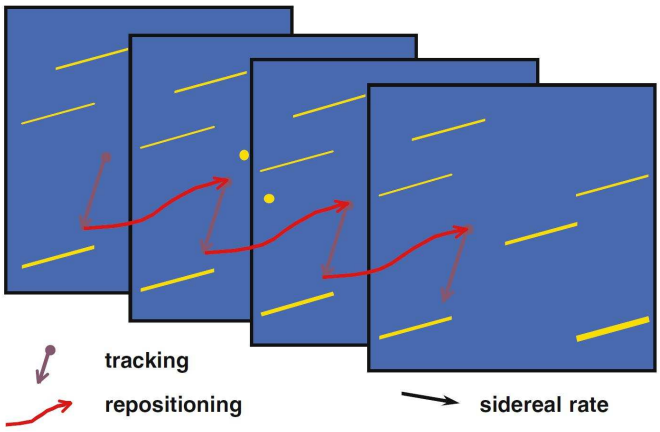

Figure 4.4: Tracking scenario for surveys and follow-up observations. In follow-up observations the object is tracked during exposure, in surveys blind tracking is used during exposure. In between exposures the telescope is repositioned thus on all frames the same star field is displayed (Schildknecht [78]).

exposures in both cases. Figure 4.4 illustrates that method. The averaged frame only shows the star background and all moving objects are eliminated, because of this observation strategy of the ESASDT.

4.3 Masking: SSMASK

4.3.1 Mask Generation

In the second step of the processing pipeline of the ESASDT, the so-called mask is generated, which is used to eliminate stars trails from the frames. The mask is generated from the object-free averaged frame from the first processing step. The output of the masking step is the mask, that is the averaged reference frame, in which the star images are *cut out*. The mask is based on a so-called symbolic image of objects (SIO), in which the star traces and background pixels are marked with symbolic pixel values.

The SIO is generated in two parts: First a background is determined on the averaged frame. The background determination is performed in two steps: an initial background determination and an improved background determination, which will be explained in detail in the next section. In the second part of the mask generation, the star images are detected on the averaged frame, the identical algorithms are also used for the object image detection in later processing steps. This star/object image search is split into two steps. First, the so-called scanning, the actual detection of star/object images, is performed, then, in the so-called recognition, the search for all pixels belonging to a specific star/object image, is performed.

After a first background determination, an improved background is determined interlocked with the object/star image detection in an iterative process.

In a last step the detected object/star images must pass final checks: Only traces, which consist of a minimum number of pixels and a minimum intensity are accepted as object/star images. As default val-

ues for the mask generation at least 20 pixels and 50 ADUs are required.

A pixel border is wrapped around each detected star image to enlarge the mask, to ensure that all star images are completely covered by the mask. Star images may vary slightly in pixel size and in the precise position on the frame due the jitter from one frame to the next and to varying brightness, which is in turn caused by differences in atmosphere.

4.3.2 Background Determination

4.3.2.1 First Background Determination

Four methods for the initial background determination are available in the ESASDT processing. The first one, simply called *background* in the menu, determines an arithmetic mean value over all pixels and a standard deviation under the assumption of a normal distribution of the intensity values. The second option, is called *backgr & mask*. First, a reference mask, which must be a priorily available, is subtracted from the single frames and then, from those frames an arithmetic average is determined. Normally, no a priori mask is available. The third and fourth option determine a median value for the background. The third option *median* determines a median over the entire frame. A median filter is applied to n subframes of the original frame. In the ESASDT processing scheme normally the frame is divided into $n = 9$ subframes. Within each subframe one value with the same subframe pixel coordinates and m values around the median of these values are chosen. In ESASDT processing m is normally set to 5. This procedure is performed in a loop over all subframe pixels. As a fourth option, called *median & sfrm*, the subframes are divided in further blocks, usually chosen to have an edge length of 40 pixels. For each block an average pixel value is determined. Instead of taken the median using each pixel within the subframes, the median is taken using each block. The *median & sfrm* background determination provides the best results in the determination of an initial background and is used by default in the ESASDT processing. A background level and a standard deviation are determined. The methods *median* and *median & sfrm* efficiently calculate a background level, as long as a fraction smaller than $(n - m)/n$ (in the default case ($4/9 \approx 0.44$) is covered by stars or candidate object images. $n - m$ should be an even number in order to not introduce a bias in the background determination.

For extremely inhomogeneous frames the background may be determined independently for each subframe. These subframes are named *tiles* in the current menu, their size may be defined by the user.

4.3.2.2 Improved Background Determination

An improved background is determined in a second step. The improved background determination is performed interlocked with the object/star image scanning steps. All pixels detected in the object scanning steps are removed and a new background is determined on the object/star image free frame. This step is repeated with the new background as the initial background. Two iterations are performed by default, which is chosen to be sufficient in the ESASDT processing. Theoretically, different background models might be applied, e.g., polynomials of different degrees. Studies have been performed by the AIUB with three different background models: a linear gradient function with three free parameters, a quadratic function with six free parameters, and a function of subframes with a flat background. Currently, no background model is implemented.

Figure 4.5: Filter geometries of spatial filters [81].

4.3.3 Star/Object Image Search: Scanning and Recognition

In the first step of the object image detection, the entire frame may be transformed by a filter. A so-called cross-filter, 2×2 or a 3×3 filter can be applied. Their geometries are illustrated in Fig. 4.5. With a pixel scale of 0.6 arcseconds per pixel, object images are normally spread over several pixels. The intensity of the pixels around the center of an object image is increased by the filters and their signal to noise ratio is improved. As a default a 3×3 binning is used.

Subsequently, the frame is scanned for pixels above the background level plus a user defined $n \cdot \sigma$, whereas n is a rational number, and σ is the standard deviation of the background level. The first step in the object/star image detection is called scanning, the second recognition. In both steps the same algorithms for object/star image detection, which are explained in detail in the next subsection, are used, but an improved background determination is performed between the steps, after the object image pixels are removed, which where detected in the scanning step. In the second step in the current implementation, the improved background level is used and all objects are newly detected without a priori knowledge from the object scanning step. For the mask generation, a higher sigma value is chosen for the object scanning step compared to the object recognition step, to ensure that all possible pixels of a star/image are added to the mask: $2.5 \cdot \sigma$ for scanning and $1.7 \cdot \sigma$ for recognition may be chosen.

4.3.3.1 Object/Star Image Recognition Algorithms

Three different algorithms are available for the object/star image detection, namely *fill*, *border & fill*, and *tree*. The simplest algorithm, the *fill* algorithm, is illustrated by Fig. 4.6a. The object image is scanned row by row and all pixels inside the first and the last pixel of an object image and the holes in the object image are filled. The *border & fill* and *tree* an initial pixel of the object image is required, determined with the fill algorithm. It is the pixel with the highest intensity value, given that it is most likely to lie well within the object image.

The mechanism of the *border & fill* algorithm is illustrated by Fig. 4.6b. Starting from the initial pixel, which is assumed to belong to the object image, a border pixel is searched by scanning, starting from the initial pixel, along the row of the initial pixel, until background level is reached for the first time. Starting from the pixel at which the background value was first reached, a so-called walk-around-the-border is invoked by testing all adjacent pixels to find counterclockwise the full border of the object. After completing of the walk, all pixels inside the border are considered to belong to the object image. By construction there are no holes within the object images.

The *tree* algorithm also starts with an initial pixel. The search for object pixels is performed along a

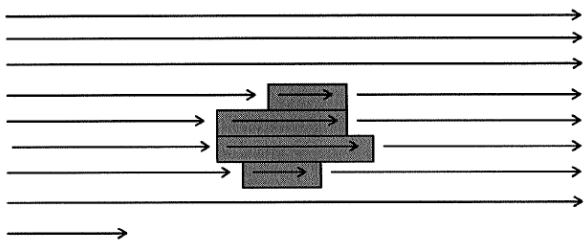

(a)

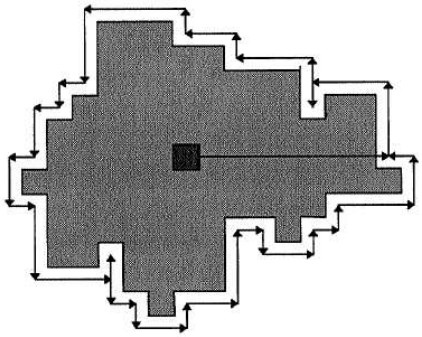

(b)

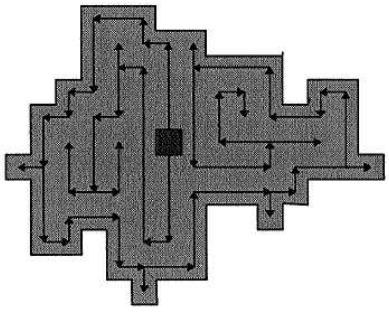

(c)

Figure 4.6: Algorithms for object detection: (a) fill algorithm (b) border & fill algorithm, (c) tree algorithm [81].

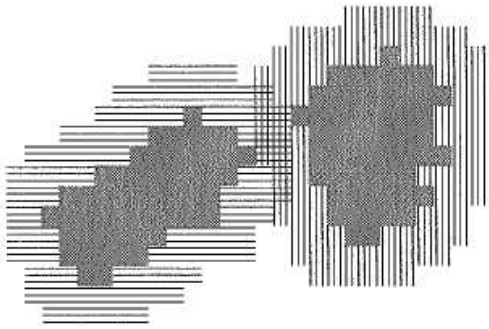

Figure 4.7: Overlap of two object images. The core of the object images is illustrated gray, the border is shaded.

tree like path as illustrated by Fig. 4.6c. Starting from the initial pixel the next node pixel is determined. The user may test for four or eight neighboring pixels to determine the next node within the object image. Thus, each pixel inside the object images is checked four or eight times. Starting from the node all pixels are tested in counterclockwise direction, whether they belong to the object image or not, i.e., whether they are above the threshold of the background level plus $n \cdot \sigma$. The full object image is determined when the node is referring to the initial pixel.

Test showed that the *border & fill* algorithm is the most efficient [81].

After the recognition, the center of each object image, has to be determined. The center of the object image determines the precise position of the object at the observation epoch. As the center, the center of the moment of light is determined. No Gaussian fit is performed. This allows to determine an exact center even of distorted object images.

4.4 Object Image Search: SSSEAR

The mask, determined in the previous step, is applied to each frame in the next step. The masking technique is illustrated by Fig. 4.8. The stars are not at the precisely same position on each of the frames due to jitter. The mask may be transformed to fit the exact positions of the star field on the individual frame. A translation by an integer number of pixels or a translation combined with a rotation may be applied. The transformation may determined from the differences of the raw pointing coordinates. Tests showed, that the raw pointing coordinates are not very precise, which lead to wrong results in the application of the transformations. Another option is implemented in the ESASDT processing: The mask is re-centered according to the brightest star on a subframe area. But, tests showed that one single star is not sufficient for a reliable and correct re-centering of the mask. It is therefore recommended not to transform the mask. Remark: Sub-pixel transformations are critical, as applying an rotation other than a multiple of 90 degrees to an image. The rotated object image has to be fit into the pixel values again. This process is called rasterization and can lead to a deformation of the original image.

The next steps are the same as those in the previous processing step. After having subtracted the mask from each frame a background is determined for each frame, a first object scanning is performed, an im-

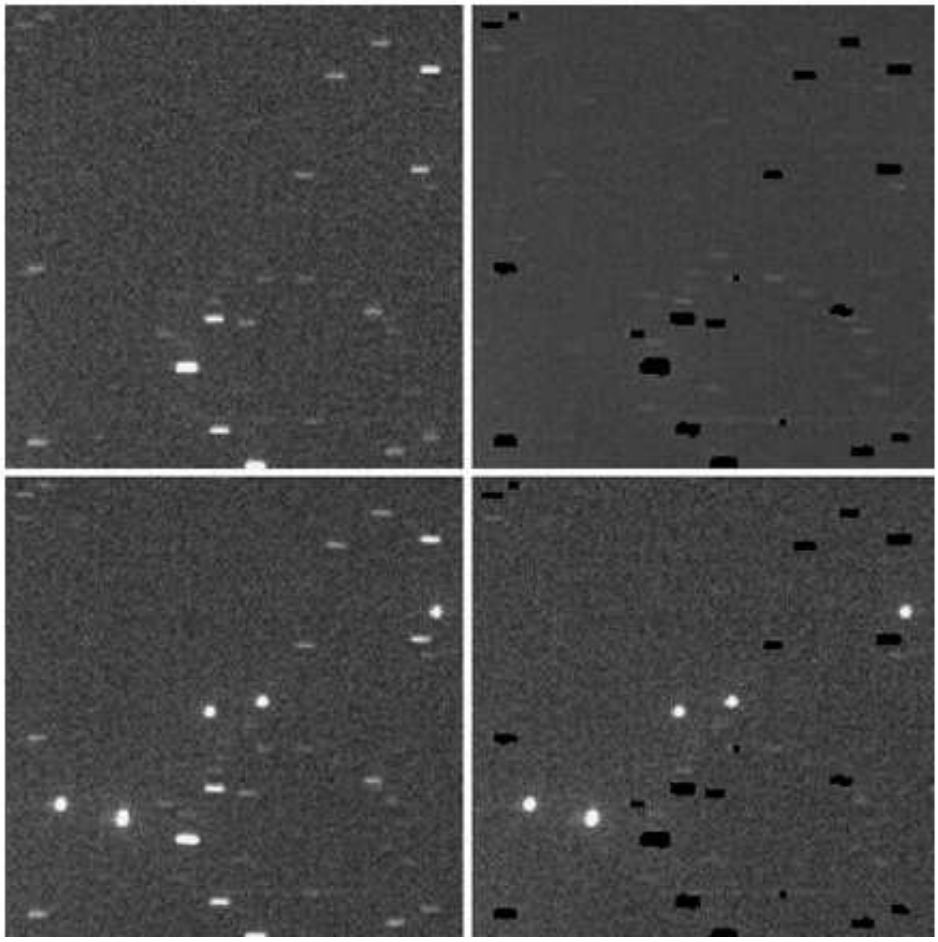

Figure 4.8: Masking technique: The upper left picture shows the stacked reference frame, the upper right one the mask that was generated out of it. The image in the bottom left corner shows a search frame before the mask was applied, the bottom right corner the same frame after the mask was applied. Only the object images, in the case displayed here, the five geostationary satellites of the Astra Cluster (Astra A-E), remain on the frame (Schildknecht [78]).

proved background is determined, and object recognition is performed using the improved background. This time, because a mask is available in the background determination, the algorithm *backgr & mask* is chosen.

The default values for the object scanning and recognition are $1.9 \cdot \sigma$ above background level for both steps. As opposed to the masking technique no border around the objects is determined. The options for the final check, which traces are finally accepted as object image, are more elaborate than in the masking step. A trace is accepted as object images, if it has at least two pixels, and an overall intensity higher than 50 ADUs. Additionally, the trace is required to have not more than 50 overlapping pixels with other traces or 99 pixels touching the mask. Those values may be changed by the user. The overlap of object/star images is illustrated by Fig 4.7. These checks are necessary to minimize the number of false detections. Only a limited number of detected objects can be stored. In the current implementation the

largest number is 100. If more objects are detected, the faintest objects are deleted from list of detected objects. This latter option can be disabled if selected by the user. In this case the detection stops as soon as 100 objects are detected.

All detected candidate object images are analyzed by a cosmic filter. In this step, cosmics should be distinguished from true object images on the single frame. Four different algorithms for cosmic filtering are available, the contrast filter, the object class filter and two edge detection filters named Sobel and Prewitt. The cosmic filters are outlined in Chapter 5. For the detection of faint objects the contrast or the object class filter are recommended.

4.5 Object Image Linking: SSESEL

The single object images on the different frames have to be linked in the next processing step, i.e., it has to be decided, which object images on the subsequent frames belong to the same physical object. This decision is called object image linking. The linked object images (and astrometric positions, respectively) are called tracklet. Object image linking is explained in detail in Chapter 6.

4.6 Matching Star Traces with Reference Stars from a Catalogue: CCDSTK

The precise astrometric analysis of the frames has to be preceded by the identification of the star traces on the single, non-averaged frames. The identification is done as follows: The raw pointing direction of the telescope is corrected by the mount model. The pixel coordinates of the different mosaics of the CCD of the ESASDT camera are corrected. The correction is necessary, since small gaps between the single parts of the CCD mosaic occur. In addition, the CCDs of the mosaic cannot be aligned perfectly parallel to each other. The actual orientation of the parts of the mosaic to each other and the gaps are captured in a so-called mapping model.

A reference star catalogue is selected. As star catalogues the Astrographic and Tycho (ACT), the Positions and Proper Motions (PPM), the Fifth Fundamental (FK5), the Carlsberg Meridian (CMC), and Guide Star Catalogue (GSC) catalogue are available. Per default GSC is selected, since it has the highest precision in general. The mount model corrected pointing of the first frame of the observation series is determined. The catalogue stars, which should be visible in this pointing direction in the FOV are marked on the observation frame. It can be chosen, in which magnitude interval catalogue stars should be marked on the observation frame, standard values are -99 as the lower limit and 12 or 13 for the upper limit. In addition, it can be chosen to explicitly not display certain catalogue stars. For the GSC catalogue this exceptions are not necessary and all stars are shown by default.

In general, an offset can be observed between the catalogue star positions and the actual positions of the star traces on the frame. A manual user input is required at this processing step, estimating the offset between the catalogue star position and the apparent position of the corresponding star traces displayed on the frame.

The precise coordinates of the catalogue stars, which are marked on the observation frame are stored. A selection can be made, in which reference system the precise coordinates may be saved. For the transformation of the catalogue coordinates into the chosen reference system a pole file has to be available. The output coordinates are usually generated in standard J2000.0.

One may overwrite the coordinates of the stars in CCD and celestial coordinates in the different output files and to correct the manually applied offset in the CCD coordinates.

4.7 Precise CCD coordinates of stars: CCDCEN

The catalogue stars as marked on the frames, have to be precisely centered on the star traces on the frames, after they have been roughly centered by the manual input only so far. The star traces on the frames have to be detected precisely and their center has to be determined.

Therefore the star traces on the single frames have to be detected. The background determination is described in Section 4.3.2. As default, the *median & sfrm* algorithm with nine subframes are chosen, within each subframe average values of squares with an edge length of 70 pixels are calculated. Five pixel values around the median are averaged for the determination of the median background, with two iterations. For the star image scanning and recognition with the new background, a threshold value of $2.8 \cdot \sigma$ is selected. The same value is chosen for the star image recognition step. For scanning and recognition, the spatial filters and object recognition algorithms, explained in Section 4.3.3 may be used. By default the 3×3 spatial filter and the *border & fill* algorithm are used. A border pixel size of one pixel is selected. Additionally, the criteria of the minimum number of pixels, the minimum intensity and the maximum number of objects are defined. The default values are, 12 pixels, 10 ADU, and 100 objects.

At this step, the precise pixel coordinates of the star traces and the catalogue coordinates are known. The decision, which star trace corresponds to which catalogue star is based on the following procedure: A search circle of 50 pixels around each catalogue star position, which is marked on the observation frame, is defined. The corresponding star trace is searched inside the area of this search circle. Two different criteria may be selected to determine, which of possibly many star traces inside the search circle is the trace corresponding to the catalogue star. Either the brightest star or the trace with the coordinates closest to the catalogue star coordinates is selected. A star trace is not accepted as corresponding to the catalogue star if it has more than 50 overlapping pixel with another star or object trace.

4.8 High Precision Astrometry: AMETRY

Precise celestial coordinates have to be determined for the detected objects. For this purpose a transformation has to be established between the CCD coordinates of the stars on the fame and the corresponding catalogue coordinates. The pixel coordinates and the catalogue coordinates are transformed into a common plane. For precise astrometric measurement of the observed object at least one star has to be available. More than two stars should be on the frame for an accurate and reliable determination of the

astrometric positions of the objects. The program can be used to either determine parameters with callibration measurements, or to determine astrometry with fixed or under estimation of very few parameters only in the processing of regular observations.

The transformation is determined iteratively. A weight may be associated with each parameter of the transformation. A common scale may be estimated. The scale is usually temperature dependent and does not have a constant value. For the orientation of the CCD plane the parameter for camera orientation as well as for the derotator and an offset of the derotator may be estimated. The symmetric and the antisymmetric part, which may be weighted differently, characterize the affine transformation. The separation of these parameters may only be determined in dedicated calibration measurements, under ideal conditions and with sufficiently large number of reference stars displayed on the frames. The symmetric affine transformations accounts for astigmatism and a possible non-orthogonality of the axis of the CCD coordinate frame. This estimation may be distorted, when an overall scale is determined. The antisymmetric affine transformation accounts for a rotation of the CCD frame. An over-parameterization is likely if the camera orientation parameter are to be determined at the same time.

Higher order terms may be estimated to account for the tilt, a decentering or a radial distortion caused by the telescope optics, which affects the optical path of the rays. They should only be determined by dedicated calibration measurements.

The CCD array parameters are determined by calibration measurements. They are associated with the mapping model. It has to be specified, if an horizontal pointing or an equatorial pointing was used to acquire the observations, to be able to estimate a parameter for correcting the pointing direction. Horizontal pointing should be used for blind tracking, equatorial for sidereal tracking.

In addition, it has to be specified, if the coordinates should be determined for the stars, for the auxiliary stars or for the moving objects (relative to the star background).

A common scale, the camera orientation and the pointing direction are estimated in routine processing, equal weights are applied. Additional options are: The parameter for the pointing direction may be chosen to determined once for the whole observation series or separately for each single frame. The tracking scenario during the observation series has to be specified, if the parameter is only estimated once per observation series. It is far more precise to determine the pointing for each frame separately, which is chosen by default.

The camera orientation may be determined once for all frames, once for every n hours (in this case a number for n has to be chosen), once for each series of frames, or once for each frame.

A default number seven iterations are chosen for the parameter determination process.

The output of the precise astrometry step are the precise coordinates of the stars displayed on the observation frames. The reference system, in which the coordinates are stored may be chosen. For a satellite a geocentric coordinate system, for a minor planet the barycenteric coordinate system may be chosen.

4.9 Determining Apparent Object Magnitudes: CCDMAG

The apparent magnitudes of the objects on the frames are determined in the next processing step. The apparent magnitudes of the stars are known from the reference catalogue and were extracted and saved by the program CCDSTK. A so-called magnitude mapping is determined: On each observation frame the ADU intensities on the frames are associated with the apparent catalogue magnitudes. The apparent magnitudes of the unknown objects displayed on the frames can be estimated with this magnitude mapping of the stars. The elevation value under which the object was observed and the magnitude value of the object image on each frame is stored. The station coordinates and the mount model are needed as input to determine the elevation.

4.10 Determination of a Circular Orbit: ODCORD

A circular first orbit is determined from two astrometric positions of the observed objects with the routine ODCORD. The procedure of circular orbit determination was developed according to the algorithms of the CelMech program system (G. Beutler [4]), details on first orbit determination can be found in Section 7.4.

4.11 Improved Orbit Determination without Perturbation: ODIORD

The program ODIORD is used to determine an improved orbit if more than two observations of an object are available. A priory orbital elements have to be available. No perturbations are applied, only the main term of the Earth gravitational potential is taken into account.

ODIORD allows to constrain one or several of the estimated elements E_i to a priori elements E_0 by introducing (linear) pseudo-observations of the type:

$$E_i - E_0 = 0 \tag{4.1}$$

with a weight $\sigma_{E_0}/\sigma_{E_i}$ for each of the elements to be constrained. σ_{E_0} is the a priori rms of the observations, σ_{E_i} the user defined rms of the orbital element. A weight of zero fixes the orbital element to the a priori value. For the short tracklets observed during an observation series, the eccentricity is constrained to zero and the perigee may be defined, e.g., to coincide with the node.

The user may select between Keplerian elements and non-singular elements to parameterized the orbit. The Keplerian elements should be transformed to non-singular elements to avoid that orbital elements become indeterminate in the parameter estimation process.

The orbit improvement is performed using the least-square method, seven iterations are the default value in ESASDT processing. The least square procedure was developed according to the algorithms of the CelMech tool, more details can be found in section 7.4.

4.12 Catalog Correlation: ODIDNT

The orbits previously determined of the tracklets of linked astrometric observations, may now be correlated with an orbital element catalogue and its propagated ephemerides, respectively. The catalogue is expected to be provided either in osculating elements or in the two line elements (TLE) format. Two independent correlation methods can be chosen: the so-called point-wise correlation based on the astrometric positions and velocities of the observed objects, which is independent of an orbit determination of the detected tracklets, and a correlation based on orbital elements. For point-wise correlation station coordinates of the observing sites are required.

Both algorithms have several empirically determined threshold values. The threshold values define correlations with the catalogue of four different qualities. A correlation of quality one is assumed to be a successful identification of the observations with a catalogue object. The correlations of lower quality are correlations, which do not fulfill all criteria to qualify for an identification with a catalogue object. All correlations of all qualities are displayed as information for the user.

Details concerning the catalogue correlation are provided in Chapter 7.

4.13 Selection of Correlated Objects: ODISEL

This program lists the names of the successfully identified objects in the output file of the processing.

4.14 Distance and Phase Angle Corrections of Object Magnitudes: ODMAGN

The apparent magnitude may be corrected for the observed objects. The user may decide to correct for the phase angle only, or for phase angle and distance, which is available via first orbit determination of the tracklets, or to perform no corrections at all. For the reflection properties either a stable plate, a tumbling plate or a sphere may be assumed. For a sphere the phase dependency is linear, for a plate, the phase angle dependency follows the cosine law. For the calculation of the tumbling plate a mean exposed effective area is assumed. Details concerning different albedo and reflection models are provided by T. Schildknecht [77]. For the distance correction the station coordinates are needed.

4.15 Generate Processing Output: CCOGET

The last processing step creates an overview of the processing output. All tracklets with their associated names, internal names and the correlation information are displayed in the so-called observation-list-file. Due to contamination with cosmics, normally all detections are deselected. A manual check to select the valid tracklets is required.

To check the detected objects and to help the decision of the user subframes of every detected object image are generated. The object images of each tracklet are provided grouped together. The size of the

subframe is defined by the user, values of 28, 64, 128, and 256 as pixel edge length are available. The default value for GEO and GTO is 28 pixels.

Tracklets and first orbits are available for all successfully detections at the end of the processing pipeline. If the correlation with a catalogue was successful, the name of the identified catalogue object, and its COSPAR number is provided.

5. Cosmic Filter

> Logisch zu sein ist immer bequem.
> Nahezu unmöglich ist es aber, logisch bis zum Ende zu sein.
>
> *Albert Camus*

5.1 The Problem of Cosmic Rays

Cosmic rays consist of particles of cosmic origin impinging on the Earth's atmosphere. These particles are mainly electrons, positron, protons, and muons, but also small amounts carbon, oxygen, neon, magnesium, silicon, iron and nickel ions do occur. Their energies cover a wide range up to $3 \cdot 10^{20}$eV. The energy spectrum is illustrated by Fig. 5.1. At the low end of the spectrum, cosmic rays hit the atmosphere with fluxes of more than one particle per square-meter per second, at the highest end only with a flux of less than one particle per square meter and century. The sources of cosmic rays are solar flares and supernovae. As additional sources of cosmic rays with higher energies the acceleration of charged particles in the vicinity of back holes are considered. Some cosmic rays are even suspected to stem from intergalactic shock waves [44].

The vast majority of cosmics impinging the atmosphere does not reach the ground, but interacts with the atmospheric molecules, leading to so-called shower effects, resulting in the creation of a large amount of secondary particles. A possible particle shower initiated by an iron nucleus is illustrated by Fig. 5.2. As a result of this shower effect, mostly muons reach sea level [28].

If charged particles hit a charged coupled device (CCD) detector photo-electrons are released punctually [36]. When the detector is read out, a cosmic ray impact leaves a trace similar to the one of a photon. Not all charged particles hitting the detector are actually cosmic rays, but may also originate from weakly radioactive materials used in the construction of the CCD dewar, see e.g. Florentin-Nielsen et al. [18]. In the current work all charged particles resolving photo-electrons at the detector are subsumed under the term *cosmics*.

A standard procedure in dealing with cosmics in astronomic imaging is, to stack several images. The cosmics are filtered out because they are *singular* events irregularly spread over the CCD frame. This technique has the additional side effect that the signal to noise ratio of the observed object is increased [36]. But stacking requires a precise alignment of the frames relative to the observed objects. For a successful stacking the images have to be aligned relative to the object's motion, an alignment with the stars would filter out the object images of fast moving objects. In surveys, when searching for new objects,

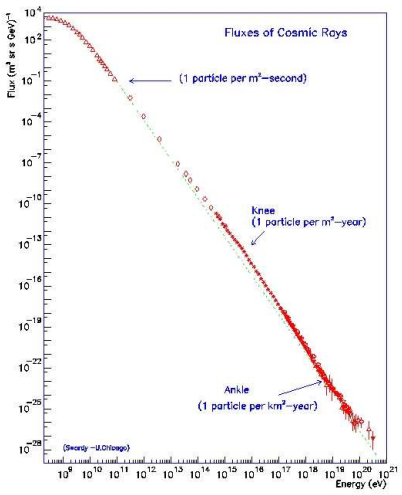

Figure 5.1: Flux of cosmic rays as a function of energy (Cronin et al [11]).

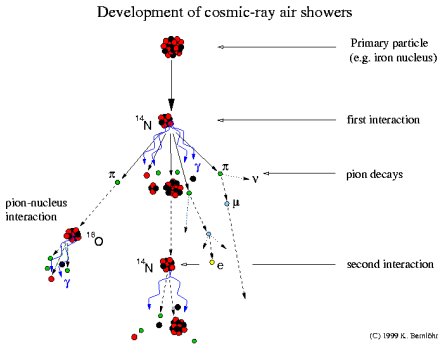

Figure 5.2: Example of a cosmic ray air shower (Max-Planck-Institute Heidelberg).

the object's position on the frame and their exact motion are unknown. Therefore, possible ranges of object velocities and inclinations have to be assumed and many different stackings of the same frames have to be checked and the results cross-checked. Such an approach is suggested and implemented by T. Yanagisawa at the Mount Nyukasa observatory of the Japanese Aerospace Exploration Agency (JAXA) [95]. This method is computationally intensive and time consuming and not (yet) feasible for real-time processing. Real-time processing is required, when tasking follow-up observations within the same night. Additionally, stacking poses limits on the object's orbits and its apparent movement at a very early processing step already. Therefore, in the ESASDT processing a filter approach is preferred on the single frames for cosmic rejection. A cosmic filter should be fast, and allow to distinguish cosmics from actual object images. As explained in further detail in Section 5.2 a filter approach acting on single frames is only feasible if the pixel scale is small enough to allow for such a discrimination, i.e., when the object images and cosmics are displayed over a couple of pixels on the frame, to allow to determine distinguishing features. Additional filtering is performed on series of frames, as gained in surveys, when the single object images are linked to so-called tracklets. This approach is also feasible at broader pixel scales. The latter step comes at the cost to impose certain limits on the object's movement. Details will be provided in Chapter 6.

5.2 Cosmic Filters

5.2.1 Cosmics at the ESASDT

Figure 5.3 and 5.4 show enlarged images of cosmics and object images of different shapes and sizes on the frame found in surveys of the ESASDT on August 26 in 2006. Figure 5.3a and 5.3b show two object images, at the size of a few pixels on the frames. The object images are compared to cosmics of similar size, Fig. 5.3c. Figure 5.3d to 5.3i show the relative intensity extracted directly from the frames of the object images. The cosmic is shown in x- and y-direction of the frame. Figure 5.4 shows an object image of about 90 pixels of a bright object and a cosmic of comparable size on the frame, as well as their relative intensity in x- and y-direction of the frame.

An analysis of several hundred candidates, which could either be real object images or cosmics, distinguished by eyesight, revealed that the main criteria to distinguish cosmics from object images is the sharp edge in the brightness from one pixel to the next. Real object images tend to have a smooth transition. This tendency is also illustrated in the intensity histories of the examples in Fig. 5.3d to 5.3i and Fig. 5.4c to 5.4f. The smoothing in the point spread function results from the transition of the light reflected by space objects through the atmosphere, when originally from the reflections of a real object, in contrast to cosmics impinging on the CCD frame directly and resolving photo-electrons immediately through their charge.

A cosmic filter on a single frame crucially depends on the pixel scale of the CCD device, especially under very good seeing conditions. A scale of 0.6 arcseconds per pixel of the ESASDT leaves a couple of doubtful events on the frames, which cannot be uniquely associated with cosmics or object images (see Fig. 5.3a and 5.3c).

On average between 15 and 100 cosmics are found in a normal survey consisting of eleven frames. In a minority of cases not real cosmics are displayed, but left over single pixels from stars, which were

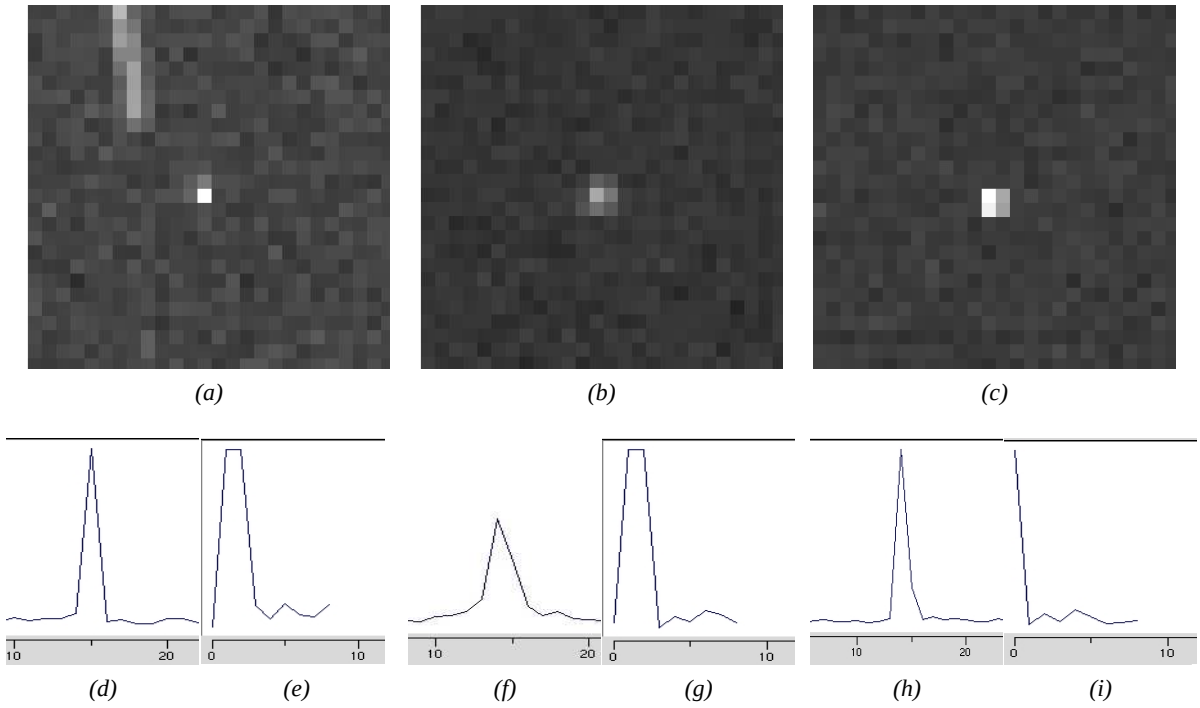

Figure 5.3: Two small real non-resolved object images ((a) and (b)), one small cosmic (c). (d),(e) relative intensity of image (a) in x- and y-direction, (f)(g) relative intensity of image (b) in x- and y-direction, (h)(i) relative intensity of cosmic (c) in x- and y-direction relative to the CCD frame axis.

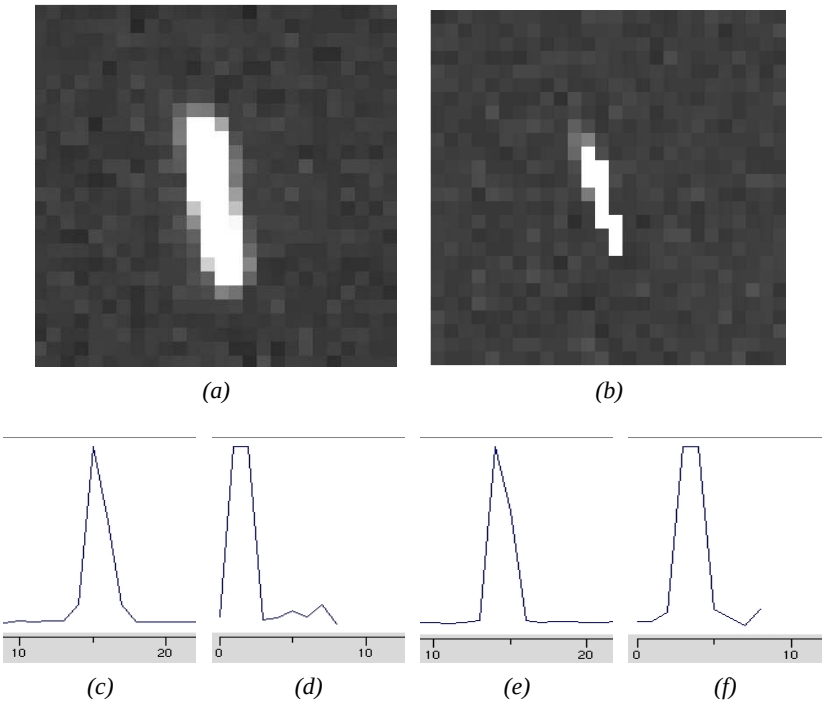

Figure 5.4: Real larger non-resolved object image (a), one larger cosmic (b). (c),(d) relative intensity of image (a) in x- and y-direction, (e),(f) relative intensity of cosmic (b) in x- and y-direction relative to the CCD frame axis.

not correctly covered by the mask on single frames. Those cases are not specifically distinguished in the further discussion.

A first cosmic filter for the ESASDT processing, called contrast filter, was developed by Hugentobler [37]. In the scope of this thesis three different approaches for cosmic filters have been developed, implemented and tested, namely, the so-called object class cosmic filter and two edge detection filters, which are implementations of Sobel and Prewitt edge detection adjusted to be used as cosmic filters. The filters are documented here and their performances are compared.

5.2.2 Old Cosmic Filter: Contrast Filter

Cosmics are filtered according to the contrast ratio of the brightest pixel (i_{peak}) compared to the mean of the brightness of the four pixels (i_{sur}) surrounding the brightest pixel in a candidate image by the contrast filter. The contrast is normalized with the improved background intensity (ρ) and a noise correction $noise$ is applied:

$$\text{threshold} = \frac{i_{peak} - \text{noise} \cdot \sqrt{\sigma_1} - \rho}{0.5(i_{sur} + \text{noise} \cdot \sqrt{\sigma_2}) - \rho} \tag{5.1}$$

$$\text{with: } \sigma_1 = \sigma_\rho^2 + \text{gain} \cdot \max(i_{peak}, \rho) \qquad \sigma_2 = \sigma_\rho^2 + \text{gain} \cdot \max(i_{sur}, \rho) \tag{5.2}$$

where σ_ρ the standard deviation of the improved background intensity, and $gain$ value for the camera gain. The contrast ratio int_{peak}/int_{sur} is a simple approximation for the value of the full width at half

maximum (FWHM) of the overall intensity function of the candidate image. In the current implementation, a default value of 3.0 for the noise correction and of 1.5 ADU for the empirical threshold for the contrast, is used. Is the contrast higher than the threshold value for the seeing, a candidate is judged to be a cosmic. The threshold value is determined empirically.

5.2.3 Empirical Method for a new Cosmics Filter: Object Class Filter

The object class filter is based on more than on threshold value. Purely empirical threshold values have been defined:

$$\text{threshold}_1 = \text{i}_{\text{peak}} - \rho \qquad \text{threshold}_2 = \text{i}_{\text{all}} - \rho \qquad \text{threshold}_3 = \frac{\text{i}_{\text{all}}}{\text{i}_{\text{peak}}} \tag{5.3}$$

$$\text{threshold}_4 = \frac{\text{FWHM}_x}{\text{FWHM}_y} \qquad \text{threshold}_5 = \frac{\text{FWHM}_x}{n_{\text{pix}}} \qquad \text{threshold}_6 = \frac{\text{FWHM}_y}{n_{\text{pix}}} \tag{5.4}$$

whereas, i_{peak} is the intensity of the brightest pixel, i_{all} the mean of the intensity of all pixel of the object image, ρ the improved background intensity, FWHM_x and FWHM_y an approximation of the FWHM in x- and y-direction with respect to the pixel coordinates, and n_{pix} the number of pixel belonging to the candidate image on the frame.

For the approximate calculation of the FWHM a simple but more precise approach is chosen than in the contrast filter. The best possible calculation of the FWHM is obtained using a Gaussian fit as, e.g., implemented in the processing software APEX II of the Keldish Institute of Applied Mathematics, see V. Kouprianov [49]. A Gaussian fit is computationally intensive and relies on a more or less Gaussian or elongated Gaussian shape of the candidate. The ESASDT processing explicitly does no Gaussian fit, because the premise of a Gaussian shaped object trace on the frames is not always fulfilled: On the frames, there are also highly distorted object images with a signal to noise ratio (SNR) close to the detection limit, where some pixels of the object image are below the background intensity (see chapter 4.3.3 for further details on the object detection). A faster and simpler approach is used for the object class cosmic filter: All pixels with higher intensities than the mean object intensity within the candidate are counted and normalized with the number of pixels of the candidate. This approximation to the FWHM is evaluated in x- and y-direction.

Five different object classes are defined in dependence of the number of pixels of the candidates on the frames. For each of the five classes different threshold values ($\text{threshold}_k, k = 1, ..5$) have been determined. Currently, the class of very small candidate object images is set to fewer than 20 pixels, small candidates to 40 pixels, medium to 80 pixels, large candidates to 100 pixels and the finally to candidates with more than 100 pixels.

5.2.4 Method of the Edge Detection Cosmic Filters

A completely different approach was evaluated in the two edge detection cosmic filters. In their linear filtering a pixel value is determined as the weighted sum of its neighbors. Sobel and Prewitt filters assume that white noise is additive and that the image surfaces are linear. The filters consists of two 3×3 kernels, requiring 18 calculation steps per pixel. Because computing time is crucial in real-time processing and because the stars were already rejected by the masking technique, the filters are not convoluted

with the whole image but only with a subframe, containing the candidate image. This so called object box is the smallest box containing the object plus a one pixel sized background border around the object. The kernel is convoluted with the object box. To avoid border effects, an additional padding at the edges of the object box is needed. The object box is not just extended because stars or other object candidates could reach into this enlarged object box and contaminate the result. The background values are used to enlarge the object box by an additional one pixel size border around the object box.

Edge detection filters deliver filtered gray-scale images with highlighted edges. To decide whether a candidate is a real object image or a cosmic, the pixel values of the convoluted object boxes are added up and normalized. Empirical threshold values are determined for each of the two filters independently.

The kernels of the Sobel and the Prewitt filter and the coefficients are of fixed size. What is normally seen as a drawback in computer science is an actual advantage, when using these kernels for cosmic filtering: The filters remain noise sensitive [96]. This is excellent, because the majority of the candidates investigated are only of a few pixel size. In computer science such candidates would be looked at as noise.

5.2.4.1 Classical Edge Detection: Sobel Filter

The Sobel filter was proposed by Irvin Sobel in 1968 and is one of the most widely used edge detection filters. The gradient of the pixel intensities on a gray scale image is estimated as the equally weighted sum of the eight neighboring pixels. The corner pixels are by a factor $\sqrt{2}$ further apart than the central pixel and their difference vectors are 45 degrees inclined relative to the x- and y- axes of pixel coordinates. This leads to the following two convolution kernels [12]:

$$\mathbf{G_x} = \begin{pmatrix} 1 & 0 & -1 \\ 2 & 0 & -2 \\ 1 & 0 & -1 \end{pmatrix} \qquad \mathbf{G_y} = \begin{pmatrix} 1 & 2 & 1 \\ 0 & 0 & 0 \\ -1 & -2 & -1 \end{pmatrix} \tag{5.5}$$

$$\mathbf{G} = \sqrt{\mathbf{G_x}^2 + \mathbf{G_y}^2} \tag{5.6}$$

The two kernels are detecting edges orthogonal to their gradient direction. To achieve rotational invariance, the pixel values of the x- and y- gradient estimation are summed up.

5.2.4.2 Classical Edge Detection: Prewitt Filter

The Prewitt filter was developed in 1970 by Judith Prewitt. The filter is fitting a quadratic surface over a 3×3 neighborhood by a least squares approach. This leads to the following convolution kernels [72]:

$$\mathbf{G_x} = \begin{pmatrix} -1 & 0 & 1 \\ -1 & 0 & 1 \\ -1 & 0 & 1 \end{pmatrix} \qquad \mathbf{G_y} = \begin{pmatrix} -1 & -1 & -1 \\ 0 & 0 & 0 \\ 1 & 1 & 1 \end{pmatrix} \tag{5.7}$$

$$\mathbf{G} = \sqrt{\mathbf{G_x}^2 + \mathbf{G_y}^2} \tag{5.8}$$

The gradients in the x- and y-direction are summed up.

	Truth	Contrast	Obj. Class	Sobel	Prewitt
detected real object images	**96**	84	85	84	79
cosmics	**1527**	679	321	917	889
real obj. det. rate	**100%**	87.5%	88.5%	87.5%	82.2%
cosmic reject. rate	**0%**	55.5%	79.0%	36.4%	41.8%

Table 5.1: Number of detected object images and cosmics on ten observation series of the ESASDT taken on August 25, 2006: True number of object image and cosmics on the frames and correctly identified object images, cosmics still present after filtering, rate of correctly identified object images and correctly rejected cosmics for four different filters: contrast filter, object class filter, Sobel filter and Prewitt filter.

5.2.5 Performance Comparison

All filters have been implemented in the ESASDT automatic processing system. They were tuned to be as conservative as possible. After the tuning based on ten nights on the ESASDT 2006 campaigns (January till July), their performance was tested for the independent observation night on August 25, 2006, which was not used in the tuning process. Randomly, ten survey observation series and three follow-up series were evaluated. All detected candidates were checked by eye and with the help of the two object image linking algorithms (details on object image linking in Chapter 6). Snapshots of the processing results are presented in Fig. 5.5 to 5.17. Figures 5.5 to 5.14 contain the results for the survey series. The surveys consisted of 15 frames, spaced by one minute. Figure 5.15 to 5.17 show the results for the follow-up series, which consisted of eleven frames each spaced by 30 seconds. The true object images are marked by blue boxes. First the number of detected true object images and detected cosmics without any filtering are displayed in each caption in parentheses. The number of correctly identified object images and the number of cosmics, which passed the filter are shown as the first and second values in parentheses for different cosmic filters.

Table 5.1 summarizes the results. 1622 candidates were detected on the single frames. 96 were judged to be real object images and 1527 were identified as cosmics. Although all filters were tuned in the most conservative way, all filters are identifying object images as cosmics. About 10 object images were misinterpreted by the contrast, the object class and the Sobel filter; only the Prewitt filter misinterpreted even 16 object images as cosmics.

Not all filters do misinterpret the same object images as cosmics. The object class filter misinterprets the bright and large object images with more than 30 pixels (e.g. Fig. 5.17), or object small object images with very few pixels, with a high peak intensity (e.g. Fig. 5.5 and 5.16). The latter cases could be as well cosmics as real object images, by eye inspection they were judged to be more likely object images.

The contrast filter algorithm misinterprets mostly the object images with a small number of pixels, similar to the object class filter, as e.g. Fig. 5.11 and 5.16 show. The filter also misinterprets object images with medium pixel size, see, e.g., Fig. 5.5. Here, the peak intensity of this object image is relatively high, but it clearly is an object image.

The two edge detection filters both seem to correctly identify the obvious object images, which are the

ones easily judged by eye already, i.e. the bright objects with a medium to large amount of pixel. In those situations both algorithms give better results than the other two algorithms, see e.g. Fig. 5.5. Both filters are inferior, when dealing with faint object images close to the signal to noise level, see Fig. 5.10 and 5.14. Whereas the Sobel filter identifies at least part of the faint objects correctly, the Prewitt filter does not, see Fig. 5.11. The Prewitt filter has the highest rate of misinterpreted true object images in the investigated series.

These rates of falsely rejected possible object images is rather high. But this also counts candidates as object images, which have few pixel and, which cannot be identified as cosmics or object images by eye. In the chosen conservative tuning, those candidates should not be identified as cosmics by the filters.

A correctly identification of the true object images is not the only criterion for the performance of a cosmic filter, but also the rate of correct rejection of cosmics. The object class filter has the highest number of correctly identified cosmics, with a rate of nearly 80 percent. The contrast filter reaches almost the same quality, with a rate of about 55 percent correctly rejected cosmics. The two edge detection filters only reject about 40 percent of the cosmics correctly. The Prewitt filter is slightly superior to the Sobel filter in this respect

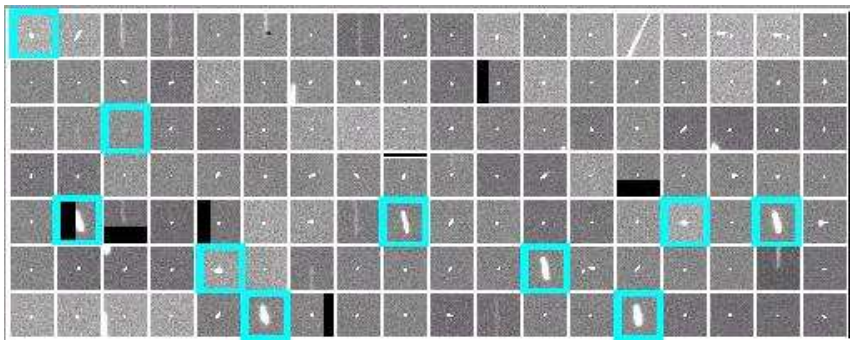

(a) no filter

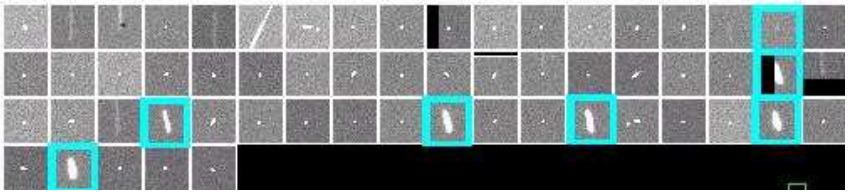

(b) contrast filter

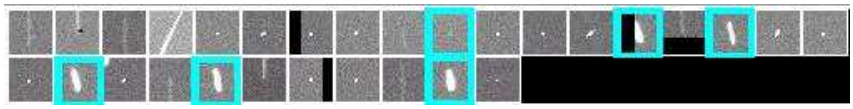

(c) object class filter

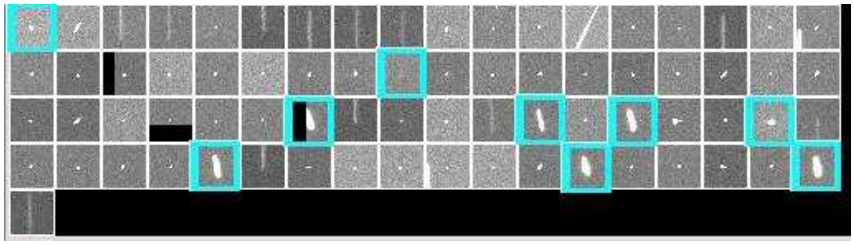

(d) Sobel filter

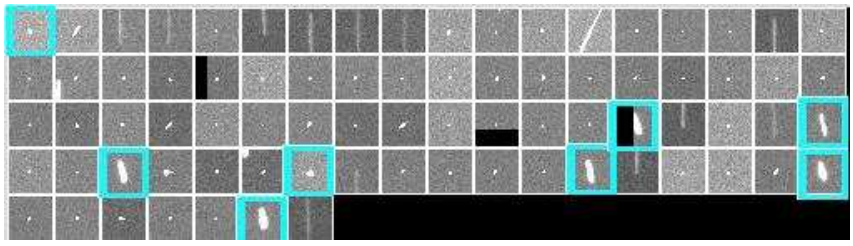

(e) Prewitt filter

Figure 5.5: (a) All detected candidates (10/116), (b) contrast filter (7/52), (c) object class filter (6/23), (d) Sobel (9/64), and (e) Prewitt (8/71) edge detection filter: SSO-10A.

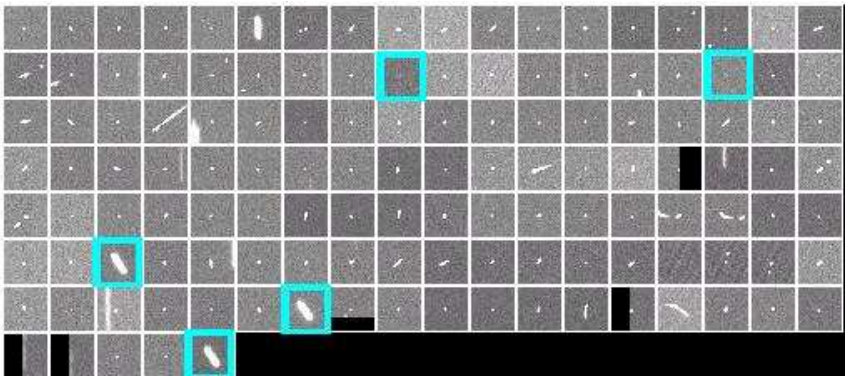

(a) no filter

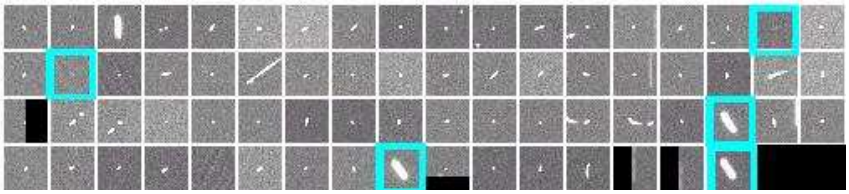

(b) contrast filter

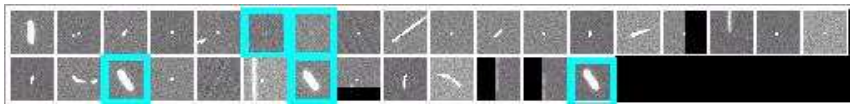

(c) object class filter

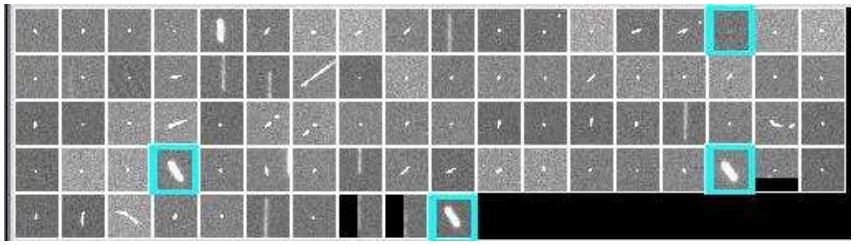

(d) Sobel filter

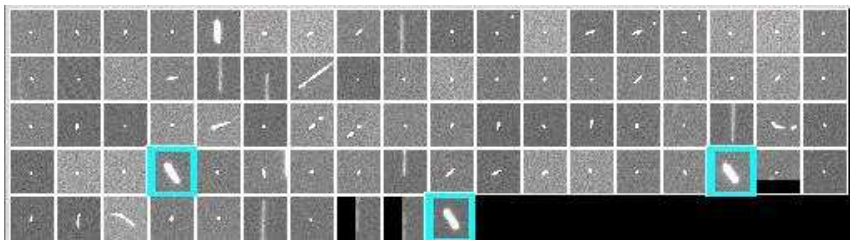

(e) Prewitt filter

Figure 5.6: (a) All detected candidates (5/126), (b) contrast filter (5/65), (c) object class filter (5/26), (d) Sobel (4/78), and (e) Prewitt (3/78) edge detection filter: SSO-10B.

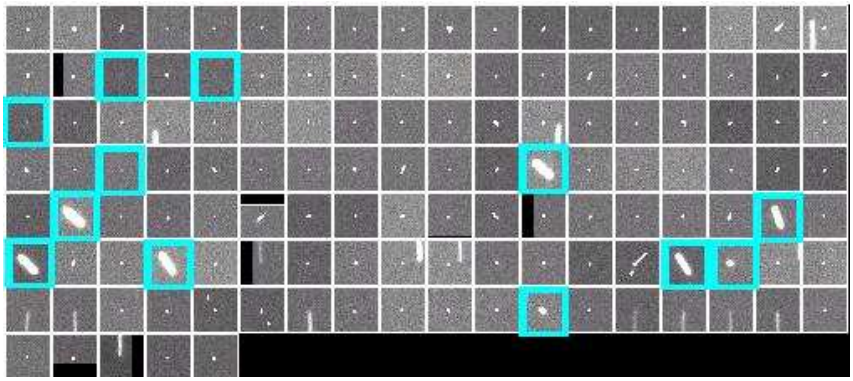

(a) no filter

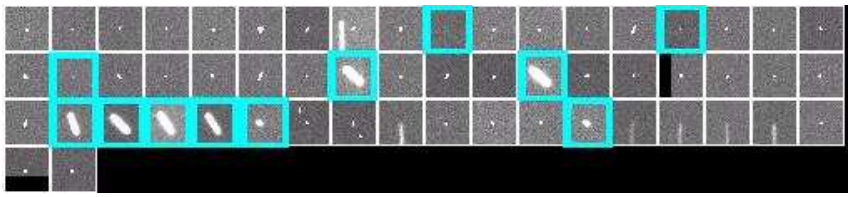

(b) contrast filter

(c) object class filter

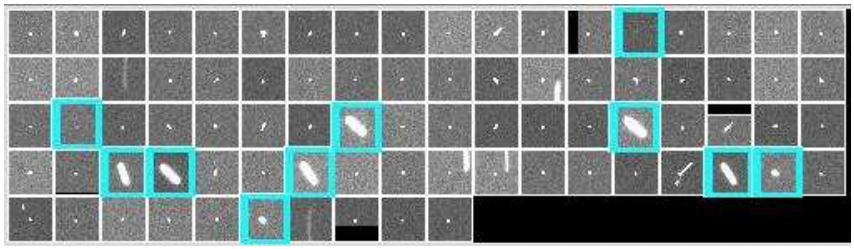

(d) Sobel filter

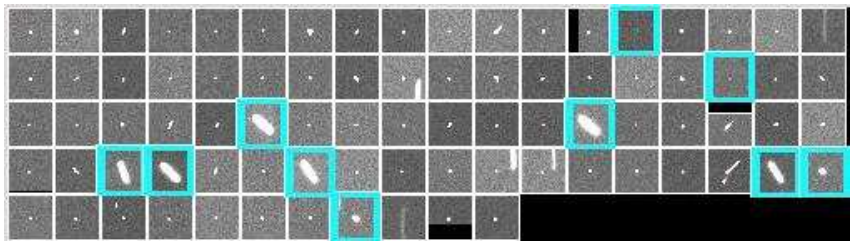

(e) Prewitt filter

Figure 5.7: (a) All detected candidates (12/142),(b) contrast filter (11/45), (c) object class filter (12/20), (d) Sobel (10/72), and (e) Prewitt (10/73) edge detection filter: SSO-12A.

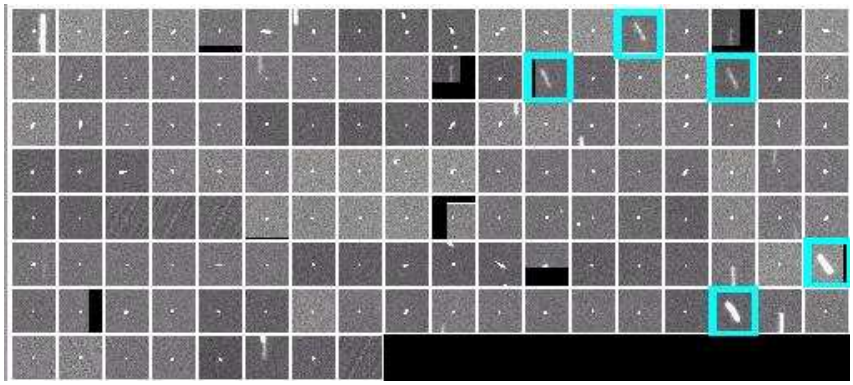

(a) no filter

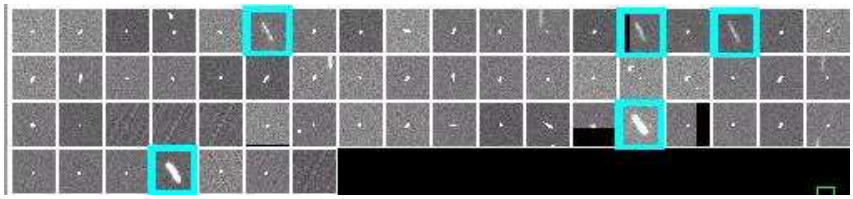

(b) contrast filter

(c) object class filter

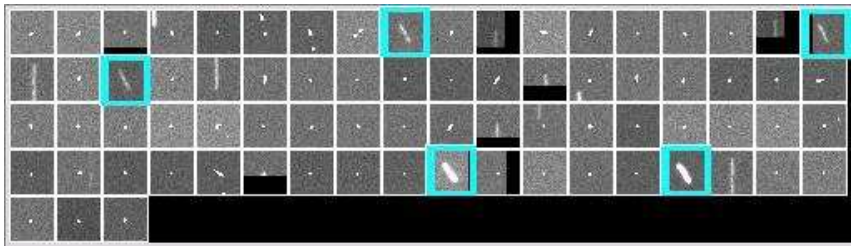

(d) Sobel filter

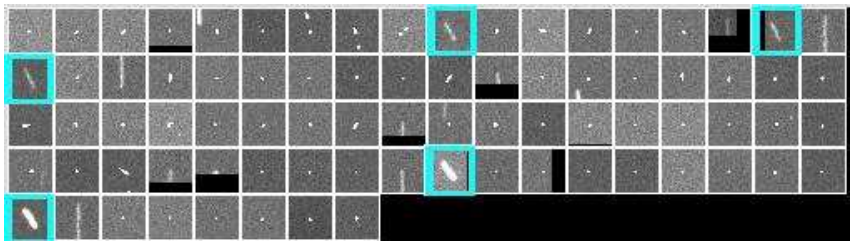

(e) Prewitt filter

Figure 5.8: (a) All detected candidates (5/125),(b) contrast filter (5/56), (c) object class filter (4/29), (d) Sobel (5/70), and (e) Prewitt (5/75)edge detection filter: SSO-12B.

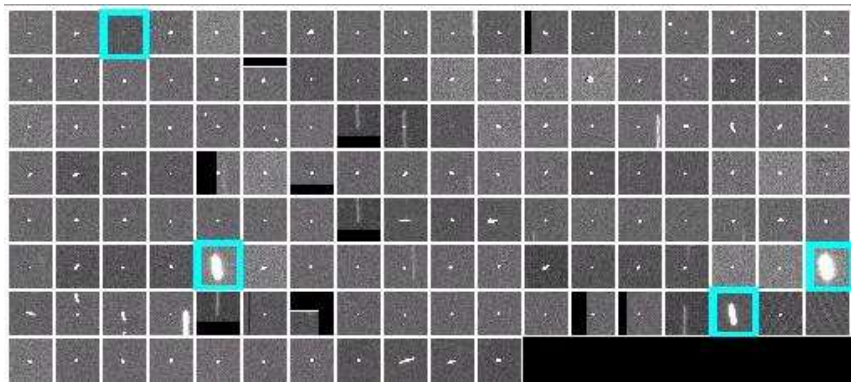

(a) no filter

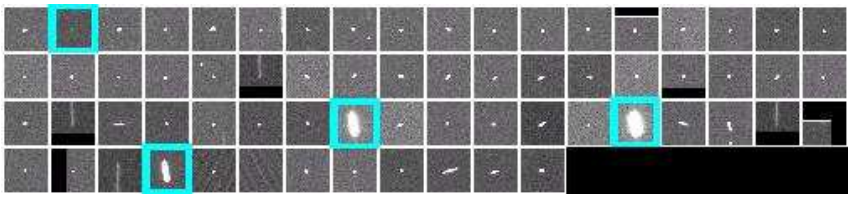

(b) contrast filter

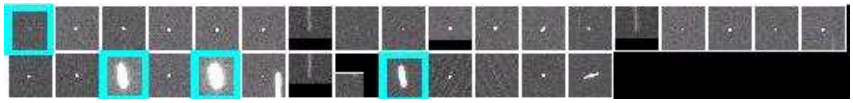

(c) object class filter

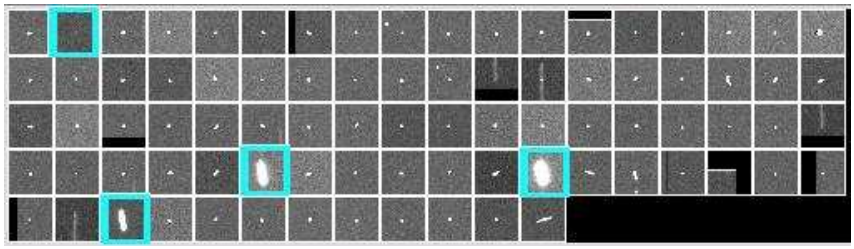

(d) Sobel filter

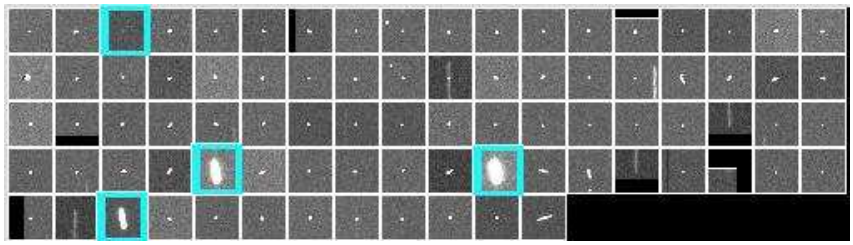

(e) Prewitt filter

Figure 5.9: (a) All detected candidates (4/133),(b) contrast filter (4/62), (c) object class filter (4/27), (d) Sobel (4/80), and (e) Prewitt (4/80) edge detection filter: SSO-15A.

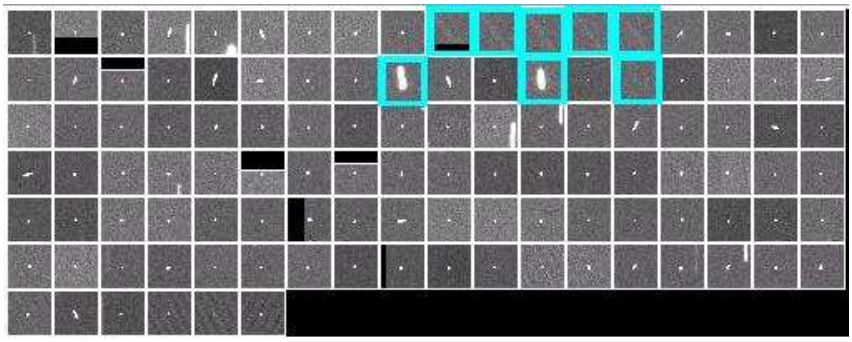

(a) no filter

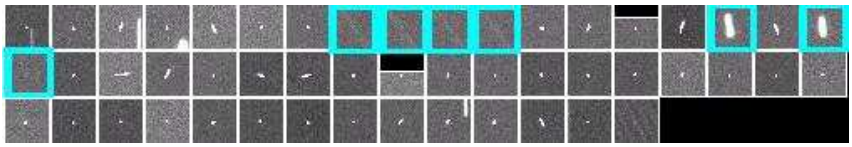

(b) contrast filter

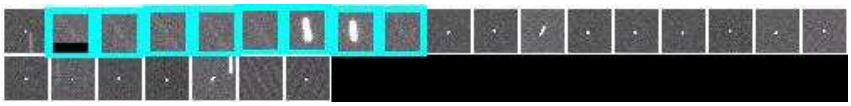

(c) object class filter

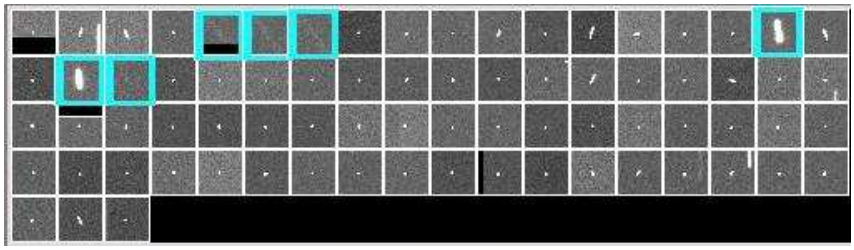

(d) Sobel filter

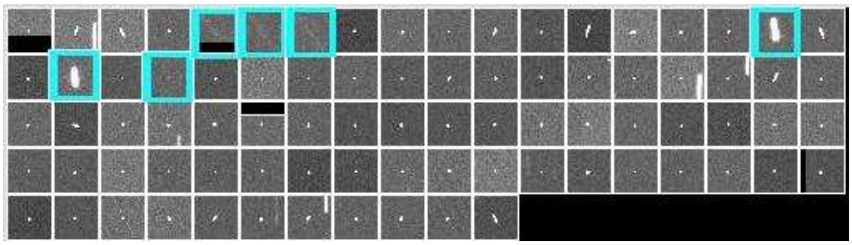

(e) Prewitt filter

Figure 5.10: (a) All detected candidates (8/106),(b) contrast filter (7/42), (c) object class filter (8/17), (d) Sobel (6/69), and (e) Prewitt (6/78) edge detection filter: SSO-15B.

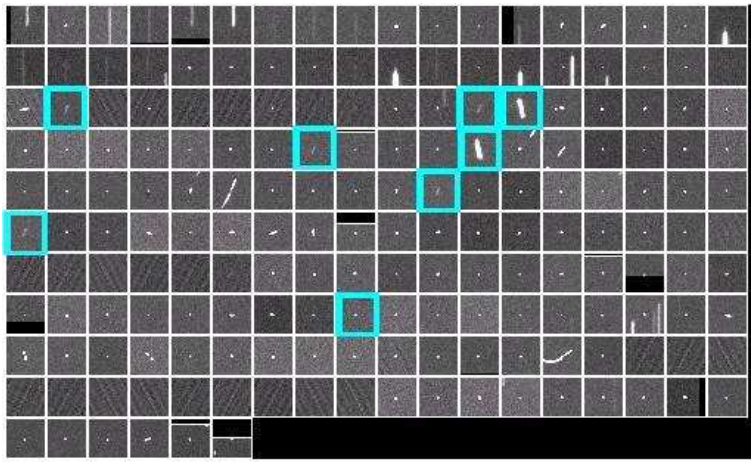

(a) no filter

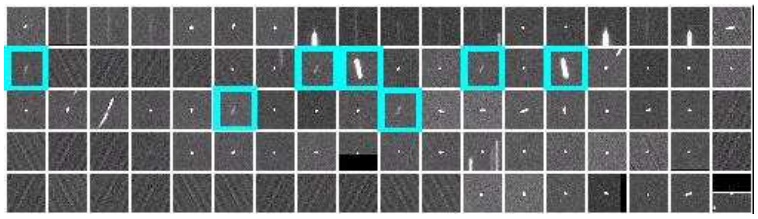

(b) contrast filter

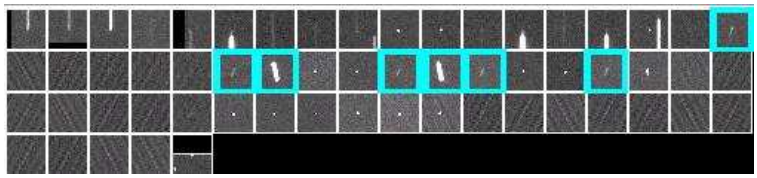

(c) object class filter

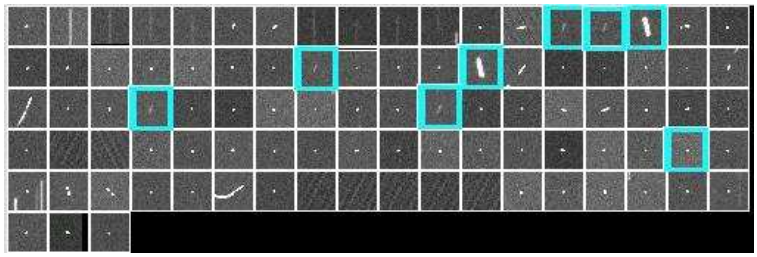

(d) Sobel filter

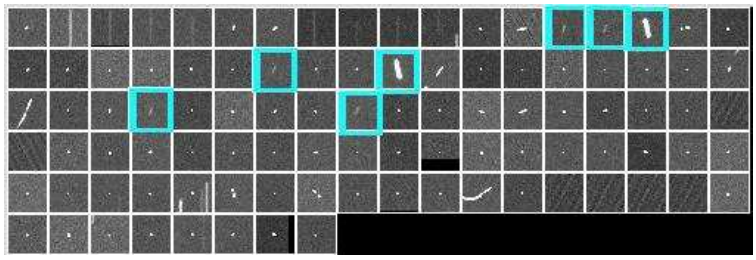

(e) Prewitt filter

Figure 5.11: (a) All detected candidates (8/178),(b) contrast filter (7/83), (c) object class filter (7/52), (d) Sobel (8/85), and (e) Prewitt (7/91) edge detection filter: SSO-27A.

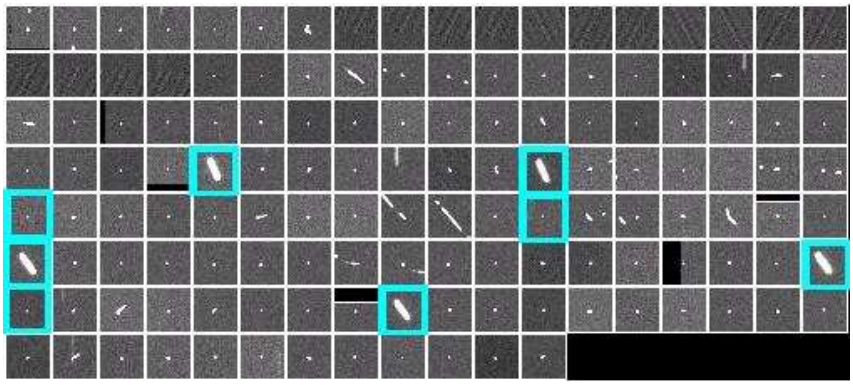

(a) no filter

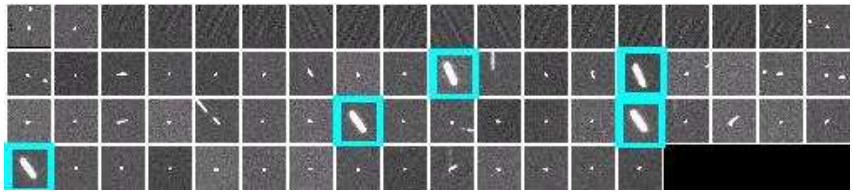

(b) contrast filter

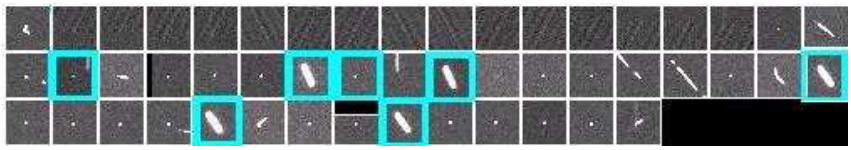

(c) object class filter

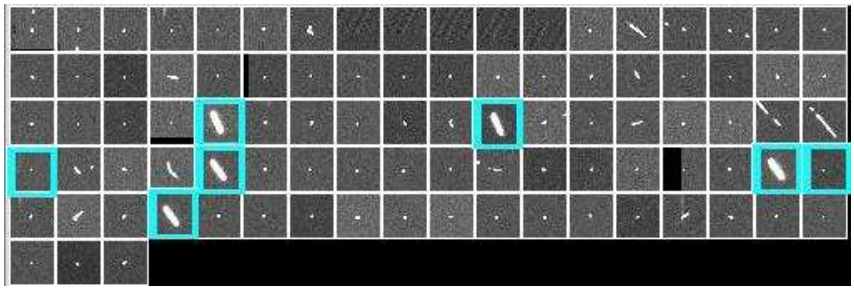

(d) Sobel filter

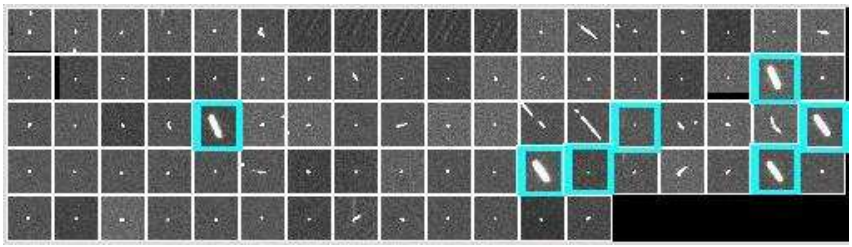

(e) Prewitt filter

Figure 5.12: (a) All detected candidates (8/130),(b) contrast filter (5/81), (c) object class filter (7/43), (d) Sobel (7/86), and (e) Prewitt (7/78) edge detection filter: SSO-27B.

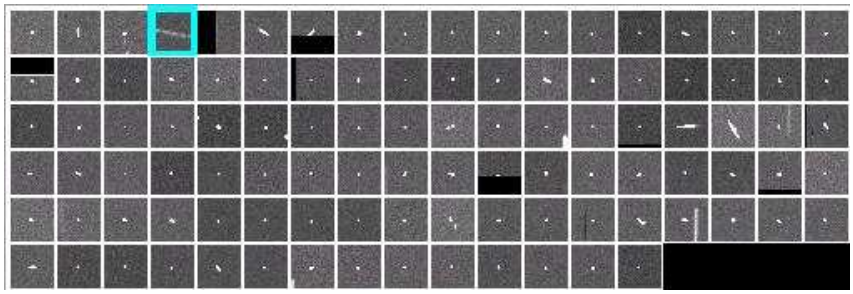

(a) no filter

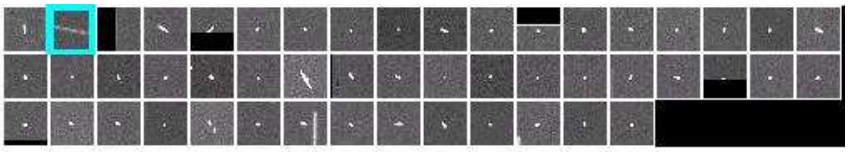

(b) contrast filter

(c) object class filter

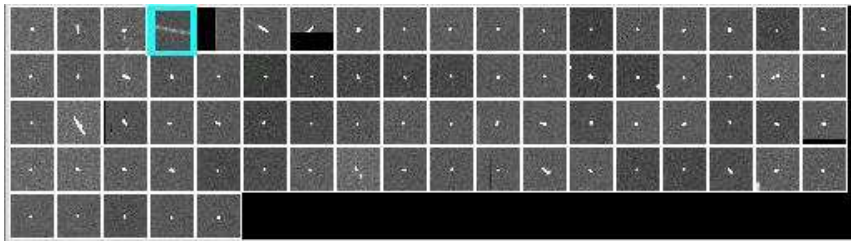

(d) Sobel filter

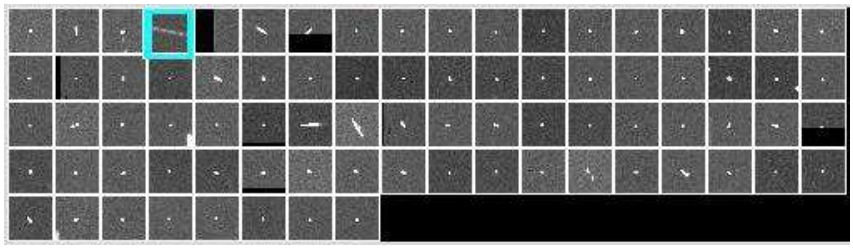

(e) Prewitt filter

Figure 5.13: (a) All detected candidates (1/103),(b) contrast filter (1/49), (c) object class filter (1/17), (d) Sobel (1/76), and (e) Prewitt (1/79) edge detection filter: SSO-33B.

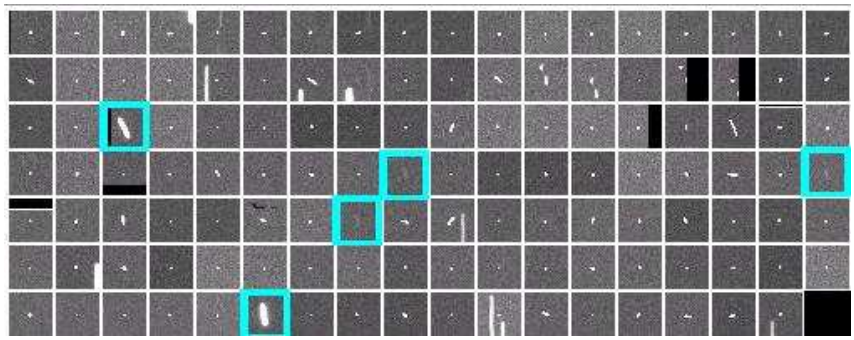

(a) no filter

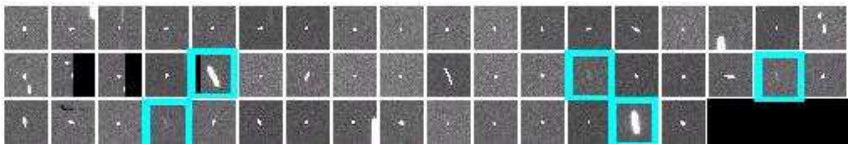

(b) contrast filter

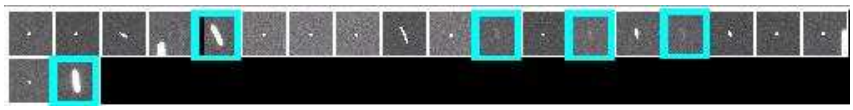

(c) object class filter

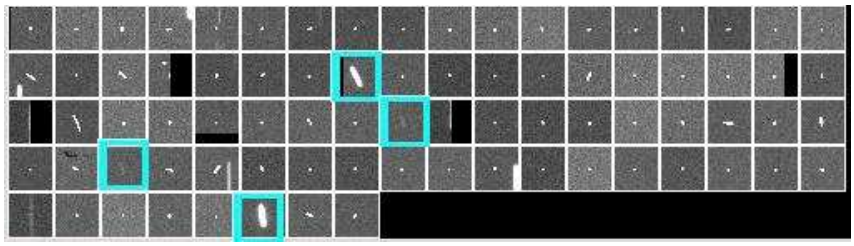

(d) Sobel filter

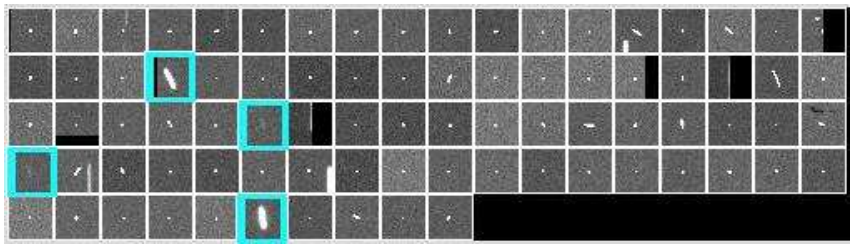

(e) Prewitt filter

Figure 5.14: (a) All detected candidates (5/122),(b) contrast filter (5/46), (c) object class filter (5/15), (d) Sobel (4/76), and (e) Prewitt (4/78) edge detection filter: SSO-35A.

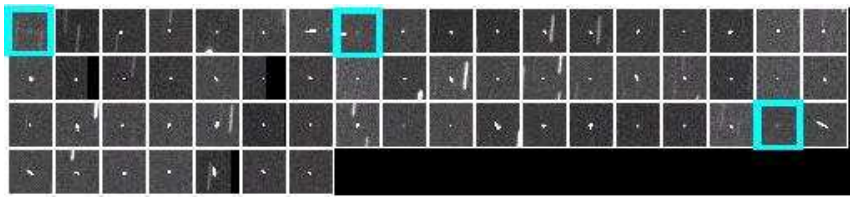

(a) no filter

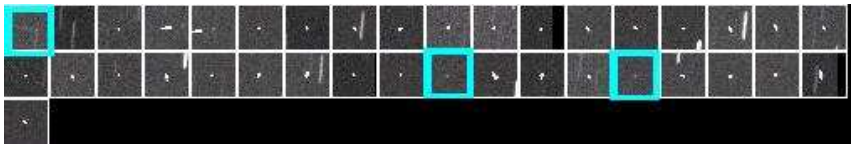

(b) contrast filter

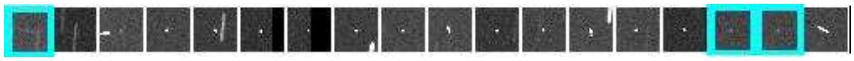

(c) object class filter

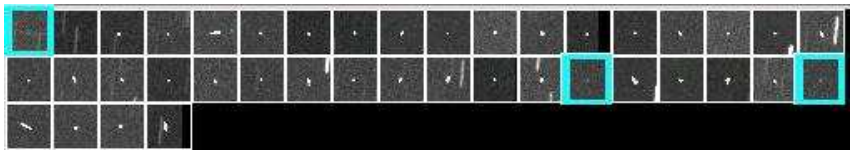

(d) Sobel filter

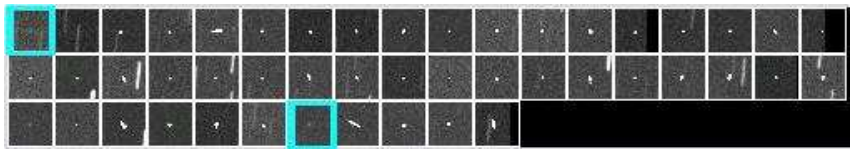

(e) Prewitt filter

Figure 5.15: (a) All detected candidates (3/58),(b) contrast filter (3/34), (c) object class filter (3/15), (d) Sobel (3/37), and (e) Prewitt (2/45) edge detection filter: SSO-11.

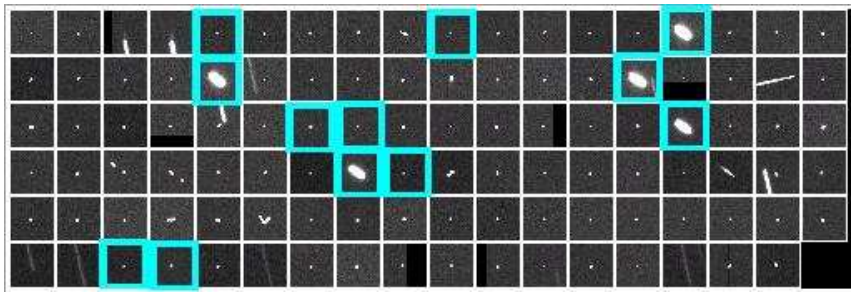

(a) no filter

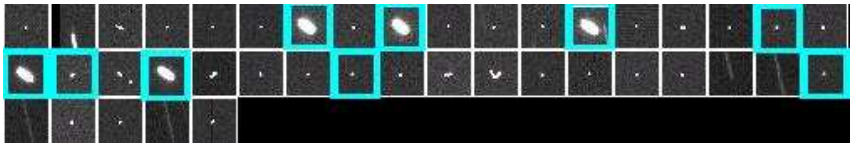

(b) contrast filter

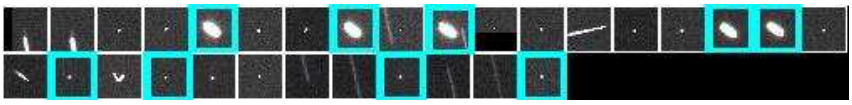

(c) object class filter

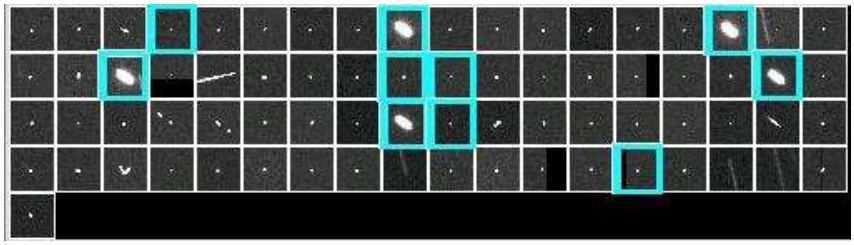

(d) Sobel filter

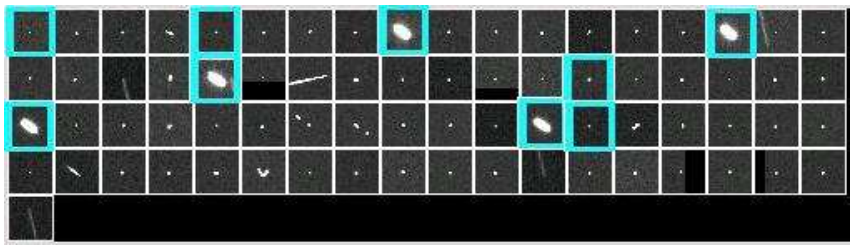

(e) Prewitt filter

Figure 5.16: (a) All detected candidates (12/95),(b) contrast filter (9/32), (c) object class filter (9/21)), (d) Sobel (9/63)), and (e) Prewitt (9/64) edge detection filter: SSO-26.

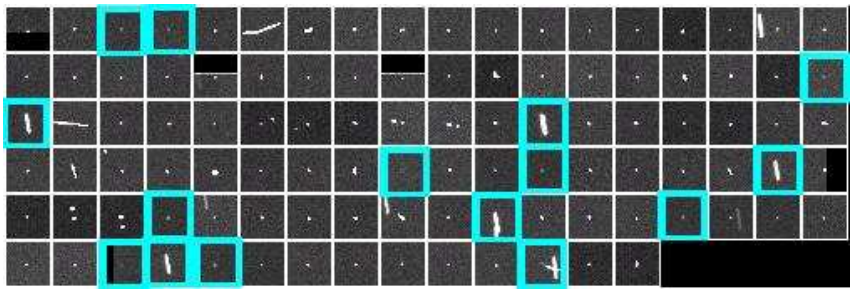

(a) no filter

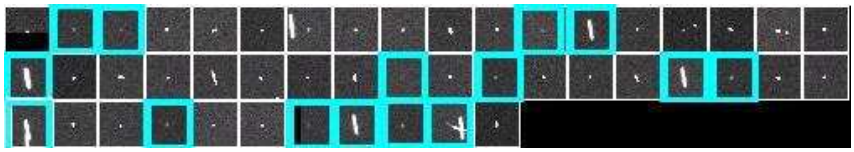

(b) contrast filter

(c) object class filter

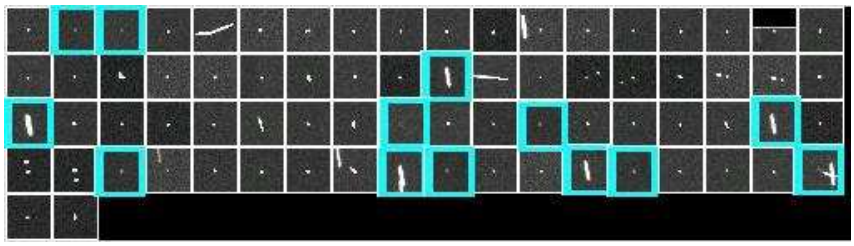

(d) Sobel filter

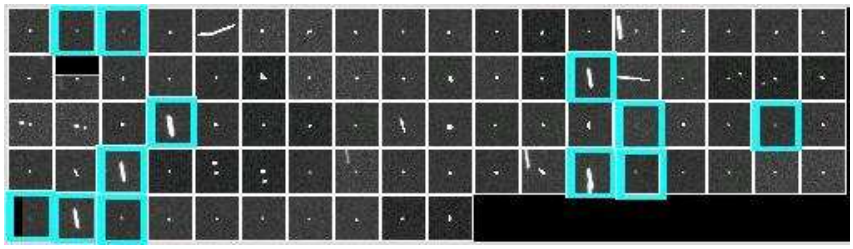

(e) Prewitt filter

Figure 5.17: (a) All detected candidates (15/89),(b) contrast filter (15/32), (c) object class filter (14/16), (d) Sobel (13/61), and (e) Prewitt (13/69) edge detection filter: SSO-30.

5.2.6 Conclusions

Three new cosmic filters were developed, implemented, and compared to the already existing cosmic filter in the ESASDT automatic processing software. All filter misinterpreted about 10 percent of the true object images, which were checked by eye and at least identified as not clearly cosmics. Only the Prewitt edge detection filter misinterprets almost 20 percent of the true object images. When interpreting these numbers, it has to be considered that in the tested night, 95 true object images were determined, only. The edge detection filters performed well by correctly identifying bright object images of all pixel numbers. The contrast and the object class filter, however, performed well by correctly identifying object images close to the signal to noise ratio level.

The object class filter was superior to the other filters with a correct cosmic rejection ratio of nearly 80 percent, the edge detection filter, Sobel and Prewitt, showed the smallest correct rejection rate with around 40 percent.

The results indicate that the decision whether a candidate is a cosmic or a real object image should not only be based on a single criterion, as e.g., the edge detection filters do. The object class filter, represents is the other extreme. It relies on many parameters and is difficult to tune. It also strongly depends on the specific telescope and camera settings.

For further improvements even more parameters, more cross-correlated selection criteria would be necessary. The effort to tune and maintain such a system would be unacceptable in relation to the expected gain.

It is recommended to switch the current top-down to a bottom-up approach. The decision process whether a candidate is a cosmic or a real object image seems to be a textbook example for the use of artificial intelligence. There are identifiable regularities and constraints, on which a decision is based. In a learning process so-called expert knowledge could be transferred to an intelligent system [94]. The actual implementation would have to show, whether it really is a simple textbook case. But it is believed to be the most promising and flexible approach for further developments.

In the current implementation, it is recommended to use the cosmic filters in dependence of the object class to be detected. For bright objects, the edge detection filters are recommended. For faint objects as they are searched for with the ESASDT, the contrast or the object class filter should be used.

6. Tracklet Linking of Object Images on Observation Series

> The human understanding is like a false mirror, which, receiving rays irregularly, distorts and discolors the nature of things by mingling its own nature with it.
>
> Francis Bacon

6.1 The Problem of Tracklet Linking

Candidate object images were identified on single frames of observation series. It now has to be decided, which of the (possibly many) object images detected on the different frames of an observation series stem from the same object. Such object images are linked together to so-called tracklets. A tracklet in a strict sense is a list of observation epochs and positions belonging to the same object. Subsequently, the term will also be used to label the linked object images of one object on the frames of an observation series, from which the exact positions will be extracted in subsequent processing steps.

The movement of an object over the frames of observation series is not known in surveys. The brightness of object images can moreover vary considerably from one frame to the next within the observation series. Brightness variations of uncontrolled objects over several magnitudes may occur within short time intervals. Details concerning rapid brightness variations are studied in Chapter 8. Figure 6.1 shows subframes containing the images of the same object on different frames of an observation series, spaced by 30 seconds. Not only the brightness but also the overall shape of the object does not necessarily have to remain the same over all frames of an observation series. Streak-shaped object images can disintegrate into several disconnected traces on single frames, when the object images are close to the signal to noise level. Thus object images do therefore not necessarily appear to *look the same*, i.e., they do not always have the same appearance on the frames.

Single frames may still be contaminated by cosmics, which were not successfully filtered out on the

Figure 6.1: Five images spaced by 30 seconds of the same object observed with the ESASDT in January 2006.

single frames, see Chapter 5. The cosmics, which are randomly distributed over the single frames, are seen as single object images in the linking process. This complicates the decision, which object images belong to the same object, because more candidates for the link are available. A high coverage of object images of the same objects is crucial in the process of successful tracklet linking. This is in particular true, when the contamination by cosmics is heavy and/or when the images of many different objects are on the frames of the series.

6.1.1 Boundary Conditions for Tracklet Linking at the ESASDT: Survey Scenarios and Coverage

Series of 15 to 30 frames spaced by a time interval of one minute between each exposure are taken in surveys of the ESASDT. When observing GEO objects the telescope is in staring mode, for GTO objects, the selected GTO classes are tracked in right ascension with about 7.5 and 10.5 arcseconds per second during exposure, in so-called blind-tacking. Follow-up series consist of 11 frames spaced by 30 seconds between exposures. The expected motion of the object is tracked during exposure. Surveys and follow-up observations are processed with the same processing software and, therefore, also with the same linking algorithm. In follow-up observations, the motion of the objects is known and this information could be used. But when follow-up observations are processed with the same algorithms as surveys observation series, objects may be (re-)detected, even when large differences between the calculated ephemerides and the observations occur, due to poor orbital information. In addition, not only objects are detected, which are followed-up, but also all other objects, which may be present on the follow-up frames. New objects are often detected in follow-up observations with the ESASDT.

Between two and three object images for GEO objects and around four to six for GTO objects near the apogee are present in search surveys with the ESASDT. The ESASDT has a field of view (FOV) of 0.7×0.7 degrees, two declination stripes are scanned in parallel. The number of frames per hour, the time available for each exposure, and the data rates for GEO objects for a two and threefold coverage with the ESASDT are provided by T. Schildknecht [78]. Table 6.1 contains the equivalent data for GEO objects for a full fourfold coverage. Tests, performed with the ESASDT, showed that a spacing of only 21 seconds, which is necessary for a full fourfold coverage, is not a sufficient time span for a reliable re-positioning of the telescope, when two declination stripes are scanned simultaneously. If only one declination stripe is scanned, the time for repositioning is sufficient, but only an area of 10.5 square-degrees per hour can be scanned with the small FOV of the ESASDT. Therefore threefold coverage for GEO objects is preferred in standard surveys with the ESASDT, but this mode complicates the linking process. The object image coverage in follow-up observations is double because the spacing between exposures is only 30 seconds.

Figure 6.2 illustrates the image linking process. It shows four frames of a follow-up observation series of the ESASDT acquired at the night of January 26, 2006. The object images of two different objects are marked on each frame. Figure 6.2 shows the linked subframes containing the object images. The subframes with the successfully linked object images are produced as one of the standard outputs of the automatic processing software of the ESASDT.

Stripes	Fr./h	Sec./exp.	Area/h	Data/h
One stripe	86	42	10.5	0.72
Two stripes	172	21	21.0	1.44
Three stripes	258	10.5	31.5	2.17

Table 6.1: Fourfold coverage of GEO objects with ESASDT: Number of frames/hour, time available per exposure, surveyed area in degrees^2/hour and data rate in GB/hour for 2×2 binned frames of a 4k×4k CCD mosaic for one, two, and three declination stripes scanned simultaneously (ESA surveys; field of view 0.7×0.7 degrees).

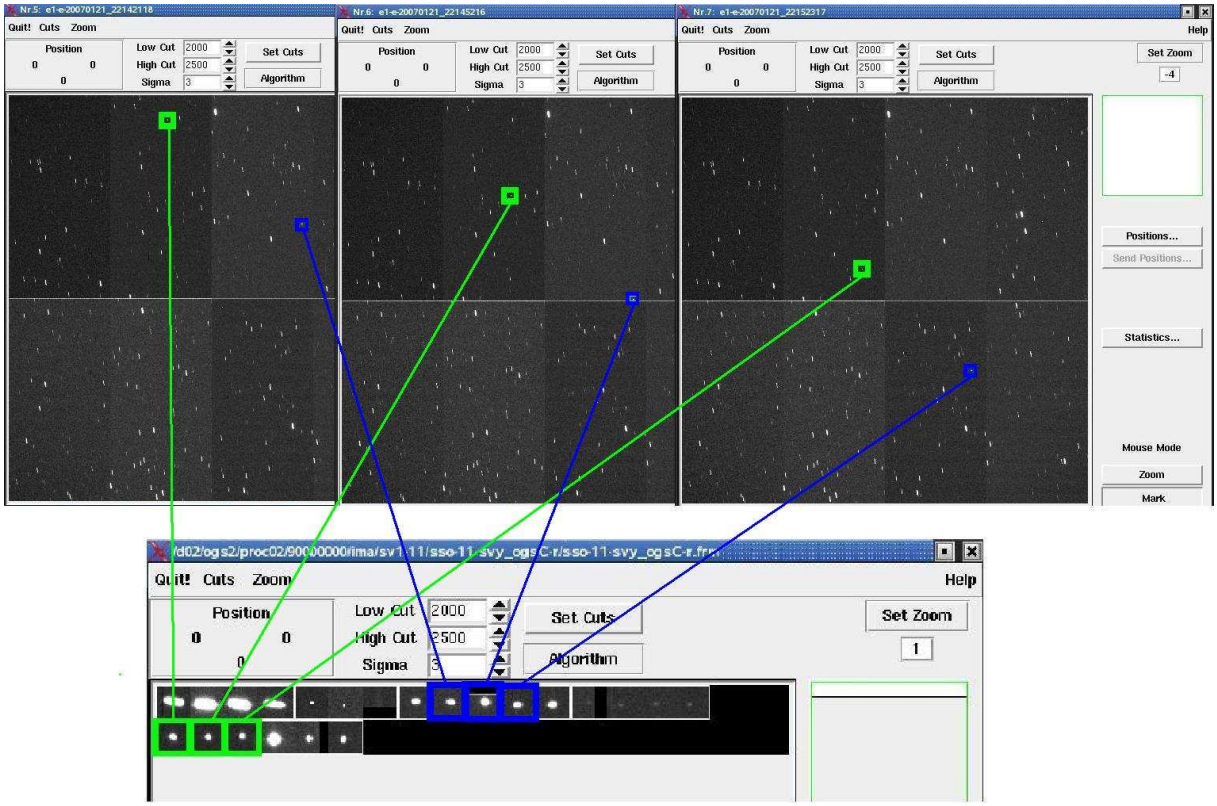

Figure 6.2: Four subsequent frames of follow-up series of the Tenerife campaign on January 26, 2006. Two objects and their images on each frame are marked. In the last picture in the right bottom corner the subframes of the linked object images, which were found on all eleven frames of the follow-up series are shown.

6.1.2 Tracklet Linking in Different Processing Schemes

For the problem of object image linking several solutions exist. One is used in the ISON network. The observation frames of the ISON network are processed with the in-house APEX II software system. The problem of object image linking is solved currently with the following algorithms [50]:

All possible permutations of candidate object images, subsequently called candidates, of two subsequent frames are linked assuming the apparent velocity they would represent is below a threshold limit. A linear movement is assumed. In addition, tracklets with one candidate are build.

All possible candidates from the third frame are now combined with the (one or two candidate) tracklets found on the first two frames. The deviation from a linear path is calculated for all possible three candidate tracklets. Those tracklets violating with their RMS a threshold value are rejected. This step is repeated for all frames of the observation series. APEX II has the feature that in cases, in which more than three candidates are linked the apparent motion of the object represented by those observations can be compared to a curved pass. The rms with respect to the curved pass can be chosen to be taken into account, when further possible candidates are linked.

In a next step, the cross-links of object images are eliminated now. A cross-link occurs, if a single candidate is linked in more than one tracklet. The cross-links is eliminated by choosing the tracklet with the smallest rms value.

A value of 30 arcseconds per second is chosen as the apparent velocity limit to link the candidates for the frames of most telescopes in the ISON network. Tracklets, which would represent an object with an apparent velocity close to the diurnal movement of stars are rejected. A minimum of five candidates per tracklet are required. Tracklets with less candidates than the half the number of frames, which the whole observation series consist of, plus one are rejected.

The Apex II algorithm produces false links of only around one percent of all tracklets linked in the ISON network. There are numerous telescopes with a large field of view generating several hundred object images per frame within the ISON network. The computational burden of the algorithms is moderate, wide field telescope series of five to seven frames require less than a few seconds processing time on a normal multi core PC.

Other processing systems, e.g. the one used for the Italian space debris telescope, use a different approach [69]. They observe only objects, which are known in a catalogue and the tracklet linking is skipped. The single observations are correlated directly with the catalogue positions. The observations, which are correlated to the same catalogue object, are automatically linked, as well. The procedure does not allow to detect new objects. In addition, as it will be shown in Chapter 7, the catalogue correlation is less reliable, when apparent velocity information is not taken into account. Apparent velocity information can be inferred directly from the candidate epochs and positions of linked tracklets; it is not available without tracklet linking prior to catalogue correlation.

6.2 Old Algorithm: Tracklet Linking with Pseudo-Inclination and Apparent Velocity Limit

The former algorithm for tracklet linking of the ESASDT was developed by Fridez and Hugentobler [38]. The candidate object images on two subsequent frames are assumed to belong to the same object, if the apparent drift and pseudo-inclination, calculated from the two positions, and the brightness contrast of the two images are below certain threshold values.

The overall brightness determined directly from the background corrected frames of the different object images in ADU are used, for the calculation of the intensity contrast. In the processing of the ESASDT, a value of 100 percent is used as a default threshold value.

The raw pixel coordinates of the observations at time t_1 and t_2 are transformed into right ascension/declination (α/δ) and azimuth/elevation (az/el) using the pointing direction of the telescope for the evaluation of the apparent drift and pseudo-inclination limits. This transformation contains errors, because the precise astrometry is not performed yet and the pointing accuracy of the telescope is limited to about one arcsecond. The apparent drift D and pseudo-inclination I are determined as the following:

$$D = \frac{\sqrt{(az_2 - az_1)^2 + (el_2 - el_1)^2}}{(t_2 - t_1} \tag{6.1}$$

$$I = \arctan\left(\frac{\delta_2 - \delta_1}{(\alpha_2 - \alpha_1)\cos(\delta_1)}\right) \tag{6.2}$$

A maximum drift limit of 15 arcseconds per second and a maximum inclination limit of 25 degrees are chosen as default values for GEO objects. These allow to link the object images of the majority of GEO objects.

The procedure is repeated for all pairs of two subsequent frames within the observation series. Tracklets with apparent velocities close to the diurnal movement of stars are rejected. Currently, a movement of less than eight arcseconds during the observation series is identified as movement of stars.

6.2.1 Limitations of the Old Algorithm

The old algorithm for object image linking only uses the information of two subsequent frames to decide, which object images belong to the same object. More than two object images are linked, if the apparent velocity and pseudo-inclination of an object represented by the second object image (already linked with the first object image) and third object image are below the threshold value. It is not checked, if the pseudo-inclination and velocity values represented by the first two object images is similar to the pseudo-inclination and apparent velocity represented by the second and the third object image. This may lead to a successfully linked tracklet, which consists of three or more object images, which would represent rapidly changing inclination and apparent velocity values from the first two object images to the subsequent object image pairs. A link with cosmics, which were not correctly recognized by the filter, is likely. Tracklets of objects, with a large pseudo-inclination and/or a large apparent drift rate, cannot be linked and therefore the objects although present on the frames, remained *undetected*. Larger thresholds lead to an unacceptable increase of false links. If single object images are missing on frames, either

because they are covered by a star trail or because the signal to noise ratio is too low for detection, the images before and after the gap cannot be linked in one tracklet. The algorithm is working its way from lower to higher pixel coordinates. If a link to a candidate on the subsequent frame has been found, this link is final. No check is performed, whether an alternative, possibly better link with a candidate exists.

It is an advantage of the old algorithm that it only has three threshold values, which can easily be tuned for new telescopes and observation setups. No further restrictions on the direction of movement are made. The old algorithm and the new one are compared in Section 6.4.

6.3 New Algorithm: Tracklet Linking

The new algorithm uses the information on all frames to link object images. In a first step, two random object images on two consecutive frames are considered as preliminarily linked. An absolute value of the velocity and the direction of the velocity vector is calculated directly in so-called normal coordinates. The standard coordinate system is defined as the tangent plane on the topocentric space-fixed celestial sphere, with its origin in the pointing direction of the telescope. The pixel coordinates of each frame are transformed in normal coordinates. In the transformation the so-called mapping model is applied. The mapping model corrects the pixel coordinates due to the actual alignment of the CCD mosaic, it accounts for the small pixel gaps in between the parts of the mosaic and for their slight shearing. The mapping model is specific for the each telescope and detector. Not applying the mapping model leads to clearly inferior results. The transformation into standard coordinates allows a tracklet linking independently of the specific observation scenario of the observation series. This is not the case, when e.g. using pixel coordinates directly.

All preceding and subsequent frames are checked for additional object images, which would, when combined with the first two object images, represent an object with a constant apparent direction of movement and a constant apparent absolute velocity, within allowed deviation thresholds for the absolute velocity and the direction. The search for additional object images is similar to a so-called first order Markov chain algorithm, see, e.g., [48] for details. The limits of the velocity vector define a so-called allowed region for possible object images on the subsequent frame. The frame is skipped, if no candidate is detected in the allowed region. The allowed region is necessarily broadened up on the subsequent (third) frame, if no object image is detected in the allowed region of the preceding (second) frame. This is called a gap, if further object images can be linked on frames, after the empty allowed region. A maximum number of allowed gaps has to be defined. The allowed region is narrowed down as soon as an additional object image is detected in the allowed region on any of the subsequent or previous frames. The velocity vector and its deviation thresholds are updated dynamically. The procedure is illustrated Fig. 6.3.

40 manually selected tracklets, which were linked with the old algorithm and manually corrected, were evaluated in order to find empirical limit values for the deviation thresholds in absolute velocity and direction of velocity. The tracklets where picked randomly from the Tenerife campaigns of the first months of 2006. Only tracklets containing many object images were selected; the average was 4.5 images per tracklet. The absolute value of the apparent velocity calculated from the first two object images be $|v_0|$ and the absolute value of the apparent velocities calculated from all subsequent object image pairs within the set be $|v_i|$; the expectation value and standard deviation of the velocity deviation thresholds

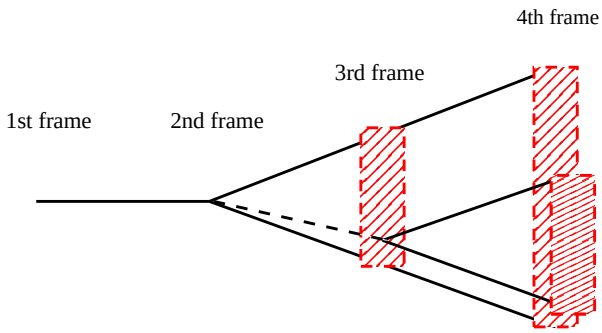

Figure 6.3: Link of three and four object images on three and four subsequent frames respectively, and the corresponding allowed regions, with and without one missing object images (gap) on the third frame. The limit values are dynamically updated as soon as a new object image is found in the allowed region, in case of a gap the allowed region is broadened up.

are determined as the following:

$$\left\langle |v_i|/|v_0| \right\rangle = 0.185\% \qquad \sigma_{|v_i|/|v_0|} = 0.156\% \tag{6.3}$$

The expectation value and standard deviation of the angle $\sphericalangle v$ between the directions of motion in standard coordinates of the object represented by the first two object images and all subsequent object image pairs within the sets are determined as the following:

$$\begin{aligned} \left\langle \sphericalangle v \right\rangle &= 0.001\text{rad} \mathrel{\hat{=}} 0.063\text{deg} \\ \sigma_{\sphericalangle v} &= 0.001\text{rad} \mathrel{\hat{=}} 0.063\text{deg} \end{aligned} \tag{6.4}$$

For a normal distribution the determined expectation value and standard deviation are unbiased estimates [31]. For the deviation in absolute velocity and in the angular of velocity a $3 \cdot \sigma$ area around the expectation values from Eq. 6.3 and Eq. 6.4 are chosen; the deviation thresholds are $(|v_i|/v_0|)_{limit} = 0.7$ percent and $\sphericalangle v_{\text{limit}} = 0.004$ radians. The maximum number of gaps for a tracklet with m candidates is selected to be $n = (m-2) \cdot 3$. In the processing of the ESASDT a linking of three object images is accepted as a valid tracklet, as long as the gap limit is not exceeded.

The algorithm is implemented as the following: after a preliminary link of object images via the allowed regions all cross-links are detected. Cross-links are links of one candidate in two or more tracklets. Tracklets consisting of more object images are preferred over shorter tracklets to resolve cross-link conflicts; for the shorter tracklets the preliminary link is unlinked. In a second run the tracklets, which are left over from the first run and the newly unlinked ones are checked again. The two steps are repeated until all cross-link conflicts are solved. In all test runs, no further cross-link conflicts occurred in the second iteration.

For performance reasons, the algorithm links object images in two steps. In the first step, only tracklets are linked, which additionally also fall with their apparent velocity within a drift and pseudo-inclination limit. In the second step, all tracklets are linked without further limits. The structure of the algorithm also allows to perform only one of those steps be performed, if requested by the user.

In order to be able to detect tracklets of objects for which only two object images are present on the

frames of an observation series, a finally step is included, in which two object images may be linked from all unlinked object images still left over from the first two steps, if they fall within the apparent drift and pseudo-inclination limits. Tracklets of two object images are accepted, if one of the two object images is very faint, or, in case both are above a brightness threshold, if their shapes on the frame resemble each other. A value of 800 ADU is chosen to distinguish faint from bright objects. For the resemblance test, the main axis of the inertial tensor of the two images are allowed to deviate by less than 20 percent.

It may be selected to disable the search for two object image tracklets by the user.

The rejection of tracklets with an apparent velocity close the diurnal motion of stars is taken over from the old algorithm.

6.3.1 Limitations of the New Method

6.3.1.1 Probability for Random Links

The rate of random links of three or more candidates has been evaluated for the new algorithm in order to find the limits of the method. Observation series are assumed consisting of single frames containing a number of q candidates. The candidates are assumed to be randomly distributed over the frame. The probability of random links of tracklets consisting of m candidates is investigated. The allowed number of gaps is assumed to be n. A square field of view is assumed. The probability for a random candidate linking, i.e., the probability that tracklets are detected, although no object is displayed on the frames, is estimated: For the estimation the candidates of a whole observation series are added up in a squared single frame, called summary frame in the following, with a given field of view (FOV). The density of candidates within this summary frame is calculated. The size of all allowed regions for a tracklet with a given number of images and gaps is determined under the premise that the whole tracklet (including gaps) can be displayed in the summary frame. This is in accordance with the ESASDT observation strategy. The probability to find a candidate in the allowed region with the given density of candidates is evaluated, which leads to the following expression:

$$P \leq \sum_{i=0}^{n} \left(\frac{8}{(i+m-1)^2} \cdot (|v_i|/|v_0|)_{\mathrm{limit}} \cdot \sin(\sphericalangle v_{\mathrm{limit}}/2) \cdot q \cdot (i+1) \right)^{m-2} \qquad \text{for } m \geq 3 \tag{6.5}$$

Table 6.2 lists the probabilities for random links for different the numbers of candidates m linked in one tracklet in dependence of the number of total candidates q present on each frame and the number of allowed gaps n within each tracklet. The table provides the probabilities for $m = 1, 2, 3$ and $q = 20, 30, 60$; these values are realistic for the ESASDT. The probability for random links is only about $6.26 \cdot 10^{-3}$ even if only three candidates object images are linked in one tracklet ($m = 3$), with a maximum number of allowed gaps of $n = 2$ and 60 candidates on each frame.

The results are different for wide-field telescopes. About 300 to 600 object candidates may be detected on a single frames of the ZimSMART telescope. A large pixel scale, as it is the case at the ZimSMART telescope, does not allow to filter cosmics on the single frames. Series gathered with the ZimSMART telescope, consist of five frames only, i.e., implying, tracklets with more than five candidates do not occur. Table 6.3 provides the probabilities for random links. The probability of random links in tracklets of

cand. per tracklets (m)	cand. per frame (q)	gaps (n)	Probability (P)
3	20	3	$2.09 \cdot 10^{-3}$
3	20	2	$1.68 \cdot 10^{-3}$
4	20	6	$5.27 \cdot 10^{-7}$
5	20	9	$6.34 \cdot 10^{-11}$
3	30	3	$3.12 \cdot 10^{-3}$
3	30	2	$2.54 \cdot 10^{-3}$
4	30	6	$1.19 \cdot 10^{-6}$
5	30	9	$2.14 \cdot 10^{-10}$
3	60	3	$6.26 \cdot 10^{-3}$
3	60	2	$5.04 \cdot 10^{-3}$
4	60	6	$4.75 \cdot 10^{-6}$
5	60	9	$1.71 \cdot 10^{-9}$

Table 6.2: Probabilities of random linking as a function of the number of candidates within the tracklet, the number of object image candidates on each frame, and the number of allowed gaps for ESASDT. The probabilities are maximum values for each scenario.

cand. per tracklet (m)	cand. per frame (q)	gaps (n)	Probability (P)
3	300	2	$2.52 \cdot 10^{-2}$
3	300	1	$1.80 \cdot 10^{-3}$
4	300	1	$4.10 \cdot 10^{-5}$
4	*300*	*2*	*6.20*$\cdot 10^{-5}$
5	300	0	$1.36 \cdot 10^{-8}$
5	*300*	*1*	*4.21*$\cdot 10^{-8}$
3	600	2	$5.04 \cdot 10^{-2}$
3	600	1	$3.61 \cdot 10^{-2}$
4	600	1	$1.63 \cdot 10^{-4}$
4	*600*	*2*	*2.47*$\cdot 10^{-4}$
5	600	0	$1.09 \cdot 10^{-7}$
5	*600*	*1*	*3.37*$\cdot 10^{-7}$

Table 6.3: Probabilities of random linking as a function of the number of candidates within the tracklet, the number of object image candidates on each frame, and number of allowed gaps for ZimSMART. The probabilities are maximum values for each scenario. The italic numbers are theoretical values for observation series with more than five frames.

only three candidates is of the order of 10^{-2}. For a ZimSMART like setup it is recommended to use at least four object images for a reliable correct tracklet linking.

In order to also reliably link tracklets of three object images only, even when many candidates are on the frame, a limit $|v|_{\mathrm{limit}}$ may be imposed as an additional criterion. Tracklets are affected by the velocity

cand. per tracklet (m)	cand. per frame (q)	gaps (n)	Probability (P)
3	20	3	$1.37{\cdot}10^{-3}$
3	20	2	$9.06{\cdot}10^{-4}$
4	20	6	$4.74{\cdot}10^{-7}$
3	30	3	$2.06{\cdot}10^{-3}$
3	30	2	$1.45{\cdot}10^{-3}$
4	30	6	$1.07{\cdot}10^{-6}$
3	60	3	$4.12{\cdot}10^{-3}$
3	60	2	$2.89{\cdot}10^{-3}$
4	60	6	$4.27{\cdot}10^{-6}$

Table 6.4: Probabilities of random links as a function of the number of candidates within the tracklet, the number of object image candidates on each frame, and the number of allowed gaps for ESASDT. In the evaluation a velocity limit of 15 "/sec was imposed. The probabilities are maximum values.

limit, if they consist of m candidates and n gaps with:

$$\sqrt{2}g/(n+m-1) > |v|_{\text{limit}} \cdot (t_2 - t_1) \tag{6.6}$$

when g is the edge length of the square field of view and $(t_2 - t_1)$ the time interval between subsequent frames. All other tracklets must necessarily have a lower apparent absolute velocity, because otherwise the object would have run out of the field of view before $m+n$ candidates could be found. The velocity limit changes the probability for random linking (Eq. 6.5) in the following way:

$$\begin{aligned} P \quad \leq \sum_{i=0}^{n} \Big(& \frac{4}{g^2} \cdot (|v|_{\text{limit}} \cdot (t_2 - t_1))^2 \cdot \\ & (|v_1|/|v_0|)_{\text{limit}} \cdot \sin(\sphericalangle v_{\text{limit}}/2) \cdot q \cdot (i+1) \Big)^{m-2} \end{aligned} \tag{6.7}$$

The probabilities for random linking according to Eq. 6.7 has been evaluated, with a value for the velocity limit of 15 arcseconds per second for ESASDT and ZimSMART and the their corresponding FOV of 0.7×0.7 and 4.2×4.2 degrees, respectively. For ZimSMART a temporal spacing of one minute was assumed between the single exposures, the same as for the ESASDT. Tracklets with five and more images are not affected by the velocity limit in the ESASDT scenario because of the smaller field of view. For ZimSMART all tracklets are affected. Table 6.4 and 6.5 summarize the results for ESASDT and ZimSMART, respectively. The probabilities for random links are significantly decreased. For ZimSMART the probability of random links of tracklets with only three candidates is well below 10^{-3}.

The following investigation illustrates the problem of random links without velocity limits: A scenario of 30 images per frame was assumed for the ESASDT. Figure 6.4 shows the probability for linking three and four candidates into tracklets as a function of the number of gaps allowed. The probability grows slowly with the number of allowed gaps. The number of gaps is, however, less crucial for the four candidate tracklet than for the three candidate tracklet. Figure 6.5 shows the probability of random links as a function of the number of candidates within the tracklet. The probability of random links rapidly decreases with every candidate added to the tracklet. Figure 6.6 shows the crucial dependence on the total

cand. per tracklet (m)	cand. per frame (q)	gaps (n)	Probability (P)
3	300	2	$4.06 \cdot 10^{-4}$
3	300	1	$2.01 \cdot 10^{-4}$
4	300	1	$2.29 \cdot 10^{-8}$
4	*300*	*2*	$6.41 \cdot 10^{-8}$
5	300	0	$3.09 \cdot 10^{-13}$
5	*300*	*1*	$2.79 \cdot 10^{-12}$
3	600	2	$8.10 \cdot 10^{-4}$
3	600	1	$4.12 \cdot 10^{-4}$
4	600	1	$9.15 \cdot 10^{-8}$
4	*600*	*2*	$2.46 \cdot 10^{-7}$
5	600	0	$2.48 \cdot 10^{-12}$
5	*600*	*1*	$2.23 \cdot 10^{-12}$

Table 6.5: Probabilities of random links as a function of the number of candidates within the tracklet, the number of object image candidates on each frame, and the number of allowed gaps for ZimSMART. The italic numbers are theoretical values for series with more than five frames. In the evaluation a velocity limit of 15 arsec/sec was imposed. The probabilities are maximum values.

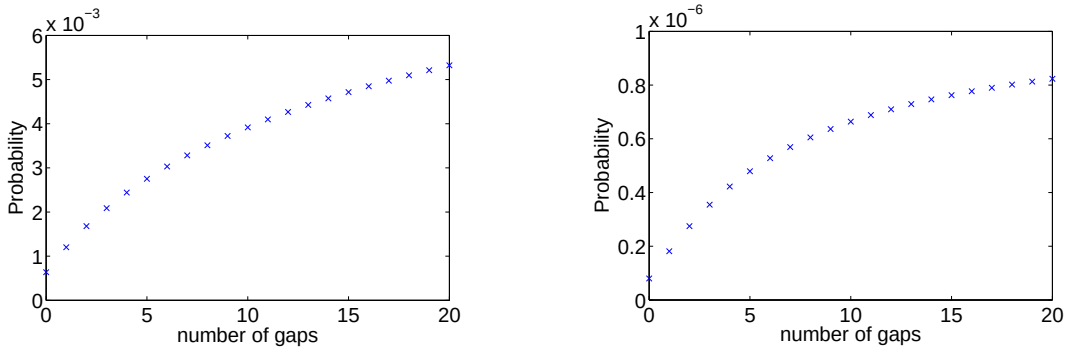

(a) tracklet of three candidates *(b) tracklet of four candidates*

Figure 6.4: Probability of random links of tracklets of (a) three and (b) four candidate object images as a function of the number of allowed gaps within the set.

number of candidates on each frame for tracklets with three or four candidates with a maximum of two and six allowed gaps, respectively. The probability for random links of candidates is generally higher for tracklets with only three candidates. The probability for random links grows quadratically with the number of candidates on the frames.

6.3.1.2 Limits Imposed by Assumption of Steady Linear Apparent Motion

The new algorithm links object images based on the assumption of constant linear apparent motion of the objects over the frames during the observation series. Several orbits were analyzed to study the limita-

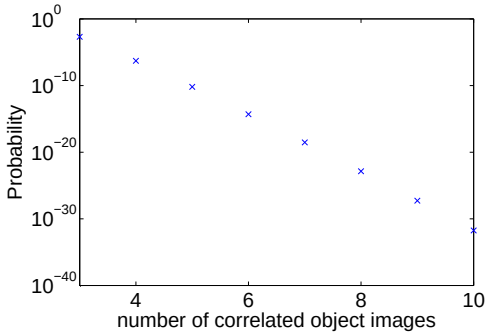

Figure 6.5: Probability of random linking as a function of the number of candidate object images in the tracklet (logarithmic scale).

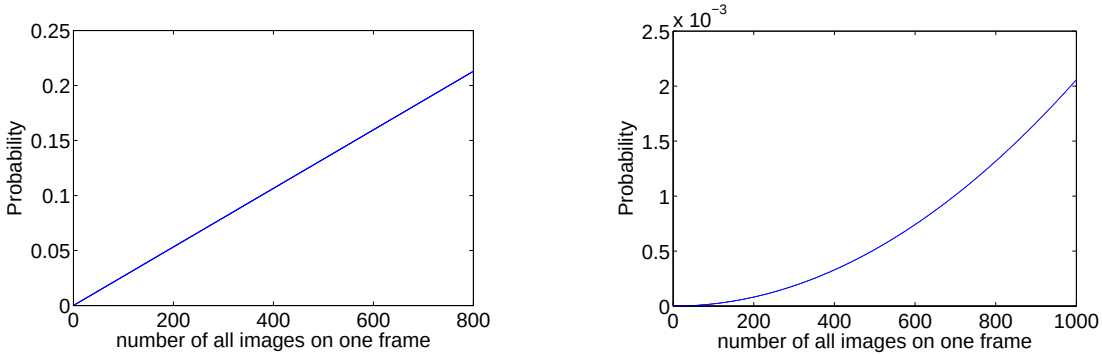

(a) tracklet of three candidates

(b) tracklet of four candidates

Figure 6.6: Probability of random links as a function of the number of candidate object images on one frame, (a) for linking of three candidates with a maximum number of two allowed gaps, and (b) for correlation of four candidates with a maximum number of six gaps.

Name	COSPAR Number	Apogee (km)	Perigee (km)	Incl. (deg)	Ecc.	Tracklets in 24h
GEO						
MSG 2	05049B	35795	35783	0.3184	0.0001	7
Gorizont 33	90102A	35761	35745	12.8753	0.0002	8
Block DM	91010F	35895	35765	12.2318	0.0015	8
GTO						
Kiku-6	94056A	38692	8548	14.9243	0.5024	88
Blok DM3	97046D	35871	8503	14.5544	0.4790	87
Deb ISO	95062C	70316	1213	3.1615	0.8199	90
Chandra Rocket (2)	99040D	71514	1808	33.4316	0.8098	91
GPS						
GPS-10	84097A	21206	20608	62.2247	0.0110	19
GPS-11	85093A	21687	20750	62.9986	0.0170	21
LEO						
Vanguard 1	58002B	3839	652	34.243	0.1848	414

Table 6.6: Test objects.

tions imposed by this assumption: Three objects in GEO were studied, one with zero inclination and two with inclinations of about 12 degrees. In addition, four objects in GTO were studied, two in orbits with moderate eccentricities $e \approx 0.5$ and two in high eccentricity orbits with $e \approx 0.8$. Two satellites of the GPS constellation in MEO (medium Earth orbit) are studied and one object in LEO. Orbit information and identifiers for all objects are provided in Tab. 6.6. The experiment was set up in the following way: For all objects, geocentric ephemerides are determined over a time interval of 24 hours with a spacing of one minute. The ephemerides were transformed to the topocentric position of the ESASDT. It was assumed that all objects are visible during 24 hours, i.e., that the earth is transparent. The topocentric ephemerides are transformed in so-called standard coordinates. A projection center has to be chosen for the transformation of the celestial coordinates into standard coordinates. In a real observation scenario this center is given by the pointing of the telescope, whereas the observations are mapped from celestial coordinates to the flat CCD and from there to standard coordinates for the linking. In the simulation, the topocentric viewing direction of the first ephemerides position is chosen as projection center. An unlimited field of view is assumed in the test setup: no new pointing is enforced by the object running out of the field of view. The theoretical telescope is assumed to be repositioned only, each time the algorithm is not able to connect the next object image to the current tracklet (because the linearity condition is violated (limit of the method is reached)). After repositioning the object position is again in the center of the tangent plane of the standard coordinate system again (coordinates 0/0).

Only linking in forward direction is performed. If no third object image can be linked, the first two object images remain linked and are counted as one tracklet in the following.

Figure 6.7 illustrates the results for the investigated objects in GEO. Figure 6.7a and 6.7b show right ascension and declination, respectively, as they appear for the topocentric position of the ESASDT for

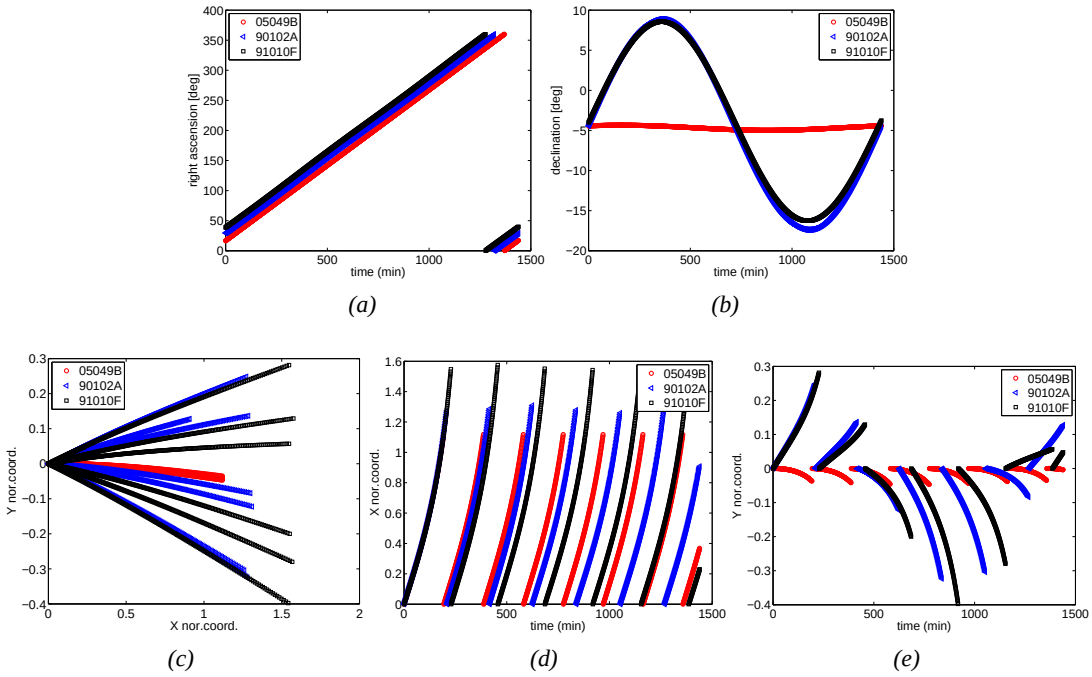

Figure 6.7: Link of simulated ephemerides of three GEO objects over 24 hours: (a) Right ascension, (b) Declination as observed from Tenerife, (c) x-y coordinates in standard coordinate. (d) x- and (e) y-standard coordinates as a function of time.

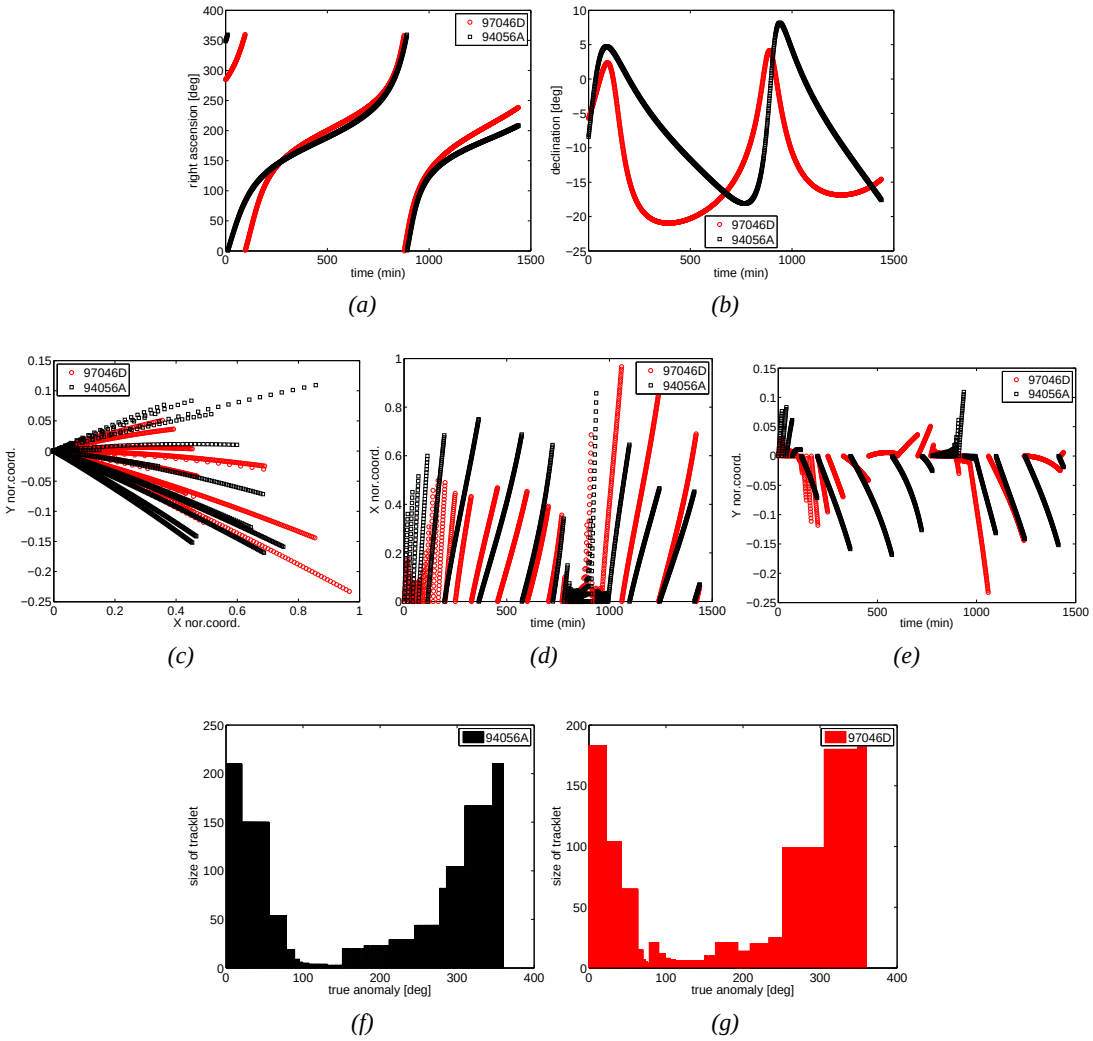

Figure 6.8: Link of simulated ephemerides of two GTO objets with moderate eccentricities over 24 hours: (a) Right ascension, (b) Declination as observed from Tenerife, (c) x-y coordinates in standard coordinate system. (d) x- and (e) y-standard coordinates as a function of time. (f) and (g) show the length of the tracklets as a function of true anomaly of the object 94056A and 97046D, respectively.

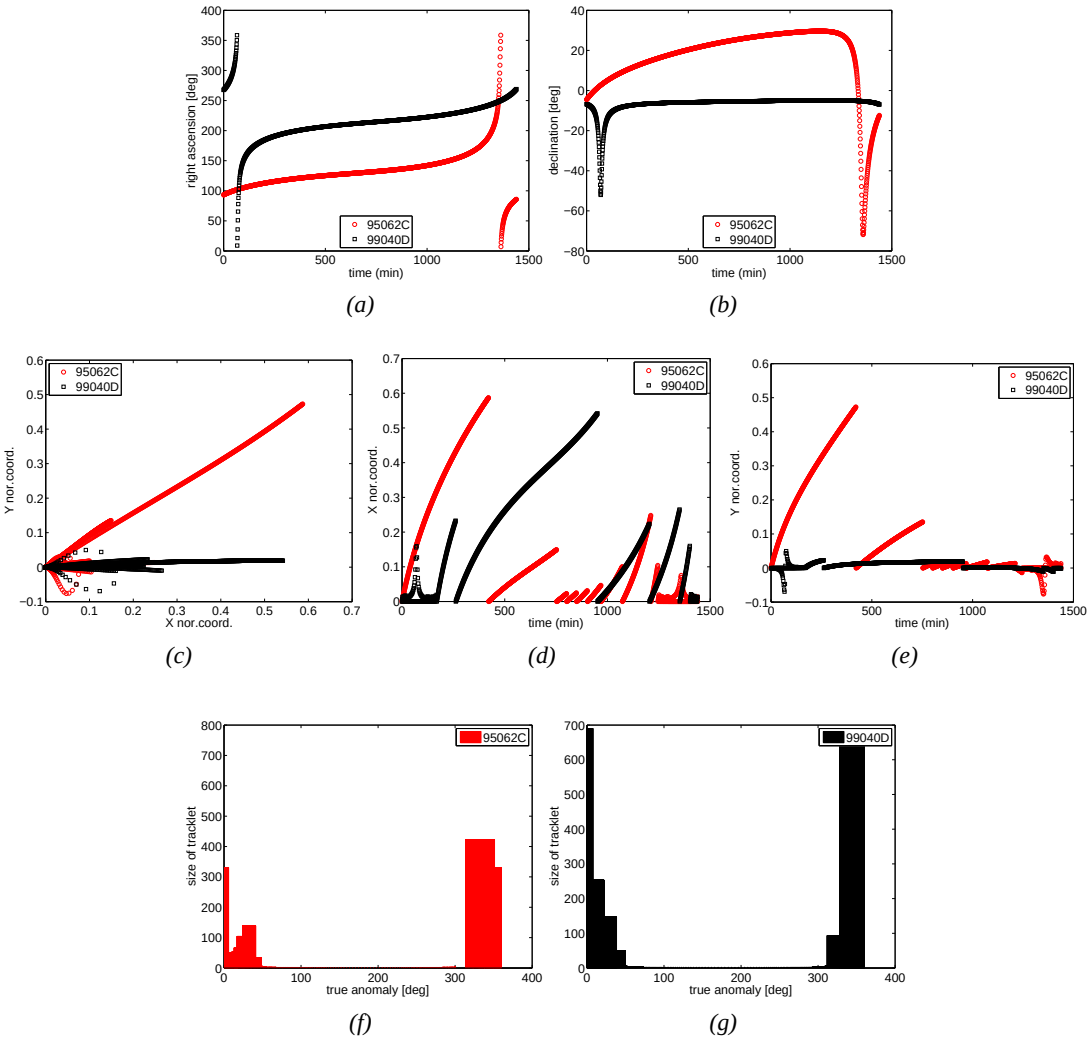

Figure 6.9: Link of simulated ephemerides of two high eccentricity GTO objects over 24 hours: (a) Right ascension, (b) Declination as observed from Tenerife, (c) x-y coordinates in standard coordinate system. (d) x- and (e) y-standard coordinates as a function of time.(f) and (g) show the length of the tracklets as a function of true anomaly of the object 95062C and 99040D, respectively.

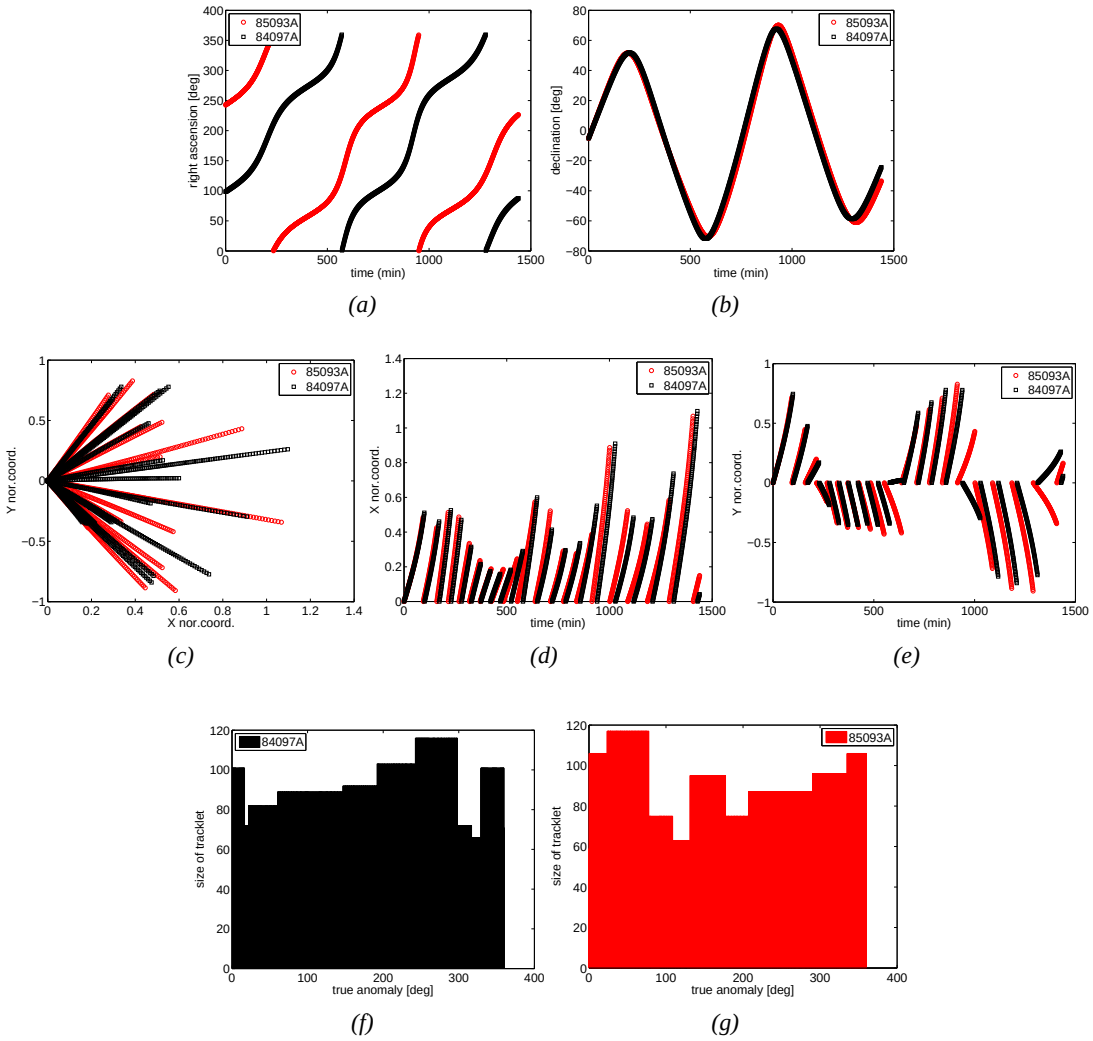

Figure 6.10: Link of a simulated ephemeris of two GPS satellites over 24 hours: (a) Right ascension, (b) Declination as observed from Tenerife, (c) x-y coordinates in standard coordinate system. (d) x- and (e) y-standard coordinates as a function of time.(f) and (g) shows the length of the tracklets as a function of true anomaly of the satellite 84097A and 85093A, respectively.

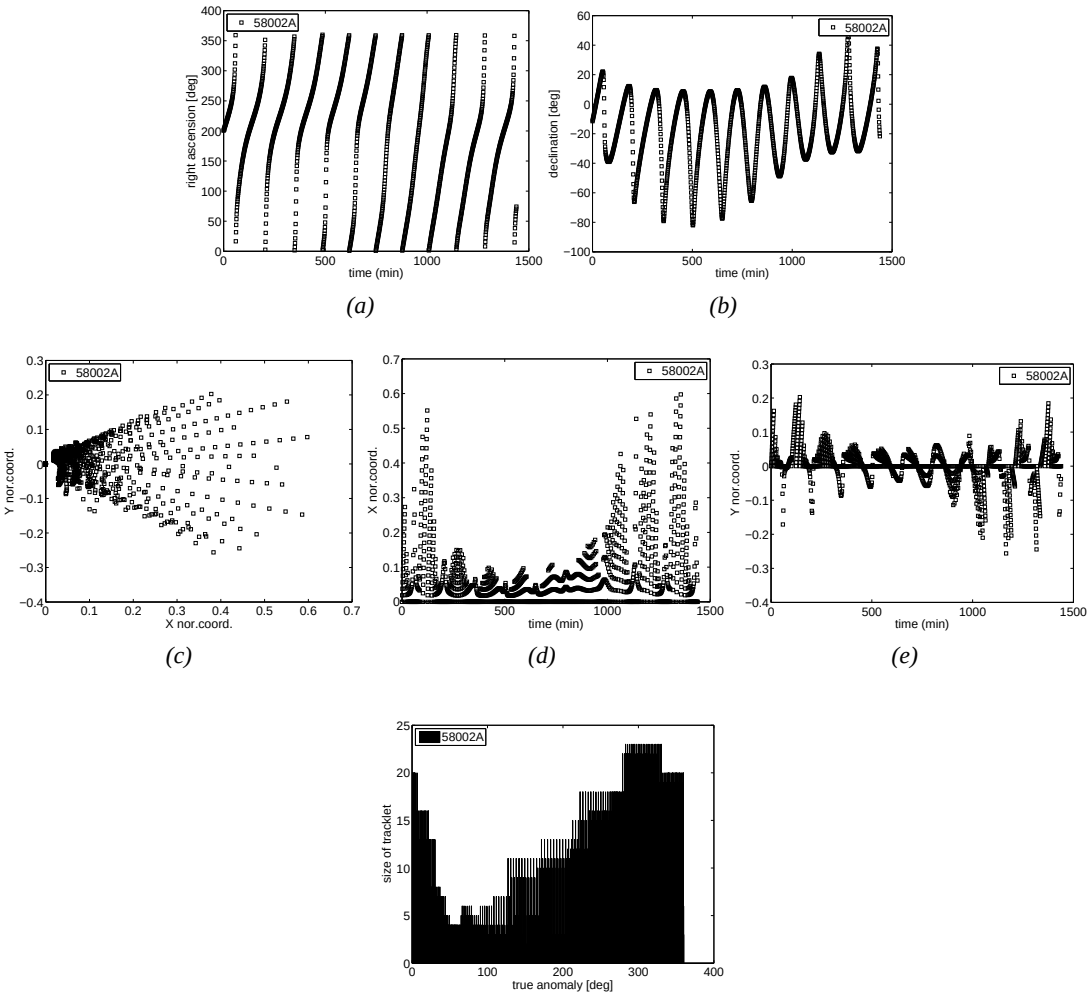

Figure 6.11: Link of simulated ephemerides of the LEO object 58002A over 24 hours: (a) Right ascension, (b) Declination as observed from Tenerife, (c) x-y coordinates in standard coordinate system. (d) x- and (e) y-standard coordinates as a function of time.(f) shows the length of the tracklets as a function of true anomaly.

a theoretical observation over 24 hours. Figure 6.7c shows the linked tracklets in normal coordinates in the tangent plane. The first object position of each tracklet appears at the origin of standard coordinates. Figure 6.7d and 6.7e show the x and y standard coordinates as a function of time. The tracklets contain in average 180 object positions, which corresponds to 180 minutes. Independently of the inclination, not more than eight tracklets for the 24 hour observation have been formed. The algorithm is able account for moderate deviations from the linear movement, because the velocity vector is dynamically updated during the linking process. Linking fails, if the deviation from the linear movement is getting too large and if the difference from the initially chosen and not updated projection center are affecting the results.

The results of the linking are illustrated in Fig. 6.8 for the GTO objects with eccentricities of $e \approx 0.5$ and in Fig. 6.9 for the objects with $e \approx 0.8$. About 90 different tracklets were linked in all cases. There are huge differences in the length of the tracklets. For observations around the apogee the length of the tracklets is of the same order as for GEO objects, as Fig. 6.8f,g and 6.9f,g show. For GTO objects with moderate eccentricities all tracklets with anomalies of over 300 and below 50 degrees are longer than 80 minutes. For objects in high eccentricity orbits tracklets longer than 150 minutes occur for anomalies larger than 320 and below 30 degrees.

Figure 6.10 shows the results for the two GPS satellites. Between 19 and 21 different tracklets were created. The apparent deviation from the linear movement in standard coordinates are smaller for the GPS satellite than for the GTO objects, which are be due to the smaller eccentricities of the GPS orbits. The GPS observation tracklets are of comparable length over all anomalies because the eccentricities are smaller than for the GTO objects. The algorithm is useful for linking MEO object observations up to series of about two hours.

Figure 6.11 shows the links of the ephemerides of Vanguard 1, a LEO satellite. The algorithm is by no means optimized for LEO environment. 414 tracklets were formed. For the LEO environment the algorithm would have to be adjusted. Short observation series below ten minutes can successfully be linked depending on the anomaly and eccentricity of the object, even without additional adjustment. The algorithm in its present form is however not recommended for LEO observations.

6.4 Performance Comparison with the ESASDT

The performance of the new algorithm is compared to that of the old one. The results of two nights of the Tenerife campaign 2006 (January 26 and August 25) were used as an example. The manually corrected (!) tracklets of the former algorithm were compared with the tracklets of the new algorithm, which were automatically processed without manual corrections. Table 6.7 shows the results.

The new algorithm represents an improvement for all investigated categories. The third column shows that the number of correct tracklets increased. Column two shows that, in total, fewer tracklets were linked. This is due to the fact that the number of wrongly linked tracklets could be slightly decreased. The large majority of remaining erroneously linked tracklets are tracklets that consist of two candidates only, as the comparison of column two with column five reveals. The link over the apparent drift and pseudo-inclination limit only is even with the additional adjustments is not powerful enough to reliably

version	sets	correct sets	correct sets $\geq$3im.	wrong sets $\geq$3im.	images/ correct set	manually corrected	high inclination
old	893	151	112	108	4.11	31%	0
new	781	158	121	2	4.19	0%	5

Table 6.7: Performance comparison of the old and new algorithm for object image linking. Two nights of the Tenerife Campaign 2006 where analyzed with in total 117 observation series.

link tracklets of two true object images only. Only slight improvements were achieved.

The new method reveals its strength when linking tracklets with three and more candidates. As the fifth column shows, the number of erroneously linked tracklets with three or more object image candidates was radically reduced. Only two erroneously linked tracklets were created with the new algorithm. Both were tracklets with three object images, whose root mean square of the first orbit determination was below 2.5 arcseconds, indicating that a real object was found. A closer investigation however, showed traces, which are typical for cosmics. Erroneously linked tracklets with more than three object images do not occur.

The improvements indicated by column four are significant. The number of correctly linked tracklets with three or more candidates is significantly higher for the new algorithm. Those also includes tracklets, which were also formed with the old algorithm, but consisted of two images only. Column six, representing the number of images per tracklet, shows the same effect: The new algorithm links more object images per tracklet, which improves the quality of the subsequent orbit determination.

The last column illustrates another advantage of the new algorithm. The old algorithm links only images of objects with an apparent movement within the drift and pseudo-inclination limits. The new algorithm links also the images of objects with any constant apparent velocity and pseudo-inclination rates as long as at least three object images are available. This results in five additional tracklets in only two nights. A new object class, which was not *detectable* before because of the limitations of the old tracklet linking algorithm is now accessible for detection.

The new algorithm requires no manual correction of the tracklets (column eight), a distinct advantage. With the old algorithm about one third of the tracklets still had to be manually corrected, because cosmics and real object images were mixed up within one tracklet or images of the same object were split into two different tracklets because of a gap. No manual corrections are needed for tracklets with three and more object images, the amount of manual corrections for tracklets with only two object images could significantly decreased.

A few examples are provided to illustrate the performance of the two algorithms. The examples stem from the Tenerife campaign of 2006. No manual corrections were made. True object images are marked with a blue box.

Figure 6.12 shows object images, which vary heavily in intensity from one frame to the next. Whereas the old algorithm cannot link all object images correctly, the new algorithm solves this difficulty without

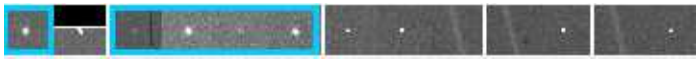

(a) old algorithm

(b) new algorithm

Figure 6.12: Link of object images varying significantly in brightness.

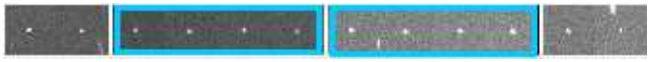

(a) old algorithm

(b) new algorithm

Figure 6.13: Images of the same object are linked in two different tracklets by the old algorithm because of a gap.

(a) old algorithm

(b) new algorithm

Figure 6.14: A cosmic is linked with object images by the old algorithm.

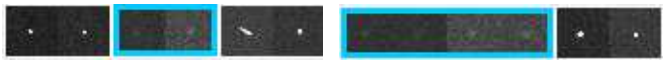

(a) old algorithm *(b) new algorithm*

Figure 6.15: The new algorithm links more object images than the old algorithm.

(a) old algorithm *(b) new algorithm*

Figure 6.16: The new algorithm links the tracklet of an object in a high inclination orbit.

manual corrections.

Figure 6.13(a) shows two tracklets (second and third tracklet), consisting of object images of the same object. The old algorithm links the images in two different tracklets because one object image is missing

(a) old algorithm *(b) new algorithm*

Figure 6.17: Less erroneous tracklets are linked by the new algorithm, in addition, images of an object in a high inclination orbit is linked.

on one of the frames (gap). The new algorithm handles gaps and links the images correctly to one tracklet. Furthermore, one additional object image is correctly linked (second tracklet).

Figure 6.14 shows the images of one object, which are split in two different tracklets (first and last tracklet (a), first tracklet (b)) by the old algorithm. In the second tracklet a cosmic is embedded in a correct tracklet instead of a leaving a gap (object image is covered by a star trail on the frame and was not detected). The new algorithm handles gaps and in addition does not embed a wrong candidate into the tracklet.

Figure 6.15 reveals that the old algorithm can link only two object images (second tracklet (a)), whereas the new algorithm links four object images (first tracklet (b)). In addition fewer erroneously linked tracklets occur.

Figure 6.16 and 6.17 illustrate that the new algorithm is able to detect new tracklets. The new tracklets consists of the images of objects in high inclination orbits, which could not be linked with the old algorithm. The first orbit determination of a circular orbit reveals an inclination of 52.99 and 69.97 degrees, respectively, for these objects.

6.5 Conclusions

The new algorithm for object image linking represents a significant improvement compared to the old one, which has been used in the automatic processing of the ESASDT. The number of erroneously linked tracklets was greatly reduced and only for tracklets with two candidate images manual interactions are required. For the ESASDT, with a worst case scenario of 60 candidates per frame, three object images spread over at most five frames are sufficient for a save tracklet link. A save tracklet link is defined to have a probability of incorrect linking of candidates of below 0.5 percent. For frames made by telescopes with a larger field of view with several hundred of candidates on each frame, four object images spread over five to six frames are required for a save tracklet linking. Alternatively a velocity limit can be imposed. With a velocity limit of 15 arcseconds per second a save tracklet linking is achieved, even if only three object images spread over five frames acquired with a spacing of one minute between subsequent observations are present.

The algorithm assumes a constant apparent linear movement of the observed objects over the frames during the observation series, but it accounts for small deviation from the linear motion, because the velocity vector is updated during an successful linking process. Object images of observation series of 180 minutes duration with one observation every minute could be successfully linked in the simulated GEO object observations. The studied images of GTO objects could be correctly linked, when the objects

were observed around perigee. The performance of the algorithm was comparable to the GEO case if the observations referred to true anomalies larger than 320 degrees and below 50 degrees. For GPS satellites the simulation showed that a correct linking took place for observation series shorter than two hours. For LEO observations a correct linking of object was not possible for observation series longer than a couple of minutes.

7. Catalogue Correlation of Optical Observations

Hell is other people.

Jean-Paul Sartre

7.1 Introduction

The next processing step is the correlation of tracklets, which have been identified on observation series in the previous processing steps. A tracklet is a series of densely spaced astrometric positions of one object. A tracklet normally spans a time interval of a few minutes only, which is not sufficient for the determination of a full six parameter GEO orbit: A one minute time interval covers only a fraction of 1/1440 of a GEO orbit. For comparison, for a minor planet with a revolution period of four years, a fraction of the orbit of 1/1440 corresponds to a time interval of one day. For a reliable orbit determination for a minor planet, an orbit determination over a fit interval of observations of two weeks is required, which is about 1/120 of the orbit. For a GEO object, this corresponds to a fit interval of 15 minutes. For an object in LEO object with a revolution period of 90 minutes, a fit interval of one minute is already sufficient.

The tracklet correlation addresses two different tasks, which are tightly interwoven: One tasks consists of correlating single tracklets directly with each other, in order to decide, which tracklets belong to the same object. A full six-parameter orbit can be determined with the correlated tracklets. These orbits may be compared using the orbital elements of a catalogue in order to identify the object and/or to update the six parameter catalogue orbits.

Alternatively, tracklets may be correlated with catalogue data directly. The catalogue data is either generated with single tracklets and consists of restricted orbits only, or with a series of already correlated tracklets, and consists of six parameter orbits. The correlation may be performed with restricted orbits from the single tracklets with the catalogue orbits. Alternatively pseudo-observation tracklets are generated from the catalogue orbits and correlated with the astrometric position of the tracklets. The identified tracklets may be used to update the catalogue orbit.

The selection, which approach is preferred is tightly related to the specific observation scenario, which is followed. Two observation and tracklet correlation scenarios for the detection of new objects and for a catalogue development from scratch are outlined here briefly: One is the so-called *survey and follow-up strategy*, the other the *survey-only strategy*.

Both methods start with so-called surveys: Declination stripes of the sky are scanned in order to cover an orbital region with the available field of view (FOV) of the telescope. From these frames tracklets are extracted. In the *survey and follow-up strategy* a restricted orbit is determined with each detected tracklet. Follow-up observations are tasked with the information of the restricted orbit in real time. The new tracklet, which is acquired in the follow-up observations, is correlated with the catalogued restricted orbit. For the tasked follow-up observations the scheduling of the observations in dependence of the available field of view, is crucial, because only a restricted orbit is available. Musci [65],[67] studied the scheduling of follow-up observations based on a circular first orbit from a single first tracklet for GEO and GTO objects for the ESASDT with a FOV of 0.7×0.7 degrees. In this setup, follow-up observations within half an hour are necessary to re-detect the object reliably in the follow-up observations. Several follow-up observations within the first night are necessary to reliably re-detect the object in the second night, because the first six-parameter orbit based on the observations of a single night has not yet the sufficient accuracy for a reliable re-detection after several days. An orbit is obtained using the observations of two subsequent nights. This orbit allows to re-detect the object after two to three days. Alternatively, follow-up observations for objects with a low area-to-mass ratio every 30 days are sufficient to maintain a so-called secured catalogue orbit for the object, which allows re-detection after longer time periods. All correlations have to be validated by a six-parameter orbit determination after correlation.

Alternatively, the tracklets without specifically tasked observations in a *survey-only* strategy may be correlated. Depending on the strategy, tracklets of the same object are gained several times within the night or only every second or third night. The numerous tracklets are gained and then correlated with each other without further information. Prominent solutions to this problem are provided by Milani and Tommei [61],[89]. The starting point for both methods is the same: Each tracklet contains position and apparent velocity information. This information may be made available in the inertial frame and stored in a four dimensional vector, called attributable [61]. Range and range-rate are then expressed as underdetermined functions of the attributables.

Tommei [89] calculates so-called admissible regions for each of these attributables. Admissible regions are comparable to a confidence region in classical orbit determination. The admissible region is determined by imposing sensible energy constraints on the allowed movements of the object and limiting the orbits of objects to certain orbital region, for which tracklets shall be correlated, via limits on the semi-major axis. Numerically generated swarms of virtual space object clouds are generated within the admissible region in a next step. Using Delaunay triangulation [13], those virtual swarm objects are nearly optimally distributed over the admissible region. For each object of the swarm an orbit is calculated and propagated. Due to the shortness of the tracklets, these orbits are erroneous. Tracklets are correlated, if two criteria are met: The covariances of the orbit determinations overlap and a so-called attribution penalty is met. The attribution penalty is a measure of how well the different attributes match. The limit of the penalty function is empirically determined. The whole procedure of tracklet correlation is recursive: a third tracklet is correlated in the next step, which is called attribution. Duplicates have to be removed after attribution, which result from the different order, in which the same tracklets are correlated in the recursive course of the method.

Milani [60] proposes a slightly different approach to correlate the attributes. For the different attributes a two body orbit is assumed, implying a constant angular momentum and energy. This leads to equations for range and range rates, which have in general 48 different solutions. Up to eleven solutions are still present, after removal of unphysical and spurious solutions. The overlap of covariance matrices is cal-

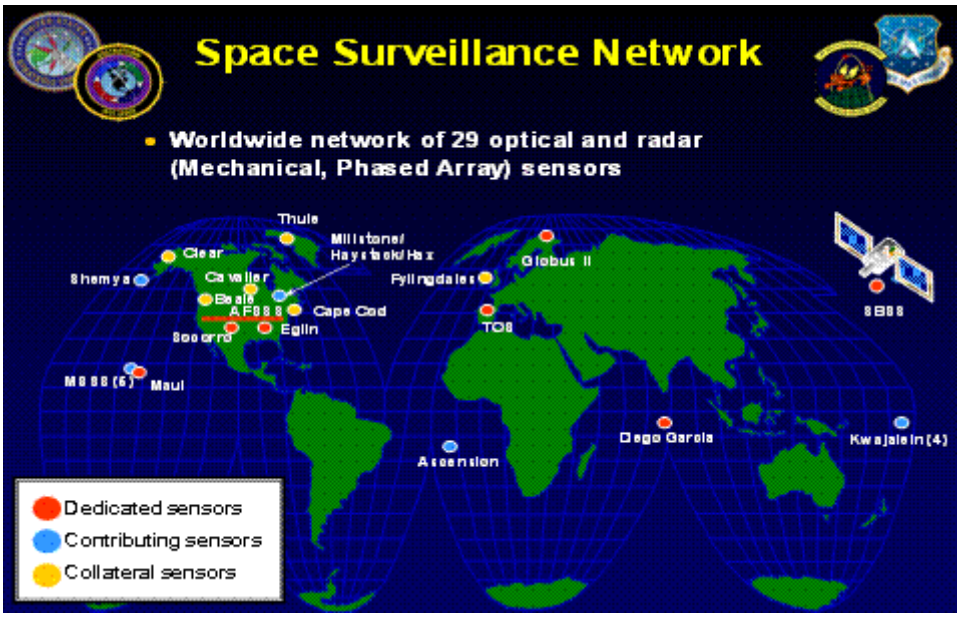

Figure 7.1: Sensor distribution of the USSTRATCOM Space Surveillance network.

culated for the remaining solutions. Solutions are rejected, if they have a penalty function above a user defined limit. The limit is empirically determined. The procedure is used recursively with attribution, duplicates have to be removed afterwards.

The procedure proposed by Tommei is thought to be valid for tracklets, stemming from the same orbital revolution (same night). The algorithm by Milani should be able to correlate tracklets from different revolutions. It is probably only limited by the assumption of a two-body orbit. A two-body orbit is assumed to be sufficient for low area-to-mass ratio objects in GEO orbits up to ten revolutions (days). Both tracklet correlation algorithms, the one by Tommei and by Milani, have been tested with the tracklets of the surveys with tasked follow-up observations, which have been gained by the AIUB with the ESASDT in 2007. Only the tracklets were provided, no further tasking information was given. Both algorithms were able to correlate a large number of tracklets. The tasking scheme of the ESASDT with survey and tasked follow-up observations provides many densely spaced tracklets spread over short time intervals. The data can only be used for a zero hypothesis testing for the algorithms. Details may be found in [89] and [60].

Different approaches are feasible, if the main objective is not a catalogue development from scratch, but the correlation of tracklets with a known precise, six-parameter orbital element catalogue. For satellites and space debris, several large orbital element catalogues exist. A publicly available catalogue of orbital elements is provided by the United States Strategic Command (USSTRATCOM). USSTRATCOM is one of the ten unified commands of the US Department of Defense. Through its Joint Space Operations Center (JSpOC), it operates a space surveillance network of 29 sensors. The locations and types of the sensors are shown in Fig. 7.1 [90]. The USSTRATCOM catalogue provides orbital data in the two-line element (TLE) format.

The DISCOS database (Database and Information System Characterizing Objects in Space) of the European Space Agency (ESA) is partially based on data supplied by USSTRATCOM [14]. It provides the data of USSTRATCOM catalogue in TLE format together with additional information, e.g., object type. No additional data with respect to the orbital elements are provided. The USSTRATCOM/DISCOS catalogue holds as of today the orbital elements of 16 000 objects of different quality. It is regarded to be complete up to an object size of ten centimeter in LEO and one meter in GEO. No covariance information is available through DISCOS/USSTRATCOM.

AIUB holds a small database of orbital elements of objects in GEO and HEO, which are not listed in the USSTRATCOM/DISCOS catalogue. Many high area-to-mass ratio (HAMR) objects are contained in the AIUB database.

Different orbital accuracies are required for different purposes. An accuracy of the predicted catalogue data of half the FOV is required for observation planning. For the ESASDT this would be 0.35 degrees, which corresponds roughly to 220 kilometers in GEO, about 2 degrees are required, e.g., for ZimSMART. The accuracy, required to safely identify the catalogue objects in the observations depends crucially on the density of the object images on single frames. Satellites in clusters like, e.g., the ASTRA clusters, have, on average, a spacing of 0.08 to 0.11 degrees on the observation frames, which corresponds to roughly 60 kilometers in GEO. This would require an accuracy of about 0.05 degrees, to correlate and identify the different objects reliably. Clusters currently represent the most dense GEO regions. The situation is different in other orbital regimes. The accuracy of orbit prediction (at least over short time intervals) must be of the order of 6 arcseconds corresponding to $1.7 \cdot 10^{-3}$ degrees for spectrographic measurements, to keep faint objects in the spectrograph slit for a long enough time period [85]. This accuracy corresponds one kilometer in GEO. For reliable collision avoidance an even higher accuracy below the level of 10^{-3} degrees (below one kilometer level in GEO) is required.

Specific difficulties are encountered in the catalogue correlation of optical observations. Only astrometric data can be extracted directly from the observations. An orbit determination is necessary to obtain information concerning the distance to the object. This lack of range data is crucial for catalogue correlation.

The correlation with catalogue data within the ESASDT processing is documented in Section 7.2, where two different algorithms are compared. The algorithms are based on the orbit determination and prediction methods, as they are already available in the real time processing of the ESASDT.

Section 7.3 discusses in detail the propagation of USSTRATCOM/DISCOS data with the specific limitations of the TLE format. In Section 7.4 the orbit determination based on AIUB observations and their prediction are investigated under various conditions. The predicted ephemerides are compared to AIUB observations, correlated with the newly developed algorithm, as described in Section 7.2.2.

7.2 Catalogue Correlation in the ESASDT Processing Pipeline

The tracklets, which are found in the processing of observations of the ESASDT with the automatic processing pipeline, are correlated with with external catalogues after a first orbit determination of a circular orbit with the single tracklet has been performed. The catalogue for the correlation is assumed to be in

TLE format or to consist of osculating elements to a specific epoch. No covariance information is available in the TLE data format. USSTRATCOM/DISCOS catalogue is chosen as external catalogue. The correlation is performed with that TLE set whose reference epoch is closest to the specific observation epoch.

7.2.1 Old Algorithm: Correlation Using Orbital Elements

The old algorithm for catalogue correlation was developed by U. Hugentobler in 1997 [38]. The orbital elements of the catalogue object are compared to the orbital elements of the first (restricted) orbit determination of a single tracklet. The orbital elements, which may be used for the correlation are: the semi-major axis, the eccentricity, the inclination, the right ascension of ascending node weighted with the inclination, and the geocentric latitude and/or longitude of the object at the observation epoch. The longitude and latitude are determined through ephemerides calculated with the catalogue data for the observation epoch of the first observation within each tracklet. The right ascension of the ascending node of the orbital elements of the catalogue objects is not predicted to the observation epoch. Usually, the eccentricity, the argument of the perigee and the mean anomaly are not used in the correlation process. Eccentricity and argument of perigee are excluded, because only circular orbits were determined in the previous processing step. The mean anomaly is not used, because it is likely to contain along-track errors.

The correlation using orbital elements is rather successful for GEO objects, due to their nearly circular orbits. It is, however, impossible to correlate orbits with significant eccentricities. Determining circular orbits for tracklets of objects on highly eccentric orbits leads a to significant mis-modeling of all orbital elements: not only the eccentricity, but also the mean motion and as a result the semi-major are erroneous. For further details consult Musci [63].

The correlation algorithm is based on the differences between the estimated orbital elements and the catalogue elements. Four quality levels are defined as a measure for the correspondence of the elements. Quality level one correlations are assumed to be correct identifications of the tracklets with the catalog objects. The allowed deviations in orbital elements have been determined empirically.

7.2.2 New Algorithm: Correlation Using Astrometric Positions and Velocity

The new algorithm correlates the observed tracklets with the catalogue not via orbital elements but directly using the observed astrometric positions and apparent velocities, which is independent of a restricted first orbit determination with a single tracklet.

The catalogue objects are predicted and ephemerides are calculated for each observation epoch. The propagation of USSTRATCOM/DISCOS orbits is discussed in Section 7.3, the orbit determination and prediction with the CelMech tool of the AIUB observations in Section 7.4.

The correlation is performed via a nearest neighbour decision. The distance between the observations and ephemerides are determined in the following values: The angular distance on the celestial sphere, the along-track distance, the cross-track distance and the angle between the velocity directions. All values are weighted and used to determine the smallest distance, that is the nearest neighbour.

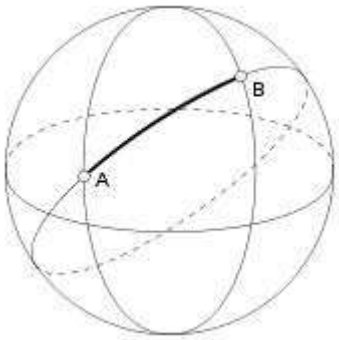

Figure 7.2: Angular distance between catalogued (A) and observed (B) position on celestial sphere.

The values are calculated as the following: The catalogue ephemerides are transformed in the topocentric system of the observations. The angle between the astrometric positions and catalogue ephemerides is determined and decomposed in an along-track and cross-track component. This decomposition is performed in the tangent plane on the topocentric celestial sphere (so-called standard coordinates [27]), as illustrated in Fig. 7.2. The along-track and cross-track distance may be scaled with the topocentric distance of the catalogue object. The angle between the direction of movement in the tangent plane is determined from the astrometric positions and the catalogue ephemerides.

Three remarks: The ephemerides are not projected directly on the CCD-frame to compare them with the astrometric positions (as done by F. Paolillo [69]), to be independent of the specific observation scenario, which would may not allow to determine apparent velocities of the observations.

More precisely, the along-track and cross-track distance between the catalogue and observed astrometric position could be determined on the (topocentric!) celestial sphere in projecting the catalogue orbit on the sphere and calculating the intersection point of the projected orbit with the great circle though the measured astrometric positions. Distortions may be introduced by the projection of elliptical orbits, and by the fact that only the topocentric sphere is available. This has not been done, since the distances between observed and catalogued position in along-track or cross-track direction regarded here, are well below 2 degrees. The difference between the calculation in (flat) standard coordinates or on the celestial sphere is of the order of half a kilometer for objects in GEO distances at a difference of two degrees:

$$\text{on celestial sphere in GEO: } \frac{2^\circ}{360^\circ} \cdot 2\pi \cdot 36\,000\,\text{km} = 1256.63\,\text{km} \tag{7.1}$$

$$\text{in tangent plane in GEO: } \tan(2^\circ) \cdot 36\,000\,\text{km} = 1257.15\,\text{km} \tag{7.2}$$

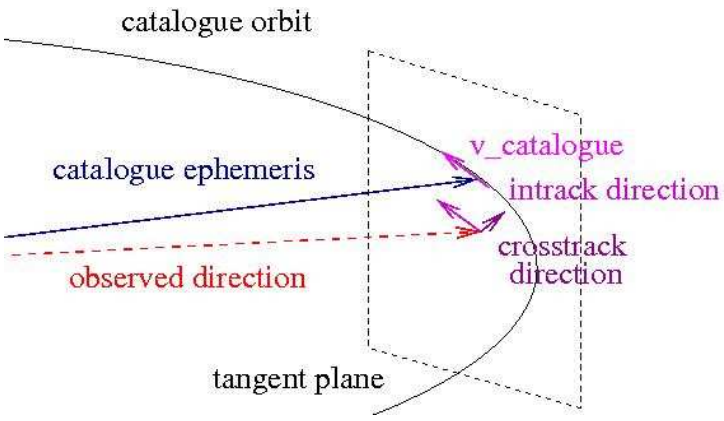

Figure 7.3: Tangent plane on topocentric viewing direction.

7.2.3 Implementation and Performance Comparison

7.2.3.1 Implementation of the New Algorithm

Empirical values for the distances have been determined in a study using USSTRATCOM/DISCOS TLE catalogue data. The details of are discussed in Section 7.3. They are: 0.16 degrees for the angular distance on the celestial sphere, ± 80 kilometers in along-track direction, 55 kilometers in cross-track direction, a deviation of 0.05 millidegrees per second for deviation in absolute velocity, and of maximal one degree in angle between the direction of velocity of the catalogue and the observed object. Different weights are applied to the parameters in the correlation process, the highest weight is given to the angular, along-track and cross-track distance, as well as to the velocity angle between the apparent directions of movement.

In the current implementation, the algorithm selects automatically the best possible correlation if various satellite ephemerides are in the vicinity of the observations via nearest neighbour decision. So-called qualities are assigned to the correlation with different catalogue objects. Four different correlation qualities are available. The quality one correlated object is assumed as being the correct identification with the catalogue object. The correlations of lower quality are displayed for information for the user. If more than one catalogue object passes all criteria of quality one, an additional consistency check is performed: only the correlation with the smallest differences is selected, all others are de-selected and are only displayed for user information.

The correlation algorithm has also been implemented in the ZimSMART routine processing after the successful implementation of the correlation algorithm in the ESASDT processing,. Details on the processing of ZimSMART data can be found in J. Herzog et. al. [32].

7.2.3.2 Performance Test of the New Algorithm

Three performance test has been made with the new algorithm. First, he was tested in comparison to the old algorithm on survey data of the ESASDT, then in correlation the observations in ASTRA satellite

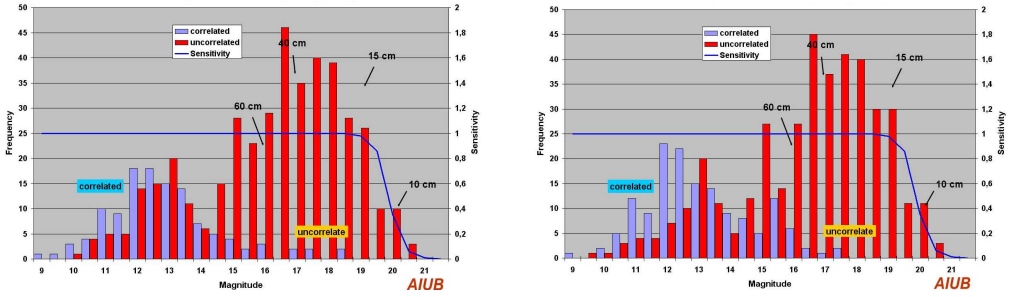

(a) old algorithm *(b) new algorithm*

Figure 7.4: Magnitude histogram: Correlated and uncorrelated tracklets of the ESASDT campaigns January 2008 to March 2008 determined (a) with the old catalogue correlation algorithm, (b) with the new catalogue correlation algorithm.

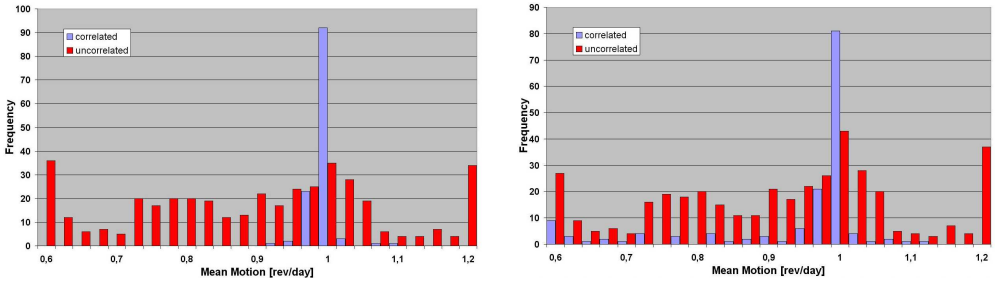

(a) old algorithm *(b) new algorithm*

Figure 7.5: Mean motion histogram (circular orbits): Correlated and uncorrelated tracklets of the campaigns January 2008 to March 2008 determined (a) with the old catalogue correlation algorithm, (b) with the new catalogue correlation algorithm.

clusters, and finally, in the routine processing of the observations of the ZimSMART telescope.

Performance Comparison with the old Algorithm: The performance of the old algorithm, which correlates the tracklets using the orbital elements of the determination of a circular orbit of a single tracklet, is compared to the newly implemented algorithm, correlating tracklets using the astrometric position and velocities in the tangent plane. The ESASDT campaigns from January to March 2008 have been reprocessed with the new algorithm and compared to the results of the old algorithm. All tracklets that have been detected in the campaigns are shown in Fig. 7.4 as a function of the averaged apparent magnitude of the tracklet. The tracklets, which could be identified with the USSTRATCOM/DISCOS catalogue are marked as *correlated*, in the figure. The tracklets, which could not be successfully correlated, are marked as *uncorrelated*. A larger number of tracklets could be correlated with the new algorithm compared to the old one, especially in smaller magnitudes. A large number of tracklets remains uncorrelated, especially in higher magnitudes. This may not be a deficiency of the algorithm: The AIUB tasks the ESASDT to follow-up the newly detected objects and determines full six parameter orbits as soon as additional tracklets are available. The secured six parameter orbits, which are determined with the follow-up observations, allow a reliable correlation with the catalog using orbital elements. This comparison confirms that many objects detected by the AIUB are not listed in the USSTRATCOM/DISCOS catalogue.

Figure 7.5 shows the frequency of detected uncorrelated and correlated tracklets as a function of the mean motion in revolutions per day. The mean motion was determined in a circular orbit determination using single tracklets only. The mean motion of observations of objects in high eccentricity orbits are likely to be mis-modeled. One revolution per day corresponds to controlled GEO objects. Far the most correlated tracklets, which were found by both algorithms have a mean motion of one revolution per day. The old algorithm could correlate only very few tracklets, with mean motions significantly different from one revolution per day, the new algorithm found catalogue objects within all ranges of mean motions. The plot is consistent with the fact, that the new algorithm is actually able to correlate objects in non-GEO orbits with catalogue objects.

Satellite Clusters: Satellite clusters are the most densely populated region in GEO, as of today. The catalogue correlation of observations of satellite clusters is highly demanding, because the angular spacing of the satellites is in the order of the catalogue accuracy. The Space Surveillance Network itself sometimes intermingles observations of satellite clusters, as D. Vallado showed [92].

ZimSMART observes clusters on a regular basis in cataloging all residents of the geostationary ring with low inclinations. Both ASTRA clusters (longitude 28 and 19 degree east), which consist of four and five satellites, respectively, were observed and correlated with the new algorithm. An orbit was determined with the tracklets that could be correlated. The single tracklets can be uniquely assigned to each other via orbit determination, when the rms in the orbit determination is below 2.5 arcseconds, as R. Musci in [64] pointed out. This is even the case for objects in very similar orbits like objects in clusters [64].

The results of the correlations are shown in Tab. 7.1 for the first cluster (longitude 28 degrees East), and in Tab. 7.2 for the second cluster (longitude 19 degrees East). The tracklets, which were detected are assigned the names T_n, with n being a consecutive number, referring to the order, in which the tracklets

Table 7.1: ASTRA Cluster at longitude 28 degrees: Correlation of observed tracklets (T_..) at three different epochs [MJD] with rms of the orbit determination; "no cor" means another object was on the frames, which could not be correlated, "-" means no other object was detected on the frames.

COSPAR	54887.876	54887.961	54888.153	rms
00054A	T_3	T_4	T_1	0.62"
00081A	T_1	T_1	T_2	1.41"
98050A	T_2	no cor	-	
01025A	T_4	T_3	T_3	0.58"

Table 7.2: ASTRA Cluster at longitude 19 degrees: Correlation of observed tracklets (T_..) at three different epochs [MJD] with rms of the orbit determination; "no cor" means another object was on the frames, which could not be correlated, "-" means no other object was detected on the frames.

COSPAR	54866.052	54866.803	54867.185	rms
96021A	T_1	T_6	T_3	2.01"
06012A	T_2	T_1	T_2	1.41"
99033A	T_3	T_3	T_5	1.41"
97076A	T_4	T_2	T_6	0.43"
07016A	-	T_5	no cor	

were detected on the observation series. The tracklets were correlated with the new correlation algorithm with USSTRATCOM/DISCOS data, independently for each observation series. An orbit determination of the tracklets assigned to the same catalogue object have been made. Table 7.1 and 7.2 show the observation epoch of the first observation within each tracklet in MJD, the rms of orbit determination of the tracklets which were correlated with the same catalogue object in arcseconds, and the COSPAR number of the correlated catalogue object for both ASTRA clusters. A hyphen indicates, that no more objects were detected on the frames of the observation series, a "no cor" indicates, that there was at least one other tracklet detected in the series, which was not correlated with one of the ASTRA satellites by the algorithm.

In the first cluster (Tab. 7.1) three of the four ASTRA satellites could be correlated and the orbit determination was successful. In the second cluster (Tab. 7.2) four of the five ASTRA satellites could be correlated. The orbit determination was successful, too.

In both cases, orbit determination was also performed with all the tracklets that could not be correlated with a catalogue object. The orbit determination was not successful. Orbit determination with the tracklets, which were not correlated and the tracklets of catalogue objects, for which only one tracklet could be correlated, were not successful either.

The correlation test with densely spaced space objects, e.g., the ASTRA clusters, showed, that the algorithm performs well even in extreme situations. An important factor for the correct correlation is that a decisions is enforced: Two tracklets on the same frame cannot be correlated to the same object, but

Table 7.3: Correlation differences of two observation tracklets (Tracklet 1 and 2), detected in the same observation series, with TLE ephemerides of the ASTRA Cluster satellites at longitude 38 degrees. The correct correlations are printed bold. Displayed are the distances in along-track, cross-track direction in angular distance on the celestial sphere, the distances in absolute velocity and the angle between the apparent observed and computed velocity angle averaged over all observations within the tracklet.

COSPAR	along-track (km)	cross-track (km)	ang.dis. (deg)	velocity angle (deg)
Tracklet 1				
96021A	-44.340352	16.536518	0.070965	0.087285
06012A	-53.942924	23.683406	0.088290	0.103623
99033A	-89.884070	40.227332	0.147853	0.132208
97076A	-26.053264	2.553318	0.039303	0.133615
07016A	**-42.586437**	**1.008498**	**0.063835**	**0.103043**
Tracklet 2				
96021A	-27.849129	7.131953	0.043121	0.091336
06012A	-37.494544	33.179749	0.074852	0.131215
99033A	-73.323011	49.499337	0.132756	0.067809
97076A	**-9.478112**	**6.695677**	**0.017448**	**0.067840**
07016A	-26.138171	10.499939	0.042072	0.129454

the best fit is selected if two or more catalogue objects pass the standard criteria for correlation. This best fit is not only determined by position distances only, but the full velocity vector information is taken into account, too. An example of the correlation of one observation tracklet is displayed in Tab. 7.3. The correctly correlated object is marked in bold fond. Both observation tracklets were on the same observation frames. The correct decision for the correlation of the object 97076A with the second instead of the first tracklet was cross checked by successfully orbit determination. The velocity information was necessary as additional information in combination with the position distances to select the best fit. See Section 7.3.3.1 for further details on the empirical determination of distances between catalogue ephemerides and observations, and the velocity angle accuracy.

Routine Processing of ZimSMART data: The new correlation algorithm is used in the routine processing of ZimSMART data. All correlations are checked by a subsequent orbit determination. Only around 2.2 percent of all correlated tracklets were wrongly correlated in the observations between 2008 and 2010. The wrong correlations also include the correlation with one experimental AIUB catalogue. This AIUB catalogue contains orbits, which are based on the orbit determination using a single tracklet only or orbits of of poor quality due to long prediction times and large gaps in the observation data. Details can be found in J. Herzog [32].

7.3 Correlation with Two Line Element (TLE) Catalogue Data

7.3.1 The Format

The TLE format is a fixed format, which was originally developed for punch cards. For every entry a fixed number of columns is reserved, including decimal points.

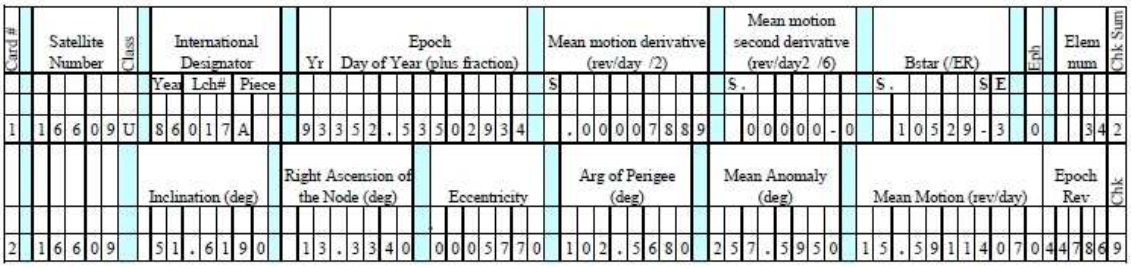

Figure 7.6: The two line element set (TLE) format [91]. Shaded cells do not contain data, S indicates that the cell is either blank or a sign, either $\pm$, can be displayed, E is the exponent to the base 10. Eccentricity, mean motion derivative and Bstar imply decimal points before the first digit. The mean motion derivative is divided by 2, the second derivative by 6. The units of the first and second derivative of the mean motion are rev/day^2 and rev/day^3.

Subsequently each entry is briefly explained [91], [10]:

1. The first number in each row indicates the row number. The TLE format consists of two rows.

2. The satellite number is the NORAD number. NORAD stands for North American Aerospace Defense Command and is a joint organization of the United States and Canada. NORAD maintains an own catalogue of artificial earth orbiting objects, called STARCAT. NORAD assigns continuous numbers to objects according to their first observation date. For a valid two line element set the NORAD number has to be repeated in the second line.

3. The class indicates, if the object is classified or unclassified. All publicly available data is unclassified. An empty entry indicates unclassified data.

4. The international launch designator is assigned by the World Data Center-A for rockets and satellites (and parts thereof) in accordance with the international *Convention on Registration of Objects launched into outer space*. The World Data Center-A cooperates with the North American Aerospace Defense Command (NORAD) and the National Space Science Data Center (NSSDC) of the National Aeronautics and Space Administration (NASA). The first two digits of the launch designator represent the year of launch, the launch number of that year, which is counted continuously within one year, and three digits reserved for letters representing the pieces of the same launch.

5. The epoch displays with the first two digits the year, with the next three digits the day of the year and after the decimal point the fraction of the day in decimal units. The epoch starts at UT midnight and is measured in UTC.

6. The mean motion derivative has an implicit leading decimal point before the first digit. It can be preceded by a sign ($\pm$). It is already divided by two to be used directly in the calculation of the resistance coefficient of the SGP/SDP model. Details on the SGP/SDP models can be found in Section 7.3.2.

7. The second derivative of the mean motion can carry a signed exponent to the base ten ($\pm$). It is already divided by six to be used directly in the calculation of the resistance coefficient of the SGP/SDP model. It is not used for the SGP4/SDP4 model, it is only valid for older SGP models. Its value is often displayed as zero. Details on the SGP/SDP models can be found in Section 7.3.2.

8. Bstar is a drag-like coefficient in SGP4. It is an adjustment to the physical quantity of the ballistic coefficient (B_c). Bstar is using a reference value for the atmospheric density, ρ_0, at the height of one Earth radius.

$$B_c := \left(c_D \cdot \frac{A}{m} \right)^{-1} = \frac{R_e \rho_0}{2 \cdot Bstar} \tag{7.3}$$

   with: c_D drag coefficient, A effective cross-sectional area, m mass, R_e earth radius, $\rho_0 = 2.461 \times 10^{-5} \mathrm{kg/m^2}$ atmospheric density at one Earth radius.

   Bstar is not a physical quantity but a free modeling parameter, the value may not be correlated to drag effects. This is the case in the presence of satellite maneuvers, significant solar radiation pressure, atmospheric perturbations, large third body effects, or mis-modeling of the Earth's gravitational field. Bstar may have a negative value.

9. The ephemeris type determines the model, with which the ephemerides were generated. Spacetrack Report Number 3 suggests the following assignments: 1=SGP, 2=SGP4, 3=SDP4, 4=SGP8, 5=SDP8. The field is blank or filled with a zero for all TLEs used outside of Cheyenne Mountain Operations Center (CMOC) of USSTRATCOM. All TLE data is generated with SGP4/SDP4 in those cases.

10. The ephemerides number is a continuous data set number, incremented each time a new data set is generated. This rule is not strictly followed, however.

11. The check sum number is a number modulo 10 check sum. The check sum is calculated as the sum of all digit entries in the current line, ignoring all letters, plus-signs and decimal points. A value of 1 is assigned to each minus sign. The majority of errors, which are likely to happen in the TLE generation process, are detected via the check sum.

12. The entries in the second row of the TLEs contain the orbital elements of the satellite orbit: Inclination in degrees, right ascension of ascending node in degrees, eccentricity with a leading decimal point, argument of perigee in degrees, mean anomaly in degrees at the epoch displayed, mean motion in revolutions per day. Those are mean orbital elements generated with SGP4/SDP4 for publicly available TLE data. The reference frame is a geocentric coordinate system using the true equator and mean equinox (TEME) of the corresponding epoch.

13. The number of revolutions at epoch is represented by five digits. The revolution is counted from the ascending node onwards. In NORAD's convention, which is adapted for the TLE generation, the time period from launch till reaching the first ascending node is counted as revolution zero. Revolution one begins, when the first ascending node is reached.

The accuracy of the TLE data is limited not only by the observations in the Space Surveillance Network, or the orbit determination, but also by the number of decimal digits available in each field [93]. With eight decimal places the accuracy of the epoch is only accurate up to 0.0004 seconds. An object in a circular LEO orbit at an altitude of 400 km has a velocity of 7.6 km/s, it therefore moves by about 3 m

in 0.0004 seconds. A GEO object in a perfectly geostationary orbit has a velocity of about 2.6 km/s. The error introduced in the position is of the order of one meter. The eccentricity is specified by seven decimal places. This introduces an error of the order of $r \sim a\delta e$ corresponding to two meters for a GEO orbit. The inclination and right ascension of ascending node are only accurate to four decimal places, with a simple estimation of the semi-major axis times the inclination angle, an estimated error of 6 meters in LEO and of around 35 meters in GEO can be calculated. Such errors are simply introduced by the TLE format.

7.3.2 The Propagators: SGP4/SDP4 and SGP8/SDP8

The development of the Simplified General Perturbation (SGP) model for orbit determination and propagation started in the 1960s and became operational in 1970 in the Space Detection and Tracking System (SPADATS) Center, located in Colorado Springs, Colorado. Further improvements (SGP4/SDP4, SGP8/SDP8) and adjustments to the different orbital regimes were developed and implemented in the 1980s. The description of the different models are taken from Hoots [35] and Vallado [91].

The first semi-analytical model, called SGP, is based on the two different astrodynamic solutions for the equations of motion of a near-Earth satellite due to Brouwer [7],[8] and Kozai [51], both developed in 1959. The gravitational field is represented only by the zonal harmonics up to degree five. For the development of the propagator theory the long- and short periodic terms, which do not have the eccentricity as an explicit factor, are adopted from Brouwer's solution. From Kozai the convention relating mean motion and semi-major axis was adopted. The solutions is transformed into non-singular coordinates to avoid the singularities for small eccentricities and inclinations close to zero degrees; this approach was based on a work by Arsenault et al. [3]. An atmospheric drag model has been included, based on the ideas of King-Hele [47]. In a semi-empirical approach the effect of drag on the mean motion is represented as a quadratic time function, where the coefficients are parameters in the orbit determination. The time rate of the change of eccentricity is based on the assumption that the perigee height remains constant as the semi-major axis diminishes.

A first enhancement was performed in implementing an analytical rather than an empirical drag model. A simplified version of the work by Lane and Cranford [52] was implemented. The simplification consists of modeling only secular effects of drag. The model is known as SGP4. It replaced SGP as the sole model for the US satellite catalogue maintenance since 1979.

In 1977 an extension of the model was implemented for so-called deep space modeling (SDP4) in the existing SGP4 routines. The approach was based on the work by Bowman [6], who modeled the influence of the lunar and solar gravity and the resonance effects of the Earth's tesseral harmonics. It was incorporated as a first order model. In the 1980s a further development leading to the SGP8/SDP8 was performed. Deficiencies in the re-entry prediction of decaying objects of the SGP4/SDP4 models were mitigated by a closed-form solution based on general trends of orbital element evolution near re-entry. The SGP4/SDP4 models are, however, still used without exception for the generation of publicly available TLEs of USSTRATCOM.

The mathematical foundation of the SGP4/SDP4 model and the equations are published in Hoots [35].

7.3.3 Correlating Predicted USSTRATCOM/DISCOS Ephemerides with AIUB Observations

The TLE format contains no covariance information. No additional information concerning the data accuracy are provided by USSTRATCOM/DISCOS. The accuracy of the orbit determination itself, as well as of the predicted orbits is unknown. So-called intrinsic errors, of the data, have been investigated e.g., by T. Flohrer [15]. Snapshots of the TLE catalogue were taken and state vectors were generated from the TLE data sets in this investigation. These 24 hour state vectors were used to determine an orbit. The distances of the determined orbit with respect to the TLE state vectors, which were used in the orbit determination, were determined. In along-track, cross-track and radial direction distances of 0.356, 0.432 and 0.086 kilometers were found for GEO objects, of 0.824, 1.367 and 1.056 kilometers for HEO objects. Intrinsic errors were determined to be 0.102, 0.471 and 0.126 in along-track, cross-track and radial direction for LEO objects. The intrinsic accuracy of the HEO TLE data is reduced compared to objects in geostationary orbits. Intrinsic errors are a measure of the theoretically possible precision, which can be obtained with the SGP4/SDP4 model.

To asses the external errors of the catalogue data, TLE ephemerides have been compared to high accuracy ephemerides, e.g. to high precision orbits of operational space crafts, as done by C. Hirose [33], who compared the USSTRATCOM TLE data sets with the closest epoch and smallest propagation intervals to the high precision operator data of the LEO satellites ALOS and ASTRO-F of the Japanese Space Agency (JAXA). The distances between the predicted TLE positions and the operator data from the satellites, were of the order of two kilometers on average. The external errors are much larger than the intrinsic errors of the TLE data sets. Hirose also detected so-called *bad TLE sets*, which resulted in much larger distances than two kilometers. She stated, that it is impossible to decide a priori whether a specific TLE set is *regular* or *bad*.

In the absence of high precision data for most of the catalogue object, the predicted TLE ephemerides may be compared with optical observations. The accuracy of ESASDT and ZIMLAT observations is of the order of 0.5 arcseconds on average, as calibration measurements, e.g., using GPS satellites showed. A value of 0.5 arcseconds correspond to $1.4{\cdot}10^{-4}$ degrees, which equals in GEO 0.04 kilometers, which is well below the intrinsic errors for GEO and HEO objects. The data in TLE format itself is limited to an accuracy of 35 meters and more (see Section 7.3.1). The optical observations serve as a reference in the following; a distance between the TLE ephemerides and the observations larger than 40 meters cannot explained by the accuracy of the observations.

The code of the SGP4/SDP4 and SGP8/SDP8 propagators as it was published in Hoots [34] has been used for the propagation of the TLE data. The distances of the observed astrometric positions and the TLE ephemerides are investigated as angular distances on the celestial sphere, and decomposed and scaled with the radial topocentric distance of the catalogue ephemerides in along-track and cross-track direction in the projected tangent plane, as described Section 7.2.3.

7.3.3.1 SDP8 and SDP4 propagation

The follow-up observations of 13 GEO[1] objects and eight HEO[2] objects have been evaluated. The observations have been acquired with ZIMLAT over a time period of more than four years. The verification that the different tracklets actually belong to the same object has been performed by orbit determination with the CelMech tool, see Musci [64] for further details. This validation method is labeled *orbit validation* in the following. In addition, the observations of GEO objects of the campaigns from January to March 2008 with the ESASDT have been evaluated. Those observations have been correlated using orbital elements of the first circular orbit determination and of the catalog data via the old algorithm, labeled *orbital elements validation* in the following. No correlations are available for HEO or GTO objects from the ESASDT via the old algorithm. The TLE sets with the reference epoch closest to the observation epoch have been used for the correlation in the subsequent evaluation. The TLE data was propagated with SDP8 propagator. Figure 7.7 and 7.8 illustrate the results of the correlations for the GEO and HEO, respectively. The correlations with the observations stemming from the ESASDT are marked in red, the correlations with ZIMLAT observations in blue. Expectation values and standard deviations are determined for each value. The expectation value and standard deviations are unbiased for a normal distribution of the distances [31].

The expectation values and standard deviations for the angular distance between the catalogue ephemerides and the observed astrometric position of the observations of ZIMLAT and ESASDT in GEO are:

$$\begin{aligned} \left\langle E_{\text{angular\_zim}} \right\rangle &= 2.01 \cdot 10^{-2} \text{ degrees} \\ \sigma_{\text{angular\_zim}} &= 1.44 \cdot 10^{-2} \text{ degrees} \end{aligned} \tag{7.4}$$

$$\begin{aligned} \left\langle E_{\text{angular\_esa}} \right\rangle &= 3.34 \cdot 10^{-2} \text{ degrees} \\ \sigma_{\text{angular\_esa}} &= 1.50 \cdot 10^{-2} \text{ degrees} \end{aligned} \tag{7.5}$$

The expectation values and standard deviations for the along-track and cross-track (absolute value) distances of ZIMLAT and ESASDT in GEO are listed in the following. They are scaled by use of the topocentric distance to the catalogue object.

$$\left\langle E_{\text{along\_zim}} \right\rangle = 11.14\,\text{km} \quad \sigma_{\text{along\_zim}} = 15.36\,\text{km} \tag{7.6}$$

$$\left\langle E_{\text{cross\_zim}} \right\rangle = 4.80\,\text{km} \quad \sigma_{\text{cross\_zim}} = 6.77\,\text{km} \tag{7.7}$$

$$\left\langle E_{\text{along\_esa}} \right\rangle = 20.23\,\text{km} \quad \sigma_{\text{along\_esa}} = 13.55\,\text{km} \tag{7.8}$$

$$\left\langle E_{\text{cross\_esa}} \right\rangle = 3.87\,\text{km} \quad \sigma_{\text{cross\_esa}} = 6.58\,\text{km} \tag{7.9}$$

The expectation values and standard deviations for the angle between apparent tangent velocities of the ZIMLAT and ESASDT observations in GEO determined via the catalogue orbits and the apparent velocity determined from observation tracklets are:

$$\begin{aligned} \left\langle E_{\text{angle\_zim}} \right\rangle &= 3.93 \cdot 10^{-2}\,\text{degrees} \\ \sigma_{\text{angle\_zim}} &= 4.33 \cdot 10^{-2}\,\text{degrees} \end{aligned} \tag{7.10}$$

[1]Cospar numbers: 78035A, 79105A, 80081A, 82044F, 83089B, 84035A, 85035B, 90061D, 91010F, 92088A, 93073B, 97049B, 99047E

[2]Cospar numbers: 00016C, 00016D, 00067D, 00068B, 70055B, 77105A, 88018C, 91015P, 91084C

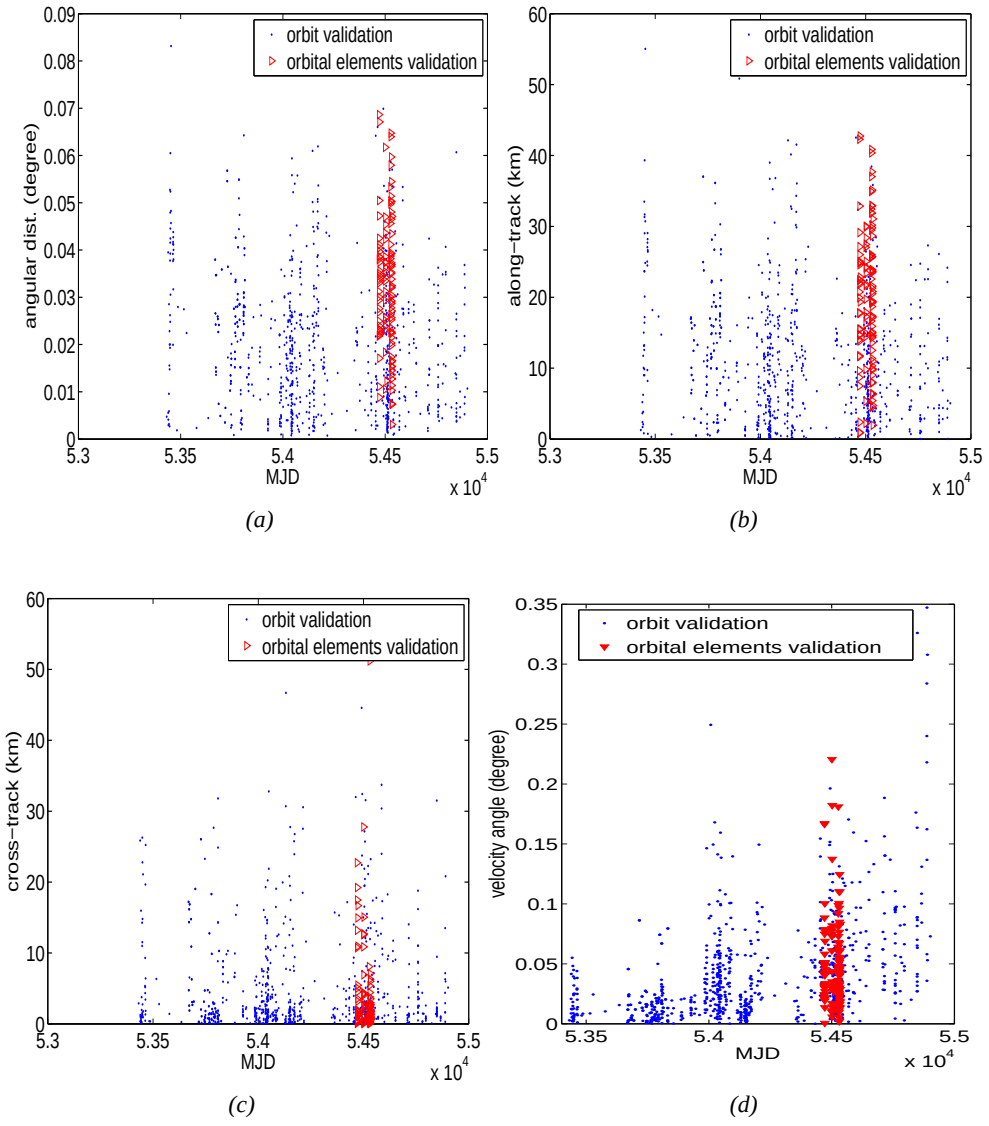

Figure 7.7: GEO: Distances of observed astrometric and calculated ephemerides position (a) in angular distance on celestial sphere, (b) along-track, (c) cross-track direction (absolute value), and (d) the angle between apparent velocities of observed and catalogue object.

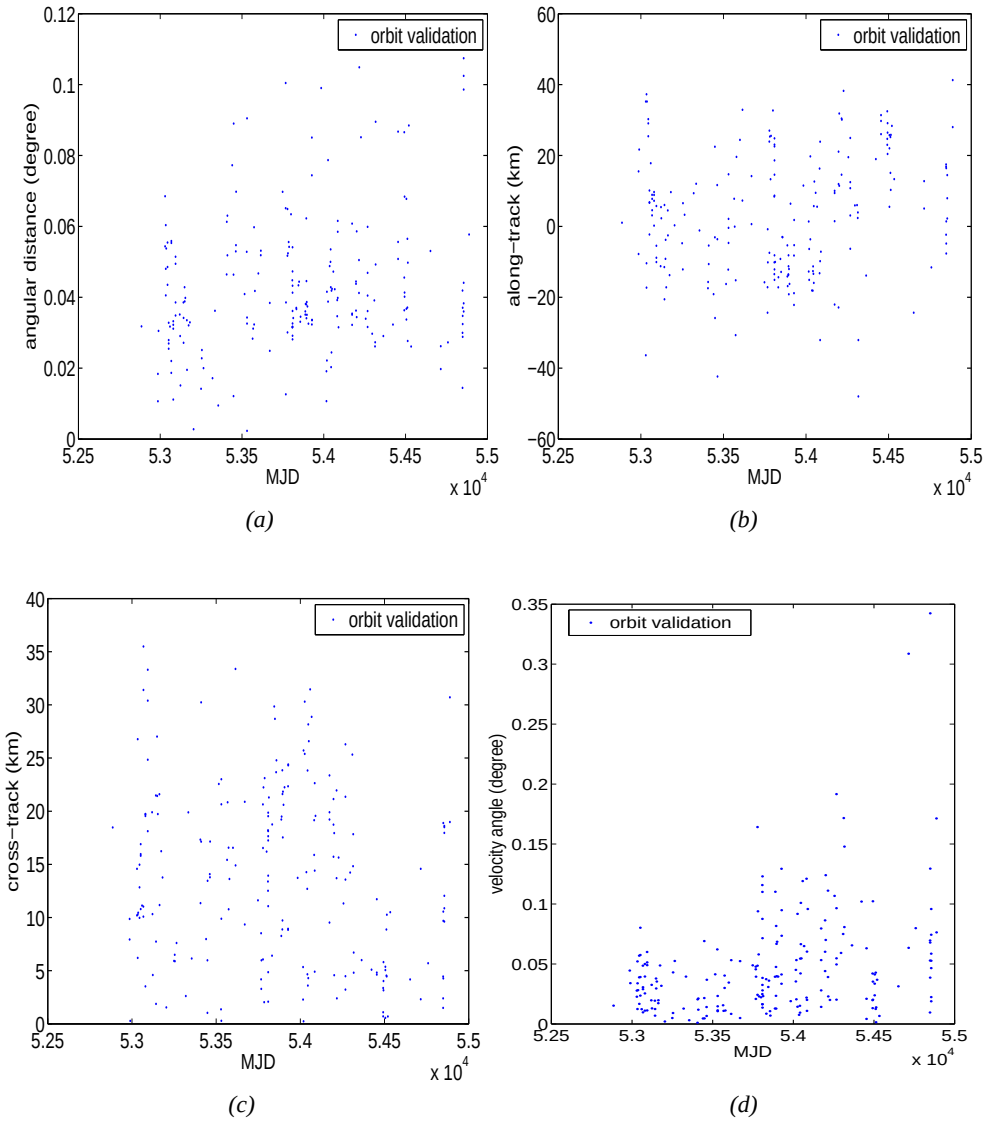

Figure 7.8: HEO: Distances of observed astrometric and calculated ephemerides position (a) in angular distance on celestial sphere, (b) along-track, (c) cross-track direction (absolute value), and (d) the angle between apparent velocities of observed and catalogue object.

$$\begin{aligned} \left\langle E_{\text{angle\_esa}} \right\rangle &= 5.19 \cdot 10^{-2}\,\text{degrees} \\ \sigma_{\text{angle\_zim}} &= 3.94 \cdot 10^{-2}\,\text{degrees} \end{aligned} \tag{7.11}$$

The expectation value and standard deviation for the angular distance between the catalogue ephemerides and the observed astrometric position of observations of ZIMLAT in HEO are:

$$\begin{aligned} \left\langle E_{\text{angular\_zim}} \right\rangle &= 4.36 \cdot 10^{-2}\,\text{degrees} \\ \sigma_{\text{angular\_zim}} &= 2.06 \cdot 10^{-2}\,\text{degrees} \end{aligned} \tag{7.12}$$

The expectation value and standard deviation for the along-track and cross-track (absolute value) distances of the ZIMLAT observations in HEO scaled with the topocentric distance to the catalogue object are:

$$\left\langle E_{\text{along\_zim}} \right\rangle = 15.28\,\text{km} \quad \sigma_{\text{zim\_along}} = 21.75\,\text{km} \tag{7.13}$$

$$\left\langle E_{\text{cross\_zim}} \right\rangle = 13.84\,\text{km} \quad \sigma_{\text{cross\_zim}} = 8.35\,\text{km} \tag{7.14}$$

The expectation value and standard deviation for the angle between apparent tangent velocity directions of the ZIMLAT observations in HEO determined via the catalogue orbits and the apparent velocity determined from observation tracklets are:

$$\begin{aligned} \left\langle E_{\text{angle\_zim}} \right\rangle &= 5.54 \cdot 10^{-2}\,\text{degrees} \\ \sigma_{\text{angle\_zim}} &= 7.5 \cdot 10^{-3}\,\text{degrees} \end{aligned} \tag{7.15}$$

The distances between observed and computed positions and velocities are in good agreement between the ESASDT data and the long term observations of ZIMLAT. All distances are very high, in the range of ten to twenty kilometers, 0.02 degrees respectively. This is accurate enough to securely re-detect the objects in follow-up observations with a standard FOV of around one degree. But it is by far too inaccurate to safely predict collisions, to plan avoidance maneuvers or to perform small slit spectral analysis. All distances are larger for HEO than for GEO objects.

The single observations of the ESASDT and ZIMLAT have an accuracy of 0.5 arcseconds, as calibration measurements showed. The velocity angle caused by the observation error itself is, with a spacing of 30 seconds between two subsequent measurements for a GEO object moving with a velocity of 15 arcseconds per second is:

$$\arctan\left(\frac{2 \cdot 0.5”}{15”/\text{sec} \cdot 30\,\text{sec}}\right) = 1.28 \cdot 10^{-1}\text{deg}. \tag{7.16}$$

The velocity angle is the only variable, in which the determined values of the comparison of observations and catalogue orbits are in the order of the observation error itself. This suggests that the orbital plane of the catalogue orbits is determined most precisely.

All distances, that could be found in the previous investigation, reveal a large standard deviation of the same magnitude than the expectation values themselves. This effect is not introduced by a minority of the observed objects only. The standard deviation as a function of the expectation value of the angular distance distances for the GEO and HEO objects of the ZIMLAT observations is given in Fig. 7.9. The quality of the TLE data itself seems to vary significantly for all objects over time.

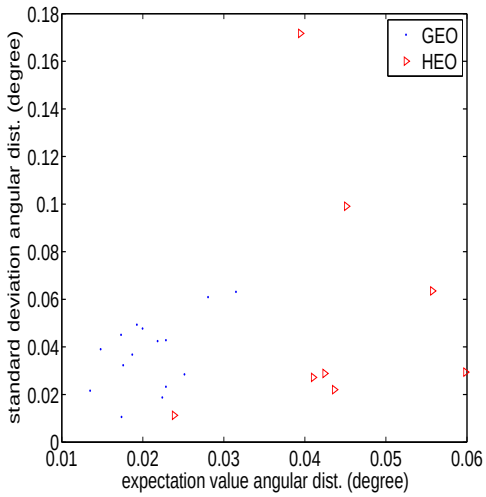

Figure 7.9: Standard deviation as a function of expectation value of the angular distance for 13 GEO and 8 HEO objects.

It is investigated in the next step, whether the distances differ when the identical TLE sets are propagated with SDP8 compared to SDP4. The TLEs of the officially available TLE data of USSTRATCOM/DISCOS were created with the SGP4/SDP4 propagators. Smaller distances of the ephemerides to the observations are expected, when the ephemerides are propagated with SDP4 rather than SDP8. The same TLE sets of the 13 GEO and the 8 HEO are propagated with SDP4 instead of SDP8 and compared with the same ZIMLAT observations as before. The distances of TLE sets propagated with SDP4 are shown in Fig. 7.10 for the GEO objects and in Fig. 7.11 for the HEO objects.

The expectation value and standard deviation for the angular distance between the catalogue ephemerides propagated with SDP4 and the observed astrometric position of observations of ZIMLAT in GEO are:

$$\begin{aligned} \left\langle E_{\text{angular\_zim}} \right\rangle &= 2.02 \cdot 10^{-2} \text{ degrees} \\ \sigma_{\text{angular\_zim}} &= 1.45 \cdot 10^{-2} \text{ degrees} \end{aligned} \tag{7.17}$$

The expectation value and standard deviation for the along-track and cross-track (absolute value) distances of the ZIMLAT observations in GEO scaled with the topocentric distance to the catalogue object are:

$$\left\langle E_{\text{along\_zim}} \right\rangle = 11.20\,\text{km} \qquad \sigma_{\text{along\_zim}} = 13.52\,\text{km} \tag{7.18}$$

$$\left\langle E_{\text{cross\_zim}} \right\rangle = 4.96\,\text{km} \qquad \sigma_{\text{cross\_zim}} = 7.54\,\text{km} \tag{7.19}$$

The expectation value and standard deviation for the angular distance between the catalogue ephemerides propagated with SDP4 and the observed astrometric position of observations of ZIMLAT in HEO are:

$$\begin{aligned} \left\langle E_{\text{angular\_zim}} \right\rangle &= 2.73 \cdot 10^{-2} \text{ degrees} \\ \sigma_{\text{angular\_zim}} &= 1.86 \cdot 10^{-2} \text{ degrees} \end{aligned} \tag{7.20}$$

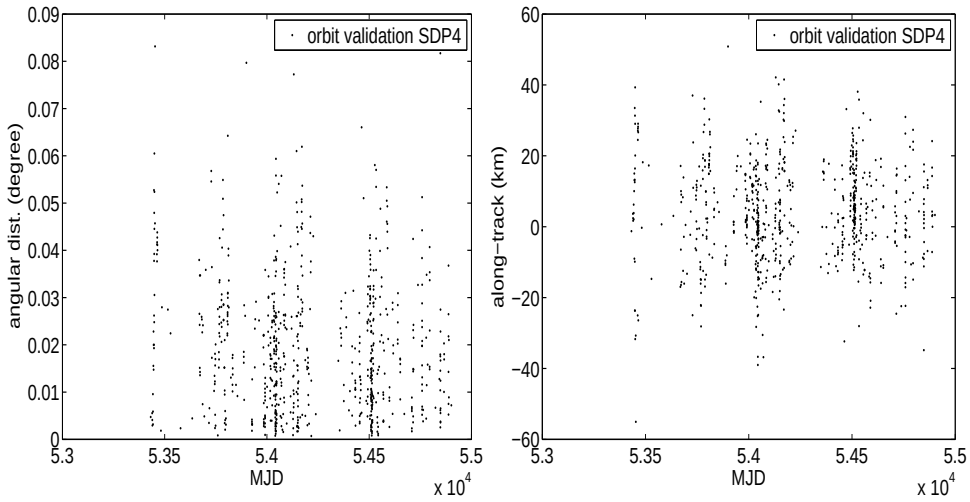

Figure 7.10: GEO: Distances of observed astrometric and calculated ephemerides position (a) in angular distance on celestial sphere, (b) along-track, (c) cross-track direction (absolute value) propagated with SDP4.

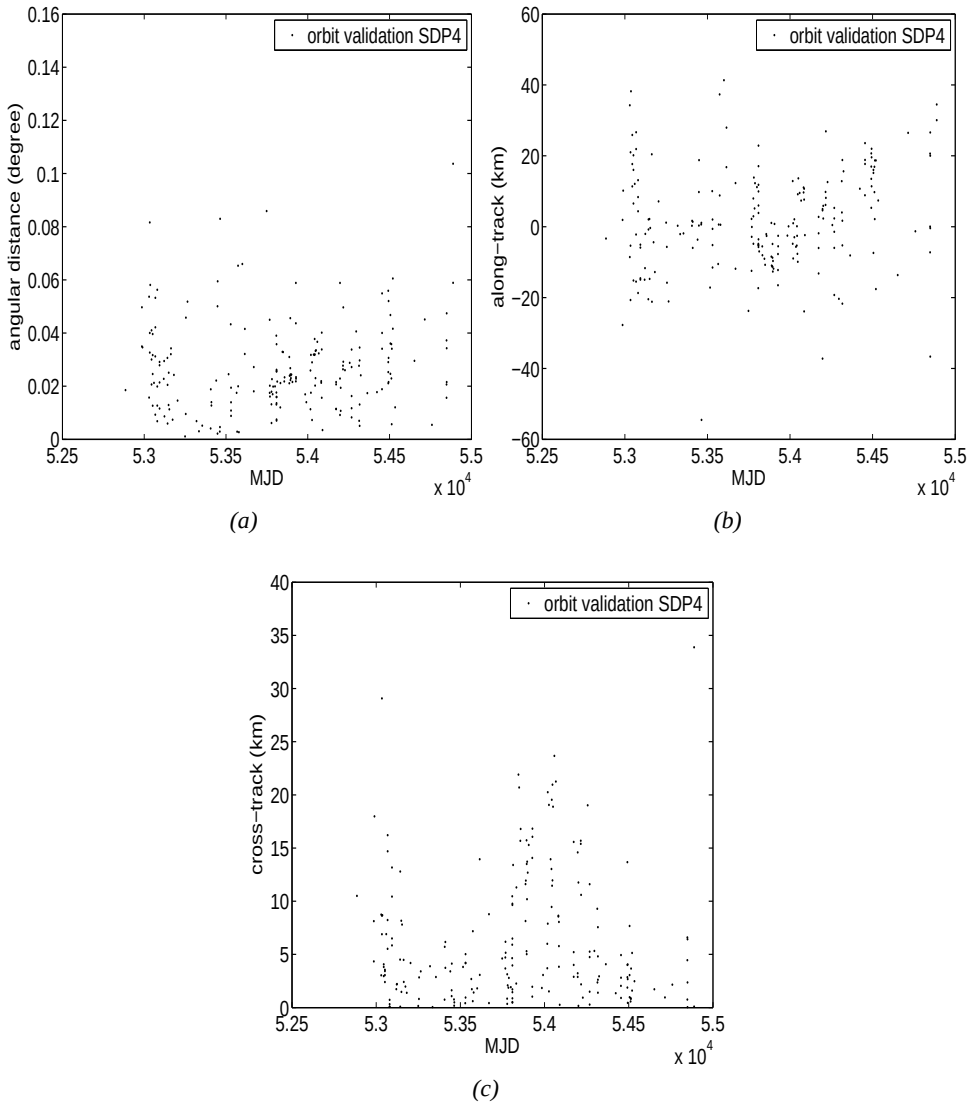

Figure 7.11: HEO: Distances of observed and calculated position (a) in angular distance on celestial sphere, (b) along-track, (c) cross-track direction (both absolute values) observed and catalogue object propagated with SDP4.

The expectation value and standard deviation for the along-track and cross-track (absolute value) distances of the ZIMLAT observations in HEO scaled with the topocentric catalogue distance are:

$$\left\langle E_{\text{along\_zim}} \right\rangle = 10.99\,\text{km} \quad \sigma_{\text{along\_zim}} = 17.11\,\text{km} \tag{7.21}$$

$$\left\langle E_{\text{cross\_zim}} \right\rangle = 6.44\,\text{km} \quad \sigma_{\text{cross\_zim}} = 6.45\,\text{km} \tag{7.22}$$

The distances in GEO are slightly larger with the SDP4 than with SDP8 as Fig. 7.12 shows, which is unexpected.

In Fig. 7.12 the difference between the distances of the observations and ephemerides propagated with SDP8 and of the same observations and ephemerides propagated with SDP4 is shown for the investigated GEO objects. Significantly, the differences are very close to zero in angular distance, along-track and cross-track direction till around February 2008 (54516.0). After that epoch larger differences between the distances between ephemerides and observations on the celestial sphere, along-track and cross-track direction occur. In some cases, the distances of the ephemerides propagated with SDP4 and the observations are smaller than of the ephemerides propagated with SDP8 and observations in others vice versa. There is no explanation, what happened after this epoch. The precise process of the generation of TLE data of the USSTRATCOM catalogue is not public.

The situation is different for the HEO objects. Propagation with SDP4 improves the results in general, the mean values and standard deviations of all distances are smaller. Figure 7.13 shows the differences of the SDP8 and SDP4 distances on the celestial sphere, in along-track and cross-track direction for the investigated HEO objects. The differences are smaller for SDP4 propagation in the majority of cases. The differences are smaller if the same model is used for the generation and propagation of the TLE data.

7.3.3.2 Epoch Dependency

A further propagation is performed to investigate the dependency of the distances between ephemerides and observations on the epoch, which is displayed in the TLEs. The angular distance distances on the celestial sphere, in along-track and in cross-track direction are displaced as a function of epoch distance between the epoch displayed in the TLEs and the epoch of the observations in Fig. 7.14 for GEO and HEO for Fig. 7.14. All TLEs have been propagated to the observation epoch with SDP4. First, the closest TLE sets with the least propagation time was chosen and correlated with the observations. Systematic offsets of five and 15 days have been introduced in a next step: The observations have been correlated with the TLE sets, which were closest to the observation epoch plus five and 15 days, respectively. The distances between observed and calculated positions do not largely differ for the closest epoch TLE data compared to the TLE data with different offset.

This finding is investigated further in a second analysis. The observations of 48 GEO[3] and three HEO[4]

[3]Cospar numbers: 82082A, 83028F, 83065A, 83077A, 83089B, 84093D, 85015B, 85048D, 86003B, 89041B, 90102A, 90112D, 92027A, 92059A, 92088A, 94030A, 94049B, 94082A, 96044B, 96053A, 96067A, 97009A, 97025A, 97031A, 97049A, 97071A, 98006B, 98013A, 98024, 98035A,00031A, 00046B, 00052A, 01005A, 01011A, 01024A, 01037A, 01042A, 01045A, 02040B

[4]Cospar numbers: 98049B, 01025C, 02030B

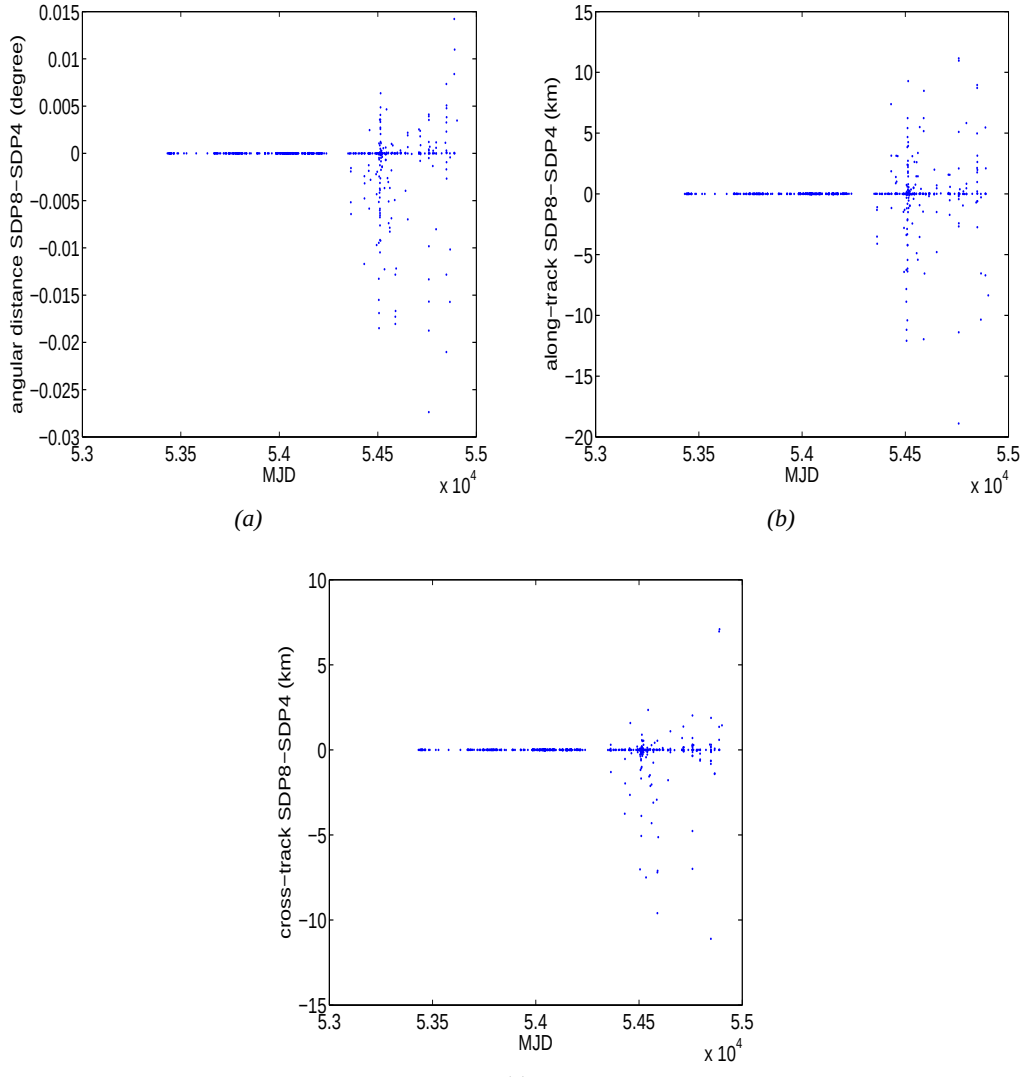

Figure 7.12: Distance of the SDP8 propagated ephemerides and observations minus the distances of SDP4 propagated ephemerides and the same observations of 13 GEO objects (a) on celestial sphere, (b) along-track, (c) cross-track direction.

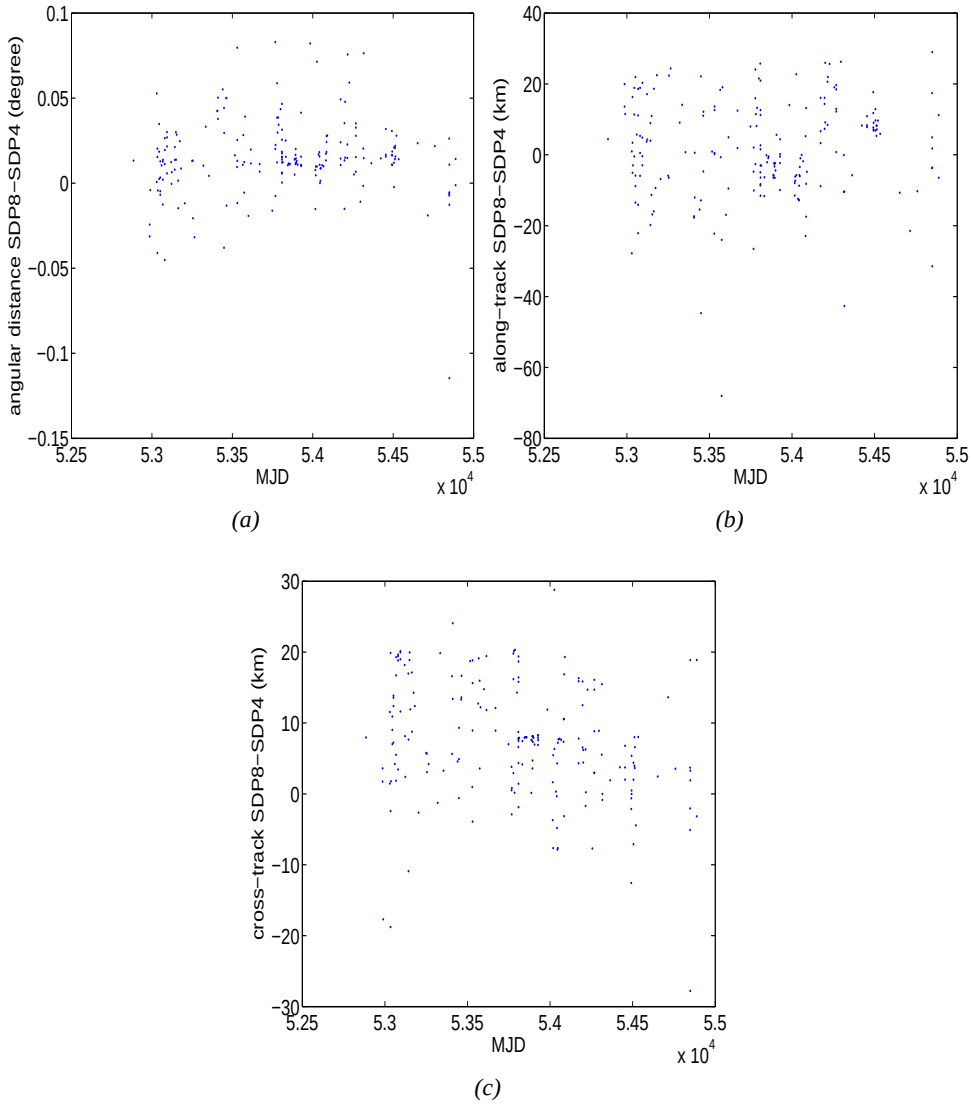

Figure 7.13: Distance of the SDP8 propagated ephemerides and observations minus the distances of SDP4 propagated ephemerides and the same observations of 8 HEO objects (a) on celestial sphere, (b) along-track, (c) cross-track direction.

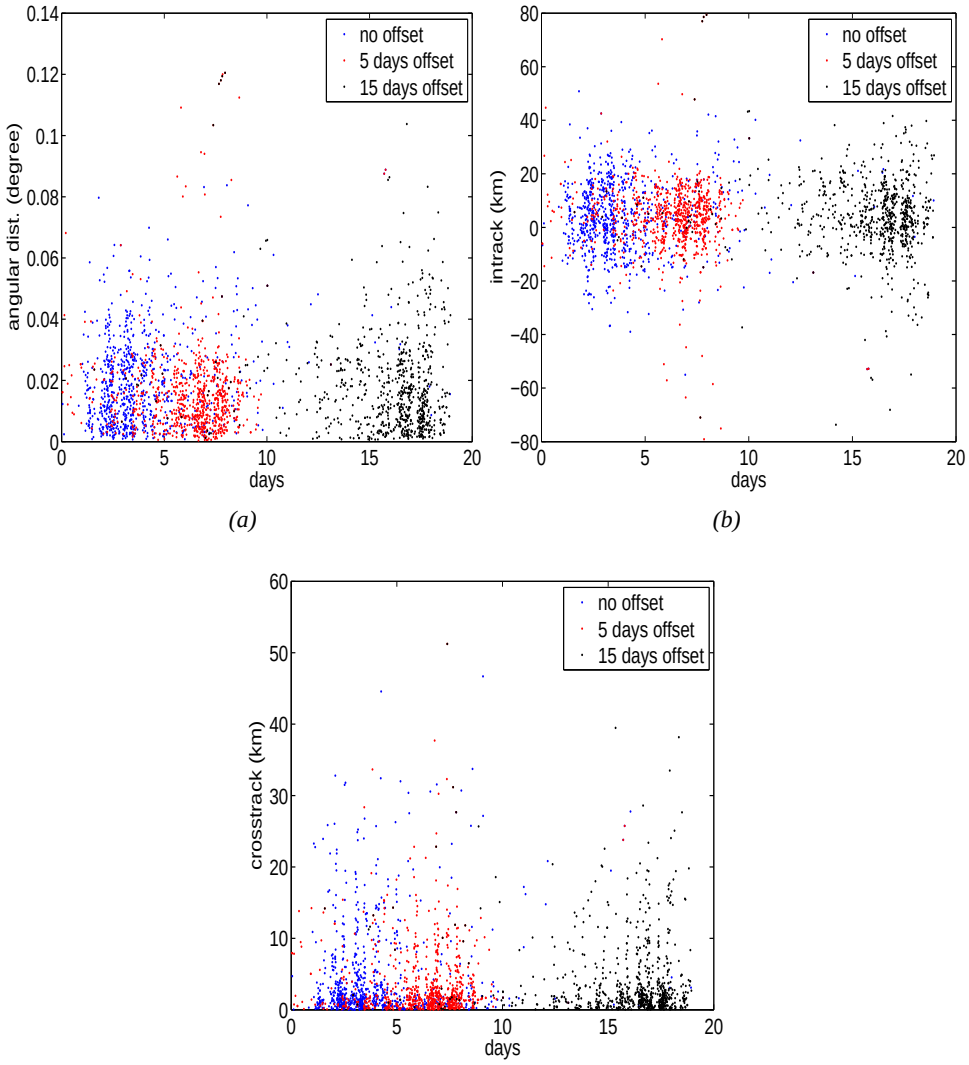

Figure 7.14: Distances of 13 GEO objects (a) on celestial sphere of (b) along-track (c) cross-track direction for TLE epoch closest to the observation epoch (blue), closest to the observation epoch plus five days, closest to the observation epoch plus 15 days.

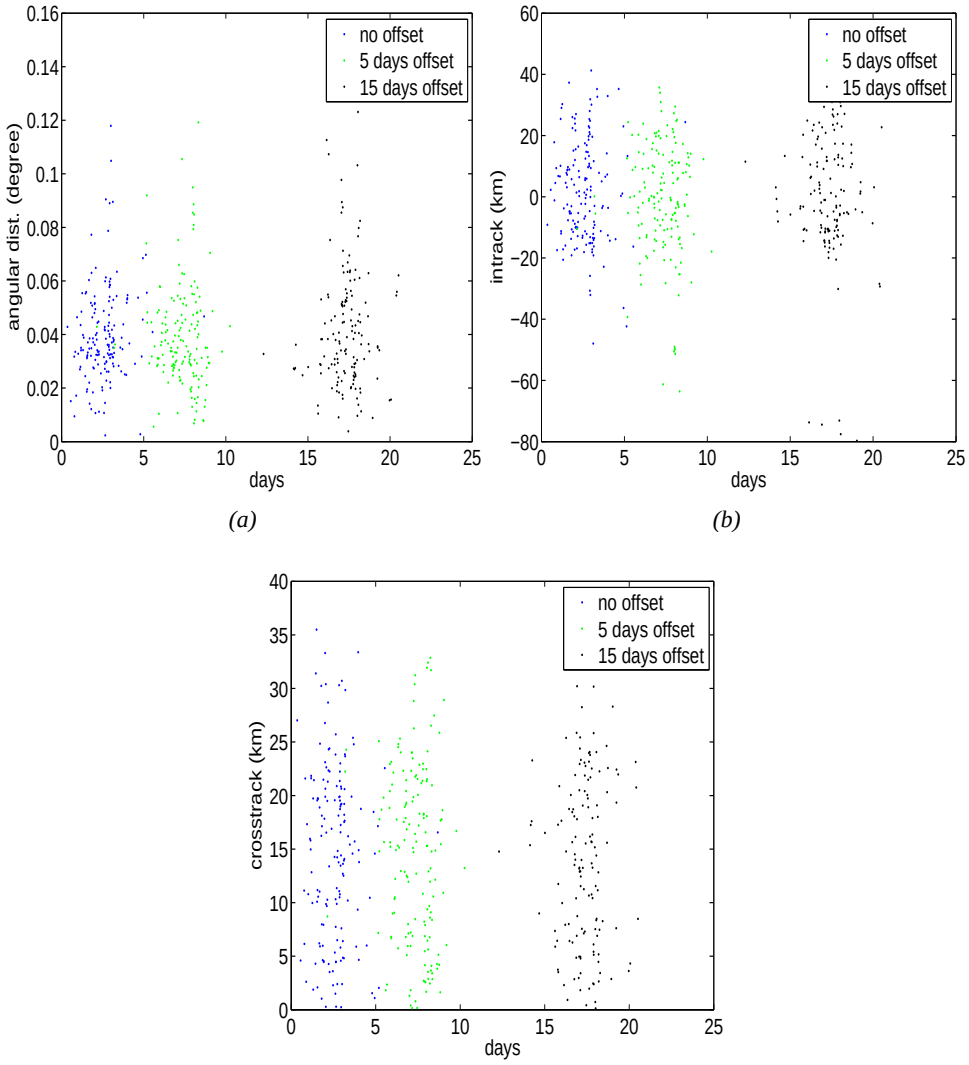

Figure 7.15: Distances of 8 HEO objects (a) on celestial sphere of (b) along-track (c) cross-track direction for TLE epoch closest to the observation epoch (blue), closest to the observation epoch plus five days, closest to the observation epoch plus 15 days.

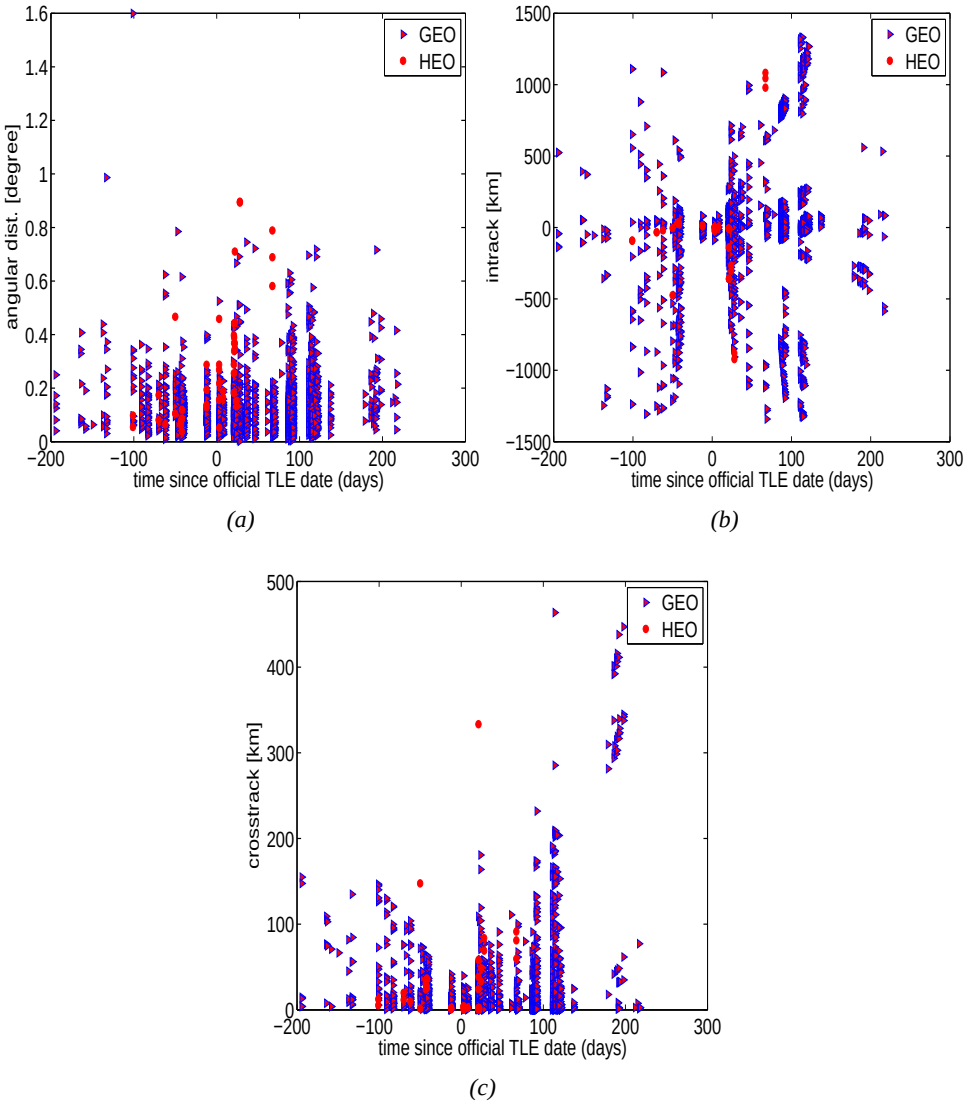

Figure 7.16: Distances in angular distance on the celestial sphere (a), projected along-track (b) and cross-track direction (c) with the SDP4 propagator for 48 GEO and 3 HEO objects

objects observed with the ZimSMART telescope were selected, stemming from surveys of the years 2008 and 2009. Unfortunately, only few HEO observations were available due to the GEO survey strategy of ZimSMART. All observations have been correlated to the TLE data set of 21 December 2008. The propagation was performed with SDP4.

Figure 7.16a shows the angular distances in degrees on the celestial sphere, Fig. 7.16b the projected along-track and Fig. 7.16c the projected cross-track distances as a function of time relative to the TLE reference epoch. A so-called *butterfly* shape of the distances around the epoch displayed in the TLE data, which is closest to the observation epoch can be observed in the along-track distances for the GEO objects. The cross-track distances, which are absolute values, display a *half-butterfly* shape. The *half-*

butterfly shape is not significantly visible in the distances on the celestial sphere. The distances of the HEO objects are not dense enough for a conclusive statement, but they do not seem to contradict the trend of the distances in GEO. The distances of the HEO objects are in general larger and show a higher variation. Variations in the distances occur for all objects. These results are in good agreement to the publication of T.S. Kelso [45], when comparing TLE data to precise GPS orbits in MEO.

7.4 Orbit Determination and Correlation with Ephemerides Data

7.4.1 Orbit Determination with the CelMech Program System

The CelMech program system (Beutler [4]) is used to determine orbits using astrometric observations of the ESASDT, as well as of ZIMLAT and ZimSMART. Orbits may be determined using data from a single site as well as merged data of different sites. CelMech has, among other features, the capability of determining a first orbit without a priori knowledge. It also may be used to improve orbits. The orbit determination and improvement program is called ORBDET. The advanced orbit determination and ephemerides generation tool is called SATORB. Both programs are briefly outlined in the next two sections. For further details consult G. Beutler [4].

7.4.2 First Orbit Determination and Improvement: ORBDET

ORBDET consists of two different steps. A first orbit is determined without knowledge of a priori elements in a first step. This first orbit is improved in a second step.

In the first step, either a circular orbit or a general two body orbit is determined. Usually, a circular orbit is determined first for satellites and space debris. When determining a circular orbit an initial value problem is solved.

Two astrometric positions, represented by the vectors $\vec{e}_i$, $i = 1, 2$, from the observer to the object, are used for the calculation. The two position vectors $\vec{r}_i$ refer to $t_i - \frac{d_i}{c}$, where t_i is the observation epoch, d_i the distance between observer and observed object at t_i and c is the speed of light. The geocentric distance to the object is then:

$$\vec{r}_i = d_i \cdot \vec{e}_i + \vec{R}_i, \tag{7.23}$$

where $\vec{R}_i$ the distance of the geocenter to the topocenter. The topocentric distance d_i may be expressed by the known quantities by squaring the equation above:

$$d_i = -\vec{R}_i \cdot \vec{e}_i + \sqrt{(\vec{R}_i \cdot \vec{e}_i)^2 - R_i^2 + r_i^2} \tag{7.24}$$

For a circular orbit with a radius a, r_i^2 can be replaced by the quantity a^2. The geocentric angle $\measuredangle(\vec{r}_1\vec{r}_2)_g$ between the two vectors $\vec{r}_1$ and $\vec{r}_2$ is:

$$\measuredangle(\vec{r}_1\vec{r}_2)_g(a) = \arccos\left(\frac{\vec{r}_1(a)\vec{r}_2(a)}{a^2}\right) \tag{7.25}$$

The same angle $\measuredangle(\vec{r}_1\vec{r}_2)_d$ follows by Kepler's third law $n = \sqrt{GM(m_0+m_1)/a^3}$, whereas G is the gravitational constant, and M the Earth mass:

$$\measuredangle(\vec{r}_1\vec{r}_2)_d(a) = n\left(t_1 - \frac{d_i(a)}{c} + t_2 - \frac{d_i(a)}{c}\right) \tag{7.26}$$

The root of the function

$$B(a) = \measuredangle(\vec{r}_1\vec{r}_2)_g(a) - \measuredangle(\vec{r}_1\vec{r}_2)_d(a) = 0 \tag{7.27}$$

allows it to determine the semi-major axis a in an iterative process. The orbital elements, Ω, the right ascension of ascending node and i, the inclination, of the orbital plane are determined using an approximated angular momentum $\vec{h}$:

$$\vec{h} = \vec{r}_1 \times \frac{\vec{r}_2 - \vec{r}_1}{t_2 - t_1} \tag{7.28}$$

$$\Omega = \arctan\left(\frac{h_1}{-h_2}\right) \tag{7.29}$$

$$i = \arccos\left(\frac{h_3}{|\vec{h}|}\right) \tag{7.30}$$

The argument of latitude u_l of the first observation epoch and the passing time through the ascending node T_0 are determined as the following:

$$a\begin{pmatrix} cosu_l \\ sinu_l \\ 0 \end{pmatrix} = R_1(i)R_3(\Omega)\cdot\begin{pmatrix} r_{1,i} \\ r_{2,i} \\ r_{3,i} \end{pmatrix} \tag{7.31}$$

$$T_0 = t_1 - \tfrac{d_1}{c} - \tfrac{u_1}{n} \tag{7.32}$$

whereas n is the mean orbital motion.

In general, Eq. 7.27 has more than one solution, different roots are determined. Usually all but one may be excluded.

In the next step the circular orbit is improved. Perturbations are included and all available observations are used in the orbit improvement step. The Earth's oblateness term (C_{20}) and the gravitational influence of Sun and Moon are included. This leads to the following differential equation of motion, see [4]:

$$\begin{aligned} \ddot{\vec{r}} = \quad & \frac{1}{r^3}\left(-GM\vec{r} + \frac{3}{2}\frac{C_{20}}{r^2}\begin{pmatrix} r_1(1-5\frac{r_3^2}{r^2}) \\ r_2(1-5\frac{r_3^2}{r^2}) \\ r_3(1-5\frac{r_3^2}{r^2}) \end{pmatrix}\right) \\ & -GM_{\leftmoon}\left(\frac{\vec{r}-\vec{r}_{\leftmoon}}{|\vec{r}-\vec{r}_{\leftmoon}|^3} + \frac{\vec{r}_{\leftmoon}}{\vec{r}_{\leftmoon}^3}\right) \\ & -GM_{\odot}\left(\frac{\vec{r}-\vec{r}_{\odot}}{|\vec{r}-\vec{r}_{\odot}|^3} + \frac{\vec{r}_{\odot}}{\vec{r}_{\odot}^3}\right) \end{aligned} \tag{7.33}$$

$\vec{r}$ is the geocentric distance to the observed object, $\vec{r}_{\odot}$ and $\vec{r}_{\leftmoon}$ are the geocentric position vectors of Sun and Moon, respectively. $M_{\odot}$ and $M_{\leftmoon}$ are the solar and lunar masses, respectively. The force model, displayed in Eq. 7.34, is precise enough to be able to represent the astrometric observations with an accuracy of below one arcsecond. Variational equations are integrated together with the equations of motion. The variational equations take the following form:

$$\ddot{\vec{z}} = \mathbf{A}\vec{z} \tag{7.34}$$

where $\vec{z}$ are the partial derivatives of the celestial body's position vector with respect to one of the six orbital parameters. Matrix $\mathbf{A}$ is defined as the following:

$$\begin{aligned}\mathbf{A} \quad &= -\frac{GM}{r^3}\big(\mathbf{E} - \frac{3}{r^2}\vec{r}\otimes\vec{r}^{T}\big) + \frac{3C_{20}}{r^2}\cdot\mathbf{D} \\ &-\frac{GM_{\leftmoon}}{|\vec{r}-\vec{r}_{\leftmoon}|^3}\big(\mathbf{E} - \frac{3(\vec{r}-\vec{r}_{\leftmoon})\otimes(\vec{r}-\vec{r}_{\leftmoon})^T}{(\vec{r}-\vec{r}_{\leftmoon})^2}\big) \\ &-\frac{GM_{\odot}}{|\vec{r}-\vec{r}_{\odot}|^3}\big(\mathbf{E} - \frac{3(\vec{r}-\vec{r}_{\odot})\otimes(\vec{r}-\vec{r}_{\odot})^T}{(\vec{r}-\vec{r}_{\odot})^2}\big)\end{aligned} \tag{7.35}$$

with $\mathbf{E}$ as the identity matrix, and

$$\mathbf{D} = \begin{pmatrix} \frac{1}{2} - \frac{2r_1^2+5r_3^2}{2r^2} + \frac{10r_1^2r_3^2}{r^4} & -\frac{r_1r_2}{r^2} + \frac{10r_1r_2r_3^2}{r^4} & -\frac{4r_1r_3}{r^2} + \frac{10r_1r_3^3}{r^4} \\ -\frac{r_1r_2}{r^2} + \frac{10r_1r_2r_3^2}{r^4} & \frac{1}{2} - \frac{2r_2^2+5r_3^2}{2r^2} + \frac{10r_2^2r_3^2}{r^4} & -\frac{4r_2r_3}{r^2} + \frac{10r_2r_3^3}{r^4} \\ -\frac{r_1r_3}{r^2} + \frac{10r_1r_3^3}{r^4} & -\frac{r_2r_3}{r^2} + \frac{10r_2r_3^3}{r^4} & \frac{1}{2} - \frac{17r_3^2}{2r^2} + \frac{10r_3^4}{r^4} \end{pmatrix}. \tag{7.36}$$

The equations of motion and the variational equations are solved via numerical integration using the collocation method with a variable step size, see [4]. The collocation method approximates the solution vector by a function through a polynomial of a degree q within user defined intervals.

The orbit is improved using the least-squares method using the right ascension and declination of the observations as observed values. The *observation equations* represent the distance between the observed function and the observations. In the linearized form (Taylor series expansion about the approximated values of the orbital elements) they read as:

$$\nu_{\alpha} = \sum_{j=1}^{6}\frac{\partial\alpha_i^C}{I_j}(I_j - I_j^C) - (\alpha^O - \alpha^C(t_i)), \tag{7.37}$$

$$\nu_{\delta} = \sum_{j=1}^{6}\frac{\partial\delta_i^C}{I_j}(I_j - I_j^C) - (\delta^O - \delta^C(t_i)), \tag{7.38}$$

where α is the right ascension of the observed object, δ its declination. The index C denotes the computed values, the index O the observed ones, I_j with $j = 1, .., 6$ denote the six orbital elements, ν_{α} and ν_{δ} are the so-called residuals. In the least square approach the sum of all the squared residuals have to be minimized:

$$\sum_{i=1}^{n}\Big([\cos\delta_i^O\nu_{\alpha_i}]^2 + \nu_{\delta_i}^2]\Big) = min \tag{7.39}$$

Note that the observations in α are weighted with $\cos\delta_i^O$ to make them equivalent with the observations in δ. The residuals may be weighted, when observations from different sites are analyzed together. The weights associated with the observations of the telescope k would be σ_0^2/σ_k^2, where σ_0 is the rms error of the weight unit and σ_k^2 the rms of an observation with telescope k. It is recommended to use an empirically determined rms value for each sensor. The minimum is reached, when all partial derivatives of the sum in Eq. 7.39 w.r.t. the orbital elements are zero. This leads to the so-called *normal equations*:

$$\mathbf{N}\Delta\vec{I} = \vec{b} \tag{7.40}$$

with:

$$\Delta I^T := (a - a^C, e - e^C, i - i^C, \Omega - \Omega^C, \omega - \omega^C, T_0 - T_0^C) \tag{7.41}$$

$$\mathbf{N_{nj}} = \sum_{i=1}^{n} \Big(\cos^2\delta_i^O \frac{\partial\alpha_i^C}{I_j}\frac{\partial\alpha_i^C}{I_k} + \frac{\partial\delta_i^C}{I_j}\frac{\partial\delta_i^C}{I_k}\Big) \qquad i,j = 1,2\ldots 6 \tag{7.42}$$

$$b_j^C = \sum_{i=1}^{n} \Big(cos^2\delta_i^O \frac{\partial\alpha_i^C}{I_j}(\alpha_i^O - \alpha^C(t_i)) + \frac{\partial\delta_i^C}{I_j}(\delta_i^O - \delta^C(t_i))\Big) \tag{7.43}$$

The variance covariance information of the solution vector $\Delta\mathbf{I}$ is given by:

$$\mathbf{cov}(\mathbf{I}) = (m_0)^2(\mathbf{N})^{-1} \tag{7.44}$$

The a posteriori variance factor m_0 (rms of the weight unit) of one observation is defined as the following:

$$m_0^2 = \frac{\sum_{i=1}^{k}\Big([\cos\delta_i^O\nu_{\alpha_i}^2 + \nu_{\delta_i}]\Big)}{2N-6} \tag{7.45}$$

where N is the number of astrometric positions. ORBDET uses internally rectangular components of the position and velocity vectors, in order to avoid singularities. UTC input is transformed to GPS time and transformed back to orbital elements in UTC for output, to ensure a continuous time scale. Inconsistencies in the time transformation could be removed, in the course of this work. The position of Sun and Moon are determined from JPL ephemerides [42].

ORBDET also allows to determine a general six parameter orbit by solving first orbit determination as a boundary value problem. For HEOs this option should be preferable. It is, however, difficult to determine a six parameter orbit with a short observation time span. Tracklets which cover only one minute may occur, which may only cover 1/1440 of the orbit. This is the reason why circular orbits are also determined for HEOs.

7.4.3 Orbit Determination and Ephemerides Calculation with Improved Force Model: SATORB

7.4.3.1 Orbit Determination

SATORB allows to determine a precise orbit from astrometric positions using a priori orbital elements. Compared to orbit improvement in ORBDET a better force model is used in SATORB. The same techniques are used as in the orbit improvement step of ORBDET.

For GEO, GTO, and HEO objects an Earth gravitational field up to degree and order 12 is used, and the gravitational attractions due to Sun and Moon are taken into account. Corrections due to Earth tides, general relativity and a model for the direct radiation pressure are taken into account, as well. The variational equations referring to dynamical parameters are solved independently of the primary equations. The following parameters may be determined in addition to the orbital elements: a combination of nine radiation pressure parameters decomposed in different directions, constant and once-per-revolution-terms, a scaling factor for the direct radiation pressure model, and so-called stochastic pulses. Empirical once-per-revolution-terms and stochastic pulses are useful for determining high precision orbits with dense, regularly spaced observations over long time spans. Such parameters are not estimated, when determining orbits of satellites and space debris, for which only short observation tracklets are available. Two tracklets, spaced by a couple of days, but stemming from different satellites in one cluster might lead to a *successful*, in terms of an rms below two arcseconds for the observations regarded here, orbit determination, when using stochastic pulses and once per revolutions parameter estimation. Orbits determined without such parameters are a reliable tool to decide, which tracklets belong to the same physical object. For LEO objects a drag model may be selected instead of or in addition to a radiation pressure model.

It is assumed that Earth shadow is entered, if the angle β between the geocentric unit vector to the sun and the orbital plane of the eclipse is smaller than:

$$\beta < \arcsin\left(\frac{a_{\oplus}^{\pm}}{a}\right), \tag{7.46}$$

where $a_{\oplus}^{\pm}$ is the mean Earth radius and a the semi-major axis of the satellite orbit. The shadow cylinder is derived under the assumption of a spherical Earth. The boundary between the sunlit and eclipsed part of space is assumed to be cylindrical, i.e., no distinction is made between umbra and penumbra. The Earth's atmosphere is neglected.

The acceleration due to the direct radiation pressure is calculated as:

$$\vec{a}_{\text{rad}} = \frac{C}{2} \cdot \frac{S}{c} \cdot \frac{AU^2}{|\vec{r} - \vec{r}_{\odot}|^2} \cdot \frac{A}{m} \cdot \frac{\vec{r} - \vec{r}_{\odot}}{|\vec{r} - \vec{r}_{\odot}|}, \tag{7.47}$$

where $\vec{r}$ is the geocentric position of the satellite, $\vec{r}_{\odot}$ the geocentric position vector of the sun, AU the astronomical unit, A the effective cross section exposed to the radiation, m the mass of the satellite, and c the speed of light. C is the reflection coefficient. The direct radiation pressure is determined under the assumption of a spherically shaped object. In contrast to the calculation of the radiation pressure acceleration by other sources (compare e.g. Vallado [93]), the coefficient C is divided by two in the formula above. A value for C has to be chosen, by default, 2.0 is selected in the standard processing. This corresponds to an assumption of full absorption. As a scaling parameter of the direct radiation pressure the area-to-mass ratio (AMR) is used. It is assumed that the AMR is constant over the orbital fit interval. A default value of 0.02 m^2kg^{-1} is selected, which corresponds to an AMR value of a standard GPS satellite, in case the AMR parameter is not estimated but kept fixed in the orbit determination. If the scaling parameter of the AMR is estimated either the standard value or a value available from a previous orbit determination is chosen as a priori value.

SATORB allows to estimate so-called empirical, constant once per revolution (DRP-) parameters decomposed in the RSW-directions:

$$\vec{a}_{\text{emp}} = R(t)\vec{e}_{\text{R}} + S(t)\vec{e}_{\text{S}} + W(t)\vec{e}_{\text{W}} \tag{7.48}$$

The unit vector $\vec{e}_{\text{R}}$ points from the geocenter to the satellite, $\vec{e}_{\text{S}}$ in the along-track direction, orthogonal to the radial direction, in direction of – but for non-circular orbits not necessarily parallel – to the velocity direction of the object. $\vec{e}_{\text{W}}$ is orthogonal to the orbital plane and completes the right hand system.

Space debris objects are likely to be irregularly shaped. The empirical parameters may account for these asymmetries laking information of the accurate shape of the vast majority of space debris objects,

7.4.3.2 Ephemerides Calculation

Ephemerides can be generated using osculating elements at the initial epoch for a user defined time interval. The same force models are used in SATORB for the orbit prediction as in orbit determination. The direct radiation pressure scaling coefficient (AMR value) can be included in the prediction and ephemerides generation. A constant AMR value is assumed. The estimated empirical parameters, which are possibly determined in orbit determination with SATORB, cannot be included in the orbit prediction and ephemerides generation in the current implementation.

Initially equally spaced ephemerides were generated with a user-selected step size. The program was changed to calculate ephemerides at irregularly spaced epochs in the context of the current work, allowing to determine ephemerides exactly at those epochs, for which observations are available, so no further errors (e.g. by (linear) interpolation) are introduced, when comparing ephemerides with real observations.

For the generation of ephemerides two different methods may be selected: A so-called exact method, which calculates ephemerides with the correct transformation between the inertial and the Earth fixed system, taking into account polar motion and Earth's variable rotation based on a Earth rotation parameter file, which is constantly updated. For longe prediction intervals so-called approximated ephemerides may be calculated, using an approximated transformation not relying on the Earth rotational parameter file. In the scope of the current work always the exact method was chosen.

7.4.4 Comparison of AIUB and USSTRATCOM/DISCOS TLE Ephemerides

Orbits were computed for objects observed with ZIMLAT, which are available in the official USSTRATCOM/DISCOS catalogue. Objects in different orbital regimes have been selected. For each object, different orbits have been determined by varying the number of dynamical parameters and the length of the fit interval, which is covered by observations. The same a priori elements were used for all orbits of the same object. The a priori orbit was determined with ORBDET, using 10 to 20 observations spanning a time interval of 30 to 55 days. The improved orbits and ephemerides were calculated with SATORB. The ephemerides of the predicted orbits were then compared to additional observations past the fit interval of orbit determination of the same objects. In addition to those orbits, also TLE data sets from USSTRATCOM/DISCOS have been evaluated. TLE data has been propagated with SDP8 and compared to the same observations. For each observation tracklet a different TLE data set was chosen:

Table 7.4: Characterization of orbits for the GEO objects 79105A, 83089B and 80081A.

	time interval (d)	No. of Obs.	rms (")	AMR m^2kg^{-1}	rms (AMR)
79105A					
$EPHM_S$	10	18	0.61	0.02000	-
$EPHM_L$	32	23	1.11	0.02000	-
$EPHM_{LDRP}$	32	23	0.48	0.00691	$\pm 8.93 \cdot 10^{-3}$
83089B					
$EPHM_{VS}$	1	5	0.17	0.02000	-
$EPHM_S$	9	12	0.40	0.02000	-
$EPHM_L$	23	24	1.04	0.02000	-
$EPHM_{LDRP}$	23	24	0.45	0.02728	$\pm 4.92 \cdot 10^{-4}$
80081A					
$EPHM_S$	5	11	0.20	0.02000	-
$EPHM_M$	15	25	0.28	0.02000	-
$EPHM_{MDRP}$	15	25	0.21	0.01255	$\pm 1.19 \cdot 10^{-3}$
$EPHM_L$	29	32	1.72	0.02000	-
$EPHM_{LDRP}$	29	32	0.26	0.01475	$\pm 9.61 \cdot 10^{-5}$

the set with the reference epoch closest to each observation epoch was chosen.

The angle between the observed astrometric positions and the corresponding astrometric positions calculated with the ephemerides are (as outlined in Section 7.2.2), decomposed in an along-track and cross-track component. Using the topocentric distance to the object (calculated with the ephemerides) to define a scaling factor, the components may be expressed in units of kilometers. The angle between the topocentric tangential motions based on the observations and the ephemerides have been determined. The values are averaged for each observation/ephemerides tracklet. A tracklet consists of three to six single observations, spaced by 30 seconds.

7.4.4.1 GEO Objects

The three GEO objects 79105A (Gorizont-3), 83089B (Insat-1B) and 80081A (Raduga-7) serve as representative examples. All have small eccentricities and inclinations between 12 and 14 degrees. 79105A and 83089B are in libration orbits around the Eastern stable point, 80081A around the Western stable point.

The orbits determined for the three objects, are characterized in Tab. 7.4. The columns show the length of the interval fit interval of orbit determination covered by observations, the number of observations within this fit interval, the root mean square (RMS) error of the orbit determination, the area to mass ratio (AMR) value and its rms error. If the AMR value is not estimated, a value of $0.02 m^2kg^{-1}$ is chosen, consequently no error for the AMR value is given in those cases.

Figure 7.17 shows the distribution of observations, which were used in the orbit determination, for all objects. The corresponding true anomalies are shown in Fig. 7.18.

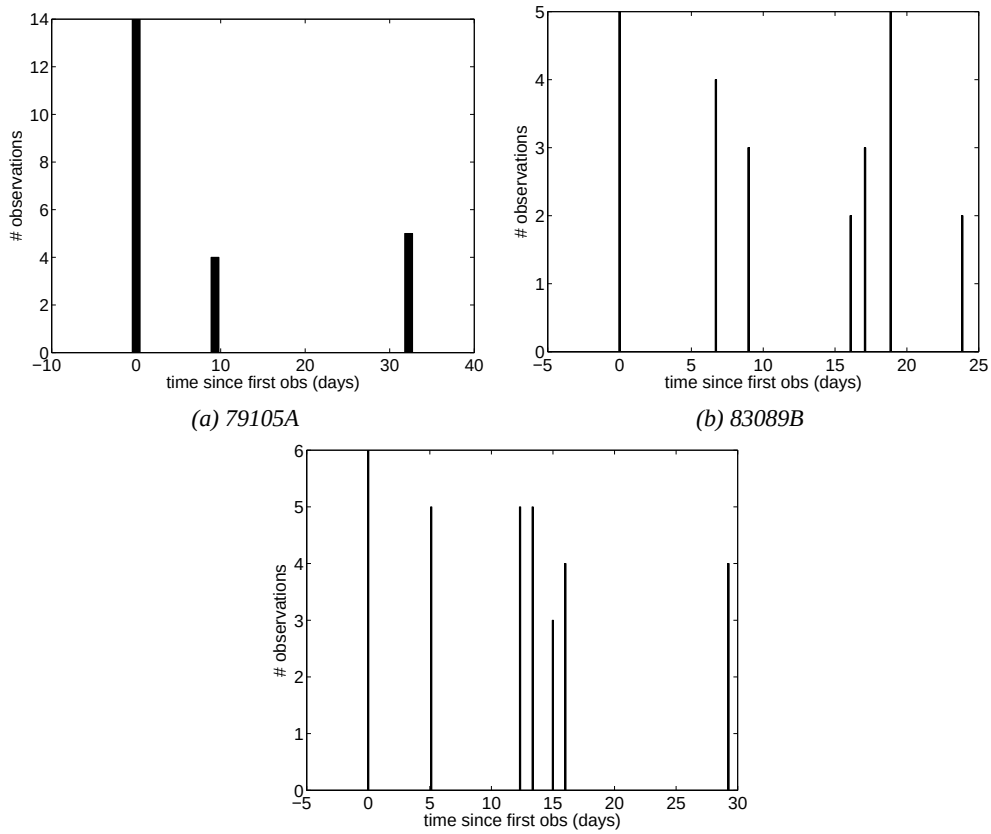

(a) 79105A *(b) 83089B*

(c) 80081A

Figure 7.17: Time distribution of the observations used in orbit determination for the GEO objects (a) 79105A, (b) 83089B, (c) 80081A.

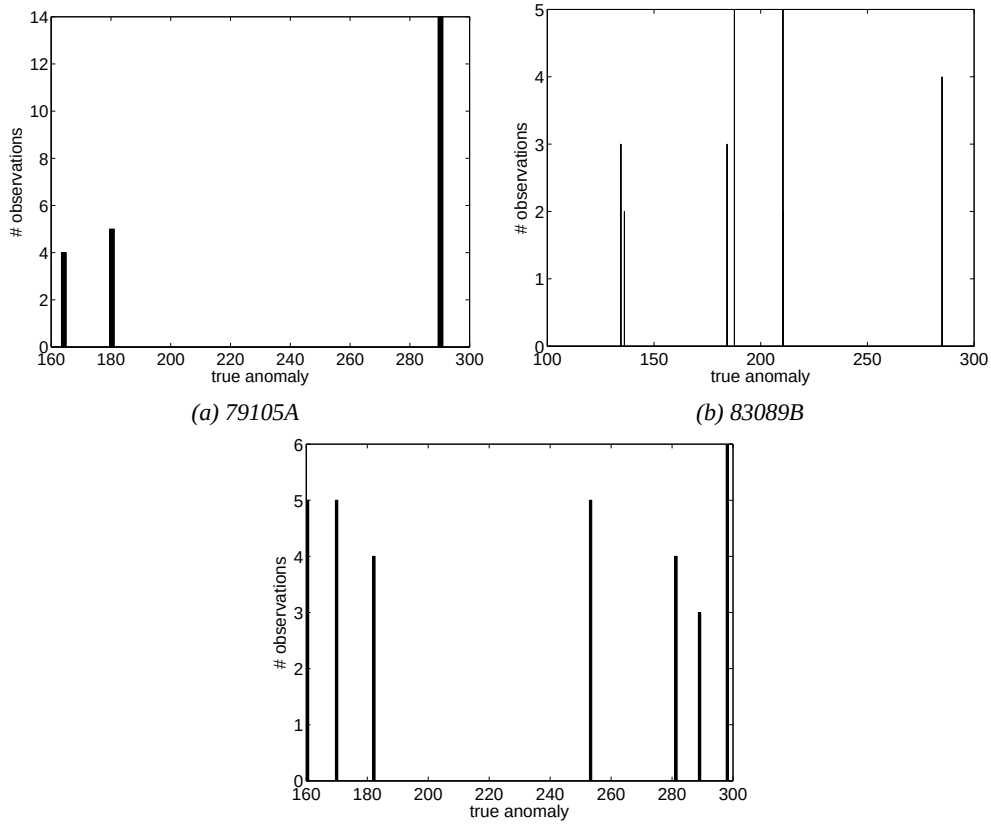

(a) 79105A

(b) 83089B

(c) 80081A

Figure 7.18: Anomaly distribution of the observations used in orbit determination for the GEO objects (a) 79105A, (b) 83089B, (c) 80081A.

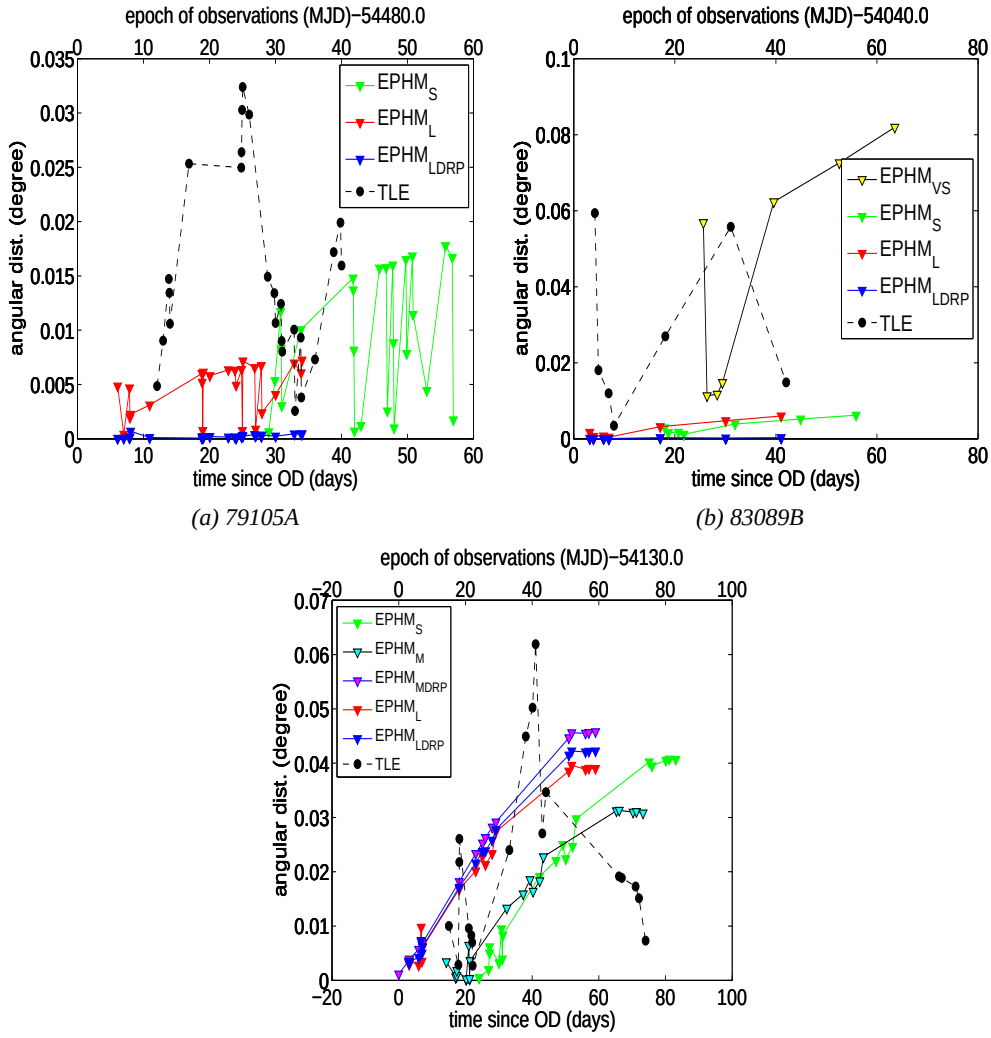

(a) 79105A *(b) 83089B*

(c) 80081A

Figure 7.19: Angular distances in degrees between the observations and predicted ephemerides using either TLE data or determined orbits for the GEO objects (a) 79105A, (b) 83089B, (c) 80081A as a function of epoch of the observations for TLE data and the time since orbit determination for the orbits.

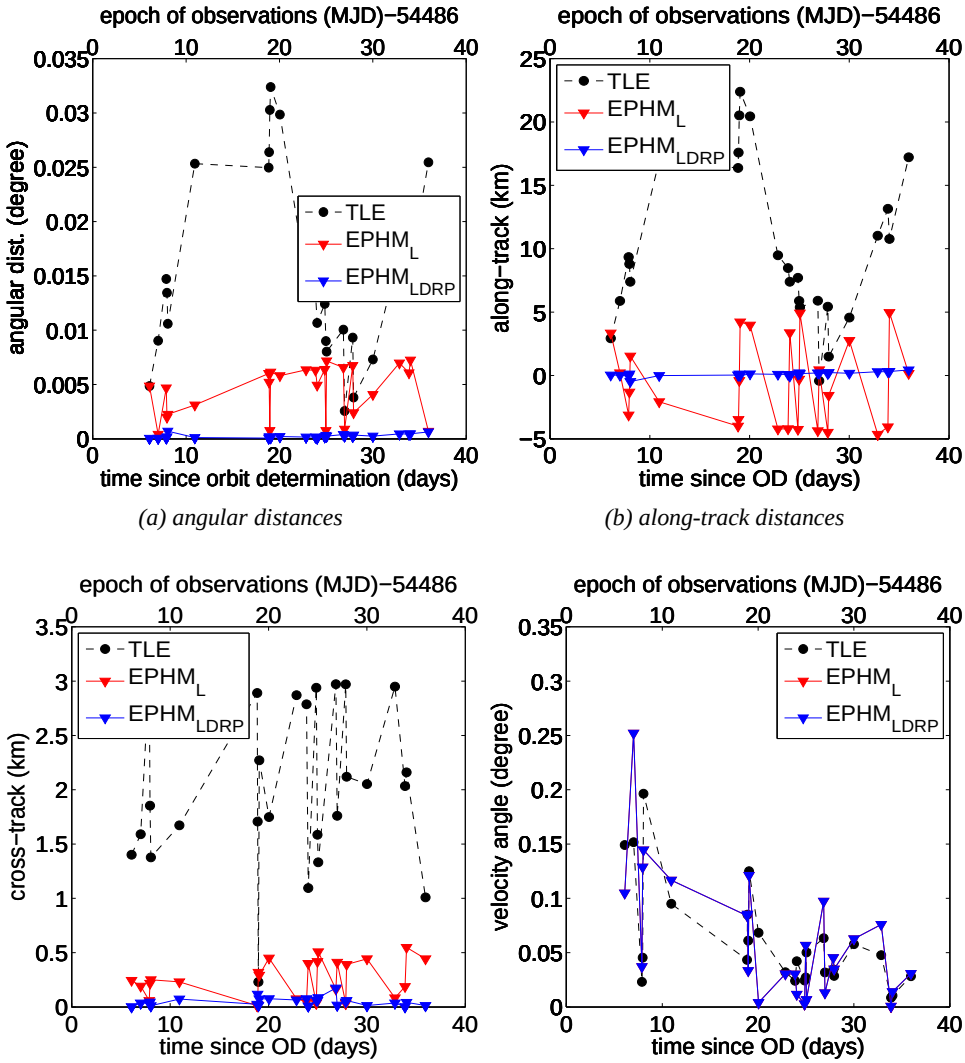

(a) angular distances

(b) along-track distances

(c) cross-track distances

(d) angle between velocity directions

Figure 7.20: Distances between observed positions and predicted ephemerides from TLEs and from orbit determinations and predictions with SATORB for GEO object 79105A as a function of epoch of the observations for TLE data and the time since orbit determination for the orbits.

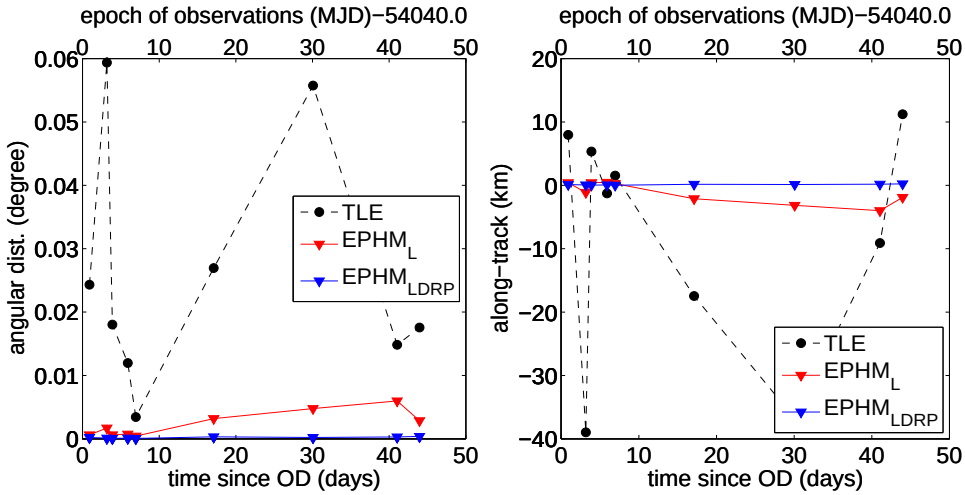

(a) angular distances *(b) along-track distances*

(c) cross-track distances *(d) angle between velocity directions*

Figure 7.21: Distances between observed positions and predicted ephemerides from TLEs and from orbit determination for GEO object 83089B as a function of epoch of the observations for TLE data and the time since orbit determination for the orbits.

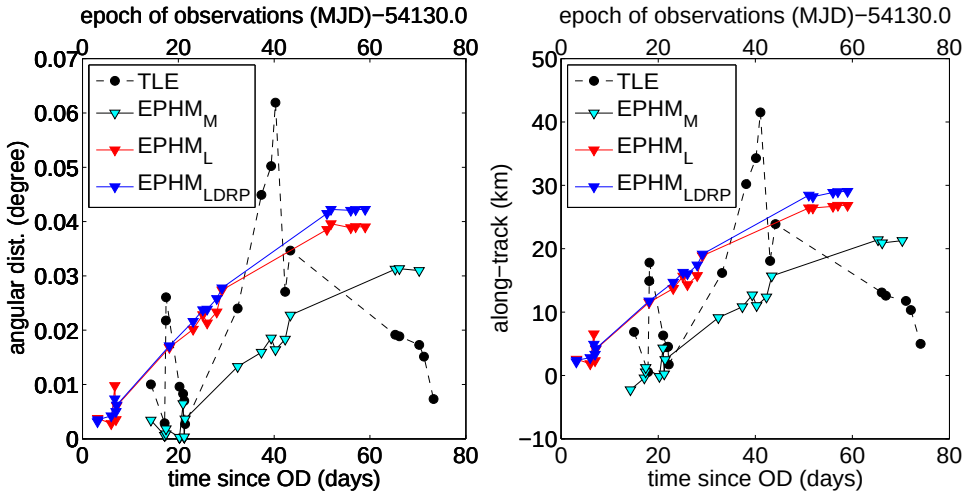

(a) angular distances *(b) along-track distances*

(c) cross-track distances *(d) angle between velocity directions*

Figure 7.22: Distances between observed positions and predicted ephemerides from TLEs and from orbit determination for GEO object 80081A as a function of epoch of the observations for TLE data and the time since orbit determination for the orbits.

Figure 7.19 shows the angular distances between the observed astrometric positions and the astrometric positions calculated from the ephemerides of the determined and predicted orbits as a function of time since the last epoch within the fit interval of the orbit determination. The additional observations were *not* used for orbit determination. In addition, the angular distances between the observed astrometric positions and TLE ephemerides are shown as a function of the epoch of the astrometric positions. The TLE ephemerides were calculated with different TLE sets, each closest to the particular observation epoch. The quality of the different TLE data sets, which were used, differs significantly. The displayed values are averages of each observation/ephemerides tracklet. A tracklet consists of three to six single data points, spaced by 30 seconds.

Figure 7.19a shows that the orbit $EPHM_S$ of object 79105A, determined over an fit interval of ten days, produces large angular distances in the prediction. The ephemerides of orbits over a larger fit interval of 32 days, $EPHM_L$ and $EPHM_{LDRP}$, show smaller distances to the observations. As Fig 7.20 shows, the ephemerides orbit $EPHM_L$, for which no AMR value was estimated show large variations, mainly in along-track but also in cross-track direction. The ephemerides of $EPHM_{LDRP}$ with an estimated AMR value of about 0.069 m^2kg^{-1} show the smallest residuals, of below 0.002 degrees. The angles between the velocity directions are very similar for the ephemerides of the different orbits and ephemerides of TLE data. As explained in Section 7.3.3.1, errors in the velocity angle below $6.4 \cdot 10^{-2}$ degrees for GEO are likely to just reflect the observation errors, which are of the order of about 0.5 arcseconds.

Figure 7.19b shows that for object 83089B, the ephemerides of orbit $EPHM_{VS}$, which were determined using an observation interval of one day only, shows large distances to the observations. The two orbits $EPHM_S$ and $EPHM_L$ determined over a fit interval of nine and 23 days, respectively, result in distances between ephemerides and observations of a similar range. A secular trend is visible. Figure 7.21 reveals, that the secular trend in the ephemerides $EPHM_L$ is mainly in the along-track component. The smallest distances between ephemerides and observations are observed for the orbit $EPHM_{LDRP}$ determined over the same fit interval of 23 days but with estimating the AMR value as additional parameter. A value of 0.028 m^2kg^{-1} was estimated. The different orbits show different angles between velocity directions.

When comparing the orbits of object 79105A and 83089B it is significant, that the ephemerides of orbit $EPHM_S$ of object 83089B show systematically smaller distances to the observations than the ephemerides of orbit $EPHM_S$ of object 79105A, compare Fig. 7.19a and 7.19b, although the fit intervals are comparable. This might be caused by the fact that the observations of object 83089B are more uniformly spread in time and anomaly over the fit interval, see Fig. 7.17a and 7.18a compared to Fig. 7.17b and 7.18b.

The distances between the observations and the computed ephemerides show a secular trend, all distances are increasing rapidly as a function of prediction time, see Fig. 7.19, for object 80081A. The distances of the observations to the TLE ephemerides are smaller than to the ephemerides of the determined orbits, despite the fact that the distances of the TLE ephemerides are of the same order of magnitude as for the other two objects. Figure 7.22 shows that particularly in along-track a large secular trend. The differences rise fast with the prediction time, the differences in cross-track direction are small and do not show a significant trend. This is the case for the orbit determined over 15 days ($EPHM_M$) or

Table 7.5: Characterization of different orbits for the object 80081A.

	OD 1	**OD 2**	**OD 3**	**OD 4**	**OD 5**
start epoch [MJD]	54115.778604	54130.767031	54147.892958	54152.176868	54171.042372
end epoch [MJD]	54145.034616	54152.176868	54170.141564	54174.158928	54196.909040
time interval [d]	30	22	23	22	25
number of obs.	32	17	13	18	20
rms [¨]	0.26	0.29	0.87	0.23	0.52
osc. elements at	54171.042372				
a [m]	42172565.001	42172568.762	42172522.508	42172466.451	42172517.235
	± 0.127	± 4.843	± 9.211	± 13.269	± 2.804
e	0.0003366	0.0003482	0.0003527	0.0003463	0.0003482
	± 0.0000005	± 0.0000028	± 0.0000027	± 0.0000038	± 0.0000013
i [deg]	14.360502	14.360504	14.360487	14.360607	14.360451
	± 0.000020	± 0.000005	± 0.000104	± 0.000044	± 0.000075
RA of node [deg]	1.392344	1.392743	1.392228	1.392291	1.392585
	± 0.000060	± 0.000016	± 0.000325	± 0.000069	± 0.000167
AMR [m^2kg^{-1}]	0.014751	0.015542	0.022678	0.006224	0.014786
	± 0.000096	± 0.000085	± 0.003698	± 0.003820	± 0.000803

over 32 days with ($EPHM_{LDRP}$) or without ($EPHM_L$) estimating an AMR value. The smallest distances are associated with the orbit $EPHM_M$ and not with the orbit $EPHM_L$, which was determined over a longer fit interval. As opposed to the objects 79105A and 83089B, the smallest differences are not achieved with orbits including the estimation of an AMR value, all differences are in general larger than for object 79105A and 83089B. The observations used for orbit determination are well distributed in time and anomaly, see Fig. 7.17c and 7.18c.

Further orbits were determined with the subsequent overlapping fit intervals. The results are listed in Tab. 7.5. OD 2 could only be determined when estimating an empirical R-parameter in addition to the DRP value. Empirical parameters are explained in Section 7.4.3.1. The osculating orbital elements at the reference epoch of all determined orbits do not differ significantly. The orbital elements show the largest errors for OD 3 and OD 4. Those orbits also show significantly different AMR values, compared to the other orbits. But the error in the AMR value is also larger than that of the other orbits. It is not possible to determine a low rms orbit over all observations of OD 1 to OD 5, from epoch 54115.8 to 54171.0: Even when estimating additional empirical parameters no orbit could be determined with an rms value of below 10 arcseconds. An orbit can be determined with the observations of the fit intervals of OD 1, OD 2, and OD 5, named OD 125 in the following, when the AMR as well as empirical R- and W-parameters were estimated. A small rms orbit resulted as well when determined with observations of the fit intervals of OD 3 and OD 4. The osculating orbital elements, AMR value, their errors and the rms are listed in Tab. 7.6. The osculating orbital elements do show small differences at the reference epochs. But a significantly different AMR value has been determined. Between epoch 54147.9 and 54152.1 a property of the object may have changed. The change may cause the differences in the estimated AMR values.

Table 7.6: Characterization of two different orbits for the object 80081A..

	OD 125	**OD 34**
start epoch [MJD]	54115.778604	54147.892958
end epoch [MJD]	54196.909040	54174.158928
number of obs.	69	31
rms [¨]	0.84	0.73
osc. elements at	54196.909	
a [m]	42172569.080	42172506.673
	± 0.613	± 2.036
e	0.0003642	0.0003504
	± 0.0000011	± 0.0000010
i [deg]	14.360498	14.360525
	± 0.000121	± 0.000052
RA of node [deg]	1.392668	1.392338
	± 0.000307	± 0.000127
AMR [m^2kg^{-1}]	0.007530	0.017921
	± 0.000363	± 0.000106

Table 7.7: Characterization of orbits for the HEO objects 00016D, 75105A and 92085D.

	time interval (d)	No. of Obs.	rms (")	AMR m^2kg^{-1}	rms (AMR)	emp. parameter
00016D						
$EPHM_{VS}$	4	10	0.28	0.02000	-	-
$EPHM_{S}$	7	15	1.20	0.02000	-	-
$EPHM_{LEMP}$	14	20	0.38	0.02000	-	x
77105A						
$EPHM_{L}$	20	100	0.68	0.02000	-	-
$EPHM_{LDRP}$	20	100	0.28	0.00815	$3.55 \cdot 10^{-4}$	-
$EPHM_{LEMP}$	20	100	0.17	0.00741	$2.46 \cdot 10^{-4}$	x
92085D						
$EPHM_{S}$	5	30	0.35	0.02000	-	-
$EPHM_{L}$	49	41	0.81	0.02000	-	-
$EPHM_{LDRP}$	49	41	0.15	0.00508	$2.85 \cdot 10^{-4}$	-

7.4.4.2 HEO Objects

Three objects were selected as representative in highly eccentric orbits: The Ariane 5 R/B rocket body 00016D, in an orbit with 6.3 degrees inclination, and two Molniya objects in orbits with inclinations of about 63 degrees, namely: Molniya-3 77105A and Blok-ML 92085D. The latter object decayed in the meantime. All object orbits had eccentricities around 0.7.

Table 7.7 shows the details of the determined orbits. Empirical parameters were estimated for some or-

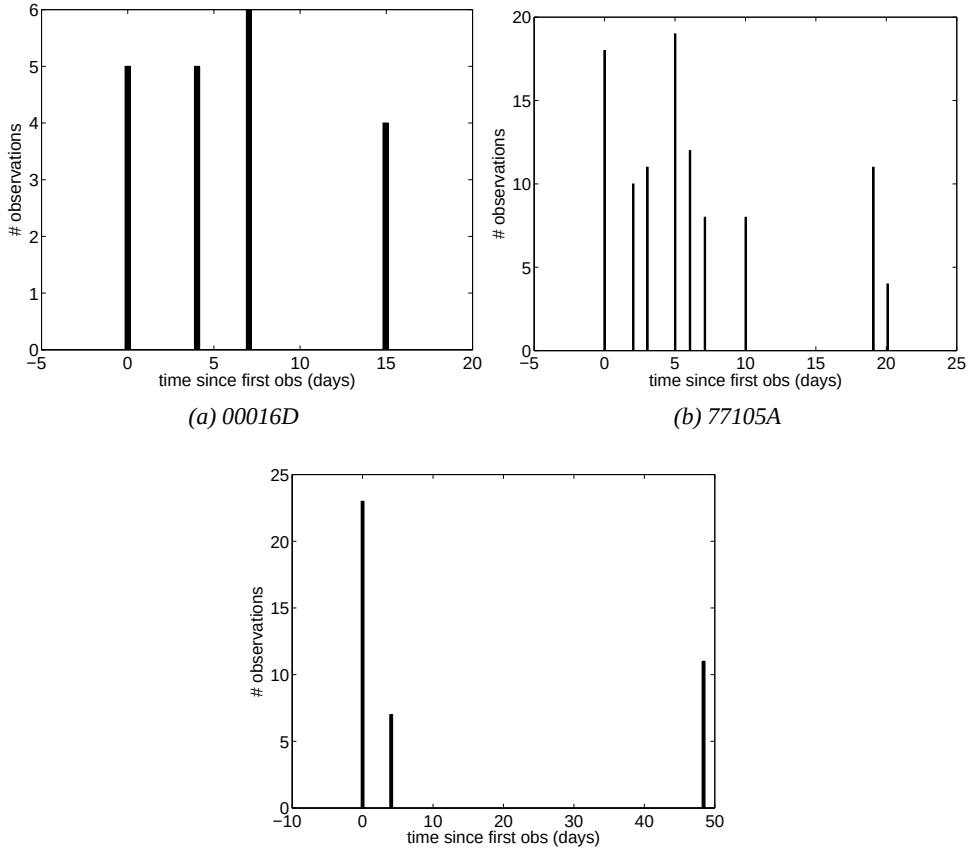

(a) 00016D

(b) 77105A

(c) 92085D

Figure 7.23: Time distribution of the observations used for orbit determination for the HEO objects (a) 00016D, (b) 77105A, (c) 92085D.

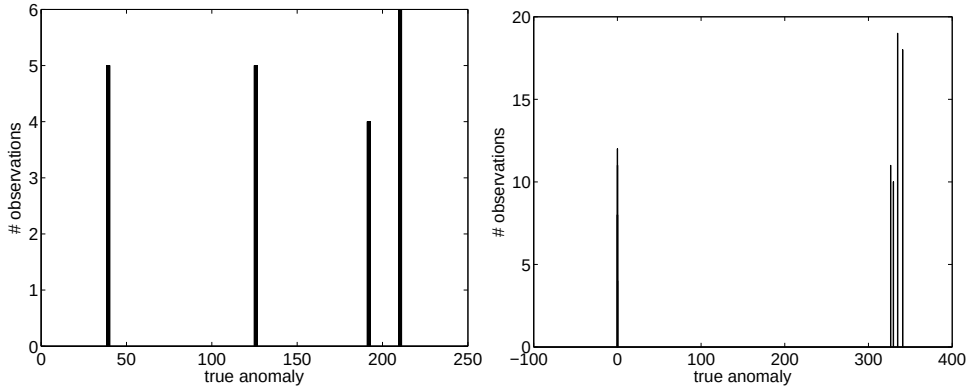

(a) 00016D *(b) 77105A*

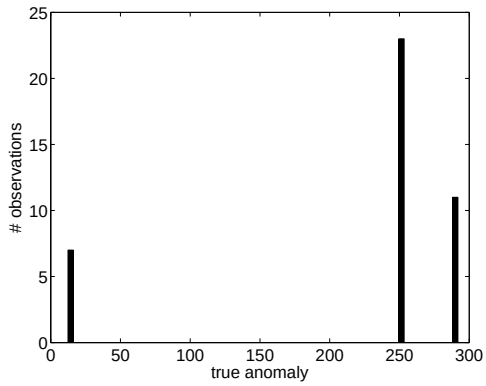

(c) 92085D

Figure 7.24: Anomaly distribution of the observations used for orbit determination for the HEO objects (a) 00016D, (b) 77105A, (c) 92058D.

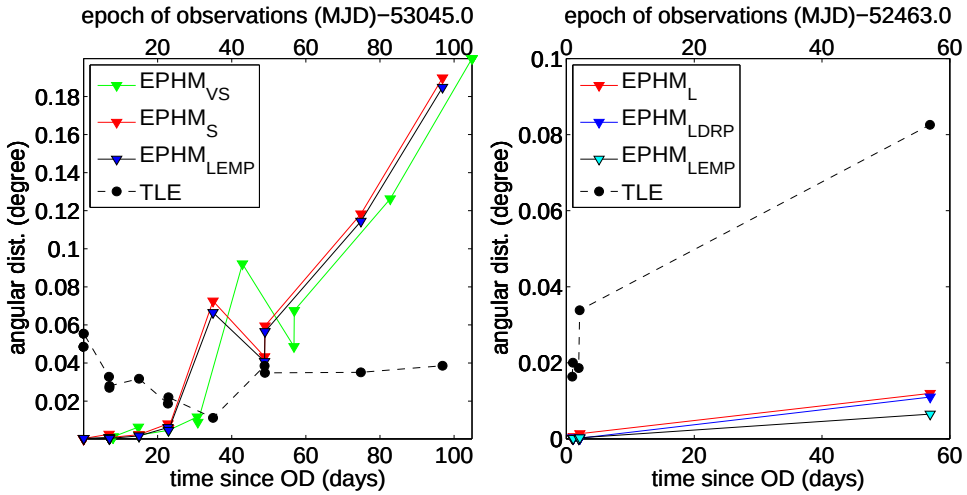

(a) 00016D *(b) 77105A*

(c) 92085D

Figure 7.25: Angular distances between observed positions and predicted ephemerides from TLE data and from orbit determination for (a) the GTO object 00016D and for the objects in Molniya orbits (b) 77105A and (c) 92085D as a function of epoch of the observations for TLE data and the time since orbit determination for the orbits.

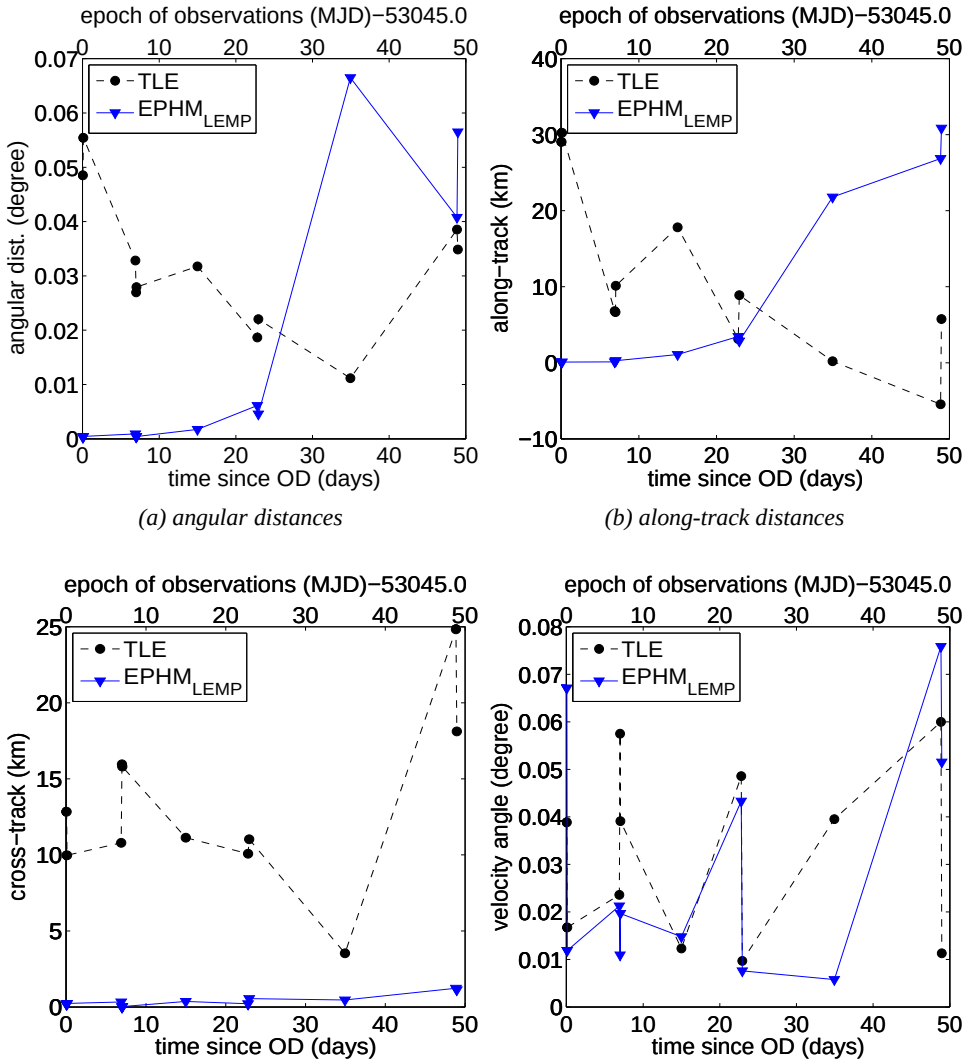

(a) angular distances

(b) along-track distances

(c) cross-track distances

(d) angle between velocity directions

Figure 7.26: Distances between observed positions and predicted ephemerides from TLEs and from orbit determination for the GTO object 00016D as a function of epoch of the observations for TLE data and the time since orbit determination for the orbits.

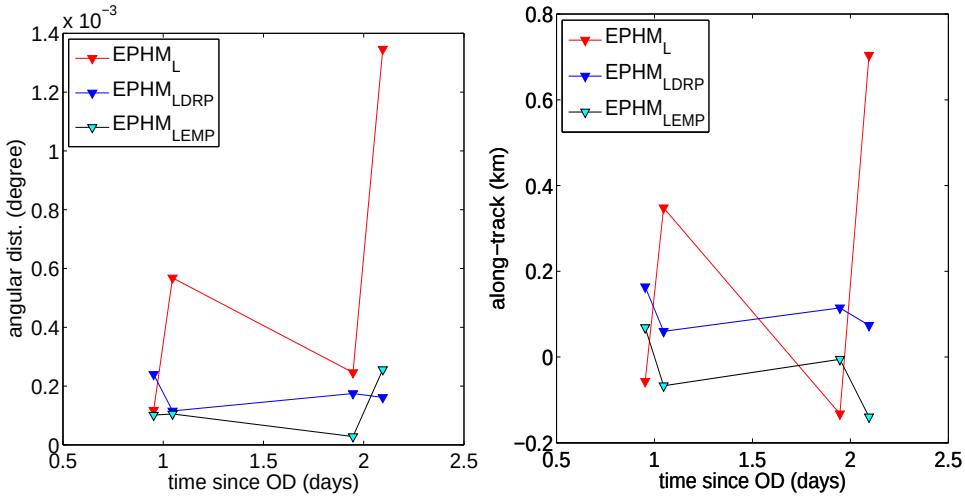

(a) angular distances

(b) along-track distances

(c) cross-track distances

(d) angle between velocity directions

Figure 7.27: Distances between observed positions and predicted ephemerides from orbit determinations for the Molniya object 77105A as a function of time since orbit determination for the orbits.

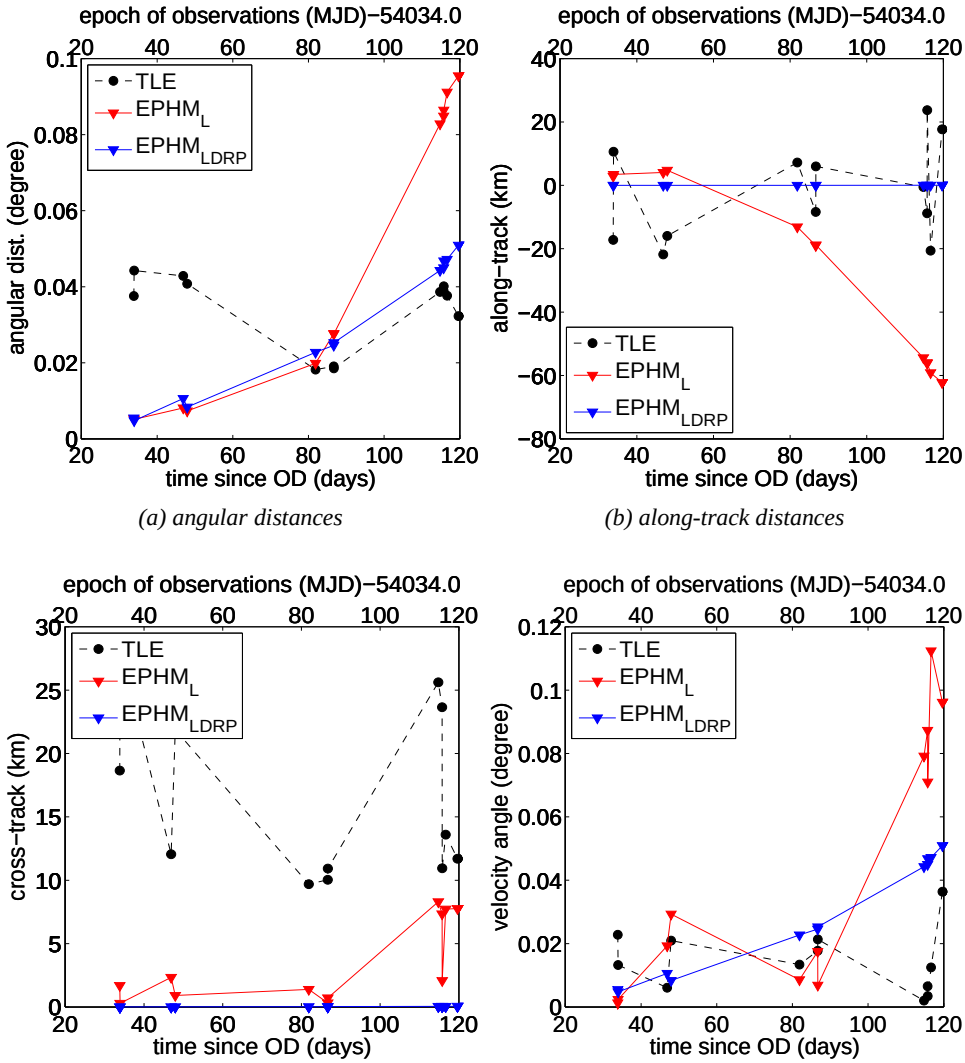

(a) angular distances *(b) along-track distances*

(c) cross-track distances *(d) angle between velocity directions*

Figure 7.28: Distances between observed positions and predicted ephemerides from TLEs and from orbit determination for the Molniya object 92085D as a function of epoch of the observations for TLE data and the time since orbit determination for the orbits.

bits. This was necessary to achieve an rms of the observations of below two arcseconds. Figure 7.23 and 7.24 show the distribution of observations in time and anomaly. Figure 7.25 contains the angular distances between the ephemerides of the predicted orbits and observations as a function of time since orbit determination. Additionally, the angular distances of the TLE data of USSTRATCOM/DISCOS ephemerides and observations are given as a function of the epoch of the observations. For the TLE ephemerides, the TLE sets with the reference epoch closest to each observation epoch were selected. Unfortunately, fewer observations than in the previous cases for GEO objects are available.

The prediction of the orbits $EPHM_{VS}$, $EPHM_S$, and $EPHM_{LEMP}$, lead to comparable angular distance values, as Fig.7.25a shows, although the orbits were determined over different fit intervals, see Tab. 7.7. The observations are spread well over anomaly and time as Fig. 7.23a and 7.24a show. A secular trend is visible in dependence of the prediction time. After 23 days the angular distances of the predicted orbits are larger than the ones of the different TLE sets. The estimation of empirical parameters in orbit $EPHM_{LEMP}$ leads to slightly smaller angular distances although the empirical parameters cannot be included in orbit prediction. Figure 7.26 provides more insight. The distances of ephemerides of orbit $EPHM_{LEMP}$ and observations are shown together with the TLE ephemerides distances decomposed in angular distance, along-track, cross-track distance and the angle between the computed and observed tangent moving directions. The angular distances between ephemerides and observations of orbit $EPHM_{LEMP}$ are very small, below 0.005 degrees within a prediction interval up to 25 days. The distances show a secular trend in along-track direction and only a small trend in the cross-track direction. A physical property, like the AMR, of the object may have changed after 25 days. Unfortunately no AMR value could be estimated. The orbit improvement process did not converge with the AMR value as additional parameter. The distances between the ephemerides of TLE data and the observations show large variations and the distances are in average one order of magnitude larger than the distances of the ephemerides based on the orbit determination for a prediction interval of less than 20 days.

Figure 7.25b shows that for object 77105A the distances between the predicted ephemerides of all orbit determinations, $EPHM_L$, $EPHM_{LDRP}$ and $EPHM_{LEMP}$, and the observations are significantly smaller than those based on the TLE ephemerides and observations. All orbits except the TLE orbits have been determined with the same observations over the identical fit interval. The orbit determination $EPHM_{LEMP}$, in which empirical parameters as well as the AMR value were estimated, shows the smallest distances. The largest distances occur for ephemerides to orbit $EPHM_L$, in which no parameters except the orbital elements were estimated. Unfortunately, there is a gap in the observations, between two and 57 days. The distances between ephemerides and observations for a prediction interval of two days are provided Fig. 7.27. The distances are larger for the orbit $EPHM_L$ than for orbits $EPHM_{LDRP}$ and $EPHM_{LEMP}$, where an AMR value was estimated.

Three different orbits have been determined for object 92085D: one based on a short fit interval without estimating any additional parameters, $EPHM_S$, and two over an interval of 49 days, $EPHM_{LDRP}$ and $EPHM_L$, with and without estimating an AMR value. No empirical parameters were estimated. The observations are not optimally distributed over the fit interval, neither in time nor in anomaly, as Fig. 7.23c and 7.24c show. Figure 7.25c reveals surprisingly small distances between the $EPHM_S$ ephemerides and observations. The distances are smaller than those resulting from the orbits $EPHM_L$ or $EPHM_{LDRP}$. Figure 7.28 shows the distances between the ephemerides and observations of the two orbits $EPHM_L$ and $EPHM_{LDRP}$, respectively, in angular distances and in topocentric along-track and projected cross-track direction as well as the difference between tangent velocity directions. A strong

Table 7.8: Characterization of orbits for the HAMR objects EGEO07, EGEO45 and E06207B.

	time interval (d)	No. of Obs.	rms (")	AMR m^2kg^{-1}	rms (AMR)	emp. parameters
EGEO07						
$EPHM_S$	2	23	6.88	0.02000	-	-
$EPHM_{SDRP}$	2	23	0.43	1.96079	$1.77 \cdot 10^{-2}$	-
$EPHM_L$	22	34	76.36	0.02000	-	-
$EPHM_{LDRP}$	22	34	0.98	1.97233	$2.86 \cdot 10^{-3}$	-
EGEO45						
$EPHM\_S$	3	47	8.07	0.02000	-	-
$EPHM\_SDRP$	3	47	0.86	3.03290	$3.12 \cdot 10^{-2}$	-
$EPHM\_L$	12	69	53.34	0.02000	-	-
$EPHM\_LDRP$	12	69	0.86	3.01037	$1.93 \cdot 10^{-3}$	-
E06207B						
$EPHM_{MDRP}$	15	7	0.54	32.31662	$7.83 \cdot 10^{-1}$	-
$EPHM_{LDRP}$	19	35	5.39	31.88871	$1.94 \cdot 10^{-1}$	-
$EPHM_{LEMP}$	19	35	0.95	32.08214	$5.89 \cdot 10^{-2}$	x

secular trend is visible in along-track direction for differences between observation and ephemerides of $EPHM_L$, where no AMR value was estimated. The differences are significantly smaller both, in along-track and in cross-track direction for the orbit $EPHM_{LDRP}$, in which an AMR value was estimated. The distances of the observations to the ephemerides based on CelMech orbit determination are smaller than the TLE data ephemerides until a prediction period of 80 days.

7.4.4.3 High Area-to-Mass Ratio (HAMR) Objects

The objects EGEO07, EGEO45 and E06207B of the internal AIUB catalogue were analyzed as examples for objects with a high area-to-mass ratio (HAMR). All objects are in more or less geostationary orbits. EGEO07's orbit has a small eccentricity and an inclination of about 16 degrees. EGEO45 is in an orbit with an eccentricity of 0.11 and an inclination close to 10 degrees, E06207E's orbit has an eccentricity of 0.43 and an inclination of 12 degrees. Those objects are not listed in the USSTRATCOM/DISCOS catalogue, but have been observed by the AIUB since several years.

The fit interval, the rms values and the parameters of those orbits are listed in Tab. 7.8. For all objects high AMR values, larger than $1m^2kg^{-1}$ estimated. Orbits, which have been determined without estimation of an AMR value, show intolerably high rms values.

For object EGEO07 four different orbits have been determined, $EPHM_S$, $EPHM_{SDRP}$, based on a fit interval of 2 days, and $EPHM_L$ and $EPHM_{LDRP}$ based on a fit interval of 22 days. Figure 7.31a shows that the orbits of EGEO07 without estimating the AMR value, $EPHM_S$ and $EPHM_L$, have very high rms values in the orbit determination, 7 and 76 arcseconds, respectively, see Tab. 7.8 and also lead to large angular distances. The orbits, $EPHM_{SDRP}$ and $EPHM_{LDRP}$, for which AMR values were estimated, lead to smaller angular distances, $EPHM_{LDRP}$ generates the smallest distances. The anomaly

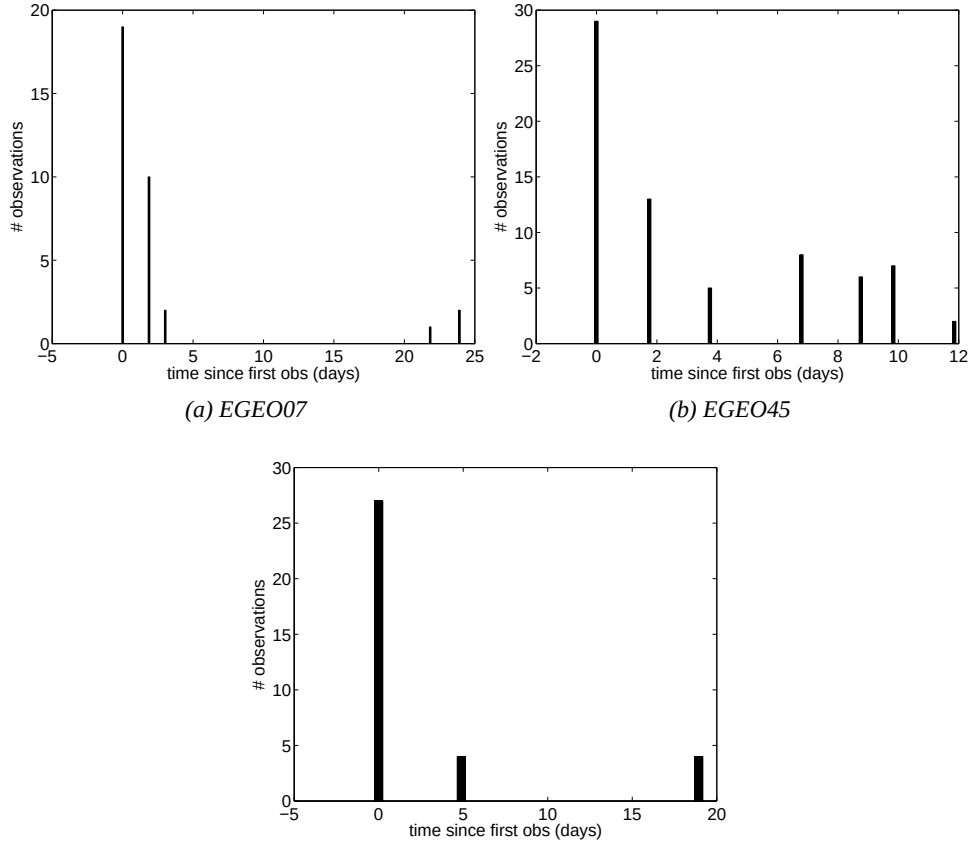

(a) EGEO07

(b) EGEO45

(c) E06207B

Figure 7.29: Time distribution of the observations used for orbit determination for the HAMR objects (a) EGEO07, (b) EGEO45, (c) E06207B.

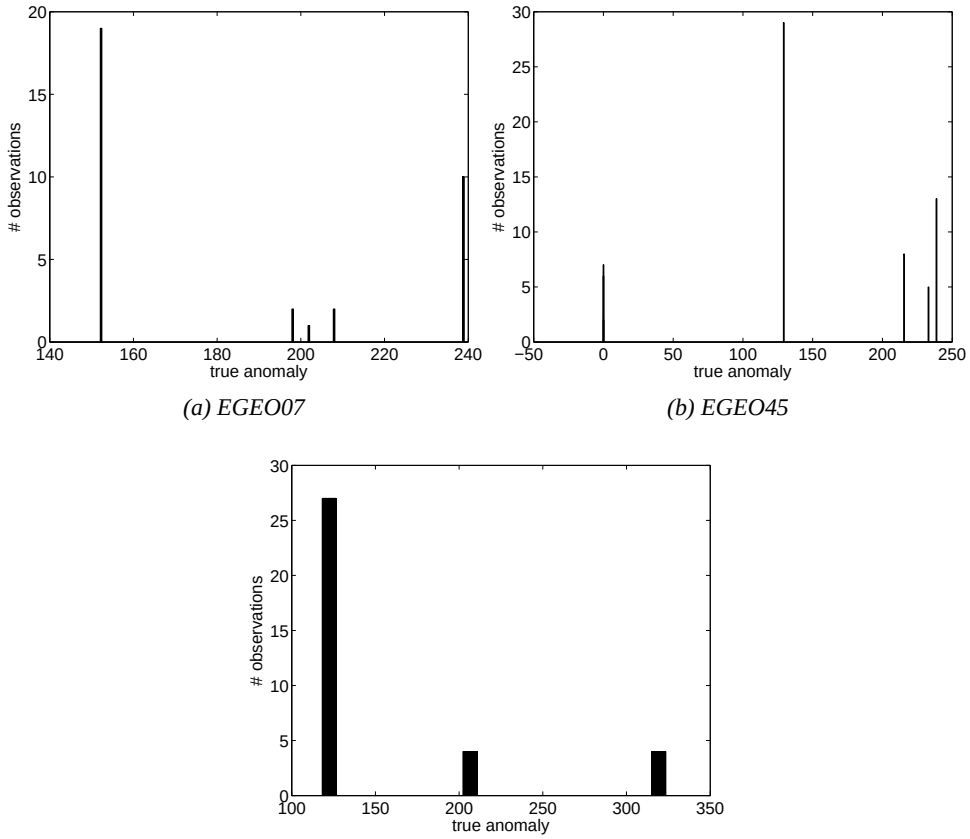

(a) EGEO07

(b) EGEO45

(c) E06207B

Figure 7.30: Anomaly distribution of the observations used for orbit determination for the HAMR objects (a) EGEO07, (b) EGEO45, (c) E06207B.

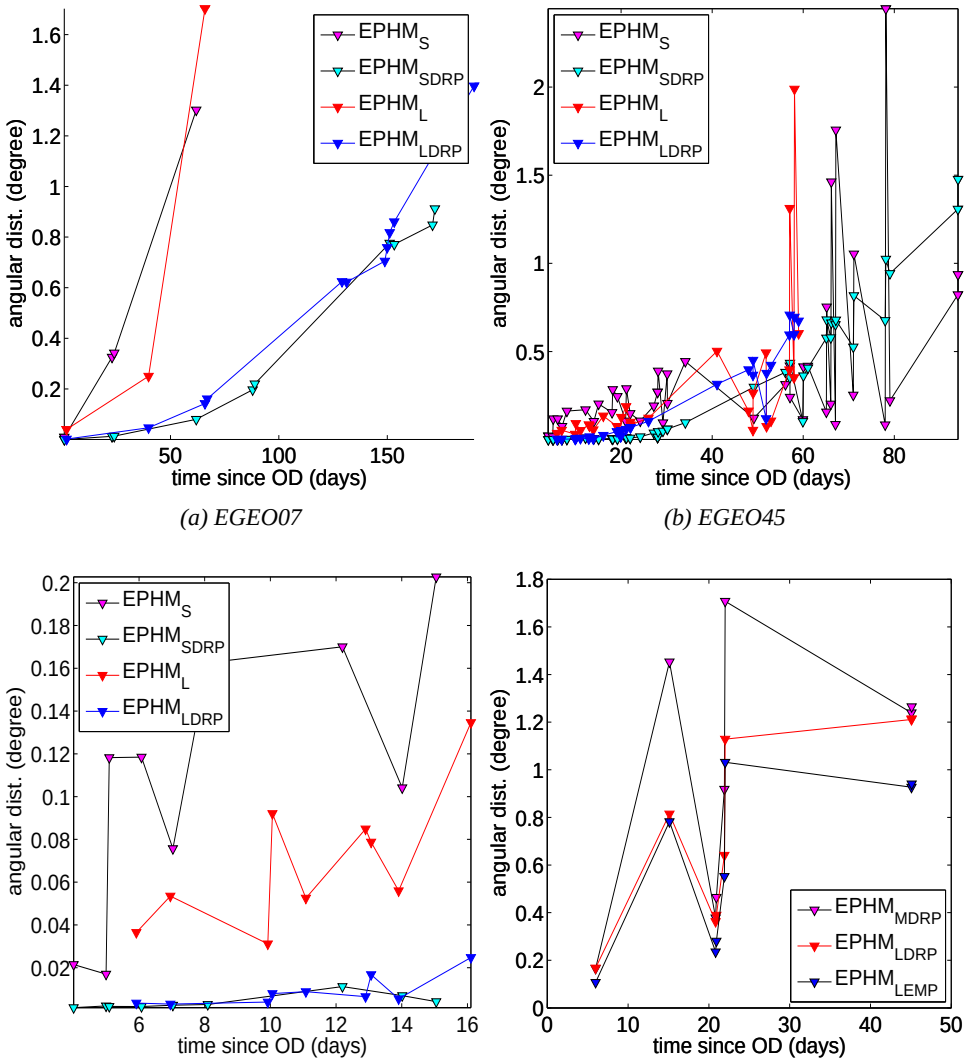

(a) EGEO07 *(b) EGEO45*

(c) EGEO45 (zoom) *(d) E06207B*

Figure 7.31: Angular distances between observed positions and predicted ephemerides from orbit determination for the high area-to-mass ratio objects EGEO07, EGEO45 and E06207B as a function of time since orbit determination.

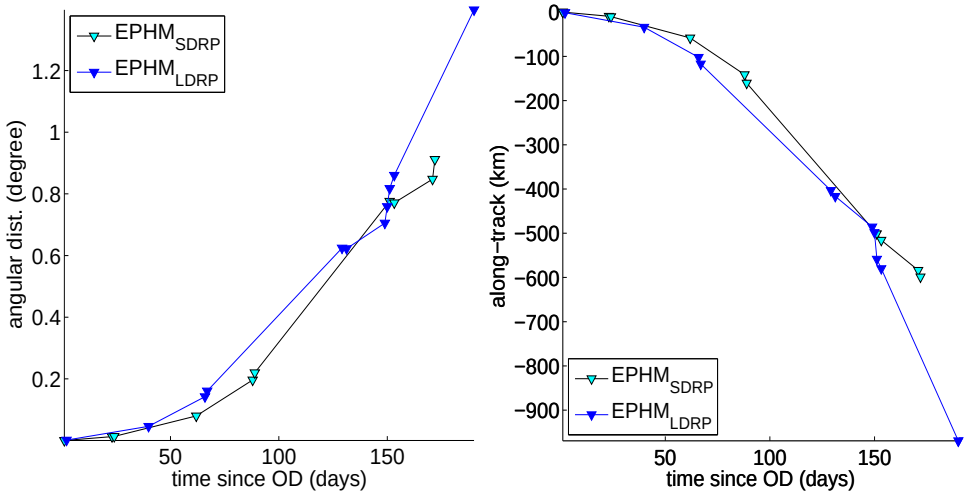

(a) angular distances *(b) along-track distances*

(c) cross-track distances *(d) angle between velocity directions*

Figure 7.32: Distances between the observed and predicted ephemerides of orbit determination for the object EGEO07 as a function of time since orbit determination.

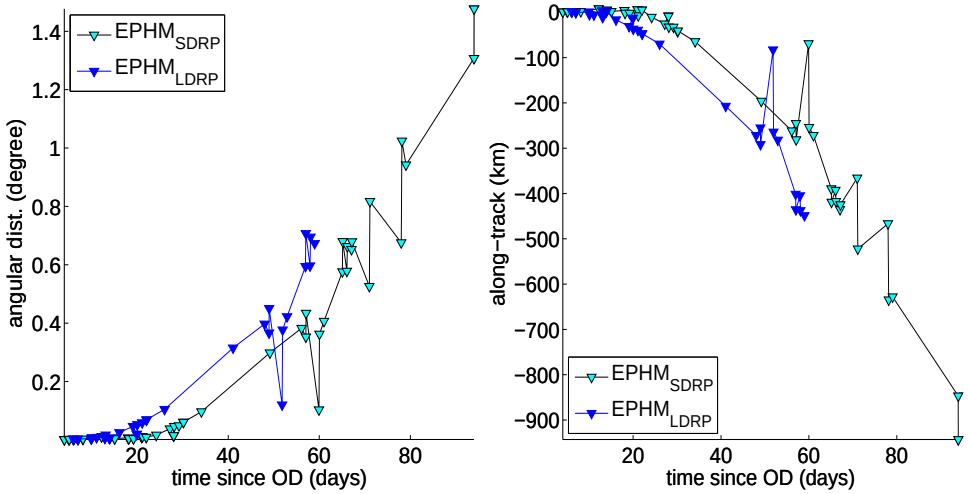

(a) angular distances *(b) along-track distances*

(c) cross-track distances *(d) angle between velocity directions*

Figure 7.33: Distances between observed positions and predicted ephemerides from orbit determination for the object EGEO45 as a function of time since orbit determination.

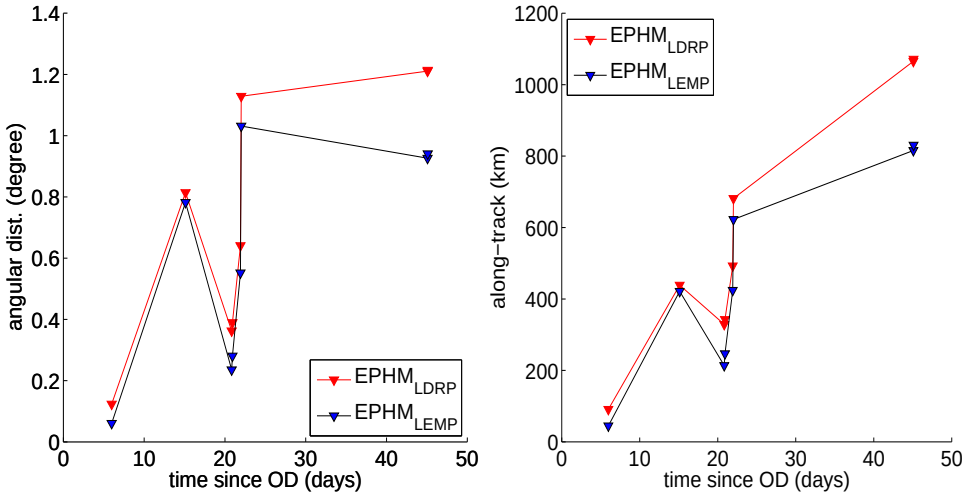

(a) angular distances

(b) along-track distances

(c) cross-track distances

(d) angle between velocity directions

Figure 7.34: Distances between observed positions and calculated ephemerides from orbit determination for the object E06207B as a function of time since orbit determination.

distribution of the observations in the fit interval of orbit determination of both orbits is comparable, as Fig. 7.29a and 7.30a show. The distances between ephemerides of $EPHM_{SDRP}$ and $EPHM_{LDRP}$ and observations are displayed in Fig. 7.32 as angular distances, decomposed in along-track and cross-track direction and angle between the observed and computed apparent tangent velocities. A pronounced secular increase is visible in the along-track component and to a smaller extent, also in the cross-track component. The angle between moving directions shows a trend to larger angles with longer prediction time.

For object EGEO45 four orbits were determined, see Tab. 7.8. The orbits, in which no AMR value was estimated, $EPHM_S$ and $EPHM_L$, have large rms values in the orbit determination, compare Tab. 7.8. They also produce large distances as Fig. 7.31b and, more clearly Fig. 7.31c, shows. A large rms value results for those orbits in the orbit determination, compare Tab. 7.8. The distances of the orbits $EPHM_{SDRP}$ and $EPHM_{LDRP}$, in which an AMR value has been estimated, are shown in Fig. 7.33 in angular distances, decomposed along-track and cross-track direction as well as the difference in the apparent tangent velocity directions. In all directions a secular trend is visible. Large variations occur in particular the cross-track direction for a prediction interval longer than 40 days.

For object E06207B three orbits have been determined, as listed in Tab. 7.8. Unfortunately, only few observations are available for the comparison to the predicted ephemerides. A very large value of around 30 m^2kg^{-1} for the AMR value has been determined for object E06207B. It was not possible to determine an orbit without estimating an AMR value with the default a priori value of 0.02 m^2kg^{-1}. The distances with respect to the observations, of all orbits, $EPHM_{MDRP}$, $EPHM_{LDRP}$ and $EPHM_{LEMP}$, vary over time and their distances are larger than those of the other HAMR objects. This may be due to the disadvantageous distribution of the observations in time and anomaly in the fit interval of the orbit determination, as Fig. 7.29c and 7.30c reveal. Figure 7.34 shows the distances of the ephemerides to the observations of two orbits, determined over long observation intervals: one orbit, $EPHM_{LDRP}$, was determined estimating only the AMR, and the second, $EPHM_{LEMP}$, including empirical parameters in addition to the AMR value. Both orbits produce similar distances and variations over time.

7.4.5 Orbit Determination and Prediction based on Sparse Data

The accuracy of predicted orbits is analyzed as a function of the distribution of the observations in time and anomaly, the total number of observations used in and the resulting rms of orbit determination, and the parametrization. The aspect of using observations from different observation sites was investigated. For the analysis was performed with a so called sparse data setup: All orbits were determined from two observation sets only. A maximum of eight observations are allowed per set. An observation set may consist of more than one tracklet. But the observations within the sets should not be distributed over more than three days. A priori elemets are available. This setup was chosen to simulate the catalogue maintenance with optical space surveillance observations, in which the objects are not always visible, e.g. when in a GEO drift orbit. Additionally weather conditions limit the use of optical sensors.

Orbits were determined for different spacings of two observation sets stemming a) from one observation site only and b) from different sites. In the first case, the observations either stem from ZIMLAT or from ESASDT only. In the second case, not only the observations of ZIMLAT and ESASDT could be combined but also observations of the ISON network, by courtesy of the Keldish Institute of Applied

Table 7.9: Objects used in the analysis.

Object	Epoch (MJD)	*a* (km)	*e*	*i* (deg)	AMR (m^2kg^{-1})	Mag
E03174A	55208.0	41900	0.001	10.1	0.01	14.6
E06321D	55275.9	41400	0.035	7.00	2.29	15.3
E06327E	54470.1	40000	0.067	12.31	0.20	17.2
E08241A	55213.0	41600	0.041	13.26	1.24	16.1

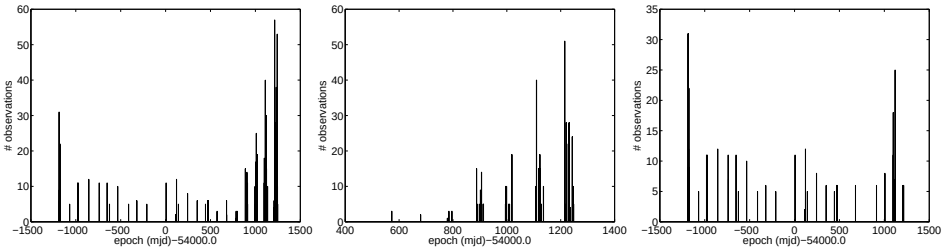

(a) *(b)* *(c)*

Figure 7.35: Observation distribution of object E03174A (a) all observations, (b) ZIMLAT, (c) ESASDT.

Mathematics. The ISON observations all stem from observatories located in the area of the former Sowjet Union. This is advantageous, because this guarantees a good East-West separation of the observing sites. When observations from different sites are used in orbit determination, the distribution is either that the first set of observations stems from one site and the second from another, or that there are observations from different sites at similar epochs used within the first and/or the last set of observations or a mixture of those options. In the figures the label *ALL* is applied, when observations of ZIMLAT (labeled *ZIM*), the ESASDT and of the ISON network are combined; the label *SDT-ZIM* is applied, if only the observations of ZIMLAT and the ESASDT are used.

The predicted ephemerides of the orbit determinations are compared to further observations, which were not used in the orbit determination. These additional observations stem from ZIMLAT, ZimSMART and ESASDT. In order to ensure that all observations actually belong to the same object an orbit was fit through all observations was performed and the residuals were checked for outliers.

7.4.5.1 Selected Objects, Data Density and Spacing

Four representative objects from the internal AIUB catalogue were chosen. Those objects are not listed in the USSTRATCOM/DISCOS catalogue and were followed by the AIUB over longer time periods. Those objects are space debris, no maneuvers were detected in the data. No information is available, concerning the shape, material or attitude of the objects. It can be concluded from their apparent magnitude that they are most likely fragmentation pieces. They represent typical objects found in GEO surveys. Some of their known properties are listed in Tab. 7.9.

Figure 7.36 through 7.38 show the temporal distribution of the available optical measurements. The observations are binned for each night. Additional observations stem from ISON.

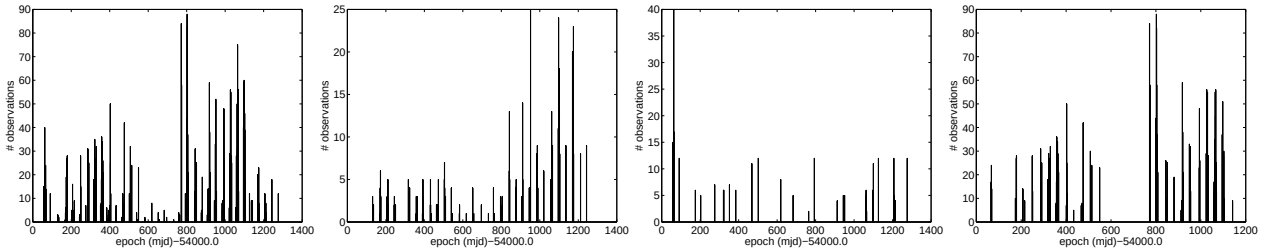

(a) *(b)* *(c)* *(d)*

Figure 7.36: Observation distribution of object E06321D (a) all observations, (b) ZIMLAT, (c) ESASDT, (d) ISON network.

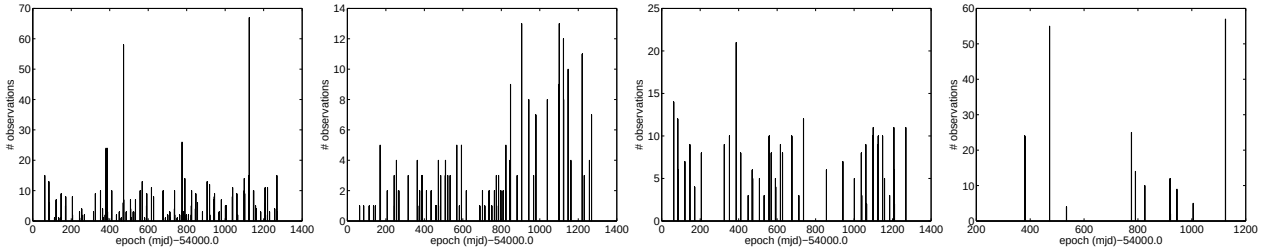

(a) *(b)* *(c)* *(d)*

Figure 7.37: Observation distribution of object E06327E (a) all observations, (b) ZIMLAT, (c) ESASDT, (d) ISON network.

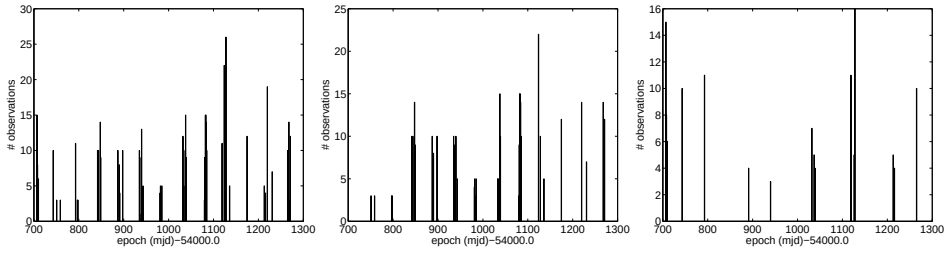

(a) *(b)* *(c)*

Figure 7.38: Observation distribution of object E08241A, (a) all observations, (b) ZIMLAT, (c) ESASDT.

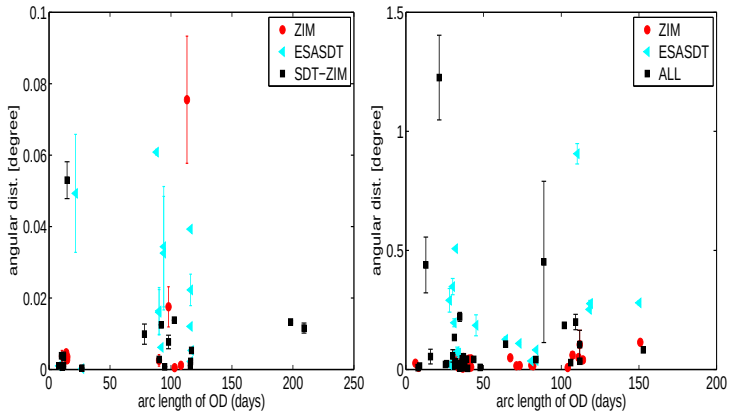

(a) E03174A

(b) E06321D

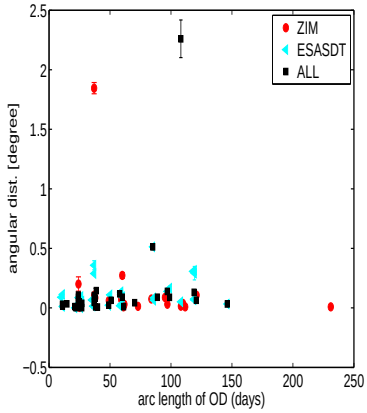

(c) E06327E

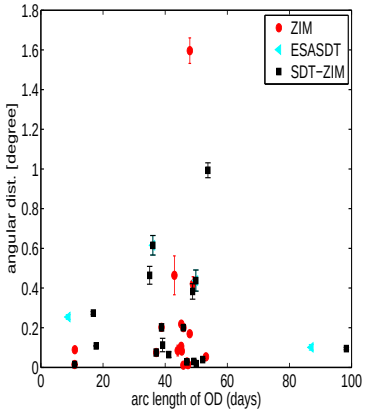

(d) E08241A

Figure 7.39: Mean value and standard deviation of angular distances within the first 50 days after orbit determination between predicted and observed positions as a function of the time interval between the first and last observations used for orbit determination.

7.4.5.2 Distances Between Ephemerides and Observations from Single and Combined Sites

The distances between the observations and the ephemerides of the predicted orbits of the four objects for a prediction interval of 50 days after the last observation used for orbit determination were determined. The distances were averaged and a mean value and standard deviation was calculated. Between six and 50 single distances between ephemerides and observations were averaged for the different orbits.

In Fig. 7.39 the means values and standard deviations of the distances between predicted and observed astrometric position are displayed in angular distance as a function of the time interval between the first and the last observation, which were used in orbit determination.

The distances are in general – even though only sparse observational data was used – all very small. The vast majority of the determined orbits produce distances smaller than 0.6 degree, as Fig. 7.39 shows.

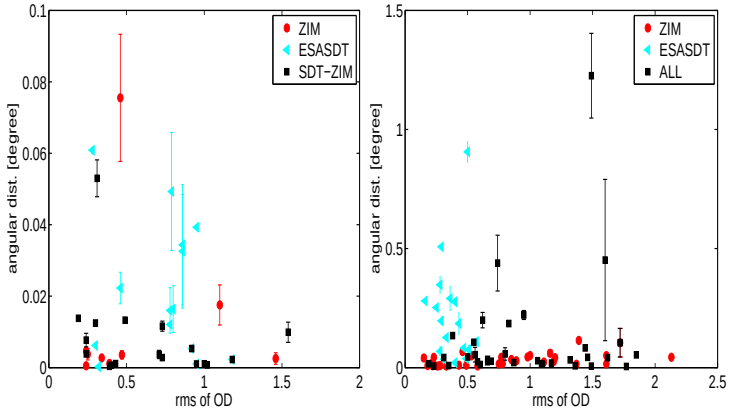

(a) E03174A *(b) E06321D*

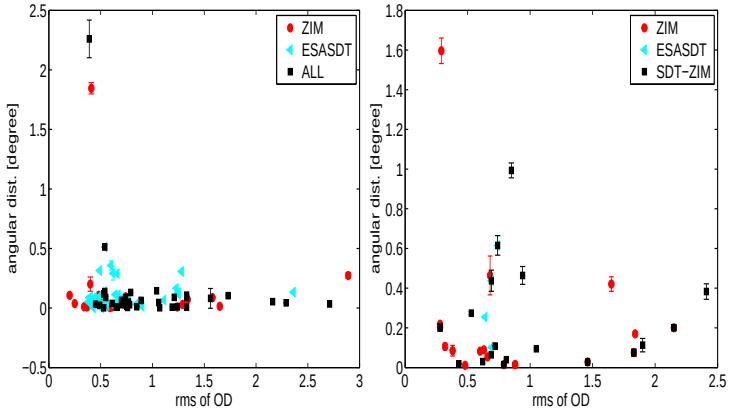

(c) E06327E *(d) E08241A*

Figure 7.40: Averaged angular distances of predicted ephemerides and observations as a function of the root mean square error of orbit determination.

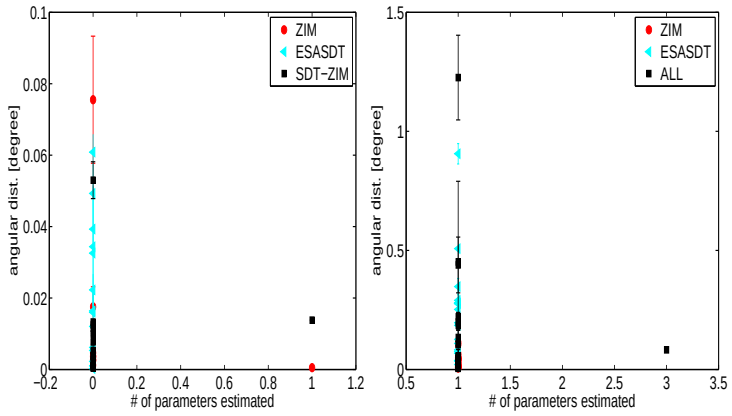

(a) E03174A

(b) E06321D

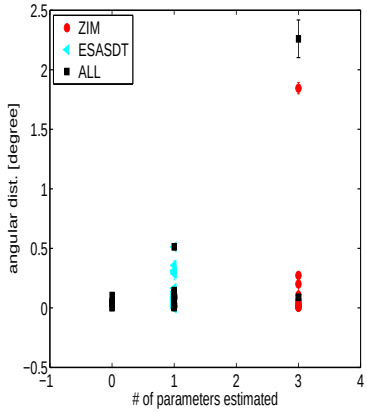

(c) E06327E

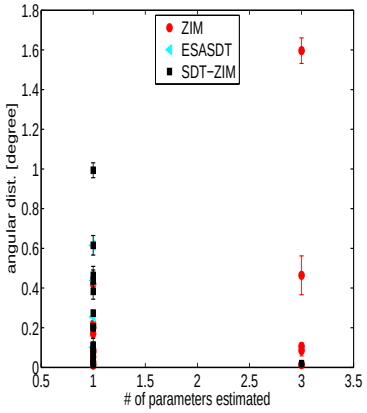

(d) E08241A

Figure 7.41: Averaged angular distances of predicted ephemerides and observations as a function of the number of additional solve-for parameters, that were estimated: x=1 DRP, x=2 DRP and R-parameter, x=3 DRP, R-parameter, and W-parameter (RSW coordinate system).

Each object, except object E03174A, also shows some distances, which are comparably large. These larger distances also tend to show larger standard deviations. In addition, the values of the distances seems to be, at least in this setup, quite independent of the length of the time interval between the first and the second observations set. There is no significant difference in using observations only from one observation site for orbit determination or using observations from different sites in this specific setup, as Fig. 7.39 shows. In Fig. 7.40, the angular distance is shown as a function rms value of the orbit determinations. No significant trend is visible, all orbits, which were used, have a small root mean square of below three arcseconds.

Figure 7.41 shows the angular distances as a function of the number of estimated parameters in addition to the osculating elements. Only the AMR value is estimated, when one parameter is listed. In addition to the AMR, the empirical parameter in R-direction, or in R- and W-direction together are estimated, when two and three parameters, respectively, are listed. No clear trend is visible.

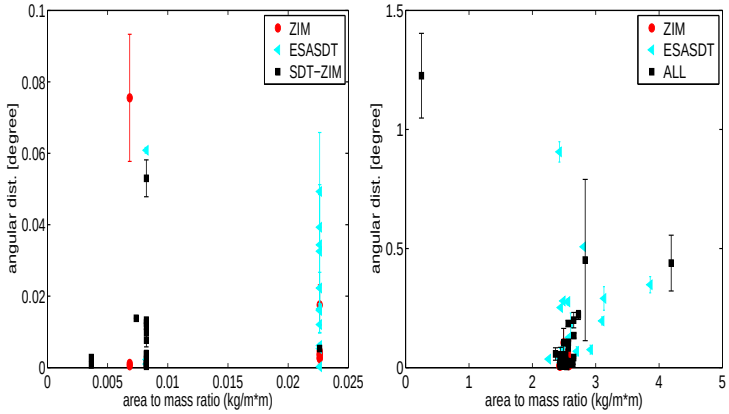

(a) E03174A *(b) E06321D*

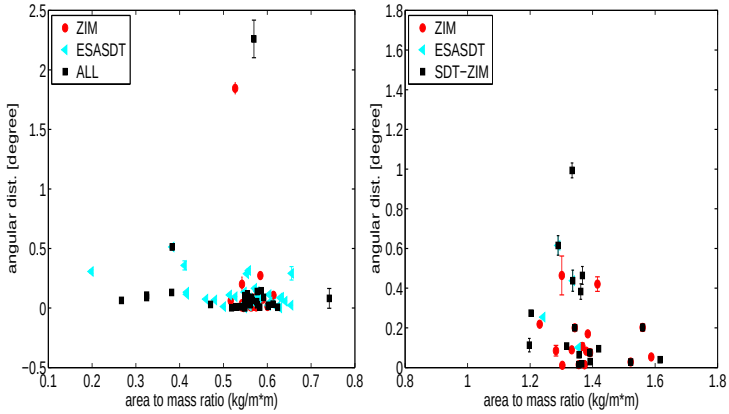

(c) E06327E *(d) E08241A*

Figure 7.42: Averaged angular distances of predicted ephemerides and observations as a function of the estimated AMR value.

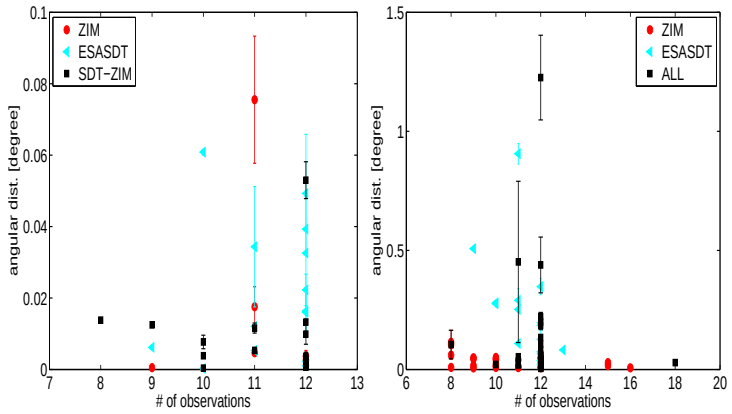

(a) E03174A

(b) E06321D

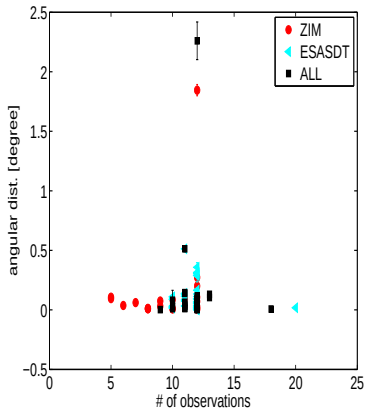

(c) E06327E

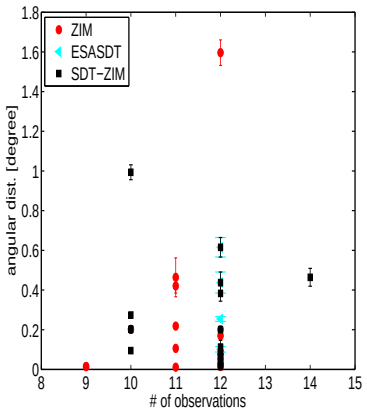

(d) E08241A

Figure 7.43: Angular distances as a function of the number of observations used for orbit determination.

In Fig. 7.42, the distances are displayed as a function of the AMR value of the orbit determination. The AMR value of the different objects varies over different ranges. In some orbit determinations, values were determined, which are far from the average AMR value for that specific object. It cannot be concluded that these values lead to larger distances in the predicted orbits.

In Fig. 7.43, the angular distances are shown as a function of the number of single observations used for orbit determination. No strong correlation seems to exist between the actual number of observations used and the angular distances. In Fig. 7.44, the angular distances are shown as a function of the actual time interval covered by observations *within* the two sets, which are used in the beginning and the end of the observation fit interval, without the time gap in between the two sets. The angular distance heavily depends on the time interval covered by the observation used in orbit determination. The angular distances are significantly smaller, for larger time intervals covered by the observations within the sets. Thus the angular distances are larger, when the observations within the sets are very densely spaced. Consequently, Fig. 7.45 shows clearly that there is no strong correlation between the actual number of observations used and the time interval covered within the sets. The timely density of observations,

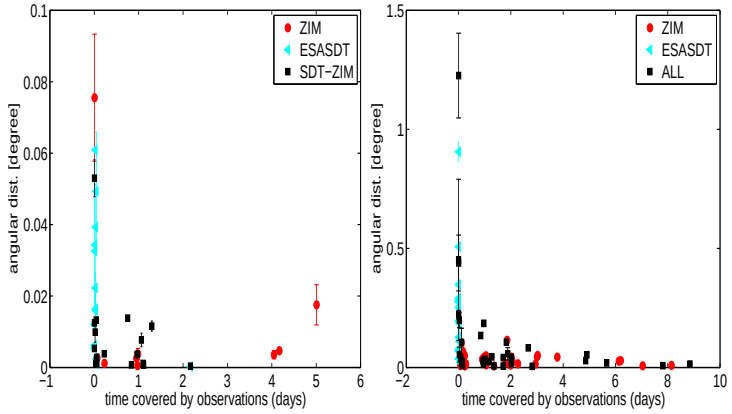

(a) E03174A

(b) E06321D

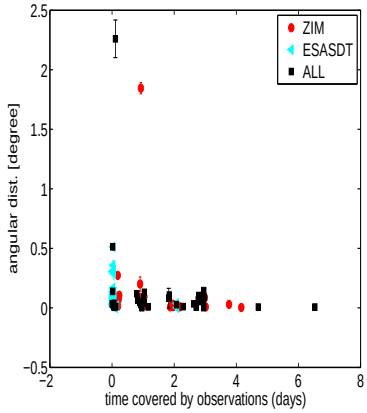

(c) E06327E

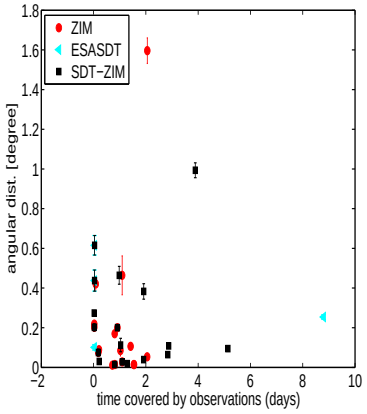

(d) E08241A

Figure 7.44: Angular distances as a function of the time interval covered within the observation sets used for orbit determination.

which are available, is highly dependent on the observation strategy of the sensors.

To find a measure for the true anomaly distribution, an anomaly distribution measure f_{ano} was defined: It would be ideal to distribute all n observations equally spaced with an angle of $2\pi/n$ between each observation. The deviation from this ideal distribution is determined and normalized with the number of observations. The smaller f_{ano}, the better distributed are the observations in anomaly.

$$f_{\text{ano}} = \frac{1}{n}\sqrt{\sum_{i=1}^{n-1}\left(\frac{2\pi}{n} - (a_{i+1} - a_i)\right)^2 + \left(\frac{2\pi}{n} - (a_1 + 2\pi - a_n)\right)^2}, \tag{7.49}$$

where as n is the number of observations and a_i with $i = 1, .., n$ are the anomalies of the single observations, in ascending anomaly order. The angular distances as a function of f_{ano} are displayed in Fig. 7.46. There is no clear correlation between the f_{ano} and the distances, as it is expected for objects with small eccentricities. Object, E06327E, with the highest eccentricity of e=0.06, has the strongest correlation with f_{ano}.

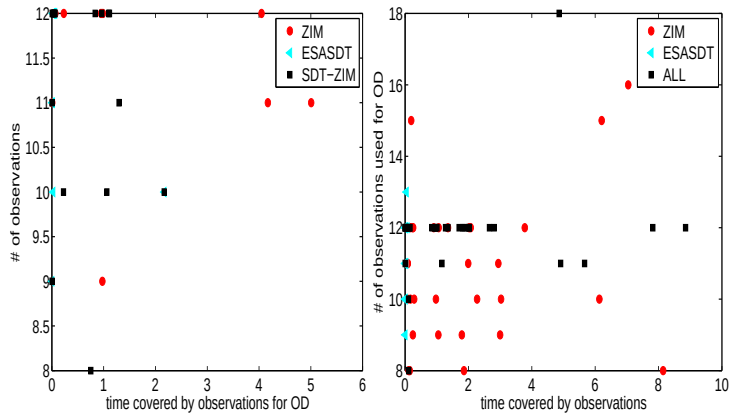

(a) E03174A

(b) E06321D

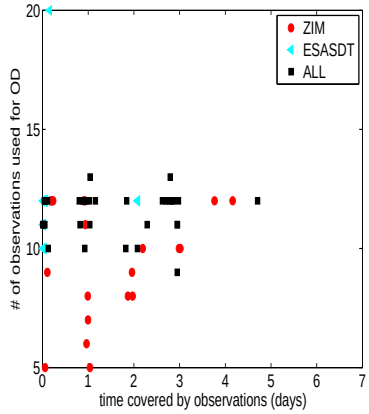

(c) E06327E

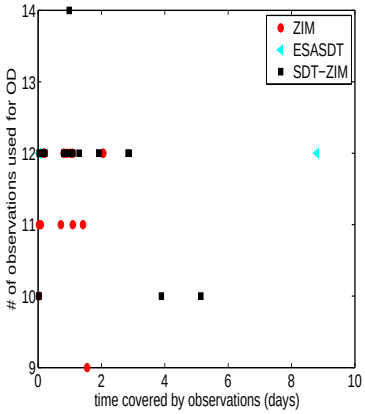

(d) E08241A

Figure 7.45: Time interval covered within the observation sets as a function of the number of observations used for orbit determination.

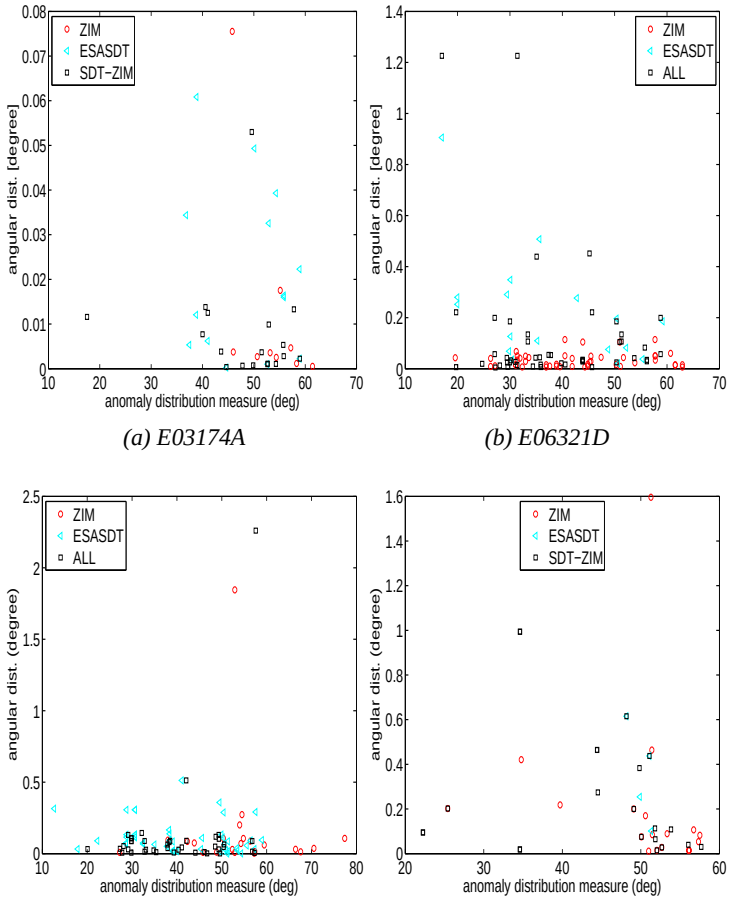

(a) E03174A *(b) E06321D*

(c) E06327E *(d) E08241A*

Figure 7.46: Angular distances as a function of anomaly distribution factor.

Table 7.10: Investigated HAMR objects.

Object	Epoch (MJD)	a (km)	e	i (deg)	AMR (m^2kg^{-1})	Mag
E08241A	55213.0	41600	0.041	13.26	1.24	16.1
E06321D	55275.9	41400	0.035	7.00	2.29	15.3
E07194A	54877.0	40900	0.005	7.31	3.37	16.8
E07308B	54416.0	35600	0.264	7.63	8.83	15.8
E06293A	54951.0	40200	0.245	11.06	15.41	16.8

Neither the total number of observations, not the number of parameters of the orbit determination nor the time gap between the observation sets, nor using observations from different sites seems to be crucial for the quality of the determined orbit. The time, which is actually covered by the observations within the sets, has the determining influence on the angular distances of the predicted orbits to further observations in the sparse data setup. The investigation of the data displayed in Fig. 7.45 showed that a coverage of at least 1.2 hours for both sets together seems to be necessary, in order to gain an orbit which allows to safely re-detect the investigated objects in more than 90 percent of all cases with a field of view of one square degree.

7.4.6 Properties of HAMR Objects Investigated in Sparse Data Setup

The dynamical properties of HAMR objects were studied in the sparse data setup established in Section 7.4.5. Orbits are determined with two observation sets only. The sets consist of four to eight observations each. The experience gained in Section 7.4.5, is used here: The observations are required to span at least a time interval of 1.2 hours within the sets and need to be well spread over the anomaly for the objects in orbits with a high eccentricity. The total fit interval for orbit determination ranges between 10 and 120 days. As shown in the previous section the quality of the orbits does not seem to be dependent on these ranges.

The orbits were first determined with observations from one observation site only, then with observations from different sites in the setup mentioned above. The observations used in this investigation stem from the ESASDT, ZIMLAT, and from several telescopes of the ISON network.

Five objects were selected for a detailed investigation. All objects were discovered and first detected by the AIUB and are not listed in the USSTRATCOM catalogue. All objects are faint debris objects. They were tracked successfully over several years, and no maneuvers were detected. A set of osculating orbital elements and an average value for the apparent magnitudes are listed in Tab. 7.10.

7.4.6.1 Evolution of Orbital Elements

The evolution of the orbital elements over time is inspected in a first step. Figure 7.47 shows the development of the inclination and its errors in inclination, of the five objects. The error bars are too small,

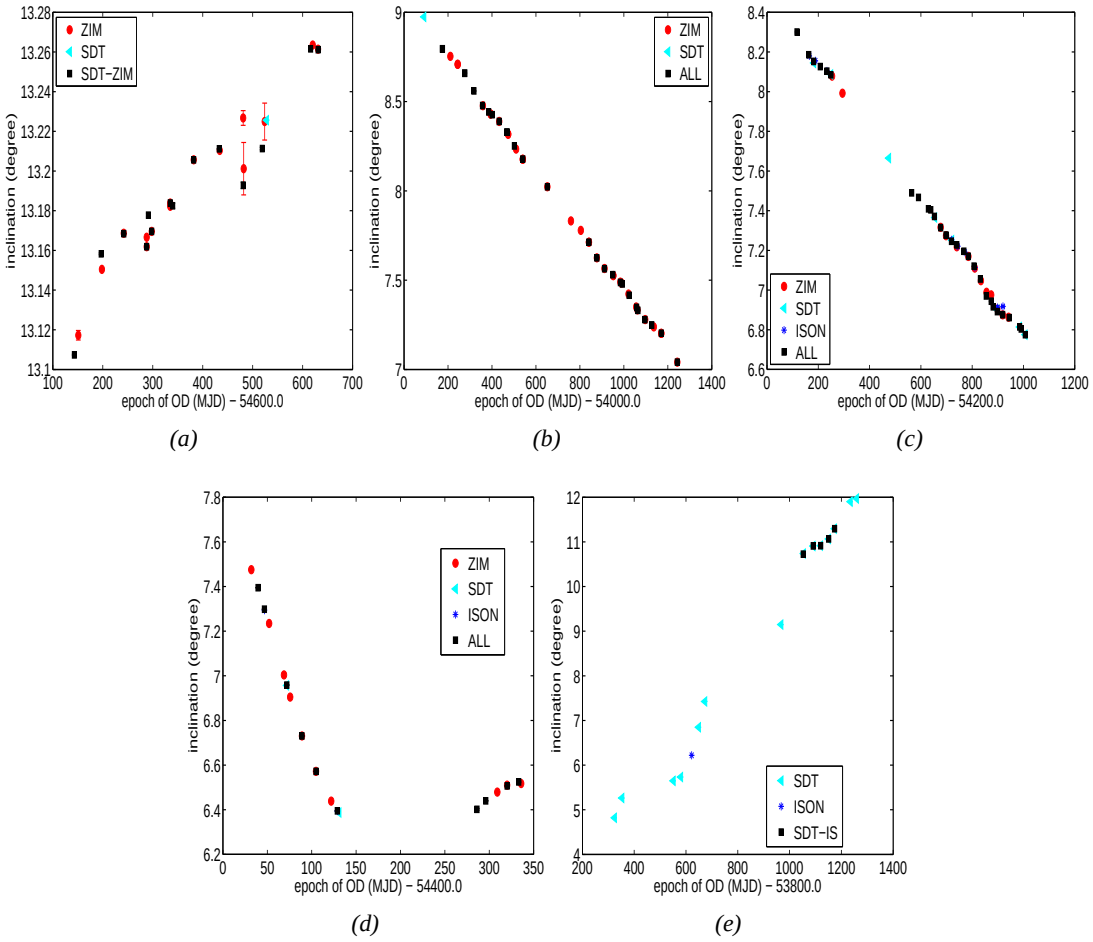

Figure 7.47: Inclination as a function of time for orbits of the object (a)E08241A, (b) E06321D, (c) E07194A, (d) E07308B, (e) E06293A.

to be visible in the plot in most cases. The inclination values of the different orbits are closely aligned to each other and mark a consistent evolution, only in the case of object E08241A in Fig. 7.47 a wider spread in the inclination values can be observed. The orbits determined with observations from the different observation sites produce almost identical results. For object E07308B and E06293A, which have the highest AMR values, the inclination seems not to follow a steady increase over time, but some smaller periodic substructure seems to be superimposed. These may very well be the perturbations with a period of one nodal year, which are well known for objects with high AMR, see e.g., J.-C. Liu [56], T. Schildknecht [82].

Figure 7.48 shows the evolution of the eccentricity values and its errors estimated in orbit determination for the different objects. Periodic variations can be observed for all objects. The different orbits with observations from one site only or from different sites result in the same eccentricities.

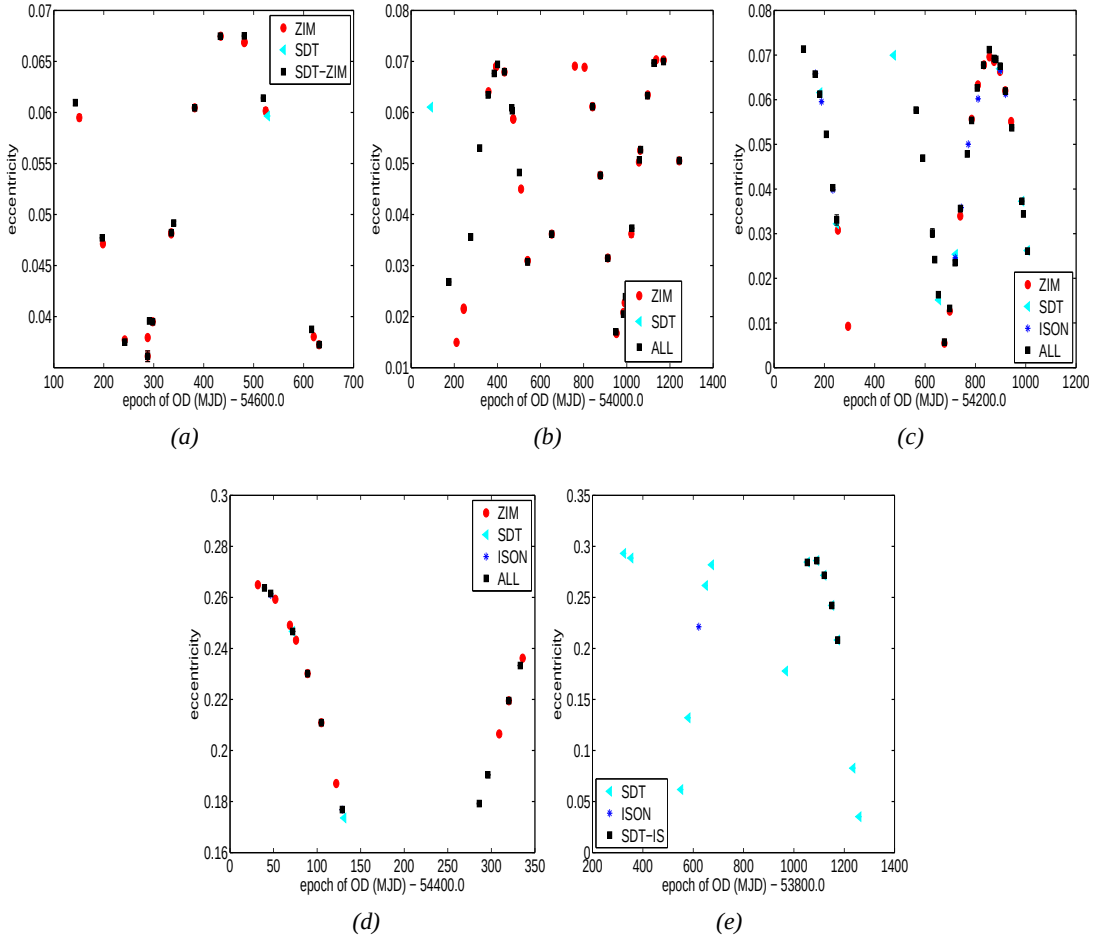

Figure 7.48: Eccentricity as a function of time for orbits of the object (a) E08241A, (b) E06321D, (c) E07194A, (d) E07308B, (e) E06293A.

7.4.6.2 Evolution of Area-to-Mass Ratio Value

Figure 7.49 shows the AMR values as a function of time for the objects listed in Tab. 7.10. In all cases, the values for the AMR do not show clear and obvious common trends, see Fig. 7.47 and 7.48.

For object E08241A, the AMR values vary around a mean value of $1.4\,\mathrm{m^2kg^{-1}}$ with no obvious trend or periodic signal, see Fig. 7.49a.

For object E06321D (see Fig. 7.49b), the AMR value seems to vary periodically with a period of about one year around a value of $2.5\,\mathrm{m^2kg^{-1}}$, but also values of $2.35\,\mathrm{m^2kg^{-1}}$ and $2.65\,\mathrm{m^2kg^{-1}}$ occur. Similar results were obtained by R. Musci [66], for the same object, in different orbit determination setups. The AMR value of object E07194A (see Fig. 7.49c) varies around $3.5\,\mathrm{m^2kg^{-1}}$, but in the orbits determined with combined observations from all the sites, so-called *outliers* of $4.5\,\mathrm{m^2kg^{-1}}$ and $2.3\,\mathrm{m^2kg^{-1}}$ occur as well. These have, however large error values.

Object E07308B (see Fig. 7.49d) seems to generally increase its AMR value over time from a value of $8.5\,\mathrm{m^2kg^{-1}}$ up to $9.0\,\mathrm{m^2kg^{-1}}$. But single orbits also show AMR values of i.e. $10\,\mathrm{m^2kg^{-1}}$.

Figure 7.49e shows that object E06293A, which is the object with the largest AMR value regarded here, has significant data gaps. A general trend of the AMR value in time, increasing from $15.5\,\mathrm{m^2kg^{-1}}$ to $16.5\,\mathrm{m^2kg^{-1}}$ cannot be excluded. But one orbit determined with ESASDT data also shows a value of $18.2\,\mathrm{m^2kg^{-1}}$, with a small formal error.

No general correlation between the AMR value itself and the variations of the AMR value could be determined, no general trend is visible. A study on the variation of AMR values was conducted by T. Schildknecht [76]. The variations of the AMR values of 47 HAMR objects were investigated and compared to the AMR variations of orbits of 40 low AMR (LAMR) value objects. No normalized or sparse data setup orbit determination setup was chosen. The AMR values in that analysis were determined in the standard orbit determination procedure at the AIUB, with fit arcs as long as possible for a successful, that is defined as leading to a small rms error, orbit determination. The results are illustrated in Fig. 7.50. No general trend in the AMR variations could be determined for either HAMR or LAMR objects. The relative variations of the AMR values of the LAMR objects were larger, than the AMR variations of the HAMR values. The AMR variations of the LAMR objects were of the order of several 100 percent.

All orbits were predicted and compared to additional observations of the same object, which were not used for orbit determination. The additional observations were all checked via dense data orbit determination, to ensure that they belong to the same object. Figure 7.51 shows the angular distances between the predicted ephemeris and observations. The values are averaged over all distances 50 days after orbit determination and their standard deviations serve as error bars.

Figure 7.51a shows, that for object E08241A, one orbit produces the largest distances of one degree. This orbit does not show up prominently in the orbital parameter plots (see Fig. 7.48a and 7.47a) or AMR value plots (see Fig. 7.49a). The orbit with ZIMLAT data, which produced the *outlier* AMR value of $0.82\mathrm{m^2kg^{-1}}$, does not show up prominently in the distance plot (Fig. 7.51a).

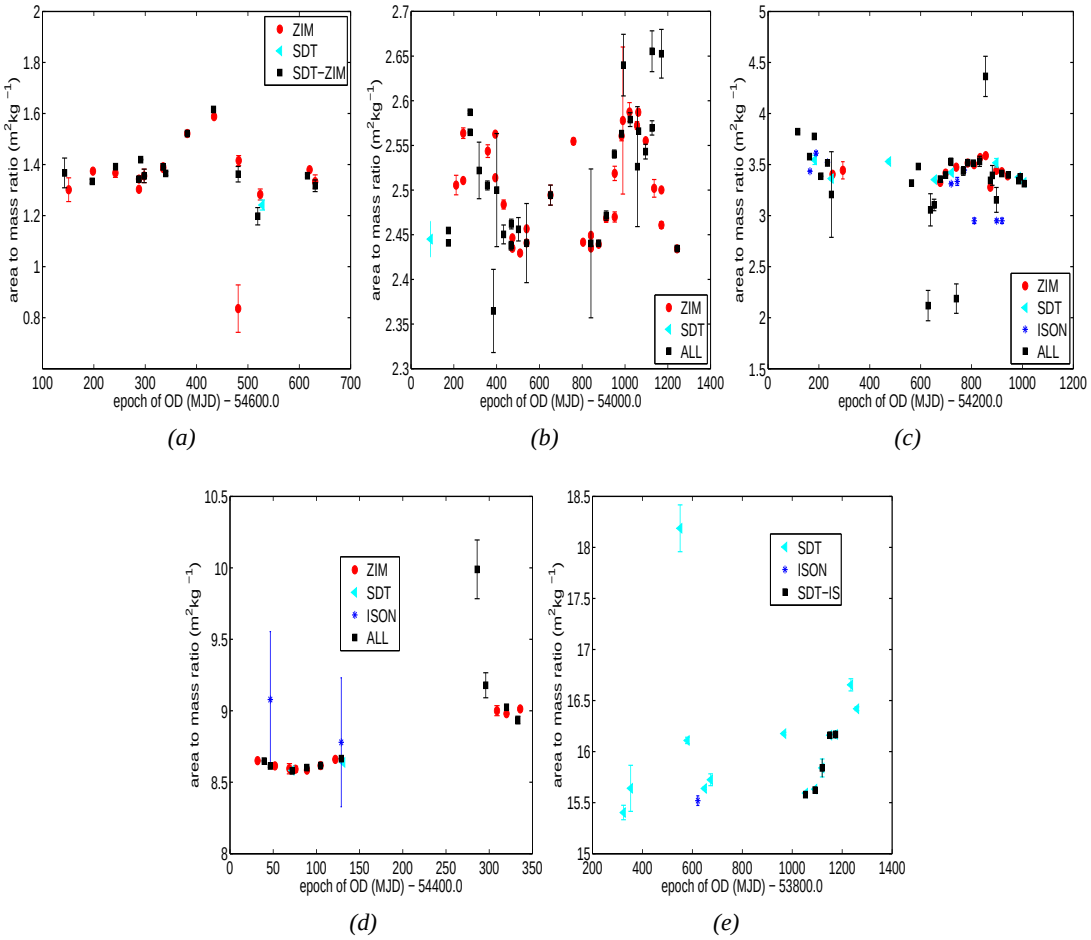

Figure 7.49: AMR as a function of time for orbits of the object (a) E08241A, (b) E06321D, (c) E07194A, (d) E07308B, (e) E06293A.

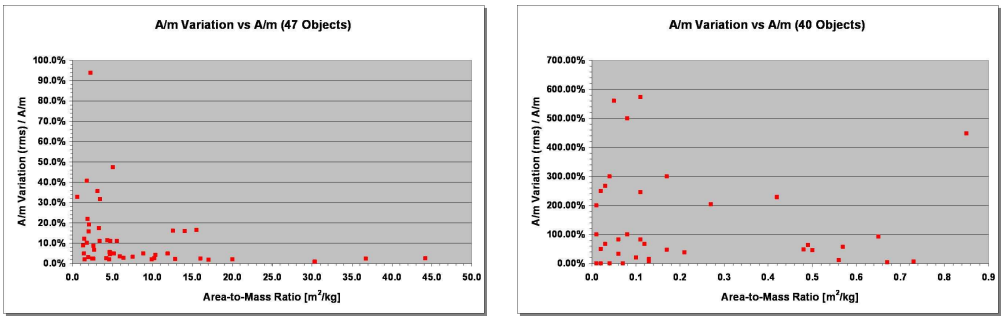

Figure 7.50: Relative variation of AMR value as a function of the absolute AMR value of (a) 47 HAMR and (b) LAMR objects [76].

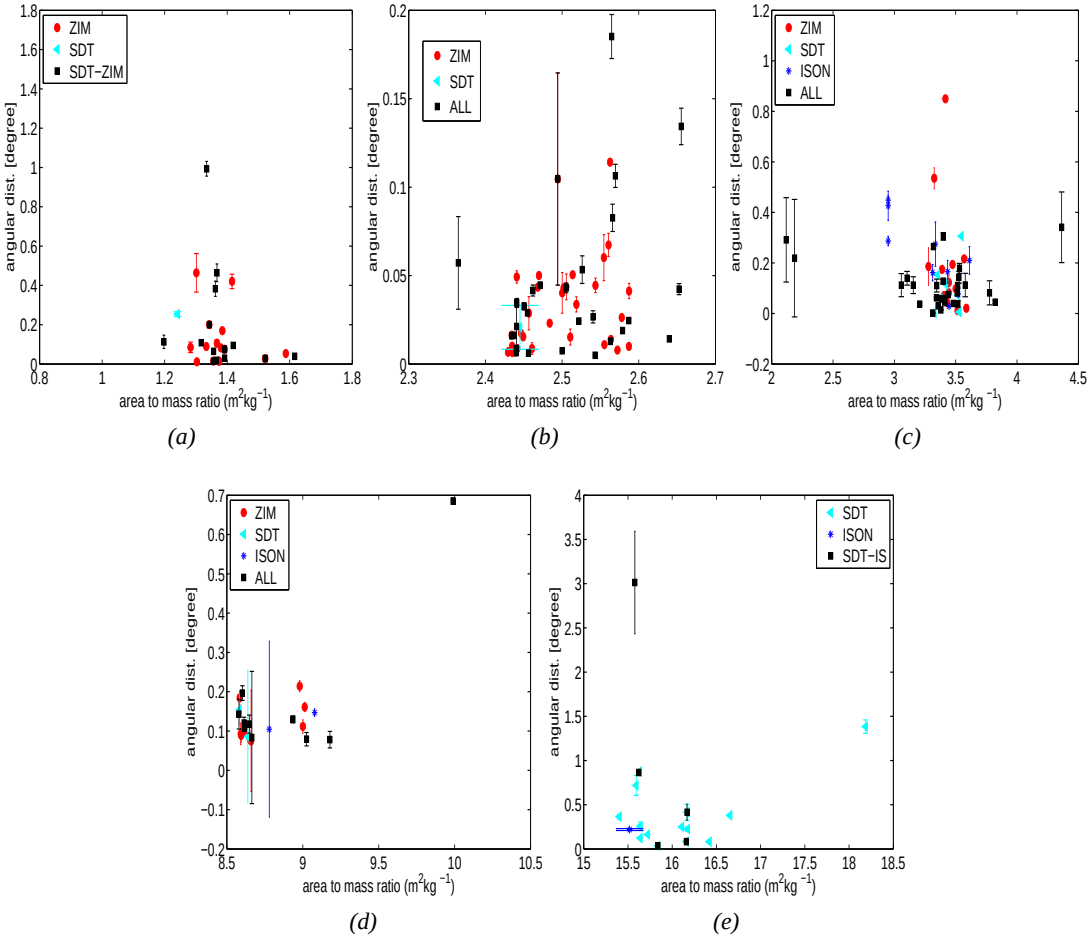

Figure 7.51: Angular distances of predicted orbits on the celestial sphere as a function of AMR for orbits of the object (a) E08241A, (b) E06321D, (c) E07194A, (d) E07308B, (e) E06293A.

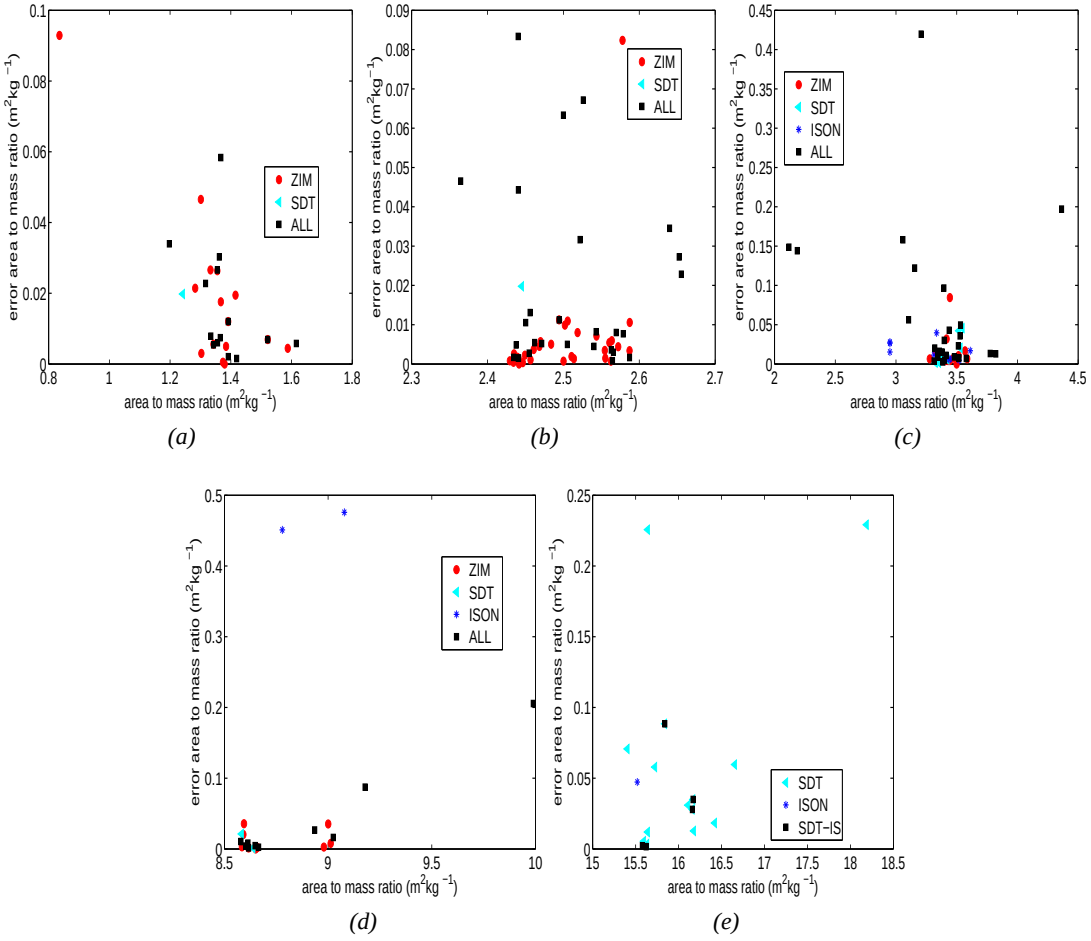

Figure 7.52: Error of the AMR value as a function of AMR as estimated in orbits of the object (a) E08241A, (b) E06321D, (c) E07194A, (d) E07308B, (e) E06293A.

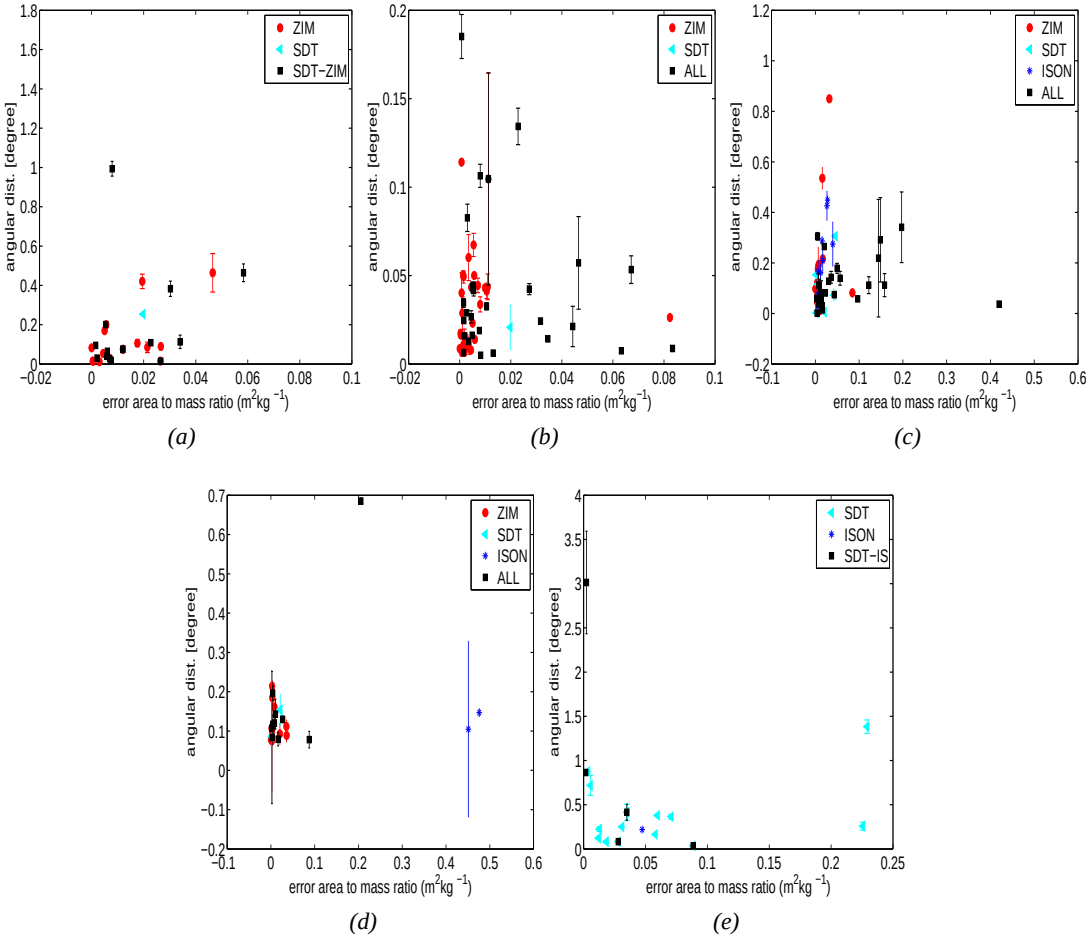

Figure 7.53: Absolute values and standard deviations of the angular distances as a function of the error of the AMR value as found in orbit determination of the object (a) E08241A, (b) E06321D, (c) E07194A, (d) E07308B, (e) E06293A.

The mean value of all angular distances of object E06321D are well below 0.2 degrees, but four orbits show large standard deviations in the angular distance, as Fig. 7.51b shows. All of them have been determined with combined observations from ZIMLAT, ESASDT, and ISON observations. Their AMR values are $2.36\,m^2kg^{-1}$, $2.50\,\mathrm{m^2kg^{-1}}$, $2.57\,\mathrm{m^2kg^{-1}}$, and $2.66\,\mathrm{m^2kg^{-1}}$. The orbits with the AMR value of $2.36\,\mathrm{m^2kg^{-1}}$ does show up also in a group of *outlier* AMR values, which do not seem to follow the periodic variation in the evolution of the AMR values. The other orbits, with large standard variations in the angular distance do not show up prominently (Fig. 7.49b). Those orbits with the largest standard variation in angular distance do not show the largest error in the AMR values either, as Fig. 7.53 shows.

Figure 7.51c shows for object E07194A three angular distances with large standard deviations. The orbits were determined with observations from all sites. They have AMR values of $2.12\,\mathrm{m^2kg^{-1}}$, $2.21\,\mathrm{m^2kg^{-1}}$, and $4.46\,\mathrm{m^2kg^{-1}}$. Those are the smallest and largest AMR values in the determined orbits for E07194A. These three values do also show up as outliers in Fig. 7.49c. For objects E07308B and E06293A, the angular distances with a large standard variation (see Fig. 7.51d and e), do not show significant outlier AMR values in Fig. 7.49d and e. For object E07308B, the orbit with an AMR value of $10.15\,\mathrm{m^2kg^{-1}}$ shows the largest mean value in the angular distance of almost 0.7 degrees but has a small standard deviation in this distance (Fig. 7.51d). This value is significantly different compared to the other determined AMR values, see Fig. 7.49d.

The dependency of the AMR value on the error of the AMR, as it was found in orbit determination, is investigated in the final step. No clear correlation could be determined between the AMR value and its rms value (Fig. 7.52).

Figure 7.53 shows the angular distance distances on the celestial sphere as a function of the error of the AMR value. As expected, for none of the objects a clear correlation between the error of the AMR value and the absolute value of the distances or the standard deviation of the distances could be determined.

7.5 Summary and Conclusions

A new algorithm to correlate observations with catalogue data, e.g., in TLE format was developed and implemented in the ESASDT processing tool. The old algorithm required an orbit to be determined for each observation tracklet, while the new algorithm is based on the comparison of astrometric positions and apparent motions. As opposed to the existing version the new tool successfully correlates GEO, GTO and MEO objects. Even the correlation of objects in clusters leads to satisfactory results. The new tool is used now in the operational processing of the ESASDT and ZimSMART data. With ZimSMART frames false correlation rate is below 2.5 percent.

The USSTRATCOM/DISCOS catalogue does not contain covariance information, which complicates the catalogue correlation (see Section 7.3). The new tool was used to determine empirical distances between astrometric positions determined with predicted ephemerides and observed astrometric positions of known objects. Different TLE data sets produce largely varying angular distance values. Currently no mean is available to predict the order of magnitude of the angular distances between single TLE ephemerides and single observations. The angular distances of ephemerides and observations, or external errors to high precision orbits, are significantly larger than the internal consistency errors of the TLE sets. In general, TLE ephemerides differ on average (one sigma confidence region) by 0.04 degrees from

the observations, or 25 kilometer in along-track and 10 kilometer in cross-track direction for GEO and 0.08 degrees, or 35 kilometer in along-track or 25 kilometer in cross-track direction for GTO. However, much larger differences may occur. Ephemerides propagated with SDP4 and SDP8, respectively, do not significantly differ for GEO objects and are negligible for GTO objects.

Ephemerides based on AIUB optical observations and predicted with CelMech are in general much more precise than the TLE data. Two observation intervals of at least 1.2 hours are required in a realistic sparse data setup to ensure a successful re-detection of the object even with a moderate field of view within 50 days after orbit determination, under the premise of availability of a priori elements. The distribution of the observations in anomaly is not crucial for GEO objects. The ephemerides of the orbits, which were determined with observations from one observation site only did not differ significantly from the ephemerides of orbits which were determined with observations from different sites. In general, observations from different sites have advantages since simply more observations are available per object.

The orbits of HAMR objects were analyzed as well, in the sparse data setup. The AMR value, that is the scaling factor of the DRP parameter, varies over time. The order of magnitude of the variation of the AMR value was not correlated with the order of magnitude of its error. This is in good agreement with R. Musci [66].

It is concluded that the variation of AMR, e.g., due to attitude motion, is not averaged out in the fit interval of orbit determination. In the evolution of the AMR value over time, no common characteristic could be determined for different HAMR objects. More knowledge on the precise attitude motion and shape, including possible deformations in time, would be needed for HAMR objects to develop and implement radiation pressure models to improve the orbit determination and prediction. As long as such information is not available, only frequent observations prevents an object from being lost.

8. Object Characterization via Light Curves

> We define only out of despair, we must have a formula... to give a facade to the void. (...)
> Under each formula lies a corpse.
>
> *Emile Cioran*

8.1 Non-resolved Imaging

8.1.1 Introduction

Only non-resolved images of space objects in GEO can be acquired with the current optical sensors. About 20×20 centimeters are integrated into one pixel at a distance to a regular LEO object, in 200 kilometer height even with a very good pixel scale of 0.2 arcseconds and under disregard of the effects of seeing. Accordingly, 3.4×3.4 meters are integrated into one pixel for a GEO object at 36 000 kilometer height. These are theoretical values; for real observations atmospheric conditions (seeing and scintillation) do blur the image of a space object even further.

So-called light curves are measurements of the overall intensity of light reflected from a space object received by an observer over time. The intensity depends on the lighting and viewing geometry, under which the object is observed, the materials of which the object is composed, the orientation of all illuminated facets, and the illumination source itself. The radiant intensity received by the observer is therefore:

$$I(t, \vec{p}_{\mathrm{attitude}}, \vec{p}_{\mathrm{body}}) = \frac{I_{\mathrm{Sun}} A_{\mathrm{eff}}(t, \vec{p}_{\mathrm{attitude}}, \vec{p}_{\mathrm{body}})}{4\pi R(t)^2}, \tag{8.1}$$

where I_{sun} is the Sun's radiation intensity arriving at the object, $R(t)$ the distance between observer and object, and A_{eff} the illuminated and visible surface and the vectors $\vec{p}_{\mathrm{attitude}}$ and $\vec{p}_{\mathrm{body}}$ symbolize all parameters related to the attitude motion, respectively the shape, orientation and reflection properties of facets of the object.

In order to determine the object's attitude motion and shape Eq. 8.1 needs to be inverted and a best fit of the attitude and body parameters to an observed light curve has to be performed. In a least square approach the following metric has to be minimized:

$$\chi^2(\vec{p}_{\mathrm{attitude}}, \vec{p}_{\mathrm{body}}) = \sum_{j=1}^{N_{\mathrm{facets}}} \left[I_{\mathrm{obs},j} - I_j(\vec{p}_{\mathrm{attitude}}, \vec{p}_{\mathrm{body}}) \right]^2 \tag{8.2}$$

The problem stated above is under-determined. Even when the viewing and lighting conditions are known, only one parameter, namely the intensity over time is available to determine three attitude parameters and – for complicated shapes – possibly an enormous number of body parameters. As Henry N. Russel [73] showed in 1906 an infinite number of solutions exist, which reproduce the identical light curve. This even applies in restricted cases as of a spherically shaped asteroid with a specific distribution of dark and bright spots on the surface, as in the case investigated by Russel. A reconstruction of the object and the spot distribution is not unique.

One way to address the non-linear problem of Eq. 8.2 is to simplify the multivariate problem into several problems of lower dimension. Another approach is to formulate the problem as completely independent integral resp. sum for body and attitude parameters, and find solutions in full knowledge of either body or attitude parameters. Several methods have been developed for the analysis of light curves of asteroids already, their applicability to light curves of satellites and space debris objects will be discussed in the Section 8.1.2 and 8.1.3. An overview of common light curve analysis methods for asteroids, which have been applied to satellites and space debris objects is presented by D. Hall [30]. The methods are divided into two groups: The first set of methods can only deal with convex objects, the second set of methods can allow or are independent of self-shadowing, self-obscureness and self-reflection.

8.1.2 Convex Objects

The effective area in Eq. 8.1 can be formulated as the following for a convex object:

$$A_{\text{eff}}(t) = \sum_{j=1}^{N_{\text{facets}}} A_j a_j \cdot (\vec{n}_j \cdot \vec{\imath})_+ (\vec{n}_j \cdot \vec{o})_+, \tag{8.3}$$

where A_j is the area of the single differently orientated facets of the convex body, and $\vec{n}_j$ the normal vector on the facet. a_j is the albedo, $\vec{\imath}$ is the light vector object-Sun, and $\vec{o}$ the vector object-observer. The effective surface is a sum over all illuminated $(\vec{n}_j \cdot \vec{\imath})_+$ and visible $(\vec{n}_j \cdot \vec{o})_+$ facets with their individual albedos a_j. The +-subscript indicates that only positive values are taken into account.

The different illuminated facets are given by the shape of the object and change under the attitude motion and the current illumination conditions. The different facets can have different reflection properties and as a result different albedos. In optical observations only the product between albedo and facet area $A_j a_j$ is accessible.

Equation 8.1 can be rewritten with Eq. 8.3 as the following:

$$I(t, \vec{p}_{\text{attitude}}, \vec{p}_{\text{body}}) = \frac{I_{\text{Sun}}}{4\pi R(t)^2} \sum_{j=1}^{N_{\text{facets}}} A_j a_j C(t, \vec{n}_j, \vec{p}_{\text{attitude}}) \tag{8.4}$$

with:

$$C(t, \vec{n}_j, \vec{p}_{\text{attitude}}) = (\vec{n}_j \vec{\imath})_+ (\vec{n}_j \vec{o})_+ \tag{8.5}$$

If an object is sufficiently smooth the sum can be transformed into an integral over the full solid angles $\vec{\nu}$:

$$I(t, \vec{p}_{\text{attitude}}, \vec{p}_{\text{body}}) = \frac{I_{\text{Sun}}}{4\pi R(t)^2} \int A(\vec{\nu}) a(\vec{\nu}) C(t, (\vec{\nu}), \vec{p}_{\text{attitude}}) d\vec{\nu} \tag{8.6}$$

If the same reflection properties for all facets is assumed and the attitude motion can be neglected, this leads to the following integral:

$$I(t, \vec{p}_{\text{attitude}}, \vec{p}_{\text{body}}) = \frac{I_{\text{Sun}}}{4\pi R(t)^2} \int A(\vec{\nu}) a C(t, (\vec{\nu})) d\vec{\nu} \tag{8.7}$$

This is a so-called Fredholm Integral Equation of the First Kind [30]. Solutions to this integral can be numerically determined via matrix factorization and gradient descent search methods, as been published in standard numerical books, e.g. [71], [54].

Man-made space objects tend to not have a smooth surface but many flat facets with different reflection properties and for non-stabilized objects, attitude motion may not be neglected. The simplifications of Eq. 8.6 and Eq. 8.7 do not apply.

8.1.2.1 Shape Analysis with Known Attitude

If all attitude parameters would be known, Eq. 8.4 is a linear problem and can be solved with standard numerical methods. To gain only physical sensible positive values, the problem can be solved by inverting the equation via matrix factorization or gradient descent search methods, see e.g., [71], [54], [9]. This method is especially promising for actively stabilized satellites, for which the attitude parameters are known. A possible shape reconstruction (up to multiples of the single areas A_j if only optical observations are available) can be compared to original payload to check for possible damages. In case a satellite is damaged, however, most likely the attitude motion is unknown. The method only applies to convex objects without self-shadowing, which does not apply to box-wing satellites. Many observations from different sites under various lighting and viewing conditions are required.

8.1.2.2 Attitude-Independent Shape Analysis

A method of the attitude-independent shape analysis, was already addressed in 1903 by H. Minkowski [62]: He provided a method of shape inversion, which can be applied to man-made convex space resident objects with different facets and non-smooth surfaces.

The method relies on the fact that a convex body is made up of a limited number, which is larger than one, of single facets, defining a so-called convex polytope. As long as the closure conditions with A_j representing the area of the facets and $\vec{n}_j = (n_1, n_2, n_3)_j^T$ their corresponding normal vectors,

$$\sum_{j=1}^{N_{\text{facets}}} A_j n_{1j} = 0 \sum_{j=1}^{N_{\text{facets}}} A_j n_{2j} = 0 \sum_{j=1}^{N_{\text{facets}}} A_j n_{3j} = 0 \tag{8.8}$$

are satisfied, and the point of main inertia may be arbitrarily within or on one of the surfaces of the object, a polytope can be reconstructed up to translations. Thus a complete shape reconstruction is not possible but an estimate on the orientation and number of facets can be given. With optical observations alone the size of the facets remains unknown. For smooth surfaces a large number of normal vectors pointing in similar directions is derived.

B. Calef et. al. [9] applied the method to recover simple simulated shapes of a cube and a house. It was assumed that all facets have Lambertian reflection properties. Optical and infrared measurements of the shapes were simulated and the inversion compared to the original shape. Convincing results could be achieved assuming several thousands of measurements are available.

8.1.3 Arbitrarily Shaped Objects

8.1.3.1 Shape-Independent Attitude Analysis

Spin State Analysis An option to determine attitude parameters, e.g., the spin axis and spin rate of an object independently of the shape has been developed by P. Magnusson [57] [58]. The method takes advantage of the fact that the apparent synodic rotation rate of an object, which is moving fast with respect to an observer, differs from the true sidereal spin rate of the object. The most prominent example of the synchronous rotation is the Moon observed from the Earth. The synodic apparent periods of the rotations are determined directly from the brightness variations of the object. For the determination of synodic modulation periods a Fourier or analogous analysis are applied, for other methods refer to J. Scargle [75], S. Larsson [53] or D. Hall [29]. For the determined periods a best fit is performed to determine a sidereal period and spin axis, accounting for the effects of changing geometry of object, illumination source and observer. The advantage of the method is that no best fit of the brightness data is performed directly but only to the synodic periods, which have been determined. D. Hall applied the method to the spin-controlled convex LEO NASA satellite IMAGE after contact was lost for a small time period; the method did deliver good results, see [29] for further details.

The method is assuming that the periodicity determined with a Fourier or similar analysis would only depend on the synodic rotation periods and would be completely independent of the shape of the object. This neglects symmetries in the shape of the observed object, glints from various non-parallel facets orthogonal to the spin axis as well as self-shadowing effects, which could lead to the determination of false rotation periods. The Fourier analysis of simulated light curves, as discussed in Section 8.3.2 discusses some of these requirements. It is furthermore assumed that the rotation is constant during the observation time with a slow spin rate around only one spin axis. This may be the case for asteroids or spin controlled satellites, which are either still active or ere just recently abandoned but may not apply to space debris objects. This point will be addressed again, when discussing the analysis of observed light curves in section 8.4. Additionally, the spin rate has to be rapid enough to determine it during an observation period and slow enough to be displayed without aliasing in the light curve. The method is not applicable to GEO or GTO objects, whose relative movement with respect to the observer is too small to determine the differences between sidereal and synodal spin rates.

Glint Analysis The so-called glint analysis is another option for a shape independent attitude analysis. Glints are produced by flat highly reflective surfaces, such as solar array panels, under the total reflection condition. The total reflection condition is fulfilled, when the incident angle of the incoming solar rays $\vec{\imath}$ equals – up to a deviation of half a degree (extension of the Sun seen from a near Earth environment) – the reflection angle in direction $\vec{o}$ to the observer, whereas $\vec{n}$ is the normal direction of the facet:

$$\frac{\vec{o}+\vec{\imath}}{|\vec{o}+\vec{\imath}|} \cdot \vec{n} = \vec{p}_{\mathrm{PAB}} \cdot \vec{n} = 1 \tag{8.9}$$

$\vec{p}_{\mathrm{PAB}}$ is the vector between incident and reflection direction, [30]. Stabilized GEO objects with solar panels tend to fulfill the glint condition, when they are close to the Earth's shadow.

Subsequently observed glints can give information on the attitude motion of a satellite, if rudimentary shape information is available – for example, box-wing shape or more cylindrical shape – if the viewing and lighting geometry is known. The glint analysis can be used to determine the correct alignment of solar panels, e.g., given the attitude state is known. Glints of unknown space objects in unknown attitude state can indicate that the object is composed of at least one highly reflective facet. Observing glints of relatively small magnitudes of a nano-satellite may give information on the number and orientation of wire antennas, as D. Hall [30] points out. A glint analysis of GEO satellites with the TAROT telescopes in Chile and France was performed by M. Bourez-Laas [5]. In her analysis the glint (called flares in the paper) epochs are calculated in advance for different GEO objects. Those simulations were cross-checked with real observations, which were in good agreement. An observation strategy to easily detect faint GEO objects under glint conditions and characterize their surface, and shape properties in one observation step was proposed.

Single Facet Orientation Analysis An approach similar to the glint analysis is used in the single facet orientation analysis. The single facet analysis requires observations of the brightness of an object as a function of the phase angle. The brightness of a stabilized box-wing satellite is dominated by the solar panels. The brightness follows a cosine law over the phase angle, if the satellite is in a controlled attitude state. A linear dependency of the brightness on the phase angle is observed for cylindrically shaped satellites, which are controlled. Possible panel misalignment of box-wing satellites or the correct pointing towards the sun can be determined via deviation from the cosine law, e.g. when the maximum brightness is not reached at a zero degree phase angle. Measurements over the full phase angle have to be collected. This may not be a problem for LEO objects with a revolution period of 90 minutes, it is more time consuming for GEO objects.

Stabilized Attitude Test A so-called stabilized attitude test can be performed in addition to the single facet analysis. The stabilized attitude test requires only few measurements and compares selectively single brightness measurements under the same specific viewing and lighting conditions. Those brightness measurements are either compared with a theoretical attitude model or with the measurements over the whole range of phase angles. The method is extremely prone to false results, since either the attitude

model may be not accurate enough or in single measurements the atmospheric conditions may dominate the results.

8.1.3.2 Attitude-Independent Shape Analysis

Shape Inversion of Concave Objects There have been efforts in developing methods for shape inversion for asteroids with concavity, e.g. by M. Kaasalainen [43]. But it appears that the methods crucially rely on smooth surface and texture of the object and a diffuse reflectance. Those methods cannot be applied to multi-facet man made objects, with various reflection properties. Further research is needed to adapt those methods.

Phase Angle Fingerprints So-called phase angle fingerprints of an object are gained through observations covering all phase angles and all possible attitude states. This method is applicable to non-controlled objects, suspected to be in tumbling attitude motion. The theory is that enough measurements of a single object are collected over time, so all possible attitude states have been observed. The observations should result in a specific brightness pattern as a function of the phase angle, which is independent of the attitude but due to the shape of the object. Catalogued brightness patterns could be compared to observed patterns of objects with unknown shapes. The disadvantage of the method is that several hundreds, as D. Hall [30] proposes, or several thousands of measurements, as E. Stansbery [87] proposes, are necessary for each shape. Even in the most favorable theoretical cases of clearly distinct simple shapes, the results are not conclusive, as simulations by D. Hall [30] show. The same analysis performed with real observations of the ISON network has been done by V. Agapov [1]. No conclusive results were obtained either. This may be due to the fact that the patterns of the different shapes differ in subtle details only, which are hidden by observation errors in real measurements. The method crucially relies on the fact that all attitude states are observed. In real observations, there may not all attitude states be observed or the object does not have a completely random tumbling motion over time but a specific rotation, which would compromise the brightness variations stemming from the shape only.

8.2 Viewing and Lighting Geometry: Phase Angle

A standard way to describe the viewing and lighting geometry for a light curve measurement is the so-called phase angle. The phase angle is defined as the angle between observer (topocentric position), observed object and Sun, that is, within their common plane. This common plane is not stable over time relative to a satellite fixed or equator equinox coordinate system. This may lead to the situation, that the same phase angle value may represent different three-dimensional geometries lighting and viewing geometries, which may lead to different light curves, as it will be shown in section 8.3.2. The most complete way to describe the lighting and viewing conditions would be a description of the viewing angles in the satellite body system. As P. Kervin [46] points out, such a description is very useful and can account for deficiencies of the traditional phase angle approach, especially in the case of objects, which are not in a stabilized attitude motion. Unfortunately the attitude motion of non-stabilized objects is in general unknown, which makes it impossible to establish the viewing geometry in such a satellite fixed reference system.

Two additional phase angles are defined in this work, to enhance the classical phase angle concept, although the attitude motion of the object is unknown. A coordinate system in the center of mass of the object is defined as a reference system. The reference plane is parallel to the Earth's equator. The new reference system defined is a quasi topocentric equator Earth fixed system, but instead of in a topocentric position on the Earth surface the origin is in the satellites position. The vector towards the Sun and to the observing topocentric position are defined in the new system. The full angle between those vectors corresponds to the classical phase angle, called ϕ in the following. Additionally, angles the projection of those vectors in the reference plane parallel to the equator plane (called xy-plane in the following, and the corresponding phase angle ϕ_{xy}) and in the plane orthogonal to it (called xz-plane in the following, and the corresponding phase angle ϕ_{xz}) are determined. These three angles can be determined even if no knowledge about the object is available at all. The geometry of the three different angles, overall phase angle ϕ, xy-plane angle ϕ_{xy} and xz-plane angle ϕ_{xz} are illustrated in Fig.8.1.

8.3 Simulated Light Curves

8.3.1 Simulation Setup

Light curves of simple shapes have been simulated. Three-dimensional scenes have been computer graphically rendered. The input, which is needed to render a scene and a typical rendering pipeline is illustrated in Fig. 8.2. The rendering pipeline is described in detail e.g. by P. Shirley [86].

The closest approach to the physical world would be rendering with so-called ray tracing. Ray tracing operates on pixel level in each step, starting out from the lighting source, following each *ray* to each pixel on the scene and calculating its path. For this preliminary study of light curves of simple shapes the faster shading option was preferred over ray tracing algorithms, especially since only Lambertian reflection was taken into account. Ray tracing is recommended, when modeling complete satellites with different physically realistic surface materials and complicated self-shadowing.

The rendering of scenes in the current work was performed in OpenGL with the OpenSceneGraph library; the rendering stack is illustrated in Fig. 8.3. OpenSceneGraph serves as a scene graph middle ware, which provides additional support on the overall performance of rendering scenes and advanced shader options; it offers support of dynamically updating scenes beyond simple draw transversal algorithms. Simple shapes have been rendered with OpenSceneGraph using the Lambertian shader only in the current work. Perspective viewing transformation was disabled, so an orthogonal transformation was performed. As a light source a spotlight has been placed, which has the extension of one degree in a Phong only shading, that is specular-only, rendered object on the screen. For the light curve simulation the viewing (camera) direction was kept fixed. The direction of the lighting source was varied but kept fixed during each the simulated light curve. The attitude state of the object was dynamically updated in the scene. The different intensities proposed by the shader were not taken into account, only the total number of (visible) white pixels of the object. An albedo of 0.8 was assumed for the simulation.

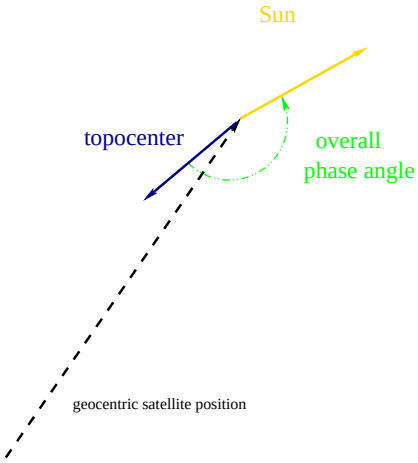

(a) overall phase angle

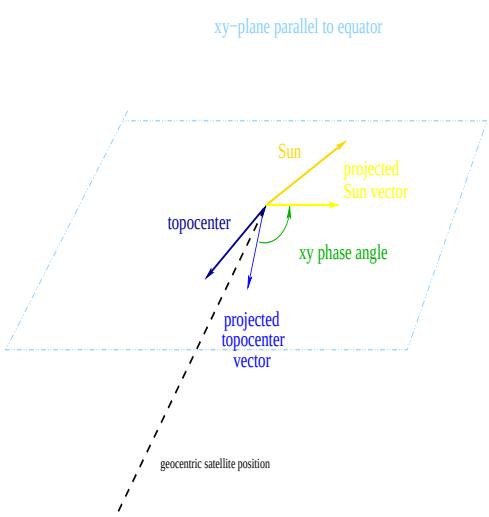

(b) xy phase angle

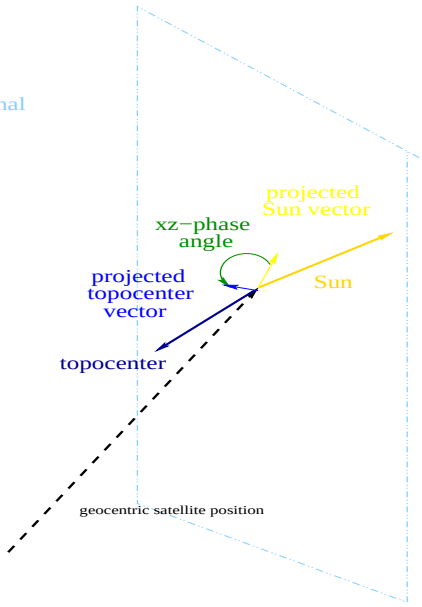

(c) xz phase angle

Figure 8.1: Lighting and viewing conditions observing an Earth orbiting space object. (a) overall (classical) phase angle ϕ (b) xy-plane phase angle ϕ_{xy}, (c) xz-plane phase angle ϕ_{xz}.

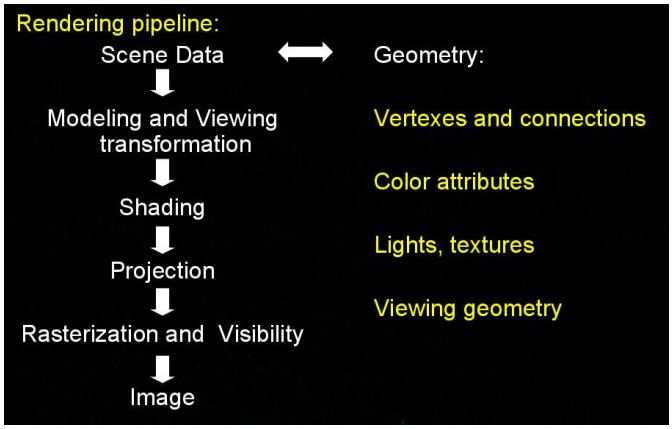

Figure 8.2: Rendering pipeline of the simulated scenes.

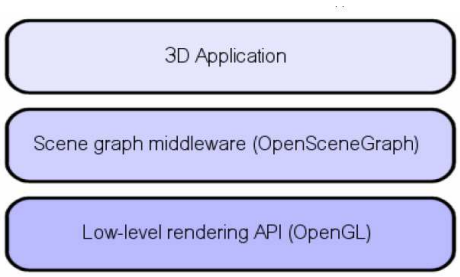

Figure 8.3: Three dimensional rendering stack [59].

8.3.2 Simulated Light Curves of Simple Shapes

Light curves of simple shapes have been simulated: a cube, a cylinder, and the shape of a thin multi-layer insulation (MLI) structure. The cube was simulated to have an edge length of two meters, the cylinder was simulated to have a height of 6.2 meters and a diameter of 3.7 meters, which represents the size of an average Russian upper stage, and the MLI structure was assumed to have a size of roughly one square meter. All objects are assumed to be in geostationary orbit with zero inclination. The observer was assumed to be located at the geocenter, without loss of generality. The coordinate system, defined in Section 8.2, is used here again. The equator plane and the xy-plane with its origin in the center of mass of the object coincide in the chosen setup. The y-axis in the fundamental plane is pointing towards the geocenter, the x-axis orthogonal to it within the xy-plane and the z-axis out of plane. At the starting point of each simulation the axis of main inertia of each object are aligned with the coordinate axis.

Four different setups were simulated for the cylinder: first, a single rotation around the x-axis, with a period of 41 minutes has been simulated, observed under an overall phase angle $\phi/\phi_{\text{xy}}/\phi_{\text{xz}} = 0/0/0$ degrees. The angles in the xy- and xz-plane are defined as described in Section 8.2 and illustrated in Fig. 8.1. Secondly, a motion of the cylinder has been simulated, in which two rotations are superimposed, one around the x-axis with a period of 49 minutes and one around the y-axis with a period of 88 minutes. This motion was simulated to be observed under three different lighting conditions: $\phi/\phi_{\text{xy}}/\phi_{\text{xz}} = 0/0/0$ degrees, $\phi/\phi_{\text{xy}}/\phi_{\text{xz}} = 90/90/0$ degrees and $\phi/\phi_{\text{xy}}/\phi_{\text{xz}} = 90/90/45$ degrees. The rotation rates were defined to have the following attitude motion: the rotation is stable over time for the cube, for the cylinder and the MLI the setup has to be regarded as a snapshot on a current attitude motion, which is subject to change over longer time periods. Figure 8.4 illustrates the rendered cylinder in the different lighting and viewing conditions. In Fig. 8.5 the different simulated light curves of the different rotation and lighting conditions extracted from the rendered images are displayed. The superimposed rotations of 49 and 88 minutes, respectively, around the x- and y-axis has also been simulated for the cube and the MLI structure. The illumination was chosen to be $\phi/\phi_{\text{xy}}/\phi_{\text{xz}} = 90/90/45$ degrees, again. In Fig. 8.6 and 8.7, the shapes and setup, as well as the light curves, are shown.

Figure 8.5 shows that the simple rotation around the x-axis only and the rotation around two axis (x- and y-axis) do not produce completely different patterns as long as the overall phase angle ϕ, ϕ_{xy}, and ϕ_{xz} are zero. The very same rotation produces different patterns, when the phase angles are changed, due to the fact that not all facets that are illuminated are visible to the observer. The pattern differs for the two simulated light curves under $\phi = 90$ degrees, but different phase angles ϕ_{xz}. The change in illumination, which leaves the overall phase angle unchanged, still has an effect on the simulated light curve.

The simulations of the cube and the MLI structure show that the light curves differ for different shapes in the same attitude motion and when observed under the same lighting conditions and viewing conditions, as the comparison of Fig. 8.5 with 8.6 and 8.7 reveals. The MLI structure, which consists of mainly two more or less flat surfaces, is not visible for the observer during longer time intervals in the observation span.

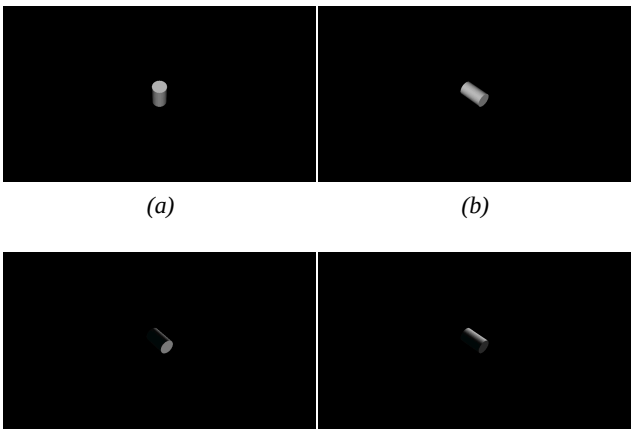

(a) *(b)*

(c) *(d)*

Figure 8.4: Simulated cylinder under different lighting and rotation conditions: (a) rotation around x-axis (41-min period), $\phi/\phi_{xy}/\phi_{xz} = 0/0/0$ degrees; (b) to (d) rotation around x- and y-axis (period 49 resp. 88 min) with: (b) $\phi/\phi_{xy}/\phi_{xz} = 0/0/0$ degrees, (c) $\phi/\phi_{xy}/\phi_{xz} = 90/90/0$ degrees (d) $\phi/\phi_{xy}/\phi_{xz} = 90/90/45$ degrees.

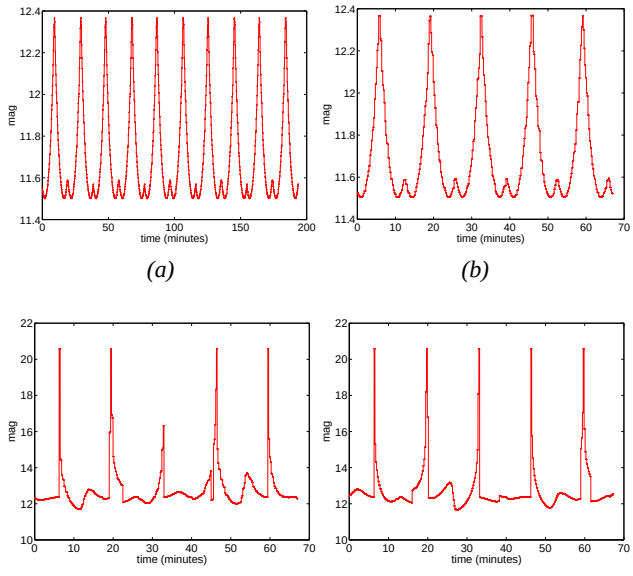

(a) *(b)*

(c) *(d)*

Figure 8.5: Simulated light curves of a cylinder under different lighting and rotation conditions: (a) rotation around x-axis (41-min period), $\phi/\phi_{xy}/\phi_{xz} = 0/0/0$ degrees; (b) to (d) rotation around x- and y-axis (period 49 resp. 88 min) with: (b) $\phi/\phi_{xy}/\phi_{xz} = 0/0/0$ degrees, (c) $\phi/\phi_{xy}/\phi_{xz} = 90/90/0$ degrees (d) $\phi/\phi_{xy}/\phi_{xz} = 90/90/45$ degrees.

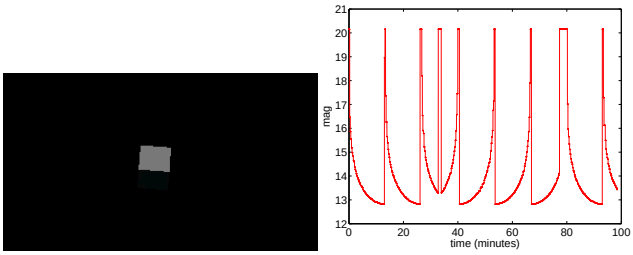

(a) *(b)*

Figure 8.6: Simulation of a cube with rotation around x- and y-axis (period 49 resp. 88 min), with $\phi/\phi_{xy}/\phi_{xz} = 90/90/45$ degrees: (a) image of the simulation, and (b) simulated light curve.

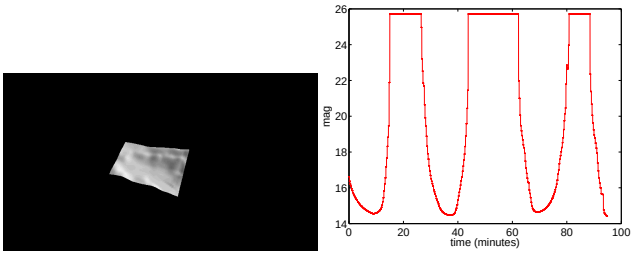

(a) *(b)*

Figure 8.7: Simulation of an MLI structure with rotation around x- and y-axis (period 49 resp. 88 min), with $\phi/\phi_{xy}/\phi_{xz} = 90/90/45$ degrees: (a) image of the simulation and (b) simulated light curve.

8.3.3 Fourier Analysis of Simulated Light Curves

The simulated light curves were Fourier analyzed. As mentioned in section 8.1.3.1 some characterization methods rely on a Fourier analysis or other methods to determine periods. The results for the cylinder are shown in Fig. 8.8. Figure 8.8a shows the Fourier spectrum for the simple x-axis rotation observed with the phase angles $\phi/\phi_{xy}/\phi_{xz} = 0/0/0$. There is one main period of 20 minutes and one with a smaller amplitude at around 10 minutes. The period of 20 minutes is actually close to half of the actual rotation period, which is due to the mirror symmetry of the cylinder shape around the rotation axis.

Figure 8.8(b) to (d) show the Fourier spectrum for the light curves of the cylinder with the superimposed rotation around the x- and the y- axis with periods of 49 and 88 minutes, respectively. All light curves, which were simulated under different phase angles, show two main periods of around six and eleven minutes. The cases observed under a phase angle different from zero, $\phi/\phi_{xy}/\phi_{xz} = 90/90/0$ degrees and $\phi/\phi_{xy}/\phi_{xz} = 90/90/45$ also show several other distinct periods but with smaller amplitudes. The Fourier decompositions of the those light curves resemble each other. Many smaller periods between a few seconds and five minutes do occur, which are less prominent as for the case, in which all phase angles were zero. The introduced rotation rates were 88 and 49 minutes. The relation between the periods of about 1.8 is preserved in the periods of the Fourier decomposition.

Figure 8.9 shows the Fourier decomposition for the simulated cube and the MLI structure for the same

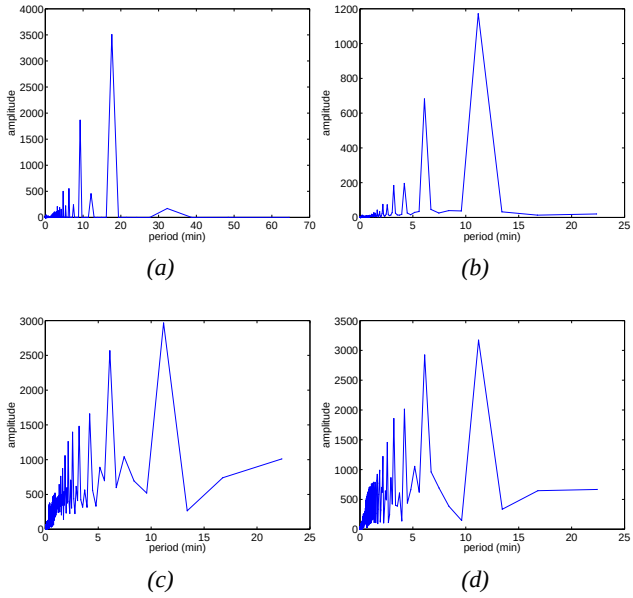

Figure 8.8: Fourier spectra of simulated light curves of a cylinder under different lighting and rotation conditions: (a) rotation around x-axis (41-min period), $\phi/\phi_{xy}/\phi_{xz} = 0/0/0$ degrees; (b) to (d) rotation around x- and y-axis (period 49 resp. 88 min) with: (b) $\phi/\phi_{xy}/\phi_{xz} = 0/0/0$ degrees, (c) $\phi/\phi_{xy}/\phi_{xz} = 90/90/0$ degrees (d) $\phi/\phi_{xy}/\phi_{xz} = 90/90/45$ degrees.

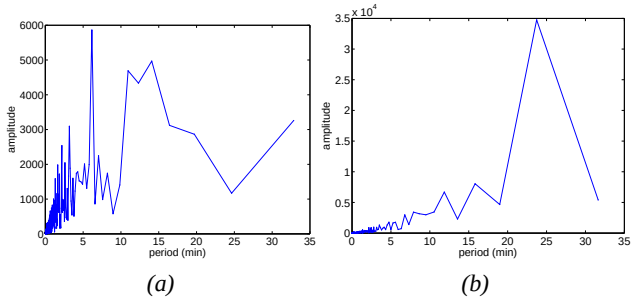

Figure 8.9: Fourier spectra of the simulated light curves of (a) a cube and (b) MLI structure with rotation around x- and y-axis (period 49 and 88 min, resp.), $\phi/\phi_{xy}/\phi_{xz} = 90/90/45$ degrees.

superimposed rotation around the x- and the y- axis with periods of 49 and 88 minutes, respectively, under the same lighting conditions of $\phi/\phi_{xy}/\phi_{xz} = 90/90/45$ degrees. The Fourier decomposition of the cube light curve (Fig. 8.9(a)) shows two main periods, one of around 6 minutes and another one of around 12 minutes, the latter consisting of two not clearly separated periods. The result is comparable to the case of the same setup for a cylinder. The situation is different for the MLI structure (Fig. 8.9(b)). The Fourier analysis shows one main dominant period at 23 minutes, and smaller ones at about 12 and 16 minutes. Obviously, with the large time intervals, in which the object is not visible for the observer due to the flat shape, the Fourier decomposition of the different rotations fails.

Table 8.1: Light curve measurements for object MSG-1 02040B.

Date	start epoch (MJD)	ϕ (deg)	ϕ_{xy} (deg)	ϕ_{xz} (deg)
Dec 4 2009	55169.8	42.1 to 37.6	28.2 to 24.4	61.0 to 61.1
Dec 9 2009	55174.7	93.1 to 88.7	90.5 to 85.6	68.4 to 68.3

8.3.4 Pattern Recognition of Simulated Curves

A pattern recognition algorithm was developed to detect pattern in light curves measurements. Therefore a set of subsequent data points of a chosen size is chosen, and all previous and remaining data points are scanned if this set of subsequent intensity values in this ascending and descending order can be re-detected within the same light curves several times. Small deviations of 20 percent of the intensity values within the set are allowed for a successful re-detection. With a sliding window all possible sets are tested, for a size of the pattern of two to half the total number of available data points in the light curve. The pattern of each size, which was re-detected most often is stored. The largest pattern which has more occurrences than the pattern the pattern of surrounding sizes is chosen as the *detected pattern*.

The algorithm has been tested with the simulated light curve of the cylinder with a rotation around the x-axis observed with $\phi/\phi_{xy}/\phi_{xz} = 0/0/0$ degrees, which is displayed in Fig. 8.5(a). The results are shown in Fig. 8.10: Figure 8.10(a) shows the size of the found patterns as a function of the number of times the pattern could be found again within the same light curves. Figure 8.10(b) shows the detected pattern. The pattern is probably slightly shifted compared to one chosen by eyesight, but the algorithm is judged to be working. The selected pattern has a size of 600 (with about 2,400 in total), it occurs three times.

8.4 Interpretation of Light Curves of Satellites and Space Debris

Light curves of space debris objects are observed on a regular basis with ZIMLAT. The sampling rate of light curves taken with ZIMLAT is of the order of three seconds.

A small subset of light curves of three objects from the USSTRATCOM/DISCOS catalog was chosen,

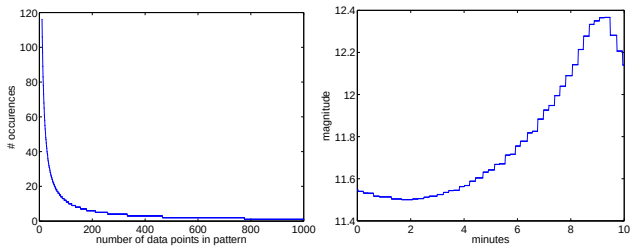

(a) *(b)*

Figure 8.10: (a) Size of the found pattern as a function of the number of detected repetitions, (b) detected pattern in light curve of Fig. 8.5(a).

Table 8.2: Light curve measurements for object Blok DM-2.

Date	start epoch (MJD)	ϕ (deg)	ϕ_{xy} (deg)	ϕ_{xz} (deg)
April 12 2008	54568.9	21.1 to 27.7	20.9 to 27.8	2.6 to 0.4
April 13 2008	54569.8	9.5 to 7.8	4.3 to 2.7	9.3 to 7.9
April 19 2008	54575.9	14.9 to 20.9	13.7 to 20.5	6.0 to 3.1
April 26 2008	54583.0	31.5 to 34.6	32.0 to 35.3	7.7 to 12.3

Table 8.3: Light curve measurements for object Gorizont 33.

Date	start epoch (MJD)	ϕ (deg)	ϕ_{xy} (deg)	ϕ_{xz} (deg)
July 21 2009	55034.0	10.2 to 6.8	10.8 to 7.2	10.0 to 5.9
July 26 2009	55039.0	11.1 to 7.8	11.8 to 8.2	10.3 to 7.0
July 28 2009	55041.0	14.9 to 13.1	15.8 to 13.9	14.4 to 12.3

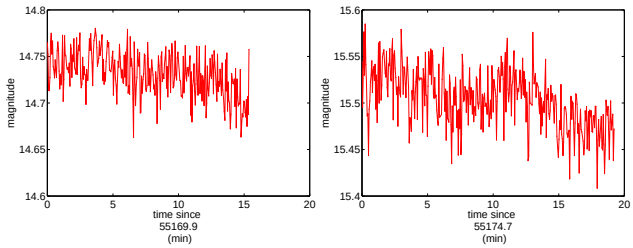

(a) Dec 4 (42.1 to 37.6 deg) *(b) Dec 9 (93.1 to 88.7 deg)*

Figure 8.11: Light curves of the MSG-1 satellite 02040B (a) Dec 4, (b) Dec 9, 2009.

to be displayed here, for which the shape is suspected to be known. The spin controlled MSG-1 satellite with the COSPAR Number 02040B is a cylindrically shaped satellite, which is still active and spin-stabilized. The Blok DM-2 upper stage 91010F has a more or less cylindrical shape; it has never been in a controlled attitude state. The abandoned Gorizont-33 satellite 90102A consists basically of a cylindrically shaped body with two larger and two smaller solar panels. It is no longer attitude controlled. All objects are in a geostationary orbit, with small eccentricities. MSG-1 is in a controlled orbit around zero degrees inclination, Blok DM-2 is in an orbit with an inclination of 11.9 degrees, and the Gorizont 33 satellite at 12.5 degrees inclination.

The phase angle is significantly changing over an observation interval of 10 to 30 minutes in contrary to the simulated light curves. All magnitudes that are determined are apparent magnitudes, calibrated with respect to the stellar background.

Two light curves of MSG-1, 02040B, are displayed in Fig. 8.11. The dates and phase angles are displayed in Tab. 8.1. Both light curves of the spin-stabilized satellite MSG-1 are very flat and only show small

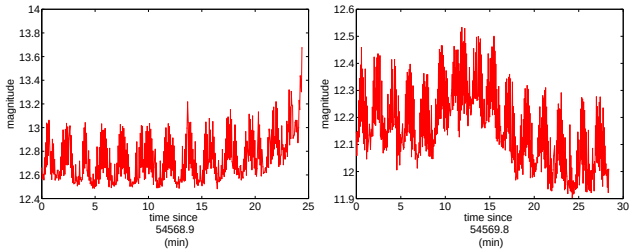

(a) April 12 (21.1 to 27.7 deg) *(b) April 13 (9.5 to 7.8 deg)*

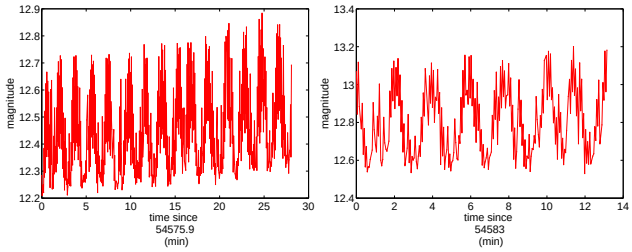

(c) April 19 (14.9 to 20.9 deg) *(d) April 26 (31.5 to 34.6 deg)*

Figure 8.12: Light curves of the Blok DM-2 satellite 91010F (a) April 12, (b) April 13, (c) April 19, (d) April 26, 2008.

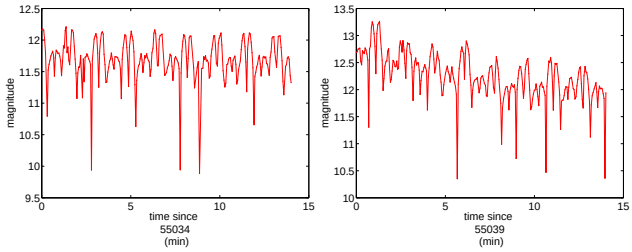

(a) July 21 (10.2 to 6.8 deg) *(b) July 26 (11.1 to 7.8 deg)*

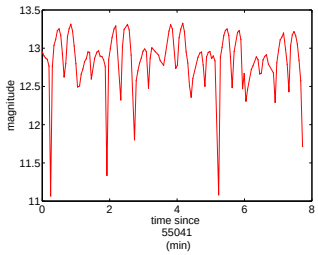

(c) July 28 (14.9 to 13.1 deg)

Figure 8.13: Light curves of the Gorizont 33 satellite 90102A (a) July 21st, and (c) July 28th, 2009.

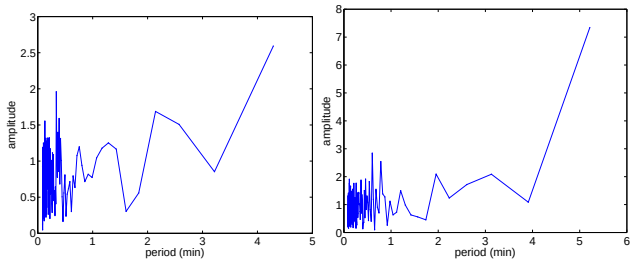

(a) Dec 4 *(b) Dec 9*

Figure 8.14: Fourier spectrum of light curves of the MSG-1 satellite 02040B (a) Dec 4, (b) Dec 9.

fluctuations within the limits of about 0.1 apparent magnitudes over the observation interval. This has been expected, due to the controlled attitude state and the cylindrical shape. The spin axis of the MSG-1 satellite is aligned perpendicular to the Earth's equator. The small fluctuations, which are visible, may represent the small antenna structures on top of the cylindrical body of the MSG-1 satellite. Furthermore, the measurement is always affected by short term fluctuations of the atmospheric extinction, too. The average magnitude seems to decline during the measurement in both cases as a function of the phase angles. The phase angle ϕ in the second case is larger than in the first case. While the phase angles ϕ_{xz} are comparable, the phase angle ϕ_{xy} of the first light curve is around 30 degrees and of around 90 degrees during the second light curve measurement. In both cases the phase angles ϕ as well as the phase angles ϕ_{xy} declines during the measurement, the angle ϕ_{xz} stays more or less stable. The classical phase angle ϕ is sufficient to explain the magnitude trends for this spin stabilized satellite, which is in good agreement with the simulations by P. Kervin [46].

Four light curves are analyzed for Blok DM-2, 91010F. The light curves are displayed in Fig. 8.12, the phase angles are displayed in Tab. 8.2. All light curves show clear structures and variations of the order of half a magnitude within few seconds. A brightness pattern with a period of around two minutes seems to be present in each of the light curves. In Fig. 8.12(a) and 8.12(c) the magnitude slowly rises during the observation, which is consistent with the increasing overall phase angle as well as the rising phase angle in the xy-plane. In Fig. 8.12(b) the overall tendency of a decreasing magnitude according with the decrease in phase angles, is interrupted by a short rise in the magnitude. The short term brightness variations, which are present in all light curves, are not affected by this. The light curve in Fig. 8.12(b) is the one observed under the smallest phase angles.

Three light curves of Gorizont-33, 90102A, are examined. The light curves are displayed in Fig. 8.13, the phase angles are listed Tab. 8.3. For this large satellite, there seems to be a pattern present in each of the observations, suspected to represent the panel-body structure. The light curves are not identical, although they are observed under similar phase angles. Only in Fig. 8.13(b) a decrease in the magnitude is visible. No clear correlation between magnitude and phase angles can be found for both objects.

8.4.1 Fourier Analysis of Observed Light Curves

The observed light curves were Fourier analyzed to gain more insight into the periods displayed in the brightness variations.

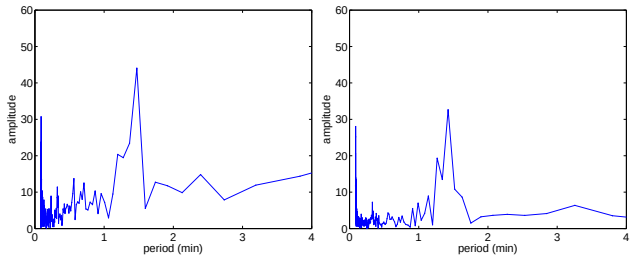

(a) April 12 *(b) April 13*

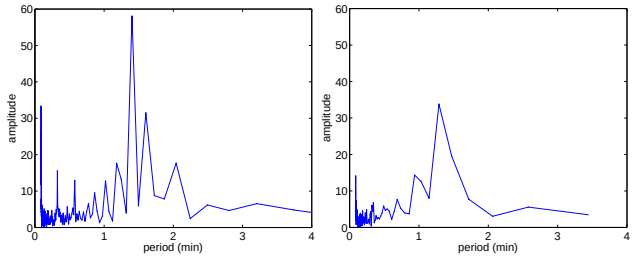

(c) April 19 *(d) April 26*

Figure 8.15: Fourier spectrum of light curves of the Blok DM-2 satellite 91010F (a) April 12th, (b) April 13, (c) April 19, (d) April 26.

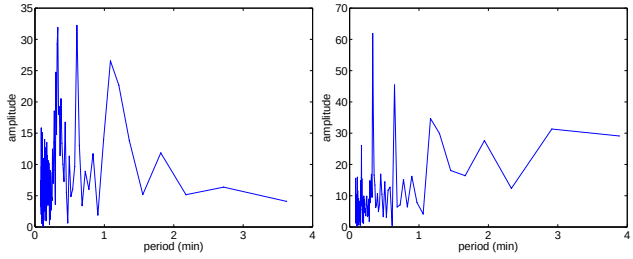

(a) July 21 *(b) July 26*

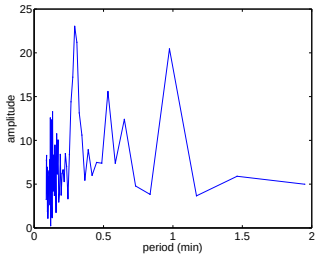

(c) July 28

Figure 8.16: Fourier spectrum of light curves of the Gorizont 33 satellite 90102A (a) July 21, (b) July 26 (c) July 28.

In Fig. 8.14, the Fourier analysis of the light curves of the controlled MSG-1 satellite are displayed. No large amplitudes for any periods are detected.

Figure 8.15 shows the Fourier spectrum for the Blok DM-2 light curves. For all four light curves, one very small period of the order of 4 to 8 seconds occurs with a large amplitude, as well as one or two not clearly separated periods around 1.3 to 1.8 minutes can be determined. These very small periods may indicate that the observed light curves are subject to aliasing effects, due to the three second sampling rate of the observations. These two main periods seem to be more or less stable over time. In Fig. 8.15(c) also a number of periods surrounding the main period of 1.5 minutes occur.

The Fourier decompositions of the three light curves of Gorizont-33 are displayed in Fig. 8.16. They show three main periods around 25 and 35 seconds and one around one minute. In Fig. 8.16(c) the second period is split into two periods, which are not completely separated. Again the periods seem to be more or less stable over time and independent of the specific phase angles, during the measurement.

The small periods detected in the Fourier decomposition of Blok DM-2 and Gorizont-33 seem to indicate very rapid rotations for the debris objects, which would be unexpected for large objects like the upper stages or a whole satellite. More likely, the periods may correspond to recurring shape patterns, which are displayed within a slower rotation. The periods seem to be constant for observations under different phase angles.

This in good agreement with the results of the simulations shown in Section 8.3.2, which illustrated the effects of symmetries in the object shapes and independency of the determined periods of the phase angle.

8.4.2 Pattern Recognition of Observed Light Curves

The pattern recognition algorithm, which has been tested with the simulated curves, is applied to the observed light curves in a next step. Figure 8.17a and 8.17b show two of the light curves of Blok DM-2; the detected pattern are highlighted. The size of the pattern as a function of the number of detected repetitions in the light curve are displayed exemplary for the light curve of April 19 in Fig. 8.12c. The detected pattern of all four light curves of Blok DM-2 are shown in Fig. 8.12d, the all consist of 15 data points. The patterns are not identical for all four light curves – the magnitudes are not the same – due to observations under different phase angles, but the detected pattern may suggest that the rapid brightness changes in the light curves are not only white noise.

Figure 8.18 shows two of the light curves with highlighted pattern of Gorizont-33 and the dependence on the pattern size of the number of detected repetitions of the pattern in the light curve. The size of the pattern that could be detected in all light curves consists of 17 to 26 measurements. The single pattern that could be found are not identical, but resemble each other. They clearly show a different structure than the pattern of the upper stage Blok DM-2, as the comparison of Fig. 8.17d and Fig. 8.18d shows. The periods found in the Fourier analyses are of the order of the time interval covered by the pattern.

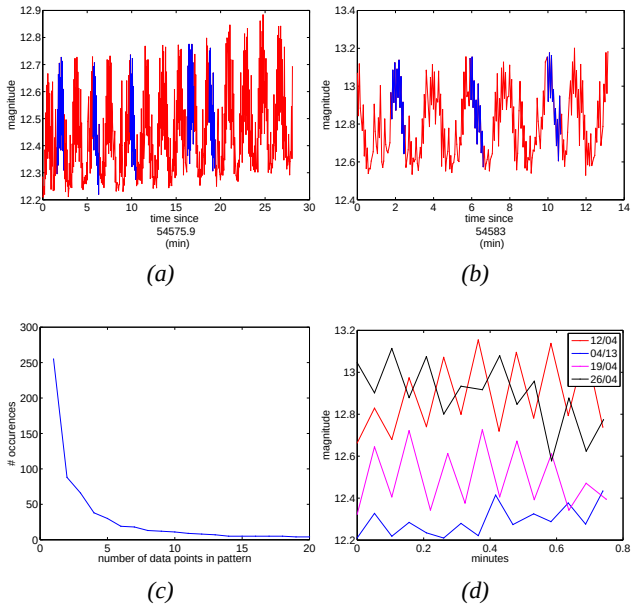

Figure 8.17: Light curves with highlighted pattern of the Blok DM-2 satellite 91010F (a) April 19 and (b) April 26. In (c), the size of the pattern as a function of the number of detected repetitions in the light curve of April 19. (d) Patterns found in all four light curves of Fig. 8.12 in one plot.

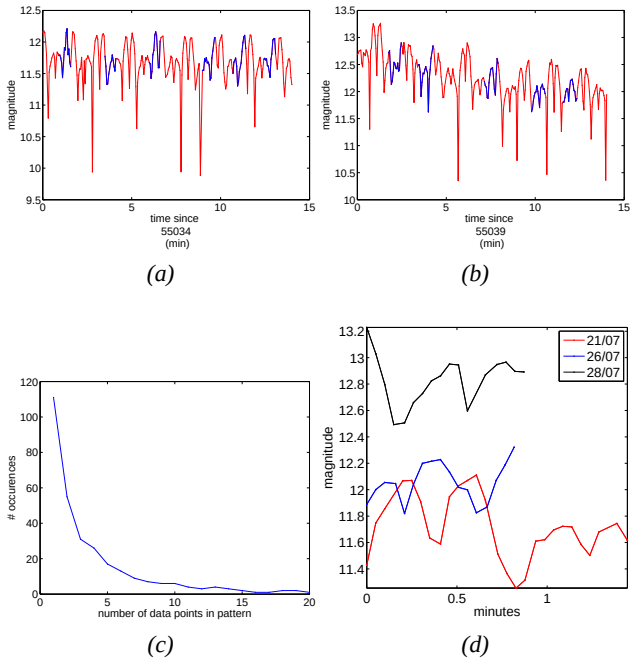

Figure 8.18: Light curves with highlighted pattern of the Gorizont 33 satellite 90102A (a) July 21 and (b) July 26. In (c), the size of the pattern as a function of the number of detected repetitions in the light curve of July 21. (d) Patterns found in all three light curves of Fig. 8.13 in one plot.

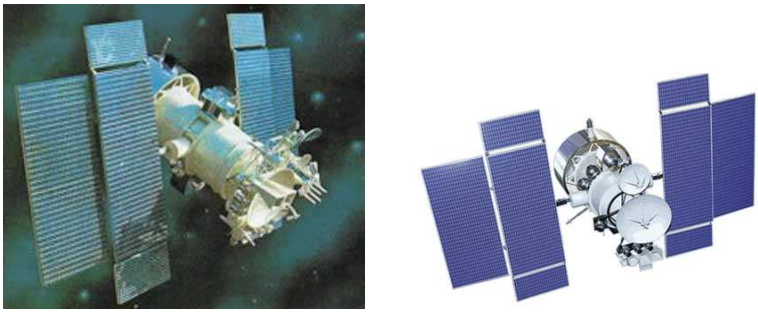

(a) Gorizont *(b) Raduga*

Figure 8.19: Russian communication satellites (a) Gorizont and (b) Raduga [88].

8.5 Light Curve Measurements in Comparison with Orbit Determination Results

In the current section light curves of four objects are investigated: two LAMR objects, 79105A (Gorizont-3) and 80081A (Raduga-7), whose orbits have been investigated in Section 7.4.4.1, and two HAMR objects of the internal AIUB catalogue, E06321D and E06293A, whose orbits have been investigated in Section 7.4.6.

8.5.1 Two Examples of Low Area to Mass Ratio Debris

Gorizont-3 and Raduga-7 are both Russian communication satellites, which are not operational anymore. The Gorizont satellites have a mass of about 2200 kg and carry eight transponders. They are 3-axis stabilized using liquid propellant micro-engines of the KAUR-3 platform during their life time. The pointing is within 0.5 degrees accuracy towards the Earth's center. The dimensions of the satellites are (including solar panels) 5.45 x 3.30 x 9.46 meters [74]. An image of the satellite model is displayed in Fig. 8.19a. The Gorizont-3 satellite 79105A is in a geostationary orbit with, at present, an inclination of around 14.6 degrees and negligible eccentricity, its estimated AMR value is about $0.007\,\mathrm{m^2kg^{-1}}$.

Raduga satellites have a mass of about 2000 kg and are 3-axis stabilized with the same KAUR-3 platform, which was first deployed in the Raduga satellites and then became a base for the Gorizont models. They have two transponders and their dimensions are (including solar panels) about 5.50 x 2.50 x 9.50 meters [74]. An image of the Raduga satellite model can be found in Fig. 8.19b. The Raduga-7 satellite 80081A is nowadays in a geostationary orbit with an inclination of about 14.4 degrees and negligible eccentricity, its estimated AMR value is about $0.018\,\mathrm{m^2kg^{-1}}$.

The orbit determinations in Section 7.4.4.1 revealed that low rms orbits over long fit intervals larger than 30 days could be determined for Gorizont-3, 79105A, and that the propagation resulted in small differences between the ephemerides and further observations. For Raduga-7, 80081A, orbit determination over long fit arcs was not successful. The propagation lead to rapidly increasing differences of the ephemerides compared to observations only 20 days after the epoch of the last observation, which was

Table 8.4: Light curve measurements for object Gorizont-3 79105A.

Date	start epoch (MJD)	ϕ (deg)	ϕ_{xy} (deg)	ϕ_{xz} (deg)
Feb 2 2008	54499.0	40.5 to 54.0	35.4 to 48.9	26.6 to 30.2
Feb 3 2008	54499.8	16.6 to 11.7	13.8 to 2.9	9.7 to 14.7
Feb 7 2008	54503.9	16.8 to 20.7	9.7 to 14.6	17.6 to 18.9
Feb 18 2008	54514.8	26.7 to 10.7	26.6 to 6.0	1.82 to 9.9
Aug 8 2010	55417.1	80.5 to 85.3	78.8 to 83.3	26.1 to 27.7
Sep 21 2010	55461.0	56.7 to 61.6	56.3 to 61.3	13.1 to 16.0
Dec 9 2010	55539.8	18.3 to 15.3	11.1 to 6.1	41.6 to 36.5
Dec 26 2010	55557.0	30.0 to 50.8	25.4 to 47.4	66.3 to 75.9
Jan 2 2011	55564.0	52.0 to 55.4	47.8 to 51.2	62.3 to 63.2

Table 8.5: Light curve measurements for object Raduga-7 80081A.

Date	start epoch (MJD)	ϕ (deg)	ϕ_{xy} (deg)	ϕ_{xz} (deg)
Sep 21 2010	55461.1	20.9 to 23.9	20.8 to 23.7	2.3 to 3.1
Oct 5 2010	55475.0	23.7 to 21.2	21.1 to 15.6	11.1 to 10.4
Dec 9 2010	55539.8	99.4 to 94.7	96.6 to 91.9	70.1 to 68.6
Dec 13 2010	55544.0	38.9 to 34.4	36.7 to 31.8	60.6 to 58.8
Dec 26 2010	55556.9	63.3 to 41.8	62.9 to 40.6	96.6 to 88.6
Jan 2 2011	55563.9	54.0 to 49.3	53.9 to 49.0	107.0 to 104.9

used in the orbit determination. Further orbit determinations with different subsequent or partly overlapping fit intervals, lead to different osculating elements and varying estimations of the AMR value. For both objects, 79105A and 80081A, light curve measurements have been taken.

Some of the light curves measured of Gorizont-3, 79105A, over the years are displayed in Fig. 8.20. The displayed light curves were taken in 2008 on January 18, in 2010 on August 8, September 21, December 9, December 26, and in 2011 on January 2. The dates, start times and the variation of the different phase angles – $\phi/\phi_{xy}/\phi_{xz}$ – during the measurement are listed in Tab. 8.4. Brightness variations of more than two magnitudes are measured. In the light curve displayed in Fig. 8.20(f) even variations of over five magnitudes do occur. This light curve was observed under an overall phase angle and phase angle $\phi/\phi_{xy}/\phi_{xz} \approx 60/60/14$ degrees. There seem to be displayed a similar but not identical brightness variation pattern in all light curves, although the light curves were observed under different phase angles. No clear dependency on the brightness or the peculiarity of the pattern on the different phase angles can be determined.

Six light curves of the object Raduga-7, 80081A, are displayed in Fig. 8.21. They have been taken on six different nights from September 2010 to January 2011. The dates, and the variation of the phase

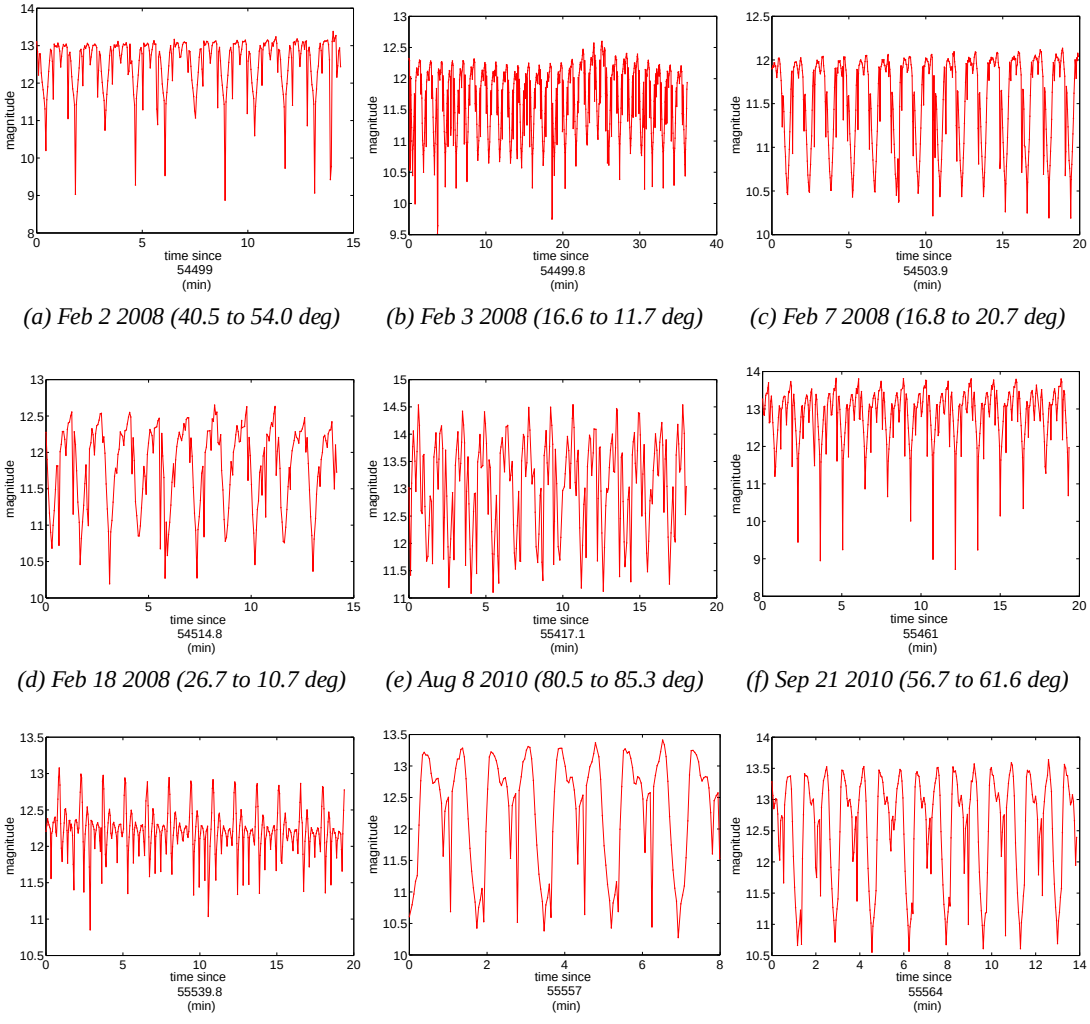

(a) Feb 2 2008 (40.5 to 54.0 deg) *(b) Feb 3 2008 (16.6 to 11.7 deg)* *(c) Feb 7 2008 (16.8 to 20.7 deg)*

(d) Feb 18 2008 (26.7 to 10.7 deg) *(e) Aug 8 2010 (80.5 to 85.3 deg)* *(f) Sep 21 2010 (56.7 to 61.6 deg)*

(g) Dec 9 2010 (18.3 to 15.3 deg) *(h) Dec 26 2010 (30.0 to 50.8 deg)* *(i) Jan 2 2011 (52.0 to 55.4 deg)*

Figure 8.20: Light curves measurements of the object of Gorizont-3 79105A over time: (a) Feb 2 2008, (b) Feb 3 2008, (c)Feb 7 2008, (d) Feb 18 2008, (f) Sep 21 2010, (g) Dec 9 2010, (h) Dec 26 2010, (i) Jan 2 2011.

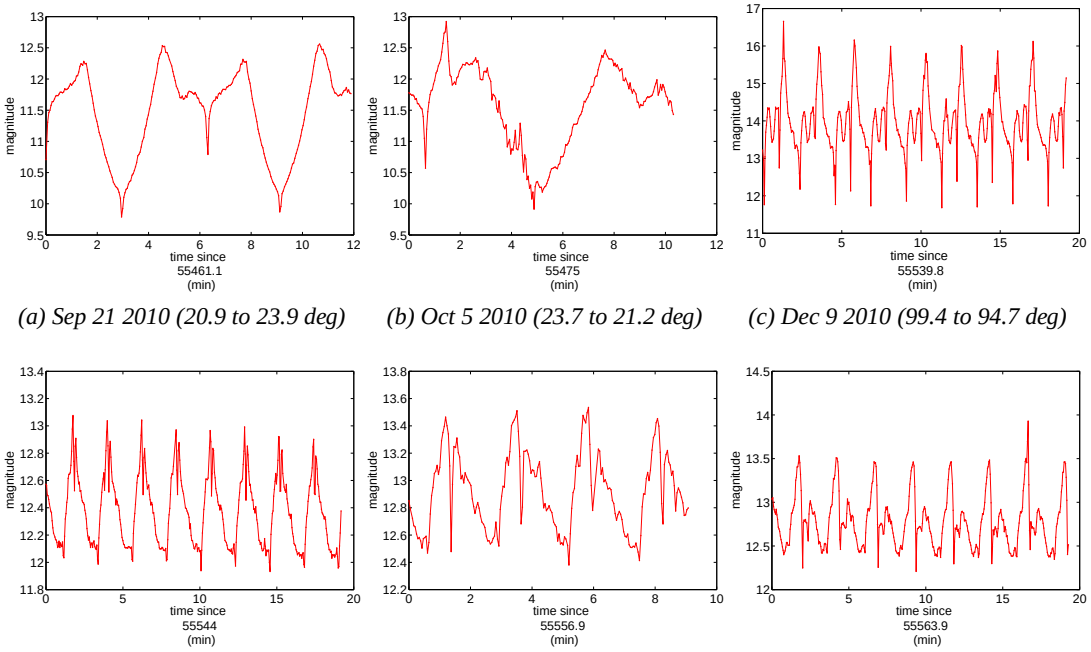

(a) Sep 21 2010 (20.9 to 23.9 deg) *(b) Oct 5 2010 (23.7 to 21.2 deg)* *(c) Dec 9 2010 (99.4 to 94.7 deg)*

(d) Dec 13 2010 (38.9 to 34.4 deg) *(e) Dec 26 2010 (63.3 to 41.8 deg)* *(f) Jan 2 2011 (54.0 to 49.3 deg)*

Figure 8.21: Light curves measurements of the object Raduga-7 80081A over time: (a) Sep 21 2010, (b) Oct 5 2010, (c) Dec 9 2010, (d) Dec 13 2010, (e) Dec 26 2010, (f) Jan 2 2011.

angles, ϕ, ϕ_{xy} and ϕ_{xz} are displayed in Tab. 8.5.

There is a similar brightness pattern visible in all light curves, but the time distribution of the pattern varies heavily. The pattern seems to be spread over far longer time intervals in Fig. 8.21(a) and Fig. 8.21(b). Those are the light curves taken under the smallest phase angle in the selection of light curves displayed in Fig. 8.21. The 79105A satellite does not show such a phase angle dependency.

The object Raduga-7, 80081A, seems to behave differently over time than the object 79105A. This would support the finding of the orbit determination, despite the huge similarities of the satellites. The light curves might be an additional hint that the object 80081A is in an unstable state. The light curves of object Raduga-7, 80081A, also clearly show, that a fingerprinting, which is stable over longer time intervals, is even for such a large space debris object not always possible, since even the similar patterns of 79105A are subject to change over time.

8.5.2 Two Examples of High Area to Mass Ratio Debris

The orbits of two objects of the internal AIUB catalogue, E06321D and E06293A, have been investigated in section Section 7.4.6. E06321D is in geostationary orbit with an eccentricity of around 0.036 and an inclination of around seven degrees. Its AMR varies around a value of $2.5\,\mathrm{m^2kg^{-1}}$. E06293A is a geostationary object, its orbit has an eccentricity around 0.092, and an inclination of around eleven degrees. Its AMR value is about $15.9\,\mathrm{m^2kg^{-1}}$. Both objects have been followed for several years by the AIUB.

Table 8.6: Light curve measurements for object E06321.

Date	start epoch (MJD)	ϕ (deg)	ϕ_{xy} (deg)	ϕ_{xz} (deg)
Apr 19 2007	54210.0	30.9 to 33.2	31.4 to 33.8	17.5 to 19.3
Feb 7 2008	54503.8	82.4 to 78.0	82.7 to 78.1	159.4 to 156.7
Mar 18 2008	54543.9	31.7 to 25.6	30.5 to 23.7	10.2 to 10.8
Sep 22 2009	55096.9	20.6 to 18.5	20.2 to 18.2	3.9 to 3.5
Sep 23 2009	55097.9	55.9 to 13.1	55.4 to 12.7	15.4 to 3.11
Dec 9 2009	55174.8	27.7 to 25.8	17.9 to 14.5	58.9 to 58.8
Jan 17 2010	55213.9	36.7 to 43.5	24.5 to 33.1	45.9 to 46.5
Dec 13 2010	55543.8	37.8 to 33.0	31.4 to 24.8	68.4 to 68.3

Table 8.7: Light curve measurements for object E06293.

Date	start epoch (MJD)	ϕ (deg)	ϕ_{xz} (deg)	ϕ_{xz} (deg)
Apr 18 2007	54207.9	31.1 to 29.7	29.7 to 28.2	11.06 to 11.2
Mar 5 2008	54531.1	9.0 to 10.3	8.6 to 10.0	3.1 to 3.0
Mar 18 2008	54543.9	55.9 to 52.7	55.8 to 52.6	6.3 to 4.9
July 21 2009	55034.0	4.3 to 5.7	1.3 to 4.6	7.2 to 8.4

The timely evolution of the orbital elements and the AMR value, determined in the orbit determination process, has been investigated in Section 7.4.6. It was shown that most of the determined AMR values of E06321D follow a periodic evolution over time, with a period of roughly one year. But also values, which do not seem to follow that trend do occur. No clear trend in the AMR values could be determined for object E06293A. AMR values range from 18 to 15.4 m^2kg^{-1}, most of the values lie between 15.5 ad 16.0 m^2kg^{-1}.

In Fig. 8.22 eight light curves of the object E06321D, taken from April 2007 to December 2010, are displayed. The dates, start epochs of the light curves, as well as the phase angles are displayed in Tab. 8.6. In Fig. 8.24 four light curves of object E06293A, taken between April 2007 and July 2009, are displayed. The epochs and phase angles are displayed in Tab. 8.7. Rapid brightness variations over several, up to four, magnitudes within shortest time intervals do occur for both objects. The average brightness of both objects is not clearly dependent on the phase angle. For object E06321D, e.g., as displayed in Fig. 8.22: The overall brightness is around 17.3 on September 22 in Fig. 8.22d, when observed under angle ϕ of 20.6 to 18.5 degrees, with a phase angle ϕ_{xy} 20.2 to 18.2 in and ϕ_{xz} 3.9 to 3.5 degrees, but the magnitude is around 12.5 in Fig. 8.22h.

The pattern visible in the light curves of both objects vary over time, a light curve finger printing does not seem to be feasible. Even light curves observed under similar phase angles, as, e.g.for object E06293A, in Fig. 8.24b and 8.24c different pattern are visible.

A sampling rate of three seconds seems even not to be rapid enough, in Figure of object E06321D overtone harmonics are visible, see Fig. 8.22a and 8.22b. For both objects the Fourier analysis revealed

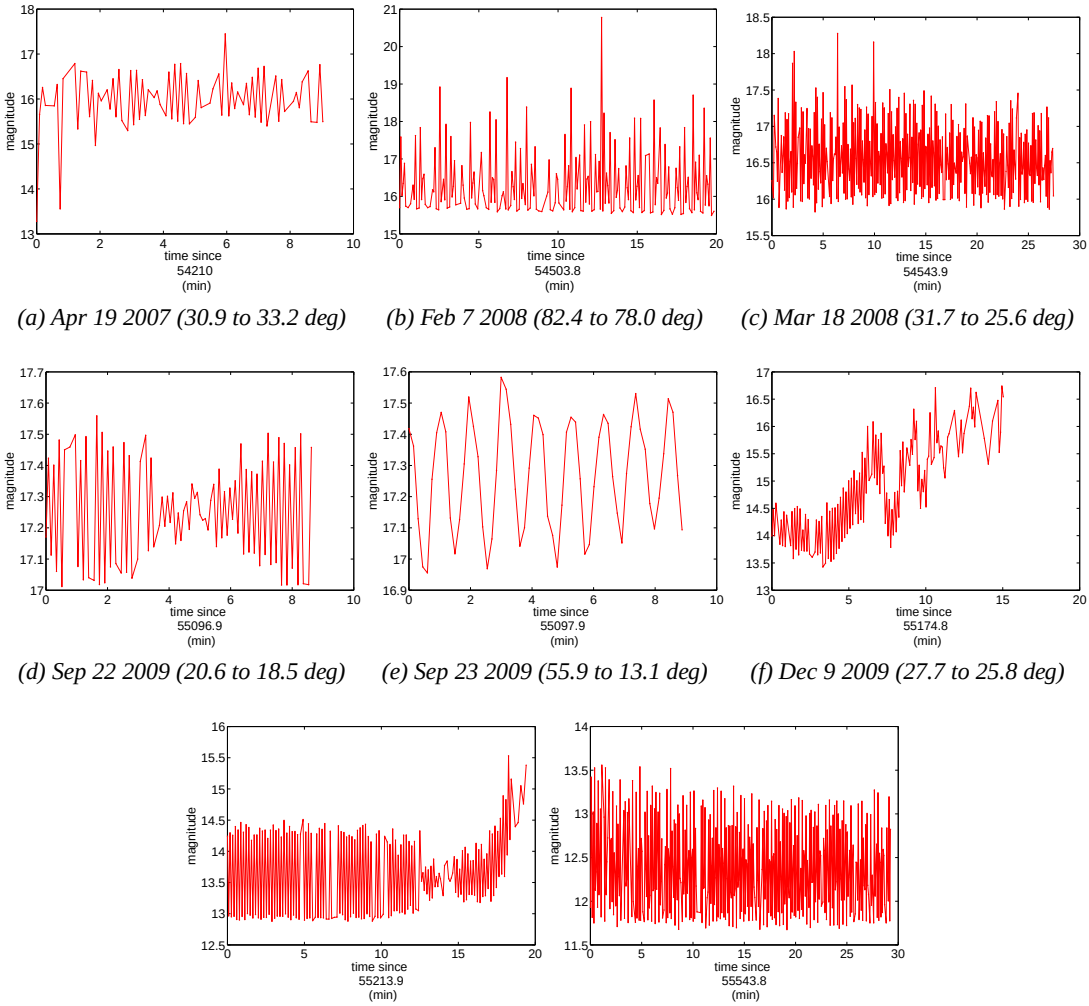

(a) Apr 19 2007 (30.9 to 33.2 deg) *(b) Feb 7 2008 (82.4 to 78.0 deg)* *(c) Mar 18 2008 (31.7 to 25.6 deg)*

(d) Sep 22 2009 (20.6 to 18.5 deg) *(e) Sep 23 2009 (55.9 to 13.1 deg)* *(f) Dec 9 2009 (27.7 to 25.8 deg)*

(g) Jan 17 2010 (36.7 to 43.5 deg) *(h) Dec 13 2010 (37.8 to 33.0 deg)*

Figure 8.22: Light curves measurements of the object E06321D over time: (a) Apr 19 2007, (b) Feb 7 2008, (c) Mar 18 2008, (d) Sep 22 2009, (e) Sep 23 2009, (f) Dec 9 2009, (g) Jan 17 2010, (h) Dec 13 2010.

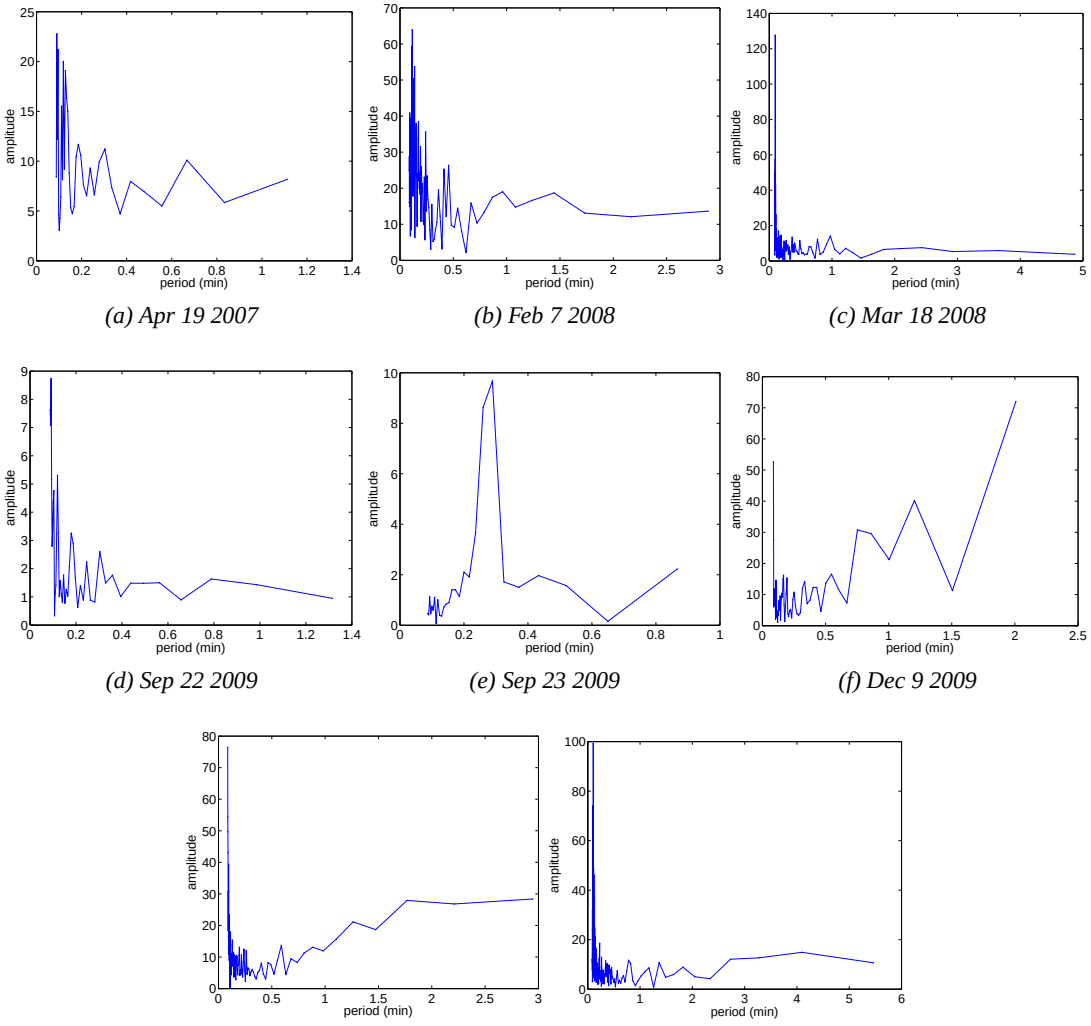

(a) Apr 19 2007 *(b) Feb 7 2008* *(c) Mar 18 2008*

(d) Sep 22 2009 *(e) Sep 23 2009* *(f) Dec 9 2009*

(g) Jan 17 2010 *(h) Dec 13 2010*

Figure 8.23: Fourier decomposition of the light curves measurements of the object E06321D over time: (a) Apr 19 2007, (b) Feb 7 2008, (c) Mar 18 2008, (d) Sep 22 2009, (e) Sep 23 2009, (f) Dec 9 2009, (g) Jan 17 2010, (h) Dec 13 2010.

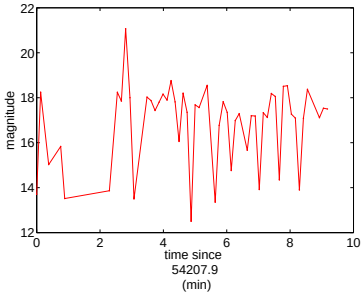

(a) Apr 18 2007 (31.1 to 29.7 deg)

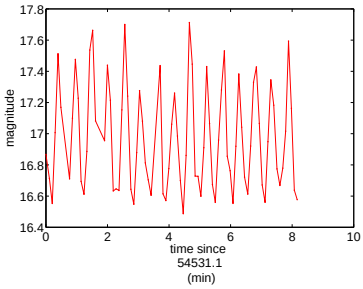

(b) Mar 5 2008 (9.0 to 10.3 deg)

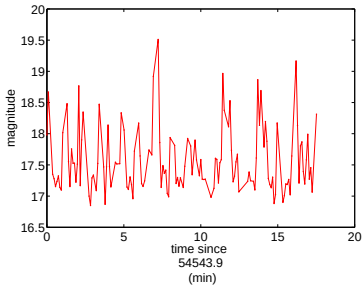

(c) Mar 18 2008 (55.9 to 52.7 deg)

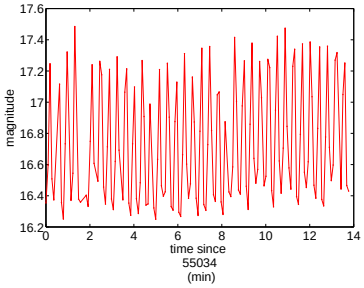

(d) July 21 2009 (4.3 to 5.7 deg)

Figure 8.24: Light curves measurements of the object E06293A over time: (a) Apr 18 2007, (b) Mar 5 2008, (c) Mar 18 2008, (d) July 21 2009.

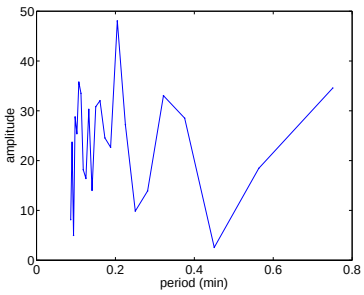

(a) Apr 18 2007

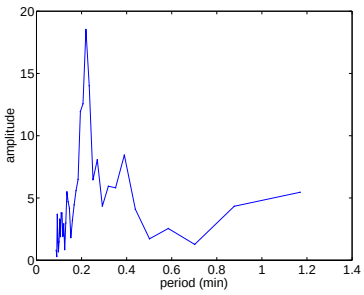

(b) Mar 5 2008

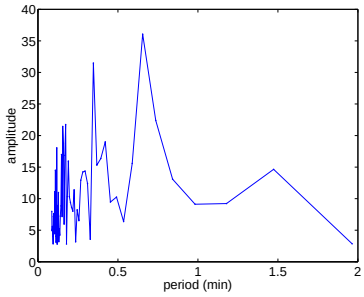

(c) Mar 18 2008

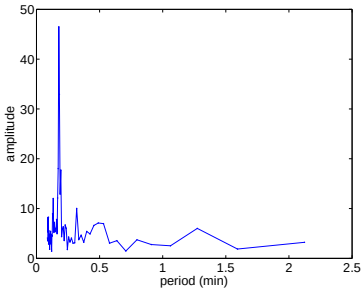

(d) July 21 2009

Figure 8.25: Fourier decomposition of the light curves measurements of the object E06293A over time:(a) Apr 18 2007, (b) Mar 5 2008, (c) Mar 18 2008, (d) July 21 2009.

very short periods. For object E06321D, a very small period of around 6 seconds, acquainted by several other very short periods, below 20 seconds, is detected, see Fig. 8.23. The Fourier decomposition of the light curves of E06293A are shown in Fig. 8.25. Very short periods could be determined in all light curves. Most significantly a period around 12 to 14 seconds shows up, in addition a period of 25 second is visible. A period of 38 seconds does occur also in Fig. 8.25c.

8.6 Conclusions

Different methods for the analysis of light curves have been discussed. The shape inversion developed by Minkowski is one possibility to derive shapes from light curves, although from optical observations only the area albedo product is available and only convex shapes can be reconstructed. Current methods of shape inversion for concave objects heavily rely on a smooth surface, which is not the case for space debris objects. A shape inversion can never be unique.

A number of methods exist, which give limited insight in the material composition, e.g., color photometry and spectral measurements. Glint and single facet analysis as well as the phase angle finger printing method, which disregards attitude motion, do not allow to distinct different shapes. The determination of the spin rate and axis of space objects via the difference between synodal and sidereal rotation is not applicable to GEO objects. The method relies furthermore on a correct decomposition of the rotation periods via a Fourier analysis, e.g., for example of the synodic rotation periods, which in turn requires that the object is rotating slowly around only one spin axis.

Light curves of simple shapes under different lighting and viewing conditions, and attitude states have been simulated. The same attitude rotation rates may produce different light curves under different lighting conditions. The Fourier analysis of the simulated light curves indicates that the detection of the main rotation periods is largely independent of the phase angle as long as – as for the MLI case – the object is not invisible for large parts of the observation interval.

The Fourier analysis of the real light curves correctly revealed no significant period for the spin-stabilized satellite, which only rotates around its symmetry axis orthogonal to the observer. For the upper stage and the Gorizont satellite, two to three rotation periods could be detected, which seem to be stable over a couple of days and independent of the phase angle during the observation. One of the detected periods is of the order of a few seconds only.

A pattern recognition algorithm was developed, tested on the simulated light curves, and applied to observed light curves. Patterns could be detected in all observed light curves. The patterns are not completely identical for different light curves of the same object, but are clearly different for the two different objects examined. The size of the patterns that could be found is of the order of the rotation periods detected in the Fourier analysis.

The light curves of two similar decommissioned Russian communication satellites with low AMR have been investigated. For both satellites light curve measurements over several years are available. They both have been in the same stabilization mode but are now decommissioned and not actively stabilized any more. The objects are in similar geostationary orbits. Orbit determination revealed that the AMR of one object does not seem to be stable, contrary to the other. The light curves are supporting the as-

sumption that the one object may not be in a stable attitude state. The light curve measurements show that even for large space debris objects the pattern in light curves can be significantly different from one measurement to the next.

The light curves of two HAMR objects have been investigated. Measurements over several years are available. Both objects show rapid brightness variations. Their Fourier decomposition revealed periods of a few seconds; an under-sampling during the measurement is very likely. The light curves of the two investigated objects undergo significant changes over time, which are not phase angle dependent. It could be an indication for a changing attitude motion over time. A slowly changing attitude motion could be one explanation, why different AMR values are found in the orbit determination of both objects over time.

9. Summary

> Ever tried. Ever failed. No matter. Try again. Fail again. Fail better.
>
> *Samuel Beckett*

From optical ground based observation of space resident objects in GEO or HEO regimes only non-resolved images are available with the current observation facilities. The identification of space resident objects based on such observations poses a significant challenge.

Space resident objects are either searched for in so-called surveys, that is scanning particular regions of the sky, or, when their orbit is known, are observed by means of so-called follow-up observations. For surveys no a priori information on the objects themselves and on their orbits is available.

The discrimination of unknown objects from so-called cosmics on single frames is a crucial step in the image processing chain. Cosmics are charged particles impinging the detector either stemming from cosmic ray showers from deep space, or from slightly radioactive substances close to the detector, e.g., in the CCD dewar. If the pixel scale is small enough, e.g., 0.6 arcseconds as for the ESASDT, the real object images are smeared over several pixels due to atmospheric turbulence. This allows a discrimination in a majority of cases between object images and cosmics by eye. For an automatic discrimination it turned out that no single reliable criterion could be found. A discrimination based on contrast or edge detection, does successfully identify part of the cosmics, but, with a conservative tuning, a significant amount of cosmics is still present after filtering. A discrimination based on various combinations of contrast and full width at half maximum threshold values of possible object images or cosmics on the frames is a successful tool, but it is far from perfect. The large number of criteria is hard to tune and highly depending on the specific camera setup. A full automation without a manual check could not be achieved. A future step would be to base the discrimination of cosmics and object images on machine learning algorithms, able to work out many different interdependent criteria. For wide-field telescopes as, e.g., ZimSMART with a pixel scale of several arcseconds per pixel a discrimination between cosmics and object images on the single frames is hardly possible.

If the pixels are too large the only chance to discriminate the object images from comics consists in linking together the possible object images on series of consecutive frames, since the cosmics are spread randomly over the frames. This object image linking process requires a decision on, which object images on the single frames of observation series are representations of the same object. For this decision, it cannot be supposed that the object images have the same appearance on all single frames, since rapid brightness changes of the object images and/or image distortions on the edges of frames from wide-field telescopes can occur. Furthermore an object image is not always detected although the object was in the

field of view during an exposure. The object image can be below the detection threshold or in front of a star. An object image linking under the assumption of a linearly constant movement derived from two subsequent object images was developed for GEO and HEO objects. Dynamically updating the velocity vector with every newly linked object image allows to account for deviations from the linear movement. Under this premise, object images of HEO objects when not close to perigee and MEO objects images are possible to be linked correctly. If only around 60 possible object image candidates are on each frame, a link of three object images is already sufficient to have a probability for random linking of below 0.5 percent. For frames from a wide-field telescope with several hundred possible object image candidates on each frame, four object images are required to be linked, or additional velocity limits have to be imposed, for a random linking rate of below 0.5 percent.

After the single object images have been successfully linked, it is checked, if the observed object is already listed in an orbit element catalogue. A six parameter orbit determination from a short observation tracklet spanning only a couple of minutes results in considerable errors in the determined orbital elements for observations of GEO and GTO objects. These elements can therefore not be used for a reliable identification of GEO objects in a catalog. For short observation tracklets a comparison of the observed position and apparent velocity on the sky with catalogue ephemerides has been proven a successful technique. Via a projection in the tangent plane, along-track and cross-track distances are determined, as well as the angle between the apparent velocity vector of the observed and the catalogued object in order to achieve a reliable identification of observation tracklets with catalogue orbits.

In publicly available catalogues, such as USSTRATCOM/DISCOS, e.g., the orbital elements are listed in the two line element (TLE) format. In the two-line element format, no information about the accuracy of the orbital data is available. The residuals, which could be determined empirically between the propagated ephemerides from two-line elements and optical observations are of the order of 0.03 degrees, or about 25 kilometers in along-track and around 10 kilometers in cross-track direction for GEO objects. For HEO objects the corresponding values are 0.05 degrees, or around 30 kilometers in along-track and 15 kilometers in cross-track direction. The difference between the SDP4 propagator, with which the TLE data is created and the SDP8 propagator, which is a newer development, is fully negligible in the GEO regime. For HEO objects the differences are of the order of 0.01 degree. In this case, the SDP4 propagator shows slightly better results.

The residuals of ephemerides of the AIUB are in general much smaller than for the TLE ephemerides. The orbits of the AIUB observations are determined and propagated with the CelMech tool, which is based on a least squares approach. Orbits are in general improved, if the parameter of the direct radiation pressure is estimated together with the orbital elements, especially for high-area-to-mass-ratio (HAMR) objects. Optical observation data is sometimes very sparse due to weather conditions or non-visibility of objects (for example GEO objects in drift orbits). When orbits are determined with sparse observations of one sensor or multiple sensors separated in latitude and longitude no significant larger or smaller differences in the propagated ephemerides to the observations do occur, as long as the overall number and temporal spacing of the observations are similar. Good orbits, in the sense of orbits, which result in small differences between the propagated ephemerides and further observations over 50 days of propagation time, can be determined even with very few observations only: It has been investigated, that two sets of only four to five observations each can be sufficient for good orbits, as long as the observations within the sets are spaced over more than one hour for GEO objects, under the premise of availability of a priori elements. The distribution of the observations in anomaly or the time interval between the first and the

second sets only plays a secondary role in this specific sparse data setup.

The orbit determination of observations of HAMR objects poses special challenges. Orbits are usually determined over fit spans of 30 to 40 days. Within each orbit determination a constant value for the AMR value is estimated. But the AMR value can differ significantly from one to the next orbit determination, although the orbital elements show a consistent trends. No dependence of the change in the AMR value to the absolute AMR value could be found. The AMR values do in general not follow a specific pattern, only some objects show signs of periodic changes. The changes in the AMR value could be due to a changing average attitude (fast rotating/tumbling objects), from one fit span to the next.

To characterize the attitude motion of space objects, brightness measurements of the non-resolved object images over time, so-called light curves can be used. The brightness received by the observer depends on the viewing and lighting condition, which are generally known, but also the attitude motion, the shape and the reflection properties of the surface(s) of the space object, which are not known in general. The inversion of light curves is an under-determined mathematical problem, which cannot be uniquely solved. Inversion methods known from asteroid research generally rely on smooth surfaces and unique Lambertian reflection properties, both do not apply to man-made space objects in general. Several methods can be used to gain some insight in shape and attitude parameters via phase angle dependencies of the brightness measurements. It is important to take the complete phase angle information, not only the projection of the angle into one plane, into account, as simulated light curves showed. The determination of spin rates via Fourier transformation, or alike, may give misleading results, due to symmetries in the object's shape and/or the limited observation time. The decomposition of light curves of space debris resulted in very small periods, which indicate possible aliasing effects. The periods are found to be the same in light curves separated by several months. Different pattern for different objects could be determined, but were found to be by no means an instrument for uniquely tagging or identifying objects.

Light curve measurements and orbit determinations suggest that large, formerly stabilized GEO objects may end up in a tumbling attitude motion. A "fingerprinting" based on light curves is not possible for all space debris objects, since the appearance of the light curves of the same object can be subject to phase angle independent changes. Space debris objects with high area to mass ratio values show rapid brightness changes and signatures, which change over time. This could be a hint for the different area to mass ratio values, estimated in the orbit determination of those objects, are real and not a deficiency of the orbit determination process.

10. Acknowledgments

> I am little concerned with beauty or perfection. I don't care for the great centuries. All I care about is life, struggle, intensity.
>
> *Emile Zola*

I would like to acknowledge that work was supported by the Swiss National Science Foundation through grants 200020-109527 and 200020-122070 and the observations from the ESASDT were acquired under ESA/ESOC contracts 15836/01/D/HK and 17835/03/D/HK.

I want to thank Gerhard Beutler, the head of the AIUB, and Thomas Schildknecht, the head of the Optical Astronomy Group at the AIUB, for the opportunity to do my PhD thesis at the Astronomical Institute of the University of Bern.

I would like to acknowledge courtesy of the Keldish Institute of Applied Mathematics and the ISON network to provide further observations of objects discovered with the ESASDT by the AIUB.

My thank goes to the Schweizerische Studienstiftung, for their financial support but also for a challenging time and opportunities to get engaged, meet people and to have the chance to come to a deeper understanding of Swiss culture. I would also like to honor the Swiss Society for Astrophysics and Astronomy, the European Space Agency and Young Researcher Support of the Faculty of Natural Science of the University of Bern for the financial support to attend conferences.

My special thanks and appreciation goes to Thomas Schildknecht for introducing me in the topic of space debris, for his help and support, and the, hopefully successful, guidance to an understanding how scientific results can profoundly be gained. It is much appreciated that he gave me all possible space and freedom for professional development and was open to almost all my (good and not so good) ideas and innovations. I want to especially thank him for the unbelievable high trust he put in me and my professional work, which, to my own surprise, could never be weakened no matter what happened.

I would like to especially thank Gerhard Beutler, who was always open to discuss about orbit determination and was never short of good advice and guidance. He took all the time to read my thesis critically, to question it profoundly, to provide suggestions and to discuss it. I would like to thank him for his endurance, his ability to ask the right questions, and his patience.

I would like to thank the co-referee of this work, Patrick Seitzer, for his time, all his efforts, helpful

discussions and fruitful meeting in Ann Arbor.

My thank goes to all my colleagues at the AIUB and especially those of the Optical Astronomy Group for the great working atmosphere and support. My special thanks goes to Reto Musci, who was a great support at the beginning of my thesis and work at the AIUB. I would like to thank him for his time, he spend unasked, his patience to answer all my questions, his advice and his efforts to enable a good start into my thesis. I would like to thank Tim Flohrer for many professional and private discussions, good hints regarding my work and his overview, which he shared with me, over relevant publications and the whole scientific community. I would like to thank Johannes Herzog and Andreas Hinze for the very good collegial work and support, their help and support their questions to challenge me and their friendship, which is much appreciated, not forgetting to mention their constant efforts to enlighten me not only in the matters of practical astronomy but also in the lost culture of the former German Democratic Republic. My thank also goes to Martin Ploner for his work on the ZimControl software and at the Zimmerwald observatory in general, to make it possible not only to gain regular observations but also light curves and for introducing the longgeo and gtolong campaigns. My thank goes to all the observers of the Zimmerwald observatory not only for the regular observations but especially for their work in helping me to gain additional light curves, my thank goes in particular to Marcel Prohaska, Johannes Herzog, Stefan Funariu, Alexander Läderach, Alexander Scartazzini, Simon Willi and Sarah Arnold. I want to thank Markus Stalder for the computer support.

I would like to thank TS Kelso for his support and helpful discussions. I also would like to thank Vladimir Agapov and Dave Vallado for their ideas in discussion of some of my papers. I would like to thank Jyri Kuusela for his midnight calls at work.

I thank P.B. Smit for the snails in glasses.

I would like to thank God and the mediation through the roman and old catholic churches for keeping me alive. I would like to thank my parents for bringing me into life, for all their never ending love and trust, for their support, hopes and pride, they set in me.

The last words should belong to the Captain, my Captain:
Jugendlicher Übermut alleine ist nicht der beste Ratgeber auf hoher See, gepaart mit den Ratschlägen eines vielgeprüften Seemannes sind jedoch schon viele neue Landen entdeckt worden.

Bibliography

[1] V. Agapov and I. Molotov. Characterization of GEO and HEO Objects Using Multi Year Statistics on Brightness Measurements. In *Proceedings of the International Astronautical Congress 2010, A6.1.6, Prague, Czech Republic, 27 Sep-1 Oct, 2010*, 2010.

[2] R.R. Allan and G.E. Cook. The Long-Period Motion of the Plane of a Distant Circular Orbit. In *Proc R Soc Lond*, volume 280: 97-109, 1964.

[3] J.L. Arsenault, L. Chaffee, and J.R. Kuhlmann. General Ephemeris Routine Formulation Document. In *Rept. ESD-TDR-64-522, Aeronutronic Publ. U-2731*, Aug., 1964.

[4] G. Beutler. *Methods of Celestial Mechanics*. Two Volumes. Springer-Verlag, Heidelberg, 2005. ISBN: 3-540-40749-9 and 3-540-40750-1.

[5] M. Bourez-Laas, A. Klotz, E. Ducrotte, M. Boer, and G. Blanchet. Rapid Brightness Variations as a Tool to Enhance Satellite Detectability. In *Proceedings of the Fifth European Conference on Space Debris, ESOC, Darmstadt, Germany, 30 March-2 April 2009*, 2009.

[6] B. Bowman. A First Order Semi-Analytical Perturbation Theory for Highly Eccentric 12 Hour Resonating Satellite Orbits. In *1st Aerospace Control Squadron Repost, Colorado Springs, CO*, Nov., 1971.

[7] D. Brouwer. *Solution of the Problem of Artificial Satellite Theory Without Drag*. U.S. Air Force Cambridge Research Center, Geophysics Research Directorate, 1959. AFCRC-TN-59-638, Bedford, MA.

[8] D. Brouwer. Solution of the Problem of Artificial Satellite Theory Without Drag. *Astronomical Journal*, (64, 1274):378 – 397, 1959.

[9] B. Calef, J. Afrikano, B. Birge, and P. Kervin. Photometric Signature Inversion. *Unconventional Imaging II ed. Gamiz, V., Procedings of SPIE*, 6307:63070E, 2006.

[10] CelesTrak. CelesTrak Homepage. `http://celestrak.com`, 2010.

[11] J. Cronin, T.C. Gaisser, and S.P. Swordy. Cosmic Rays at the Energy Frontier. *Sci. Amer.*, 276(1):44, 1997.

[12] P. Danielsson and O. Seger. Generalized and Separable Sobel Operators. *Machine Vision for Three-Dimensional Scenes, Academic Press, Inc., edited by H. Freeman*, pages 347 – 375, 1990.

[13] B.N. Delaunay. Sur la sphère vide. *Bulletin of Academy of Sciences of the USSR 7*, No 6:793 – 800, 1934.

[14] European Space Agency. European Space Agency Website. `http://www.esa.int/esaCP/SEMHDJXJD1E_FeatureWeek_0.html`, 2005.

[15] T. Flohrer, H. Krag, and H. Klinkrad. Assessment and Categorization of TLE Orbit Errors for the US SSN Catalogue. In *Proceedings of the 2008 AMOS Technical Conference, 10-14 September 2008, Maui, Hawaii, USA*, 2008.

[16] T. Flohrer, H. Krag, H. Klinkrad, B.Ãastida Virgili, and C. Früh. Improving ESA's Collision Risk Estimates by an Assessment of he TLE orbit errors of the US SSN Catalogue. In *Proceedings of the Fifth European Conference on Space Debris, ESOC, Darmstadt, Germany, 30 March-2 April 2009*, 2009.

[17] T. Flohrer, T. Schildknecht, C. Früh, R. Musci, and M. Ploner. Optical Observations at the Zimmerwald Observatory. In *Proceedings of the International Astronautical Congress 2007, Hyderabad, India, 21 - 28 Sep, 2007*, 2007.

[18] R. Florentin-Nielsen, M. Anderson, and S. Nielsen. Cosmic Rays at the Energy Frontier. *eds. A.G.D. Philip, K.A. Janes and A.R. Upgren, Kluwer*, (1):207ff, 1995.

[19] C. Früh, R. Musci, and T. Schildknecht. Improved Method for Recognizing unknown Space Debris Objects on Series of CCD Frames. In *Proceedings of the International Astronautical Congress 2008, A6.5.2, Glasgow, Scotland, Great Britain, 29 Sep- 3 Oct, 2008*, 2008.

[20] C. Früh and T. Schildknecht. Analysis of Observed and Simulated Light Curves of Space Debris. In *Proceedings of the International Astronautical Congress 2010, A6.1.9, Prague, Czech Republic, 27 Sep-1 Oct, 2010*, 2010.

[21] C. Früh and T. Schildknecht. Investigation of Properties and Characteristics of High-Area-to-Mass Ratio Objects Based on Examples of Optical Observation Data of Space Debris Objects in GEO-like Orbits. In *Proceedings of the 2010 AMOS Technical Conference, 14-17 September 2010, Maui, Hawaii, USA*, 2010.

[22] C. Früh and T. Schildknecht. Orbit Propagation and Validation with Angle-Only Observations. In *Proceedings of the 20th AAS/AIAA Astrodynamics Specialist Conference,Toronto, Canada, August 2nd - 5th, 2010*, volume Toronto, Canada, 2010.

[23] C. Früh and T. Schildknecht. Combination of Light Curve Measurements and Orbit Determination for Space Debris Identification. In *Proceedings of the International Astronautical Congress 2011, A6.1.14, Cape Town, South Africa, 3 - 7 Oct, 2011*, 2011.

[24] C. Früh, T. Schildknecht, A. Hinze, and M. Reber. Optical Observation Campaign in the Framework of the ESA Space Surveillance System Precursor Services. In *Proceedings of the European Space Surveillance Conference, Madrid, Spain, 7 - 9 June, 2011*, 2011.

[25] C. Früh, T. Schildknecht, R. Musci, and M. Ploner. Catalogue Correlation of Space Debris Objects. In *Proceedings of the Fifth European Conference on Space Debris, ESOC, Darmstadt, Germany, 30 March-2 April 2009*, 2009.

[26] C. Früh, T. Schildknecht, and M. Ploner. Comparison of different Methods of Ephemeris Retrieval for Correlation of Observations of Space Debris Objects. In *Proceedings of the 2009 AMOS Technical Conference, 1-4 September 2009, Maui, Hawaii, USA*, 2009.

[27] R. Green. *Spherical Astronomy*. Cambridge University Press, Cambridge, 1985. ISBN 3-521-31779-7.

[28] Particle Data Group. Review of Cosmic Rays, Revised August 2007 by T.K. Gaisser and T. Stanev (Bartol Research Inst., Univ. of Delaware). 2007.

[29] D. Hall, J. Africano, D. Archambeault, B. Birge, D. Witte, and P. Kervin. AMOS Observations of NASA's IMAGE Satellite. In *Proceedings of the 2006 AMOS Technical Conference, September 2006, Maui, Hawaii, USA*, 2006.

[30] D. Hall, C. Brandoch, K. Knox, M. Bolden, and P. Kervin. Seperating Attitude and Shape Effects for Non-resolved Objects. In *Proceedings of the 2007 AMOS Technical Conference, 16-19 September 2007, Maui, Hawaii, USA*, 2007.

[31] J. Hartung, B. Elpelt, and K.-H. Klösner. *Statistik*. R. Oldenbourg Verlag GmbH, München Wien, 2005. ISBN 3-486-57890-1.

[32] J. Herzog, C. Früh, and T. Schildknecht. Build-up and Maintenance of a Catalogue of GEO Objects with Zimsmart and Zimsmart2. In *Proceedings of the International Astronautical Congress 2010, A6.5.2, Prague, Czech Republic, 27 Sep-1 Oct, 2010*, 2010.

[33] C. Hirose, N. Kudo, I. Matsude, G. Adachi, I. Kurata, and Y. Furuwatari. Evaluation of the TLE Prediction Errors for Cinjunction Assessment. In *Proceedings of the International Astronautical Congress 2010, A6.2.8, Prague, Czech Republic, 27 Sep-1 Oct, 2010*, 2010.

[34] F.R. Hoots, R.L. Roehrich, and T.S. Kelso. Models for Propagation of NORAD Element Sets. *Spacetrack Report*, No 3, 1980.

[35] F.R. Hoots, P.W. Schuhmacher, and R.A. Glover. History of Analytical Orbit Modelling in the U.S. Space Surveillance System. *Journal of Guidance, Control and Dynamics*, 27(2): 174 – 185, 2004.

[36] S.B. Howell. *Handbook of CCD Astronomy*. Cambridge University Press, 2001. ISBN 0-521-64834-3.

[37] U. Hugentobler. Sssear search objects on masked frame, release 1997. In *Processing Software of the ESA Space Debris Telescope, developed by the Astronomical Institute of the University of Bern (AIUB), Switzerland*, 1997.

[38] U. Hugentobler and P. Fridez. Ssesel object image linking, release 1997. In *Processing Software of the ESA Space Debris Telescope, developed by the Astronomical Institute of the University of Bern (AIUB), Switzerland*, 1997.

[39] IAA. Position Paper on Orbital Debris. In *Acta Astronautica*, volume 31, pp 169-191, 1993.

[40] IAA. Position Paper on Orbital Debris (2001), updated version of IAA Position Paper on Orbital Debris 1993. 2001.

[41] N.L. Johnson. Medium Earth Orbits: Is There a Need for a Third Protected Region? In *Proceedings of the International Astronautical Congress 2010, A6.1.4.1, Prague, Czech Republic, 27 Sep-1 Oct, 2010*, 2010.

[42] JPL. Jet Propulsion Laboratory: Solar System Dynamics. `http://ssd.jpl.nasa.gov`.

[43] B. Kaasalainen et al. Optimization Methods for Asteroid Lightcurve Inversion I. Shape Determination. *Icarus*, 153:37 – 51, 2001.

[44] H. Karttunen, P. Kröger, H. Oja, M. Poutanen, and K.j. Donner. *Fundamental Astronomy*. Springer-Verlag, Berlin Heidelberg, 3rd Edition, 1996. ISBN: 3-540-60936-9.

[45] T.S. Kelso. Validation of SGP4 and IS-GPS-200D Against GPS Precision Ephemerides. In *17th AAS/AIAA Space Flight Mechanics Conference, Sedona, Arizona, USA, Jan 28th - Feb 1st, 2007,* 2007.

[46] P.W. Kervin, D. Hall, M. Bolden, and J. Toth. Phase Angle: What is it good for? In *Proceedings of the 2010 AMOS Technical Conference, 14-17 September 2010, Maui, Hawaii, USA,* 2010.

[47] D. King-Hele. *Theory of Satellite Orbits in an Atmosphere*. Butterworths London, 1964. Chapter 4, pp. 40 – 77.

[48] D.E. Knuth. *The Art of Computer Programming*. Volume 1: Fundamental Algorithms. Addison-Wesley, Third Edition, 2007. ISBN: 0-201-89683-4.

[49] V. Kouprianov. Distinguishing Features of CCD Astronomy of Faint Objects. *Advances in Space Research*, (41):1029 – 1038, 2008.

[50] V. Kouprianov. Advanced Image Processing Techniques for Automatic Reduction of GEO Survey Data. In *Proceedings of the 8th US-Russian Workshop on Space Surveillance, Wailea Marriott Resort Wailea, Maui, HI, 18-23 April 2010, 331 – 452,* 2010.

[51] Y. Kozai. The Motion of a Close Earth Satellite. *Astronomical Journal*, 1274(64):367 – 377, 1959.

[52] M.H. Lane and K.H. Cranford. An Improved Analytical Drag Theory for the Atrificial Satellite Problem. In *AIAA Paper 69 – 925*, August, 1969.

[53] S. Larsson. Parameter Estimation in Epoch Folding Analysis. *Astron. Astrophys. Supp. Ser.*, 117:197 – 201, 1996.

[54] C. Lawson and R. Hanson. *Solving Least Squares Problems*. Prentice-Hall, Inc., Englewood Cliffs, 1974.

[55] J.-C. Liou. A Parametric Study on Using Active Debris Removal for LEO Environtment Remediation. In *Proceedings of the International Astronautical Congress 2010, A6.2.5, Prague, Czech Republic, 27 Sep-1 Oct, 2010,* 2010.

[56] J.-C. Liou and J.K. Weaver. Orbital Dynamics of High Area-to-Mass Ratio Debris and Their Distribution in the Geosynchronos Region. In *Proceedings of the Forth European Conference on Space Debris, pp. 119-124, ESOC, Darmstadt, Germany, 18-20 April 2005*, 2005.

[57] P. Magnusson et al. Determination of Pole Orientations and Shapes of Asteroids. *Asteroids II (edited by R. Binzel et. al.)*, 153:24 – 36, 1981.

[58] P. Magnusson et al. Distribution of Spin Axis and Senses of Rotation of 20 Asteroids. *Icarus*, 68:1 – 39, 2001.

[59] P. Martz. *OpenSceneGraph – Quick Start Guide*. Computer Graphics Systems Development Corporation, Mountain View, California, 2007.

[60] A. Milani, G.F. Gronchi, D. Farnocchia, G. Tommei, and L. Dimare. Optimization of Space Surveillance Resources by Innovative Preliminary Orbit Methods. In *Proceedings of the Fifth European Conference on Space Debris, ESOC, Darmstadt, Germany, 30 March-2 April 2009*, 2009.

[61] A. Milani, M.E. Sansaturio, and S.R. Chesley. The Asteroid Identification Problem IV: Attributions. *Icarus*, 151:150 – 159, 2001.

[62] H. Minkowski. Volumen und Oberfläche. *Mathematische Annalen*, 57:447 – 495, 1903.

[63] R. Musci. *Identification and Recovery of Objects in GEO and GTO to Maintain a Catalogue of Orbits*. Astronomical Institute, University of Bern, 2006. PhD thesis.

[64] R. Musci, T. Schildknecht, T. Flohrer, and G. Beutler. Concept for a Catalogue of Space Debris in GEO. In *Proceedings of the Fourth European Conference on Space Debris, pp. 601-606, ESOC, Darmstadt, Germany, 18-20 April 2005*, 2005.

[65] R. Musci, T. Schildknecht, and M. Ploner. Orbit Improvement for GEO Objects Using Follow-up Obervations. *Advances in Space Research*, 34(5):912–916, 2004.

[66] R. Musci, T. Schildknecht, and M. Ploner. Analyzing long Observation Arcs for Objects with high Area-to-Mass Ratios in Geostationary Orbits. In *Acta Astronautica*, volume 66, pp 693-703, 2010.

[67] R. Musci, T. Schildknecht, M. Ploner, and G. Beutler. Orbit Improvement for GTO Objects Using Follow-up Obervations. *Advances in Space Research*, 35(7):1236–1242, 2005.

[68] J.N. Opiela, J.-C. Liou, P.D. Anz-Meador, and Q.L. Juarez. Data Collected During the Post-Flight Survey of Micrometeiroid and Orbital Debris Impact Features on the Hubble Wide Field Planetary Camera 2. In *Proceedings of the International Astronautical Congress 2010, A6.1.10, Prague, Czech Republic, 27 Sep-1 Oct, 2010*, 2010.

[69] F. Paolillo, M. Profilio, and F. Piergentili. First Italian Space Debris Observatory: The Image Processing Automation. In *Proceedings of the International Astronautical Congress 2007, IAC-07-A6.I.05., Hyderabad, India, 21 - 28 Sep, 2007*, 2007.

[70] M. Ploner, T. Schildknecht, C. Früh, and A. Vananti. Space Surveillance Observations at the Zimmerwald Observatory. In *Proceedings of the Fifth European Conference on Space Debris, ESOC, Darmstadt, Germany, 30 March-2 April 2009*, 2009.

[71] W. Press et al. *Numerical Recipes in FORTRAN: The Art of Scintific Computing*. Cambridge University Press, New York, 1992. second edition.

[72] J. Prewitt. Object Enhancement and Extraction. *Picture Processing and Psychopictorics, Academic Press, New York – London, Edited by B.S. Lipkin and A.Rosenfeld*, pages 75 – 149, 1970.

[73] H.N. Russel. On the Light-Variations of Asteroids and Sattelites. *Astrophys. J.*, 24(5):1–18, 1906.

[74] Russian Space Web Homepage. by Anatoly Zak. `http://www.russianspaceweb.com/`, 2011.

[75] J. Scargle. Studies in Astronomical Time Series Analysis II. Statistical Aspects of Spectral Analysis of Unevenly Spaced Data. *The Astrophysical Journal*, 263:834 – 53, 1982.

[76] T. Schildkecht, C. Früh, A. Hinze, and J. Herzog. Dynamical Properties of High Area to Mass Ratio Objects in GEO-Like Orbits. *Advances in Space Research*, to be published 2011.

[77] T. Schildknecht. *Optical Astrometry of Fast Moving Objects Using CCD Detectors*. Astronomical Institute, University of Bern, 1994. PhD thesis.

[78] T. Schildknecht. Optical Surveys for Space Debris. *Astron. Astrophys. Rev.*, 14:14–111, DOI 10.2007/s00159–006–003–9, 2007.

[79] T. Schildknecht, W. Flury, C. Früh, J. Herzog, A. Hinze, and A. Vananti. Using Optical Observations to Survey, Track, and Characterize Small-Size Objects at High Altitudes. In *Proceedings of 28th International Symposium on Space Technology and Science, June 5-12, Okinawa, Japan, 2011*, 2011.

[80] T. Schildknecht, U. Hugentobler, P. Fridez, and P. Kunszt. CCD Off-Line Data Processing System: Software User Manual. In *ESA/ESAOC Contract No. 11435/95/D/IM, ESA Study Managers: W. Flury and A. Massart*, November, 1998.

[81] T. Schildknecht, U. Hugentobler, A. Verdun, and G. Beutler. Final Report: CCD Algorithms for Space Debris Detection. In *ESA/ESAOC Contract No. 10623/93/D/IM, ESA Study Managers: W. Flury*, September, 1995.

[82] T. Schildknecht, R. Musci, W. Flury, J. Kuusela, J. de León Cruz, and L. de Fatima Domínguez Palmero. Properties of the High Area-to-Mass Ratio Space Debris Population in GEO. In *Proceedings of the 2005 AMOS Technical Conference, 5-9 September 2005, Maui, Hawaii, USA*, 2005.

[83] T. Schildknecht, R. Musci, C. Früh, and M. Ploner. Color Photometry and Light Curve Observations of Space Debris GEO. In *Proceedings of the International Astronautical Congress 2008, A6.1.4, Glasgow, Scotland, Great Britain, 29 Sep- 3 Oct, 2008*, 2008.

[84] T. Schildknecht, R. Musci, M. Ploner, G. Beutler, J. Kuusela, J. de León Cruz, and L. de Fatima Domínguez Palmero. Optical Observations of Space Debris in GEO and in Highly-Eccentric Orbits. *Advances in Space Research*, 34(5):901–911, 2004.

[85] T. Schildknecht, A. Vananti, H. Krag, and C. Erd. Physical Characterization of High AMR Debris by Optical Reflectance Spectrometry. In *Proceedings of the International Astronautical Congress 2010, A6.1.7, Prague, Czech Republic, 27 Sep-1 Oct, 2010*, 2010.

[86] P. Shirley. *Fundamentals of Computer Graphics*. A K Peters, Ltd, 2002. ISBN 1-56881-124-1.

[87] Stansbery, E. Presentation and Private Communication. 37th COSPAR Scientific Assembly, 18-25 July, Bremen, 2010.

[88] Sykrocket Homepage. by Gunter Krebs. `http://www.skyrocket.de/`, 2011.

[89] G. Tommei, A. Milani, D. Farnocchia, and A. Rossi. Correlation of Space Debris Observations by the Virtual Debris Algorithm. In *Proceedings of the Fifth European Conference on Space Debris, ESOC, Darmstadt, Germany, 30 March-2 April 2009*, 2009.

[90] US Air Force. United States Strategic Command Website. `http://www.stratcom.mil/factsheets/jspoc/`, 2010.

[91] D. Valado, R. Crawford, R. Hujsak, and T.S. Kelso. Revisiting Space Track Report #3. *AIAA 2006-6753*, American Institute of Aeronautics und Astronautics, 2006.

[92] D. Vallado, V. Agapov, and I. Molotov. Orbit Determination Issues and Results to Incorporate Optical Measurements in Conjunction Operations. In *Proceedings of the Fifth European Conference on Space Debris, ESOC, Darmstadt, Germany, 30 March-2 April 2009*, 2009.

[93] D. Vallado and W. McCain. *Fundmentals of Astrodynamics and Applications*. Microcosm Press, El Segundo, California, 2001. ISBN 0-7923-6903-3.

[94] P.H. Winston. *Artificial Intelligence*. Addison-Wesley Publishing Company, 3rd Edition, 1992. ISBN: 0-201-53377-4.

[95] T. Yanagisawa, H. Kurosaki, and A. Nakajima. Present Status of Space Debris Optical Observational Facility of JAXA at Mt. Nyukasa. In *Proceedings of the Fifth European Conference on Space Debris, ESOC, Darmstadt, Germany, 30 March-2 April 2009*, 2009.

[96] D. Ziou and S. Tabbone. Edge Detection Techniques - An Overview. *International Journal on Pattern Recognition and Image Analysis*, (8(4)):537–559, 1998.

And we hear his voice, we read his lips, and in our work we give birth to the children of God who sing his praise. And if we are not that, then we are nothing.
Stephen J. Rivele

Carolin Früh studied physics and philosophy at the University of Karlsruhe, Germany and the University of British Columbia, Canada. After a master thesis in theoretical particle physics, she completed her PhD in Physics with Special Qualification in Astronomy at the Astronomical Institute of the University of Bern, Switzerland, in 2011.